

# **COMPUTER AIDED DESIGN AND OPTIMIZATION OF BI-LAYERED TUBE HYDROFORMING PROCESS**

**By**

**Abed Alaswad, B. Eng.**

This thesis is submitted to Dublin City University in fulfilment of the requirement for the  
awarding of the degree of

**DOCTOR OF PHILOSOPHY**

**Supervisors:**

**Dr. A. G. Olabi**

**Dr. Khaled Benyounis**

**School of Mechanical and Manufacturing Engineering**

**Dublin City University**

**November 2012**

## Declaration

I hereby certify that this material, which I now submit for assessment on the programme of study leading to the award of Ph.D. is entirely my own work, that I have exercised reasonable care to ensure that the work is original, and does not to the best of my knowledge breach any law of copyright, and has not been taken from the work of others have and to the extent that such work has been cited and acknowledged within the text of my work.

ID No.: 56122969

Date: \_\_\_\_\_

Signed: \_\_\_\_\_

## DEDICATION

*“My friends, leave just one wall*

*For wash lines*

*Leave a night to sing*

*I will hang your names wherever you want, so sleep a little*

*And sleep on the steps of the lemon vines*

*May I guard your dreams from the daggers of your guardians”*

*Mahmoud Darwish*

**THIS WORK IS DEDICATED TO ALL SYRIAN MARTYRS.**

## **ACKNOWLEDGEMENTS**

There were a great number of people who helped make this journey possible. Foremost, I would like to express my sincere gratitude to my supervisor, Dr. Abdul Ghani Olabi, of the School of Mechanical and Manufacturing Engineering, Dublin City University, for his relentless, encouragement, constructive guidance and words of motivation throughout the duration of this research study and moreover for the inspiration he provided to ensure the completion of this work. His expertise, availability to discuss ideas and willingness to give of his knowledge were instrumental. My genuine appreciation to Dr. Khaled Benyounis for all of his help and support. For this, I will be eternally grateful.

Special thanks to both Mr. Liam Domican and Mr. Chris Crouch for their helpful discussions and technical support and assistance.

Last but not least, I would like to express my thanks to my wife and best friend, Nour Kadan, without whose love and encouragement, I would not have finished this thesis. I would also thank my parents, Humam Al-Asswad and Shoula Aboudan, for all their heartfelt prayers and especially to my brother and sisters, my friends and colleagues for all their good wishes of encouragement and support over the last few years, which will always be remembered with deep gratitude.

**Abstract:**

Tube hydroforming is one of the unconventional metal forming processes in which high fluid pressure and axial feed are used to deform a tube blank in the desired shape. However, production of bi-layered tubular components using this process has not been investigated in detail in spite of the large number of research studies conducted in this area. Bi-layered tubing can be useful in complex working environments as it offers dual properties that a single layer structure doesn't have. Consequently, for wider implementation of this technology, a detailed investigation on bi-layered tube hydroforming is required.

In this research, both single and bi-layered tube hydroforming processes were numerically modelled using the finite element method (ANSYS LS-DYNA). Experiments were conducted to check the numerical models validation. In addition, Response Surface Methodology (RSM) using the Design-Expert statistical software has been employed along with the finite element modelling to attain a detailed investigation of bi-layered tube hydroforming in the X-type and T-type dies. The process outputs were modelled as functions of both the geometrical factors (tube length, tube diameter, die corner radius, and thicknesses of both layers.) and the process parameters (internal pressure coordinates, axial feed, and coefficient of friction.). Furthermore, the desirability approach was used in conjunction with the RSM models to identify the optimal combinations of each the geometrical factors and process parameters that achieve different objectives simultaneously. In addition, a different optimization approach that applies the iterative optimization algorithm in the ANSYS software was implemented in the process optimization.

The finite element models of single and bi-layered tube hydroforming processes were experimentally validated. A comparison of both processes was carried out under different loading paths. Also, response surface modelling of the bi-layered tube hydroforming process outputs was successfully achieved, and the main effects and interaction effects of the input parameters on the responses were discussed. Based on the RSM models, the process was optimized by finding the inputs levels at which the desired objectives are satisfied. Finally, a comparison of the RSM based optimization approach and the iterative optimization algorithm was performed based on the optimum results of each technique.

## TABLE OF CONTENTS:

<b>DECLARATION.....</b>	<b>I</b>
<b>DEDICATION.....</b>	<b>II</b>
<b>ACKNOWLEDGMENTS.....</b>	<b>III</b>
<b>ABSTRACT.....</b>	<b>IV</b>
<b>TABLE OF CONTENTS.....</b>	<b>V</b>
<b>LIST OF FIGURES.....</b>	<b>VIII</b>
<b>LIST OF TABLES.....</b>	<b>XIV</b>
<b>LIST OF PUBLICATIONS .....</b>	<b>XVIII</b>
<b>CHAPTER ONE .....</b>	<b>1</b>
<b>INTRODUCTION.....</b>	<b>1</b>
1.1. INTRODUCTION.....	1
1.2. BI-LAYERED TUBE HYDROFORMING .....	3
1.3. MOTIVATION AND RESEARCH OBJECTIVE .....	5
1.4. THESIS LAYOUT .....	6
<b>CHAPTER TWO .....</b>	<b>7</b>
<b>LITERATURE REVIEW .....</b>	<b>7</b>
2.1. INTRODUCTION.....	7
2.2. ANALYTICAL STUDIES.....	7
2.3. FINITE ELEMENT MODELLING .....	10
2.4. INVESTIGATION OF THE FACTORS AFFECTING THE PROCESS OUTPUT.....	13
2.4.1. <i>Effect of material properties on the process output:</i> .....	13
2.4.2. <i>Effect of geometrical factors on the process output</i> .....	15
2.4.3. <i>Effect of process parameters on the process output</i> .....	16
2.4.4. <i>Effect of friction and lubricating on the process output</i> .....	18
2.5. INSTABILITIES AND FAILURES .....	21
2.5.1. <i>Instabilities overview</i> .....	21
2.5.2. <i>Forming limit diagrams (FLD)</i> .....	23
2.5.3. <i>Improvements resulting in delayed bursting</i> .....	24
2.6. PROCESS OPTIMIZATION .....	26
2.7. SUMMARY .....	28
<b>CHAPTER THREE .....</b>	<b>30</b>
<b>EXPERIMENTAL DESIGN .....</b>	<b>30</b>
3.1. INTRODUCTION.....	30
3.2. TUBE HYDROFORMING MACHINE .....	30
3.2.1. <i>Machine design</i> .....	32
3.2.2. <i>Dies details</i> .....	34

3.2.3. <i>Machine control</i> .....	35
3.3. TUBES USED IN THE BI-LAYERED TUBE HYDROFORMING PROCESS.....	40
3.3.1. <i>Brass tubes annealing</i> .....	41
3.3.2. <i>Effect of material annealing on the hydroformability of brass tubes</i> .....	43
3.3.3. <i>Material properties</i> .....	46
3.4. MEASURING EQUIPMENTS: .....	48
3.5. EXPERIMENTAL STUDY.....	50
3.6. SUMMARY .....	57
<b>CHAPTER FOUR .....</b>	<b>58</b>
<b>NUMERICAL ANALYSIS.....</b>	<b>58</b>
4.1. INTRODUCTION.....	58
4.2. FINITE ELEMENT MODELLING OF X- AND T- BRANCH BI-LAYERED TUBE HYDROFORMING .....	58
4.3. EXPERIMENTAL VALIDATION OF THE BI-LAYERED TUBE HYDROFORMING NUMERICAL MODELING .....	63
4.3.1. <i>Loading paths adjustment</i> .....	63
4.3.2. <i>Numerical and experimental results comparison</i> .....	66
4.4. FINITE ELEMENT COMPARISON OF SINGLE AND BI-LAYERED TUBE HYDROFORMING.....	76
4.4.1. <i>Finite element model of single layer tube hydroforming</i> .....	76
4.4.2. <i>Experimental validation of the single layer tube hydroforming numerical model</i> .....	78
4.4.3. <i>Single and bi-layered tube hydroforming comparison</i> .....	84
4.5. SUMMARY .....	89
<b>CHAPTER FIVE .....</b>	<b>90</b>
<b>INVESTIGATION ON THE EFFECT OF DESIGN PARAMETERS ON BI-LAYERED TUBE HYDROFORMING PROCESS</b>	
<b>OUTPUT .....</b>	<b>90</b>
5.1. INTRODUCTION.....	90
5.2. DESIGN OF EXPERIMENTS OUTLINE .....	90
5.3. RESPONSE SURFACE METHOD .....	91
5.4. INVESTIGATION OF THE EFFECT OF DESIGN PARAMETERS ON THE BI-LAYERED TUBE HYDROFORMING.....	93
5.4.1. <i>Geometrical factors analysis of X-shape bi-layered tube hydroforming</i> .....	94
5.4.2. <i>Process parameters analysis of X-shape bi-layered tube hydroforming</i> .....	117
5.4.3. <i>Geometrical factors analysis of T-shape bi-layered tube hydroforming</i> .....	132
5.4.4. <i>Process parameters analysis of T-shape bi-layered tube hydroforming</i> .....	146
5.5. SUMMARY .....	156
<b>CHAPTER SIX .....</b>	<b>157</b>
<b>OPTIMIZATION STUDY .....</b>	<b>157</b>
6.1. INTRODUCTION.....	157
6.2. RESPONSE SURFACES MODELS BASED OPTIMIZATION .....	157
6.2.2. <i>Optimization approach in Design-expert V7 software</i> .....	160
6.3. MULTI-RESPONSE OPTIMIZATION IN X-SHAPE BI-LAYERED TUBE HYDROFORMING .....	161
6.3.1. <i>Geometrical factors optimization in X-type bi-layered tube hydroforming</i> .....	161
6.3.2. <i>Process parameters optimization in X-type bi-layered tube hydroforming</i> .....	165
6.4. MULTI-RESPONSE OPTIMIZATION IN T-TYPE BI-LAYERED TUBE HYDROFORMING .....	170
6.4.1. <i>Geometrical factors optimization in T-type bi-layered tube hydroforming</i> .....	170

6.4.2. <i>Process parameters optimization in T-type bi-layered tube hydroforming</i> .....	174
6.5. INVESTIGATION OF THE PROCESS OPERATING COST MINIMIZATION .....	178
6.5.1. <i>Evaluation of the process operating cost function</i> .....	178
6.5.2. <i>Operating cost minimization</i> .....	178
6.6. BI-LAYERED TUBE HYDROFORMING OPTIMIZATION USING ANSYS OPTIMIZER .....	182
6.6.1. <i>Optimization method overview</i> .....	182
6.6.2. <i>Application of the ANSYS optimizer in single objective optimization</i> .....	186
6.6.3. <i>Application of the RSM based technique in single objective optimization</i> .....	188
6.6.4. <i>Comparison of ANSYS optimization technique and RSM based optimization method for bi-layered tube hydroforming design</i> .....	190
6.7. SUMMARY .....	191
<b>CHAPTER SEVEN .....</b>	<b>192</b>
<b>CONCLUSIONS AND RECOMMENDATIONS FOR FUTURE WORK .....</b>	<b>192</b>
7.1. CONCLUSIONS .....	192
7.2. FUTURE WORK .....	192
<b>APPENDIX. A .....</b>	<b>194</b>
A.1. BOX BEHNKEN DESIGN DESIGNING FOR THREE FACTORS: .....	194

## LIST OF FIGURES

LIST OF FIGURES.....	VIII
FIGURE 1.1: TUBE HYDROFORMING SYSTEM.....	2
FIGURE 2.1: STAGES OF TUBE HYDROFORMING [20]. ....	8
FIGURE 2.2: EFFECT OF MATERIAL PROPERTIES ON WALL THICKNESS DISTRIBUTION [38]. ....	14
FIGURE 2.3: EFFECTS OF MATERIAL PROPERTIES ON BURSTING PRESSURE [44]. ....	15
FIGURE 2.4: EFFECT OF GEOMETRICAL FACTORS ON PROTRUSION HEIGHT [32].....	16
FIGURE 2.5: LOADING PATHS TYPES (A: PRESSURE ADVANCED, B: LINEAR, C: FEED ADVANCED) [59].....	18
FIGURE 2.6: FRICTION ZONES IN TUBE HYDROFORMING FOR T-SHAPE [61]. ....	20
FIGURE 2.7: FRICTION COEFFICIENT CHANGES WITH BOTH LUBRICATION VISCOSITY AND SURFACE ROUGHNESS [66]. ....	20
FIGURE 2.8: FORMING LIMITS FOR DIFFERENT ANISOTROPIC PARAMETERS AND STRAIN HARDENING EXPONENTS [81]. ....	23
FIGURE 2.9: OPERATING WINDOWS FOR DIFFERENT METALS [85]. ....	24
FIGURE 2.10: DIE STRUCTURE IN TUBE HYDROFORMING WITH COUNTER PUNCH [86]. ....	25
FIGURE 2.11: HYDROFORMING OF Y- SHAPES [87]. ....	25
FIGURE 2.12: APPLICATION OF A COUNTER PUNCH IN ASYMMETRIC BULGING, AND APPLICATION OF A DUAL PRESSURE SYSTEM IN AXISYMMETRIC BULGING [88]. ....	26
FIGURE 2.13: (A) DIRECT OPTIMIZATION. (B) APPROXIMATE OPTIMIZATION [89]. ....	27
FIGURE 3.1: THE TUBE HYDROFORMING MACHINE OF DUBLIN CITY UNIVERSITY.....	31
FIGURE 3.2: THE POWER SOURCE OF THE TUBE HYDROFORMING MACHINE. ....	32
FIGURE 3.3: THE HYDRAULIC CIRCUIT OF THE HYDROFORMING MACHINE [31]. ....	33
FIGURE 3.4: LOWER HALVES OF X-SHAPE AND T-SHAPE DIES. ....	35
FIGURE 3.5: CONTROL SWITCHES OF THE TUBE HYDROFORMING MACHINE.....	36
FIGURE 3.6: SOLENOID SWITCH CONNECTIONS OF THE MANUAL CONTROLS OF THE HYDROFORMING MACHINE [31]. ....	38
FIGURE 3.7: PROCESS FLOW DIAGRAM SHOWING CONTROL AND RECORDING SYSTEMS [47]. ....	39
FIGURE 3.8: A SCREEN SHOT SHOWING THE AUTOMATED CONTROL PANEL OF THE TUBE HYDROFORMING MACHINE [102]. ....	40
FIGURE 3.9: ANNEALING FURNACE.....	42
FIGURE 3.10: PANEL CONTROL FOR THE FURNACE ....	42
FIG 3.11: ANNEALED SAMPLES INSIDE THE FURNACE. ....	43
FIGURE 3.12: TUBES AT AXIAL PRESSURE 50 [BAR]. ....	43
FIGURE 3.13: TUBES AT AXIAL PRESSURE 60 [BAR]. ....	44

FIGURE 3.14: TUBES AT AXIAL PRESSURE 70 [BAR].	44
FIGURE 3.15: TUBES AT AXIAL PRESSURE 80 [BAR].	44
FIGURE 3.16: TUBES AT AXIAL PRESSURE 90 [BAR].	45
FIGURE 3.17: TUBES AT AXIAL PRESSURE 100 [BAR].	45
FIGURE 3.18: EFFECT OF AXIAL LOAD ON THE BULGE HEIGHT OF ANNEALED AND NON-ANNEALED HYDROFORMED SAMPLES.	46
FIGURE 3.19: TENSILE TEST MACHINE	47
FIGURE 3.20: THE TRUE STRESS STRAIN CURVE FOR THE ANNEALED BRASS MATERIAL (OUTER LAYER).	47
FIGURE 3.21: THE TRUE STRESS STRAIN CURVE FOR THE COPPER MATERIAL (INNER LAYER).	48
FIGURE 3.22: COORDINATE MEASURING MACHINE.	49
FIGURE 3.23: OPTICAL MICROSCOPE.	50
FIGURE: 3.24: X-SHAPE HYDROFORMED PARTS.	52
FIGURE. 3.26: EFFECT OF AXIAL FEED ON X-SHAPE BULGE HEIGHT.	53
FIGURE 3.27: EFFECT OF AXIAL FEED ON X-SHAPE BRANCH TOP THICKNESS.	54
FIGURE 3.28: BI-LAYERED T-SHAPE HYDROFORMED PARTS FROM DIFFERENT TUBES LENGTHS.	55
FIGURE 3.29: EFFECT OF TUBE LENGTH ON THE T-SHAPE BULGE HEIGHT.	56
FIGURE 3.30: EFFECT OF THE TUBE LENGTH ON THE T-SHAPE BULGE TOP THICKNESS.	56
FIGURE. 4.1: SIMULATION OF X-BRANCH BI-LAYERED TUBE HYDROFORMING (ONE EIGHTH).	59
FIGURE. 4.2: SIMULATION OF T-BRANCH BI-LAYERED TUBE HYDROFORMING (ONE FOURTH).	60
FIGURE 4.3: WRINKLE HEIGHT VALUE WITH DIFFERENT MESH DENSITIES.	61
FIGURE 4.4: A COMPARISON OF INTERNAL ENERGY AND HOURGLASS ENERGY (1: OUTER LAYER AND 2: INNER LAYER)	63
FIGURE 4.5: EXPERIMENTAL AND SIMULATED LOADING PATHS IN X-BRANCH BI-LAYERED TUBE HYDROFORMING (TEST-A).	64
FIGURE 4.6: EXPERIMENTAL AND SIMULATED LOADING PATHS IN X-BRANCH BI-LAYERED TUBE HYDROFORMING (TEST-B).	65
FIGURE 4.7: EXPERIMENTAL AND SIMULATED LOADING PATHS IN T-BRANCH BI-LAYERED TUBE HYDROFORMING (TEST- C).	65
FIGURE 4.8: EXPERIMENTAL AND SIMULATED LOADING PATHS IN T-BRANCH BI-LAYERED TUBE HYDROFORMING (TEST- D).	66
FIGURE. 4.9: NUMERICAL RESULT OF X-TYPE BI-LAYERED TUBE HYDROFORMING (TEST- A).	67
FIGURE 4.10: EXPERIMENTAL RESULT OF X-TYPE BI-LAYERED TUBE HYDROFORMING (TEST- A).	67
FIGURE 4.11: NUMERICAL RESULT OF X-TYPE BI-LAYERED TUBE HYDROFORMING (TEST- B).	68
FIGURE 4.12: EXPERIMENTAL RESULT OF X-TYPE BI-LAYERED TUBE HYDROFORMING (TEST- B).	68

FIGURE 4.13: NUMERICAL RESULT OF T-TYPE BI-LAYERED TUBE HYDROFORMING (TEST-C).....	69
FIGURE 4.14: EXPERIMENTAL RESULT OF T-TYPE BI-LAYERED TUBE HYDROFORMING (TEST-C).....	69
FIGURE 4.15: NUMERICAL RESULT OF T-TYPE BI-LAYERED TUBE HYDROFORMING (TEST-D). ....	70
FIGURE 4.16: EXPERIMENTAL RESULT OF T-TYPE BI-LAYERED TUBE HYDROFORMING (TEST-D). ....	70
FIGURE 4.17: EXPERIMENTAL AND NUMERICAL HYDROFORMED BRANCH PROFILE (TEST-A).....	71
FIGURE 4.18: EXPERIMENTAL AND NUMERICAL HYDROFORMED BRANCH PROFILE (TEST-B).....	71
FIGURE 4.19: EXPERIMENTAL AND NUMERICAL HYDROFORMED BRANCH PROFILE (TEST-C). ....	72
FIGURE 4.20: EXPERIMENTAL AND NUMERICAL HYDROFORMED BRANCH PROFILE (TEST-D).....	72
FIGURE 4.21: EXPERIMENTAL AND NUMERICAL WALL THICKNESS DISTRIBUTION (TEST- A).....	73
FIGURE 4.22: EXPERIMENTAL AND NUMERICAL WALL THICKNESS DISTRIBUTION (TEST- B).....	73
FIGURE 4.23: EXPERIMENTAL AND NUMERICAL WALL THICKNESS DISTRIBUTION (TEST- C).....	74
FIGURE 4.24: EXPERIMENTAL AND NUMERICAL WALL THICKNESS DISTRIBUTION (TEST- D). ....	74
FIGURE 4.25: DISPLACEMENT NUMERICAL RESULT FOR THE DEFORMED LAYERS OF TEST-A.....	75
FIGURE 4.26: STRESS NUMERICAL RESULT FOR THE DEFORMABLE LAYERS OF TEST-A.....	76
FIGURE 4.27: FINITE ELEMENT SIMULATION OF SINGLE LAYER TUBE HYDROFORMING. ....	77
FIGURE 4.28: EXPERIMENTAL AND SIMULATION LOADING PATHS IN A T-BRANCH SINGLE LAYER TUBE HYDROFORMING (TEST- E).....	79
FIGURE 4.29: EXPERIMENTAL AND SIMULATION LOADING PATHS IN A T-BRANCH SINGLE LAYER TUBE HYDROFORMING (TEST- F).....	79
FIGURE 4.30: NUMERICAL RESULT OF TEST- E. ....	80
FIGURE 4.31: EXPERIMENTAL RESULT OF TEST- E. ....	80
FIGURE 4.32: NUMERICAL RESULT OF TEST- F. ....	81
FIGURE 4.33: EXPERIMENTAL RESULT OF TEST- F. ....	81
FIGURE 4.34: EXPERIMENTAL AND NUMERICAL HYDROFORMED BRANCH PROFILE (TEST-E). ....	82
FIGURE 4.35: EXPERIMENTAL AND NUMERICAL HYDROFORMED BRANCH PROFILE (TEST-F). ....	82
FIGURE 4.36: EXPERIMENTAL AND NUMERICAL THICKNESS DISTRIBUTION (TEST- E). ....	83
FIGURE 4.37: EXPERIMENTAL AND NUMERICAL THICKNESS DISTRIBUTION (TEST- F). ....	83
FIGURE 4.38: APPLIED LOADING PATHS FOR SINGLE AND BI-LAYERED TUBE HYDROFORMING.....	85
FIGURE 4.39: HYDROFORMED PARTS PRODUCED BY DIFFERENT LOADING PATHS TYPES. ....	86
FIGURE 4.40: BULGE HEIGHT COMPARISONS BETWEEN SINGLE AND BI-LAYERED TUBE HYDROFORMING.....	87
FIGURE 4.41: THICKNESS REDUCTION COMPARISONS BETWEEN SINGLE AND BI-LAYERED TUBE HYDROFORMING.....	87
FIGURE 4.42: A COMPARISON OF BI-LAYERED TUBE HYDROFORMING (A) AND SINGLE TUBE HYDROFORMING (B) UNDER LOADING PATH (E). ....	89

FIGURE 5.1: A SCHEMATIC DIAGRAM FOR BBD OF THREE FACTORS [114].....	92
FIGURE 5.2: INTERNAL PRESSURE COORDINATES (INITIAL VALUES).....	94
FIGURE 5.3: SCATTER DIAGRAM OF BULGE HEIGHT.....	101
FIGURE 5.4: SCATTER DIAGRAM OF THICKNESS REDUCTION.....	101
FIGURE 5.5: SCATTER DIAGRAM OF WRINKLE HEIGHT.....	102
FIGURE 5.6: PERTURBATION OF THE BULGE HEIGHT.....	103
FIGURE 5.7: CONTOUR GRAPH SHOWING THE EFFECT OF D AND $T_1$ ON BULGE HEIGHT.....	104
FIGURE 5.8: CONTOUR GRAPH SHOWING THE EFFECT OF D AND $T_2$ ON BULGE HEIGHT.....	104
FIGURE 5.9: WALL THICKNESS REDUCTION OF THE HYDROFORMED COMPONENT.....	105
FIGURE 5.10: PERTURBATION OF THE WALL THICKNESS REDUCTION. ....	106
FIGURE 5.11: INTERACTION EFFECT OF THE DIE CORNER RADIUS AND INNER LAYER THICKNESS ON THE WALL THICKNESS REDUCTION.....	107
FIGURE 5.12: INTERACTION EFFECT OF THE TUBE DIAMETER AND INNER LAYER THICKNESS ON WALL THICKNESS REDUCTION. ....	108
FIGURE 5.13: INTERACTION EFFECT OF THE TUBE DIAMETER AND OUTER LAYER THICKNESS ON WALL THICKNESS REDUCTION. ....	109
FIGURE 5.14: WRINKLE FORMATION IN THE BI-LAYERED TUBE HYDROFORMING PROCESS. ....	110
FIGURE 5.15: PERTURBATION OF THE WRINKLE HEIGHT.....	111
FIGURE 5.16: INTERACTION EFFECT OF THE DIE CORNER RADIUS AND TUBE LENGTH ON WRINKLE HEIGHT. ....	112
FIGURE 5.17: INTERACTION EFFECT OF THE TUBE DIAMETER AND TUBE LENGTH ON WRINKLE HEIGHT. ....	113
FIGURE 5.18: INTERACTION EFFECT OF THE TUBE LENGTH AND OUTER LAYER THICKNESS ON WRINKLE HEIGHT.....	114
FIGURE 5.19: INTERACTION EFFECT OF TUBE LENGTH AND INNER LAYER THICKNESS ON WRINKLE HEIGHT. ....	115
FIGURE 5.20: INTERACTION EFFECT OF INNER LAYER THICKNESS AND TUBE DIAMETER ON WRINKLE HEIGHT.....	116
FIGURE 5.21: INTERACTION EFFECT OF THE OUTER AND INNER LAYER THICKNESS ON WRINKLE HEIGHT. ....	117
FIGURE 5.22: SCATTER DIAGRAM OF BULGE HEIGHT.....	123
FIGURE 5.23: SCATTER DIAGRAM OF THICKNESS REDUCTION.....	123
FIGURE 5.24: SCATTER DIAGRAM OF WRINKLE HEIGHT.....	124
FIGURE 5.25: PERTURBATION OF THE BULGE HEIGHT.....	125
FIGURE 5.26: INTERACTION PLOT BETWEEN THE INTERNAL PRESSURE ( $P_2$ ) AND THE AXIAL FEED (S). ....	126
FIGURE 5.27: PERTURBATION OF THE WALL THICKNESS REDUCTION. ....	127
FIGURE 5.28: INTERACTION PLOT BETWEEN THE INITIAL INTERNAL PRESSURE ( $P_2$ ) AND AXIAL FEED DISPLACEMENT (S). ....	128

FIGURE 5.29: INTERACTION PLOT OF THE COEFFICIENT OF FRICTION (F) AND AXIAL FEED DISPLACEMENT (S). .....	129
FIGURE 5.30: PERTURBATION OF WRINKLE HEIGHT.....	130
FIGURE 5.31: INTERACTION PLOT OF INITIAL INTERNAL PRESSURE ( $P_2$ ) AND AXIAL FEED DISPLACEMENT (S)....	131
FIGURE 5.32: INTERACTION PLOT OF COEFFICIENT OF FRICTION (F) AND AXIAL FEED DISPLACEMENT (S).....	132
FIGURE 5.33: SCATTER DIAGRAM OF BULGE HEIGHT. ....	136
FIGURE 5.34: SCATTER DIAGRAM OF THICKNESS REDUCTION. ....	137
FIGURE 5.35: PERTURBATION PLOT OF BULGE HEIGHT .....	138
FIGURE 5.36: INTERACTION EFFECT OF THE TUBE DIAMETER AND OUTER TUBE THICKNESS ON BULGE HEIGHT. ....	139
FIGURE 5.37: INTERACTION EFFECT OF THE TUBE DIAMETER AND INNER TUBE THICKNESS ON BULGE HEIGHT. ....	140
FIGURE 5.38: INTERACTION EFFECT OF THE INNER AND OUTER LAYER THICKNESSES ON BULGE HEIGHT.....	141
FIGURE 5.39: PERTURBATION PLOT OF WALL THICKNESS REDUCTION. ....	142
FIGURE 5.40: INTERACTION EFFECT OF THE TUBE DIAMETER AND TUBE LENGTH ON WALL THICKNESS REDUCTION. ....	143
FIGURE 5.41: INTERACTION EFFECT OF THE TUBE DIAMETER AND OUTER LAYER THICKNESS ON WALL THICKNESS REDUCTION. ....	144
FIGURE 5.42: INTERACTION EFFECT OF THE TUBE DIAMETER AND INNER LAYER THICKNESS ON WALL THICKNESS REDUCTION. ....	145
FIGURE 5.43: INTERACTION EFFECT OF THE INNER AND OUTER LAYER THICKNESSES ON WALL THICKNESS REDUCTION. ....	146
FIGURE 5.44: SCATTER DIAGRAM OF BULGE HEIGHT. ....	150
FIGURE 5.45: SCATTER DIAGRAM OF THICKNESS REDUCTION. ....	151
FIGURE 5.46: PERTURBATION OF BULGE HEIGHT. ....	152
FIGURE 5.47: PERTURBATION OF THICKNESS REDUCTION. ....	153
FIGURE 5.48: INTERACTION PLOT BETWEEN $P_2$ AND AXIAL FEED VELOCITY. ....	154
FIGURE 5.49: PLOT SHOWING THE INTERACTION BETWEEN $P_2$ AND COEFFICIENT OF FRICTION.....	155
FIGURE 5.50: PLOT SHOWING THE INTERACTION BETWEEN COEFFICIENT OF FRICTION AND AXIAL FEED DISPLACEMENT. ....	156
FIGURE. 6.1: OPTIMIZATION STEPS [114]. ....	160
FIGURE 6.2: GRAPHICAL OPTIMIZATION OF THE FIRST CRITERION. ....	163
FIGURE 6.3: GRAPHICAL OPTIMIZATION OF THE SECOND CRITERION. ....	164
FIGURE 6.4: GRAPHICAL OPTIMIZATION OF THE FIRST CRITERION. ....	168
FIGURE 6.5: GRAPHICAL OPTIMIZATION OF THE SECOND CRITERION. ....	169

<b>FIGURE 6.6: GRAPHICAL OPTIMIZATION OF THE FIRST CRITERION .....</b>	<b>172</b>
<b>FIGURE 6.7: GRAPHICAL OPTIMIZATION OF THE SECOND CRITERION .....</b>	<b>173</b>
<b>FIGURE 6.8: GRAPHICAL OPTIMIZATION OF THE FIRST CRITERION .....</b>	<b>176</b>
<b>FIGURE 6.9: GRAPHICAL OPTIMIZATION OF THE SECOND CRITERION .....</b>	<b>177</b>
<b>FIGURE 6.10: GRAPHICAL INVESTIGATION OF COST REDUCTION IN THE FIRST CRITERION OF THE GEOMETRICAL FACTORS OPTIMIZATION (X-TYPE).....</b>	<b>180</b>
<b>FIGURE 6.11: GRAPHICAL INVESTIGATION OF COST REDUCTION IN THE SECOND CRITERION OF THE GEOMETRICAL FACTORS OPTIMIZATION (X-TYPE).....</b>	<b>181</b>

## LIST OF TABLES

TABLE 3.1: MANUAL CONTROL OF TUBE HYDROFORMING MACHINE.....	35
TABLE 3.2: MATERIAL PROPERTIES OF BOTH LAYERS.....	48
TABLE 4.1: EXPERIMENTAL AND NUMERICAL VALUES OF THE FINAL BULGE HEIGHT OF THE HYDROFORMED PARTS.....	75
TABLE 4.2: EXPERIMENTAL AND NUMERICAL VALUES OF FINAL BRANCH HEIGHT FOR T-BRANCH SINGLE LAYER TUBE HYDROFORMING.....	84
TABLE 5.1. THE GEOMETRICAL FACTORS AND EXPERIMENTAL DESIGN LEVELS THAT WERE USED IN THIS STUDY. ....	93
TABLE 5.2: PROCESS PARAMETERS AND EXPERIMENTAL DESIGN LEVELS USED.....	94
TABLE 5.3: DESIGN MATRIX WITH ACTUAL INDEPENDENT PROCESS VARIABLES .....	95
TABLE 5.4: NUMERICAL MEASURED RESPONSES. ....	96
TABLE 5.5: ANOVA TABLE FOR THE BULGE HEIGHT FINAL QUADRATIC MODEL. ....	97
TABLE 5.6: ANOVA TABLE FOR THE THICKNESS REDUCTION FINAL QUADRATIC MODEL. ....	97
TABLE 5.7: ANOVA TABLE FOR THE WRINKLE HEIGHT FINAL QUADRATIC MODEL. ....	98
TABLE 5.8: CONFIRMATION EXPERIMENTS. ....	102
TABLE 5.9: DESIGN MATRIX WITH ACTUAL INDEPENDENT PROCESS VARIABLES. ....	118
TABLE 5.10: NUMERICAL MEASURED RESPONSES .....	119
TABLE 5.11: ANOVA TABLE FOR BULGE HEIGHT REDUCED QUADRATIC MODEL .....	120
TABLE 5.12: ANOVA TABLE FOR THICKNESS REDUCTION REDUCED QUADRATIC MODEL .....	120
TABLE 5.13: ANOVA TABLE FOR WRINKLE HEIGHT REDUCED QUADRATIC MODEL .....	121
TABLE 5.14: CONFIRMATION EXPERIMENTS .....	124
TABLE 5.15: NUMERICAL MEASURED RESPONSES. ....	133
TABLE 5.16: ANOVA TABLE FOR BULGE HEIGHT REDUCED QUADRATIC MODEL. ....	134
TABLE 5.17: ANOVA TABLE FOR THICKNESS REDUCTION REDUCED QUADRATIC MODEL. ....	134
TABLE 5.18: CONFIRMATION EXPERIMENTS.....	137
TABLE 5.19: DESIGN MATRIX WITH NUMERICAL MEASURED RESPONSES.....	147
TABLE 5.20: ANOVA TABLE FOR BULGE HEIGHT REDUCED QUADRATIC MODEL. ....	148
TABLE 5.21: ANOVA TABLE FOR THICKNESS REDUCTION REDUCED QUADRATIC MODEL. ....	148
TABLE 5.22: CONFIRMATION EXPERIMENTS .....	151
TABLE 6.1: THE FIRST CRITERION OF NUMERICAL OPTIMIZATION. ....	161
TABLE 6.2: THE SECOND CRITERION OF NUMERICAL OPTIMIZATION. ....	162
TABLE 6.3: OPTIMAL CONDITIONS BASED ON THE FIRST CRITERION .....	162

TABLE 6.4: OPTIMAL CONDITION BASED ON THE SECOND CRITERION.....	162
TABLE 6.5: UPPER AND LOWER LIMITS FOR THE RESPONSES IN THE TWO CRITERIA.....	163
TABLE 6.6: NUMERICAL VALIDATION OF THE OPTIMIZATION RESULTS.....	164
TABLE 6.7: THE FIRST CRITERION OF NUMERICAL OPTIMIZATION. ....	165
TABLE 6.8: THE SECOND CRITERION OF NUMERICAL OPTIMIZATION.....	165
TABLE 6.9: OPTIMAL CONDITION BASED ON THE FIRST CRITERION .....	166
TABLE 6.10: OPTIMAL CONDITION BASED ON THE SECOND CRITERION.....	166
TABLE 6.11: UPPER AND LOWER LIMITS FOR THE RESPONSES IN THE TWO CRITERIA.....	168
TABLE 6.12: NUMERICAL VALIDATION OF THE OPTIMIZATION RESULTS. ....	169
TABLE 6.13: THE FIRST CRITERION OF NUMERICAL OPTIMIZATION .....	170
TABLE 6.14: THE SECOND CRITERION OF NUMERICAL OPTIMIZATION.....	171
TABLE 6.15: OPTIMAL CONDITIONS BASED ON THE FIRST CRITERION.....	171
TABLE 6.16: OPTIMAL CONDITIONS BASED ON THE SECOND CRITERION .....	171
TABLE 6.17: UPPER AND LOWER LIMITS FOR THE RESPONSES IN THE STUDIED CRITERIA. ....	172
TABLE 6.18: CONFIRMATIONS EXPERIMENTS.....	173
TABLE 6.19: THE FIRST CRITERION OF NUMERICAL OPTIMIZATION. ....	174
TABLE 6.20: THE SECOND CRITERION OF NUMERICAL OPTIMIZATION.....	174
TABLE 6.21: OPTIMAL CONDITIONS BASED ON THE FIRST CRITERION.....	175
TABLE 6.22: OPTIMAL CONDITIONS BASED ON THE SECOND CRITERION .....	175
TABLE 6.23: UPPER AND LOWER LIMITS FOR THE RESPONSES IN THE STUDIED CRITERIA. ....	176
TABLE 6.24: CONFIRMATION EXPERIMENTS.....	177
TABLE 6.25: OPERATING COST OF BI-LAYERED TUBE HYDROFORMING PROCESS .....	178
TABLE 6.26: OPERATING COST CONSIDERATION FOR X-TYPE BI-LAYERED TUBE HYDROFORMING OPTIMIZATION CRITERIA .....	179
TABLE 6.27: OPERATING COST CONSIDERATION FOR T-TYPE BI-LAYERED TUBE HYDROFORMING OPTIMIZATION CRITERIA .....	179
TABLE 6.28: OPTIMAL CONDITION BASED ON THE FIRST CRITERION AFTER COST REDUCTION .....	180
TABLE 6.29: OPTIMAL CONDITION BASED ON THE SECOND CRITERION AFTER COST REDUCTION .....	180
TABLE 6.30: NUMERICAL VALIDATION OF THE OPTIMIZATION RESULTS .....	181
TABLE 6.31: EFFECT OF COST MINIMIZATION ON THE OPTIMUM OUTPUTS IN THE OPTIMIZATION CRITERIA FOR X-TYPE BI-LAYERED TUBE HYDROFORMING .....	182
TABLE 6.32: EFFECT OF COST MINIMIZATION ON THE OPTIMUM OUTPUTS IN THE OPTIMIZATION CRITERIA OF T-TYPE BI-LAYERED TUBE HYDROFORMING .....	182
TABLE 6.33: SUB-PROBLEM OPTIMIZATION RESULTS (X-SHAPE) .....	187

**TABLE 6.34: SUB-PROBLEM OPTIMIZATION RESULTS (T-SHAPE)..... 188**  
**TABLE 6.35: SINGLE OPTIMIZATION RESULTS (X-SHAPE) ..... 189**  
**TABLE 6.36: SINGLE OPTIMIZATION RESULTS (T-SHAPE) ..... 189**  
**TABLE 6.37: CONFIRMATION EXPERIMENTS..... 190**  
**TABLE 6.38: A COMPARISON OF SUB-PROBLEM AND RSM OPTIMIZATION RESULTS ..... 191**  
**TABLE A.1: DESIGN MATRIX FOR BBD, CODED VALUES. .... 194**  
**TABLE A.2: ANOVA TABLE FOR FULL MODEL ..... 197**

### List of Abbreviations:

<b>Abbreviation</b>	<b>Meaning</b>
<b>ANOVA</b>	Analysis of variance
<b>D</b>	Outer tube diameter
<b>DOE</b>	Design of Experiments
<b>df</b>	Degree of freedom
<b>f</b>	Coefficient of friction
<b>f<sub>0</sub></b>	The reference objective function value
<b>FEA</b>	Finite element analysis
<b>F-value</b>	A continuous probability distribution which is used to test hypothesis in ANOVA
<b>Fy</b>	compressive force required to yield the tube at the beginning of the bulging
<b>H</b>	Final bulge height
<b>L</b>	Tube length
<b>MS</b>	Mean square for each term
<b>N</b>	Total number of experiments
<b>n<sub>0</sub></b>	Number of centre points
<b>P</b>	Number of coefficients in the model
<b>P-value</b>	The probability at which the model is not significant
<b>P<sub>iy</sub></b>	The yield pressure
<b>P1, P2, P3, P4, P5</b>	Internal pressure coordinates
<b>Pk</b>	response surface parameter that increases with each design iteration
<b>r</b>	Die corner radius
<b>R<sub>p0.2</sub></b>	Yield strength
<b>RSM</b>	Response surface methodology
<b>S</b>	Axial feed displacement
<b>SS</b>	The sum of squares for each term
<b>t<sub>0</sub></b>	The initial wall thickness
<b>t<sub>1</sub></b>	Outer layer thickness
<b>t<sub>2</sub></b>	Inner layer thickness
<b>THF</b>	Tube hydroforming
<b>Tr</b>	Maximum wall thickness reduction
<b>Wr</b>	Wrinkle height
<b>Wt</b>	the weight value which decide the shape of the desirability function
<b>X</b>	the penalty function used to enforce design variable constraints
<b>Y</b>	The actual value of the response
<b>Y<sup>^</sup></b>	The estimated value of the response

## LIST OF PUBLICATIONS

### **Peer-Reviewed journals**

Tube hydroforming process: A reference guide. *Materials & Design*, Volume 33, January 2012, Pages 328-339.

A. Alaswad, K.Y. Benyounis, A.G. Olabi.

Employment of finite element analysis and Response Surface Methodology to investigate the geometrical factors in T-type bi-layered tube hydroforming. *Advances in Engineering Software*, Volume 42, Issue 11, November 2011, Pages 917-926.

A. Alaswad, K.Y. Benyounis, A.G. Olabi.

Experimental and finite element investigation of formability and failures in bi-layered tube hydroforming. *Advances in Engineering Software*, Volume 42, Issue 10, October 2011, Pages 815-820.

A.G. Olabi, A. Alaswad.

Finite element comparison of single and bi-layered tube hydroforming processes. *Simulation Modelling Practice and Theory*, Volume 19, Issue 7, August 2011, Pages 1584-1593.

Abed Alaswad, K.Y. Benyounis, A.G. Olabi.

Integration of finite element analysis and design of experiments to analyse the geometrical factors in bi-layered tube hydroforming. *Materials & Design*, Volume 32, Issue 2, February 2011, Pages 838-850.

A. Alaswad, A.G. Olabi, K.Y. Benyounis.

Multi- response optimization of geometrical factors in bi-layered tube hydroforming. *AIP Conference Proceedings (2010) 1315*, Pages 481- 486.

A. Alaswad, A.G. Olabi, K.Y. Benyounis.

An analytical Comparison of single and bi-layered tube hydroforming systems using finite element method. *AIP Conference Proceedings (2010) 1252*, Pages 1047- 1054.

A. Alaswad, A.G. Olabi, K.Y. Benyounis.

### **International Conferences:**

Comparison study of single and bi-layered tube hydroforming using FE simulation. TCN conference 2008. Venice, Italy.

Abed Alaswad, A. G. Olabi.

A numerical study of the effect of geometrical factors on bi-layered tube hydroforming, *Proceeding of 7<sup>th</sup> European LS-DYNA Conference*. Austria.

Abed Alaswad, A. G. Olabi.

A numerical study of the effect of process parameters on bi-layered tube hydroforming. IMC 26 conference. Trinity College Dublin, 2nd – 4th September 2009.  
Abed Alaswad, A. G. Olabi.

Finite element simulation of bulge forming of multi-layered tubular components using a solid pressurizing medium. Proceeding of Enginsoft 2009 Conference. 1st-2nd October 2009. Bergamo, Italy.  
Abed Alaswad, S. M. Ahadulzaman, A. G. Olabi, M. S. J. Hashmi.

An Analytical Comparison of Single and Bi-layered Tube Hydroforming Systems Using Finite Element Method, 10th International Conference on Numerical Methods in Industrial Forming Processes, 13-JUN-10 - 17-JUN-10, Pohang, South Korea, 1047 – 1054.  
A.G.Olabi and A.Alaswad.

A comparison between RSM and classical iterative optimization algorithms for bi-layered tube hydroforming. IMC27 Conference. Galway Mayo Institute of Technology, Ireland. 1st – 3rd September 2010. P185- 192.  
Abed Alaswad, A. G. Olabi, K. Y. Benyounis.

A finite element comparison between single and bi- layered tube hydroforming processes. Enginsoft 2010. Fiera Montichiari (BS), Italy. Oct. 21-22, 2010.  
Abed Alaswad, A. G. Olabi, K. Y. Benyounis.

Multi-response optimization of geometrical factors in bi-layered tube hydroforming. AMPT 2010 Conference. Paris, France. Oct. 24- 27, 2010.  
Abed Alaswad, A. G. Olabi, K. Y. Benyounis.

Employment of finite element modelling and design of experiments to investigate the geometrical factors in T-type bi-layered tube hydroforming. SheMet 2011. 14th International Conference on Sheet Metal. Katholieke Universiteit Leuven. April 18- 20, 2011.  
Abed Alaswad, A. G. Olabi, K. Y. Benyounis.

Investigation of the production cost minimization in bi- layered tube hydroforming process design. IMC 2011, Dublin City University, Ireland.  
Abed Alaswad, A. G. Olabi, K. Y. Benyounis.

# CHAPTER ONE

## INTRODUCTION

### 1.1. Introduction

Tube hydroforming is one of the most popular unconventional metal forming processes that is widely used to produce various tubular components. Tube hydroforming (THF) has been called by many other names such as bulge forming of tubes (BFT's), liquid bulge forming (LBF), and hydraulic pressure forming (HPF) depending on the time and country in which it was used [1]. Establishment of this process goes back to 1939 when Grey et al [2] investigated manufacturing of seamless copper fittings with T and X branches using a combination of internal pressure and axial load. The technology used allowed control of the internal hydraulic pressure and tube end axial load to avoid rupture of the blank. In his work, axial feed was applied to the tube ends by means of plungers, while internal pressure was obtained via high pressure liquid through a drilled hole in one of the plungers.

The principle of tube hydroforming is displayed in Figure 1.1. The tubular blank is firstly placed between the two die halves and then filled with high-pressure liquid through holes in the plungers. The tube blank is then forced to adopt the inner contour of the tool by the application of internal pressure (via high pressure liquid) and two axial forces (via plungers) simultaneously. For limited applications, the tube can be formed by the increasing internal pressure only. This means that the axial plungers do not feed more material into the expansion zone. However, the axial forces acting on the tube ends must exceed a certain level to prevent pressure liquid leakage. This limit is known as sealing.

In many cases, internal pressure can be transmitted by means of an elastomer (e.g. rubber or polyurethane). A polyurethane rod was acting as the pressure-transmitting medium in Al-Qureshi [3]. The same author replaced polyurethane with rubber to provide internal pressure [4]. In another study, tubular components were formed by pouring soft metal (filler material) into a copper tube [5] and then applying end axial forces to both the filler material and copper tube.

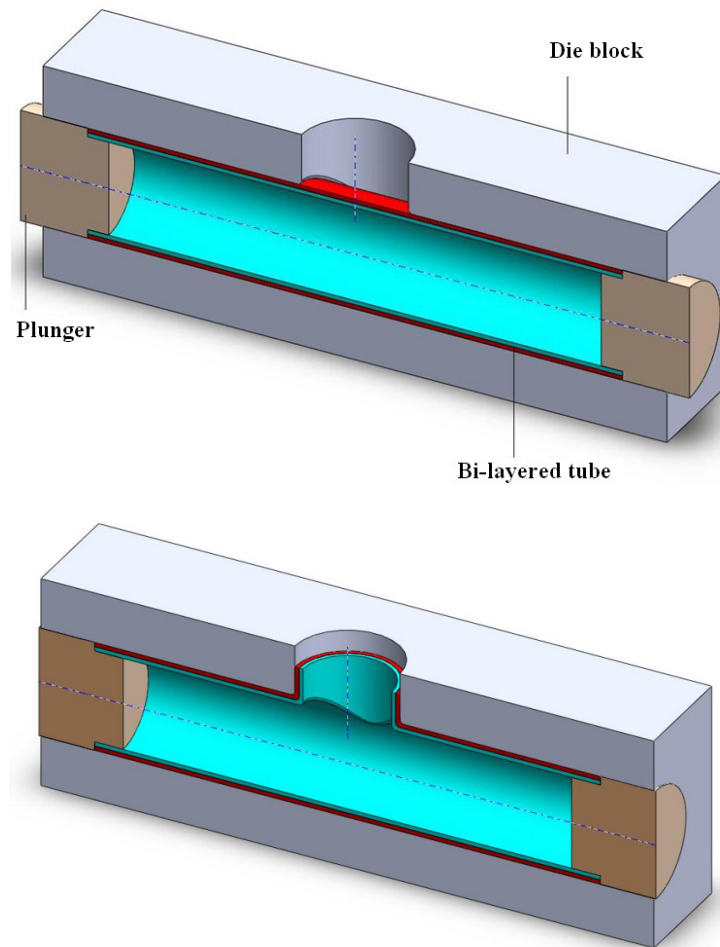


Figure 1.1: Tube hydroforming system.

The tube hydroforming system consists of the following units [1]:

1. Press or clamping device: A clamping device is used to open and close the die and to provide enough clamping load during the forming period to prevent elastic deflections and die separation. The tonnage of the press is dependent on the required closing force. The magnitude of the closing load depends on the maximum internal pressure and the blank size [6].
2. Tooling: Hydroforming tooling consists of the die holders, the die, and the inserts. In general, the following are the main requirements for THF tooling [7, 8]: (a) High strength to withstand the high internal pressure and axial loading applied during the process, (b) Good surface finish to minimize friction and increase formability, (c)

Flexibility by interchangeable inserts, (d) Good guiding systems, and (e) Balanced design to minimize the closing force requirements.

3. Pressure system: The pressure system (pump, intensifier, and control valves) are designed to provide the required pressure levels for a wide range of parts.
4. Axial hydraulic cylinders and plungers: The axial plungers are necessary to seal the end of the tube to avoid pressure losses and to feed material into the expansion regions.

Tube hydroforming offers several advantages as compared to conventional manufacturing methods. Tube hydroforming offers the following advantages:

1. Better part quality (tighter tolerances, part consolidation, weight reduction through more efficient section design, improved structural strength and stiffness, and good surface finish).
2. Lower manufacturing costs resulting from a reduced number of forming and assembly operations, lower tooling cost due to fewer parts, fewer secondary operations (no welding of sections required, and holes may be pierced during hydroforming) and less waste.

The main application of this method has been found in manufacturing of reflectors and household appliances, as well as components in the hygiene, aerospace, automotive, and aircraft industries. Many companies in the automotive sector are experiencing great success with this process as it reduces weight, overall costs, and the number of parts per vehicle [9]. Automotive applications can be seen in exhaust parts, camshafts, radiator frames, front and rear axles, engine cradles, crankshafts, seat frames, body parts, and space frame. Tube hydroforming is also used for the manufacturing of bathroom faucet spouts, aluminium riflescopes, and steel panic bars.

## **1.2. Bi-layered tube hydroforming**

The study of bi-layered tubes began in the 1980s as it was applied to the situations of severe corrosion mainly in order to reduce costs. For example, it was observed that, replacing a single-layer stainless steel tube with a bi-layered tube consisting of a carbon steel inner tube packaged by a stainless steel outer tube, can be used for sea floor piping.

On the other hand, a bi-layered tube consisting of a stainless steel inner tube packaged by a carbon steel outer tube would be convenient for the transportation of corrosive media. Such replacements result in large economic savings when compared to a tube made of a single alloy, since the use of precious materials is reduced to a minimum [10]. Moreover, bi-layered tubing, which consists of two different layers, can be practical in complex working environments as they offer dual properties that single layer structure doesn't have [11,12]. The CRA-lined pipe (corrosion-resistant-alloy) is a well known example of bi-layered tubes that has been increasingly utilized in oil production, nuclear power plants, and the refining industry. It consists of a liner pipe made of corrosion-resistant-alloy and an outer pipe made of low-cost steel. The lined pipe with the internal CRA liner provides corrosion resistance to the process environment, with the less expensive outer pipe providing the required strength and toughness to maintain the mechanical integrity. Many other examples of bi-layered tubes can be found in the following application [13]:

- Heat exchangers for power plants (electric, nuclear, thermal, and geothermal power plants).
- High corrosive systems (condensers, evaporators, sea water desalinations, fertilizing, urea systems, ammonia, gas, and corrosive acids).
- Chemical and petrochemical industries.
- Food processing and refrigeration industries.

Bi-layered tubular components can be formed by hydroforming of bi-layered tubes [14]. Two tubes of different materials can be fitted into each other and then hydroformed simultaneously. Mac Donald and Hashmi [15] simulated cross branch bulge forming of bimetallic tubes using the finite element method. A thin layer made of stainless steel was used to protect a copper tube, but no experiments were reported to validate the finite element work. More recently, the feasibility of producing bi-layered tubular components by hydroforming was investigated by Islam et al [16]. A copper tube was inserted in a brass tube with a clearance fit. After that, the tubes combination was hydroformed in the desired shape. Finite element simulations using implicit code ANSYS were performed to investigate stress distribution in the hydroformed part.

### **1.3. Motivation and research objective**

In spite of the important applications of the bi-layered tube hydroforming, a knowledge base does not exist for the process like it does for the single layer tube hydroforming. Consequently, a detailed investigation on the bi-layered tube hydroforming process is required to help engineers to attain better understanding of the process and allow a detailed explanation of the effects of the design parameters on the bi-layered hydroformed part. Particularly, big bulge height, and uniform wall thickness without wrinkling, buckling, or bursting is the goal of most manufacturers.

The main objective of this study can be summarized in the following points:

- 1- Numerical modelling of the bi-layered tube hydroforming process (X-type and T-type) using the finite element method to help engineers to gain greater efficiency in the process development, avoiding the cost and limitations of compiling a database of real world parts.
- 2- Experiments to check the numerical models validation.
- 3- A finite element comparison of single and bi-layered tube hydroforming.
- 4- Employment of the Design of Experiments technique and Finite Element Method to model the X-type and T-type bi-layered tube hydroforming process outputs as functions of the geometrical factors (tube length, die corner radius, tube diameter and thicknesses of inner and outer layers) and the process parameters (internal pressure coordinates, axial feed displacement, and coefficient of friction). By means of these models, a quick estimation of the process output can be obtained. Furthermore, the main effects and their interactions on the process outputs can be graphically displayed.
- 5- A multi-response optimization study by which different objectives can be optimized together. In the proposed study, a desirability approach was used to evaluate the optimal geometrical factors and process parameters that result in the desired hydroformed parts according to different practical criteria.
- 6- A comparison of the RSM modelling optimization technique and the iterative optimization algorithm of the ANSYS optimizer based on the bi-layered tube hydroforming design.

#### **1.4. Thesis layout**

In the first chapter, a general introduction on the tube hydroforming process is outlined and the importance of the bi-layered tubing is highlighted. This chapter also presents the research motivation and the objective of the current work. The second chapter presents a literature review on the tube hydroforming studies in which the factors affecting the process output are addressed, and the process failure types and the optimization techniques used are outlined. Chapter three describes the experimental design and the experimental procedures using the tube hydroforming machine of Dublin City University. In the fourth chapter, numerical models are created for X-shape and T-shape bi-layered tube hydroforming. In addition, a finite element comparison of single and bi-layered tube hydroforming processes is conducted. Chapter five presents a detailed investigation of the influence of the design parameters (geometrical factors and process parameters) on the bi-layered tube hydroforming process output using a combination of Design of Experiments technique and the developed finite element models. Chapter six illustrates the optimization of the process parameters and geometrical factors according to different practical criteria. Chapter seven outlines the conclusions of this study and makes recommendations for future work.

## **CHAPTER TWO**

### **LITERATURE REVIEW**

#### **2.1. Introduction**

The objective of this chapter is to present a literature review on tube hydroforming (THF) process studies. Initially, a number of analytical studies are summarized. A guideline is then proposed for employing finite element modelling (FEM) in the process analysis. Factors affecting the process output are addressed by a number of research studies which are categorized and reviewed in the present chapter. Common types of failure of the process are introduced and improvements to avoid them are proposed. Also, different optimization algorithms to select the input parameters that will produce the desired hydroformed component are outlined. In conclusion, production of bimetallic tubular junctions by means of the bi-layered tube hydroforming process is found to need more investigation.

#### **2.2. Analytical studies**

Researchers started to study tube hydroforming theoretically in order that they could predict the hydroformed component shape using a certain combination of process parameters, or to identify the necessary process parameters that obtain the desired shape using mathematically developed equations, with experiments being carried out to validate the analytical results.

In one of his studies, Hashmi [17] presented an analysis of wall thickness distribution around the dome of T-branches formed by tube hydroforming. In this analysis the developed dome was assumed to be spherical. A comparison with experimental results indicates that the analysis over-estimated the thinning of the wall. In a separate work [18], the same author reported an analytical method to predict the bulge height and wall thickness distributions of both axisymmetric and asymmetric hydroformed parts. The analysis was based on the geometry of the forming bulge but did not take into account key parameters such as pressure, friction, die corner radius, etc. Later, experiments were conducted Hashmi and Crampton [19] to compare experimental results with the analytical ones and a fairly close agreement was discovered.

In a different approach, calculation of the internal pressure and the axial force values required to reach the yield limit in tube hydroforming process was achieved by Asnafi [20] taking into consideration sealing and frictional forces. The analysis was done using the formulas of thin walled tubes subjected to internal pressure and axial loads with an assumption that stress condition is bi-axial in nature. The predicted values were useful in the free forming stage of the tube hydroforming process Figure. 2.1.

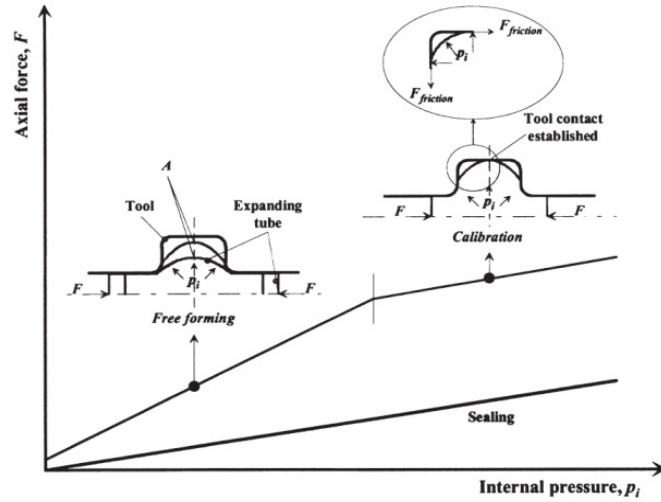


Figure 2.1: Stages of tube hydroforming [20].

The yield pressure ( $P_{iy}$ ) and compressive force ( $F_y$ ) required to yield the tube at the beginning of the bulging were described in equations 2.1- 2.2.

$$p_{iy} = \frac{R_{p0.2}}{(1 - \alpha + \alpha^2)^{1/2}} \cdot \frac{2t_0}{(d_0 - t_0)} \quad (2.1)$$

$$F_y = p_i \cdot \pi \cdot \frac{(d_0 - t_0)^2}{4} \cdot (1 - 2\alpha) \quad (2.2)$$

Where  $R_{p0.2}$  is the yield strength,  $t_0$  is the initial wall thickness,  $d_0$  is the outer diameter of the tube while  $\alpha$  represents the ratio of the axial stress to the tangential stress.

Ahmad and Hashmi [6] developed a theoretical estimation of the internal pressure, axial load, and clamping force for different materials and blank geometries. From the analytical study, it was evident that the axial punch has to deliver more force when stronger materials are used, higher friction is faced, or bigger tube diameters are utilized. Al-Qureshi [21] presented a theoretical study which predicts the limiting bead height, the total applied load,

and the total axial feed required to form circumferential cylindrical bead in a tube. A close agreement with experimental results was noticed using tubes made from different materials. Instabilities and failures were studied by different researchers in attempting to theoretically determine the onset of instabilities. Saver et al [22] worked on the theory of failure of bulge formed tubes due to buckling and fracture. A numerical algorithm was developed based on different principles of solid mechanics to compute values of axial load and internal pressure from increments in the diameter of the bulge. Analytical solutions were presented by Mellor [23] to predict the strain at instability of a thin-walled tube subjected to internal pressure and independent axial load. In this study, it was assumed that the circumferential to axial stress ratio remains constant during the process. It was shown that the greatest ductility of a material can be gained when the ratio of the hoop stress to axial stress has the value of one half. In a subsequent work Jones and Mellor [24] did experiments to validate Mellor's model. A close correlation was found between the two sets of results.

Tensile instability of thin walled cylinders of finite lengths was checked theoretically by Weil [25]. Results showed that burst pressure increase progressively as the length/diameter ratio of the cylinder is reduced. In another study, Koc and Altan [26] formulated analytical models to predict buckling, wrinkling, and bursting in the free bulge forming process using plasticity, membrane, and thin-thick walled tube theories. The critical axial compressive stress for wrinkling was formulated as a function of the tube material properties and the tube geometry Equation. 2.3. Similarly the critical strain at bursting was given as shown in Equation. 2.4.

$$\sigma_{cr} = \frac{1}{\sqrt{3(1-\nu^2)}} E \frac{t}{r} \quad (2.3)$$

$$\bar{\varepsilon} = \frac{2n\sqrt{1-\alpha+\alpha^2}}{(1+\alpha)} \quad (2.4)$$

Where,  $E$  and  $\nu$  are the tangent modulus and Poisson's ratio of the tube material,  $t$  is the wall thickness,  $r$  is the tube radius,  $n$  is the strain-hardening exponent of the material while  $\alpha$  represents the stress ratio.

Due to the complexity of tube hydroforming processes, theoretical studies have produced a limited understanding of the process. Therefore, it would seem important to employ

numerical capabilities to provide a valuable insight into the process and to increase the understanding of its parameters.

### **2.3. Finite element modelling**

Through the last decades it has been discovered that it is expensive and time consuming to use trial and error for the investigation of tube hydroforming process, as well as the conventional metal forming process. The application of numerical simulation for the hydroforming process was found to help engineers to efficiently improve the process development avoiding the cost and limitations of compiling a database of real world parts. Finite element analysis permits arbitrary combinations of input parameters including design parameters and process conditions to be investigated at limited expense. The finite element method (FEM) is a numerical technique by which differential equations are solved approximately up to a selected degree of accuracy [27]. In FEM, the behaviour of a continuum, which is normally impossible to determine exactly, is approximated by idealization. For this purpose, the shape and behaviour of the continuum is redefined by a mesh which is composed of a finite collection of sub-domains called finite elements and nodal points where the values of the function (displacements) and its derivatives (velocity and acceleration) are specified.

The analysis and design of metal forming has increased considerably in recent years due to the advances in computer performance. FEM came of age in the early 1960's with the replacement of analogue with digital computers and the development of the first commercial finite element analysis code. At this early stage, the application was confined to the contained elastic-plastic deformation where the plastic strain is of the order of 0.1%. The extension to the large strain regime was achieved in the late 1970's when limited nonlinear solvers were developed and made available. With the continuous development of computers, the use of FEM for hydroforming process simulations has become a standard development tool after investigations and validations conducted by many researchers since the early 1990's [28] and the application of current commercial FEM software, such as LS-DYNA, PAM-STAMP, ABAQUS, MARC, AUTOFORM, and DEFORM into tube hydroforming process was performed and successfully presented.

The application of numerical methods to the analysis of hydroforming is not so straightforward as it may appear. The THF process is highly non-linear due to large displacements, material non-linearity, and non-linearity due to contact. In many cases, a three-dimensional analysis is required in order to properly represent hydroforming operations and to be able to identify defects such as wrinkling and buckling. Thus, in order to simulate the hydroforming process sufficiently, non-linear three-dimensional models with large contact surfaces are required. Formulation selection is a very important matter; usually static analyses are studied using the implicit method, whereas dynamic analyses are conducted by the explicit method. Furthermore, there are a few processes which are quasi-static in nature. These processes can be analysed by either implicit or explicit methods. Considering the low strain rates during deformation of the typical tube hydroforming, the process can be categorized as a quasi-static deformation and different researchers [29 , 30, 31, 32] have taken this advantage to simulate the process with a scaled down simulation time with respect to the actual experiment time as the process is time independent. However, it has been noticed that for more complex models, with more refined meshes, the explicit method is much more effective than the implicit method. Explicit finite element codes have much better capabilities to handle such kind of nonlinear behaviour exhibited by the metal forming process and provide a better understanding of the plastic deformation mechanism over implicit finite element analysis. On the other hand, the implicit method is reasonably effective and can be faster than the explicit method in simplified problems [33].

Ahmed and Hashmi [29] simulated the T-branch bulge forming process using the commercial explicit finite element code LS-DYNA. Taking the advantage of asymmetry, one fourth represents the numerical model which was built with brick elements to simulate both the die and the tube blank. The tube was assigned a piecewise linear plastic material model, while the die was considered as rigid. Finite element simulation of solid medium bulge forming of cross-joint components was performed by MacDonald and Hashmi [34]. By taking the advantage of symmetry it was possible to model one-eighth of the system. Both the die and the tube were modelled using eight-node solid elements. The interfaces between the die and the tube, and between the bulging medium and the tube, were modelled using the automatic surface-to-surface contact algorithm. The algorithm uses the material properties of both contacting surfaces to calculate the stiffness of the contact elements. The

internal pressure was generated by applying a prescribed displacement to the nodes at the end of the filler material, while axial load is obtained by applying a prescribed displacement to the nodes at the edge of the tube end. In further work, finite element models for the X and T-branches tube hydroforming were constructed using ANSYS/LS-DYNA pre-processor by Ray [31]. The blank was modelled with four node 3D explicit thin shell elements with fully integrated advanced Belytschko Wong Chiang shell element formulation. Shell elements are treated as two dimensional, with a thickness for the element entered, but not shown on the model. However, thin shells theories are successfully adopted if the ratio of tube thickness to the diameter of tube is smaller than 0.1 [35]. The interfaces between the tube and the die, and the tube and the end plunger, were modelled with an advanced automatic surface-to-surface contact algorithm with an elastic coulomb friction law. Another contact parameter with single surface entity was defined for the tube shell that becomes effective in case of wrinkling or buckling. Bi-layered tube hydroforming was simulated using the ANSYS program by Islam et al [16]. Tubes were modelled with solid brick elements where the die was considered as a rigid surface. The pressure was applied on the inner surfaces of the internal tube and the axial displacement was applied at the end of both tubes.

As a result of the rapid IT revolution in recent years, there has been a significant increase in the processing power, and a considerable increase in the availability of commercial finite-element analysis (FEA) packages capable of simulating three-dimensional hydroforming processes. However, a successful application still requires the existence of a well-defined physical problem, for which a numerical analysis can provide a solution [27] and the accurate idealization of this problem (simplifications, assumptions, detection of governing physical phenomena). The significant spatial discretization of the idealized problem (type of elements, topology of the element mesh, and density of element mesh) is essential in the numerical analysis. Moreover, accurate boundary conditions (friction, machines, dies) and material laws and parameters (flow curve, anisotropy) needs to be defined. Furthermore, proper numerical parameters (convergence limits, increment sizes, re-meshing criterion) should be selected. In addition, reasonable computational times and storage requirements are necessary to gain an economical finite element analysis. Nevertheless, because of the limitation of the experimental study and theoretical analysis, the application of finite

elements numerical simulation became a very essential tool for the investigation of the factors affecting the process output.

#### **2. 4. Investigation of the factors affecting the process output**

Tube hydroforming process output was found to be affected by the properties of the material used and the die and tube geometry, as well as to the applied process parameters and friction. Each of these components plays an important role in the success of the process and they have to be addressed during the stage of the development of the process.

##### **2.4.1. Effect of material properties on the process output:**

Material properties were found to fundamentally affect the tube hydroforming process output. Several tests are used in industry to determine material properties. As a consequence of its simple and easy implementation, the uni-axial tensile test is widely used to determine material parameters and stress–strain relationship. Due to the different stress state encountered in the tensile test (uni-axial stress state) and in tube hydroforming (bi-axial stress state), it is better to use the bi-axial test in order to understand reliable material parameters and stress–strain relationships [36].

Experimental research on the effect of the hydroformed material tensile strength was conducted by Fuchs from 1966 onwards [37], who performed tube hydroforming experiments on different materials and concluded that a small increase in tensile strength of the material would lead to a considerable increase in the process formability. Assuming that the tube materials obey the power law of strain hardening, the influence of strain hardening of the material ( $n$ ) was investigated by Orban and Hu [38]. Increasing the strain-hardening exponent was found to lead to a better thickness distribution along the tube wall Figure. 2.2, which indicates a decrease in corner thinning during the expansion of a circular tube into a square die. The same conclusion was arrived at analytically and numerically by Kridli et al [39] and the two sets of results were in good agreement with each other. Bulge forming of finite-length thin-walled cylinders was studied by Fuchizawa [40] using the incremental plasticity theory, and the effect of strain-hardening exponent on the bulge height limits was covered. In a subsequent work, Fuchizawa [41] explored the influence of plastic anisotropy  $r$  on the deformation behaviour of thin-walled tubes under internal pressure. Longitudinal anisotropy was reported to have a significant effect on the thinning

ratio and the critical expansion limit while anisotropy in the hoop direction was found to affect the maximum internal pressure required.

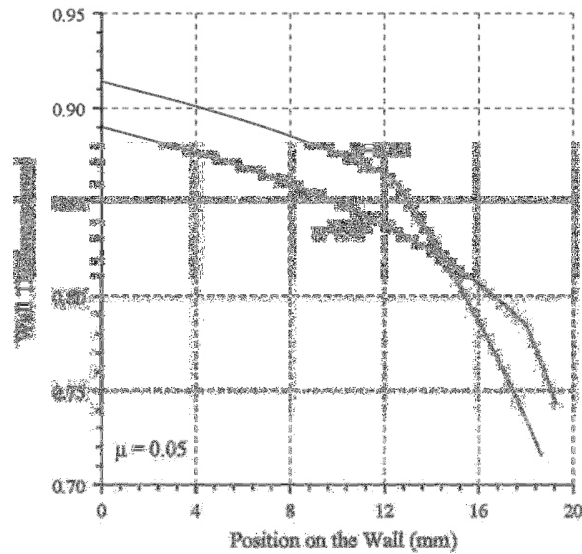


Figure 2.2: Effect of material properties on wall thickness distribution [38].

Carleer et al [42] investigated the influence of various parameters on the process formability. The parameters that were studied included the anisotropy parameter ( $r$ ) and strain hardening coefficient ( $n$ ). In their study they found that  $r$  and  $n$  have a large impact on the shape of the free expanded tube and on the strain distribution. Higher values for  $r$  and  $n$  result in more evenly distributed strain and will favour larger deformations.

Furthermore, a tube material with a higher strain hardening exponent can be formed to a smaller die corner radius than a material with a low strain hardening exponent since it can achieve a higher amount of strain at a given stress (pressure) level [39]. It was also found that with hydroforming materials with less  $r$  value, smaller axial displacement is required in order to obtain the same formed profile [43]. The influence of the material properties on bursting pressure was examined by Kim et al [44]. It can be seen from figure. 2.3, that bursting pressure can be increased either by decreasing of the hardening exponent  $n$ -value or by increasing the strength coefficient  $K$ -value.

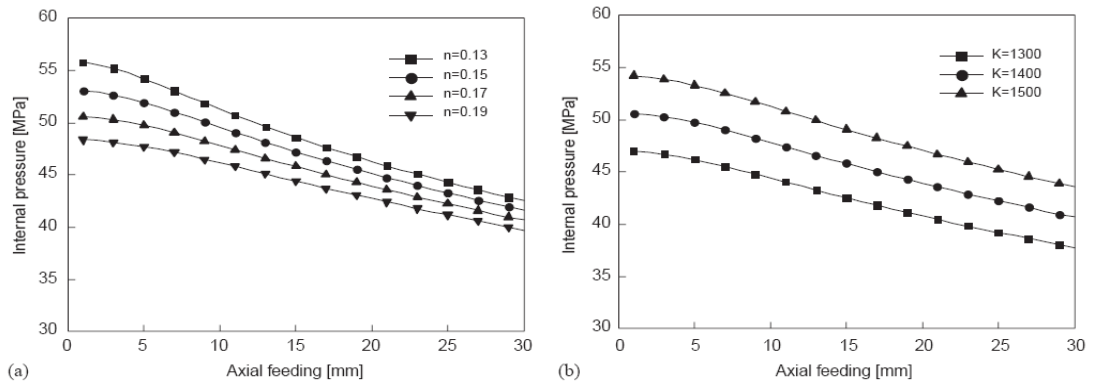


Figure 2.3: Effects of material properties on bursting pressure [44].

#### 2.4.2. Effect of geometrical factors on the process output

The geometry of the tube and die was indicated by different researchers to have an important influence on THF process success. A series of experiments were carried out by Hutchinson [45] to explain the limits of the process. Tee pieces and cross joints were formed successfully from various dimensioned sizes of copper tubes. It was concluded that the ratio between the wall thickness and the outside diameter gives the extent of the forming range (the lower the ratio, the larger the forming range). The tube diameter effect on the process formability was investigated for a member with a complex section of a vehicle bumper rail by Kang et al [46]. In their study it was observed that a remarkable reduction to about one-third in thinning rate and more uniform thickness distribution were reported when bigger diameter tubes were used. Moreover, pre-pressure influence was found more effective when applied to bigger diameter tubes. Based on the finite element modelling of X-branch tube hydroforming [47], it was found that with the initial tube length increase, a smaller bulge height has resulted simultaneously with an increase of wall thinning at the branch top and a decrease of wall thinning at the X-junction.

An integration of finite element modelling and design of experiment was conducted by Koc et al [32] to study the influence of geometrical factors on the tube hydroforming process. Bulge height was modelled as a function of the geometrical parameters and plotted for the corresponding levels of the factors Figure. 2.4. Distances between the protrusion and the tube edges ( $L_{pe1}$  and  $L_{pe2}$ ) were concluded as the most influential factors. Forming of shorter tubes yields higher protrusions than that of longer tubes with less thinning in the

protrusions. The influences of the tube diameter and die corner radius were also determined.

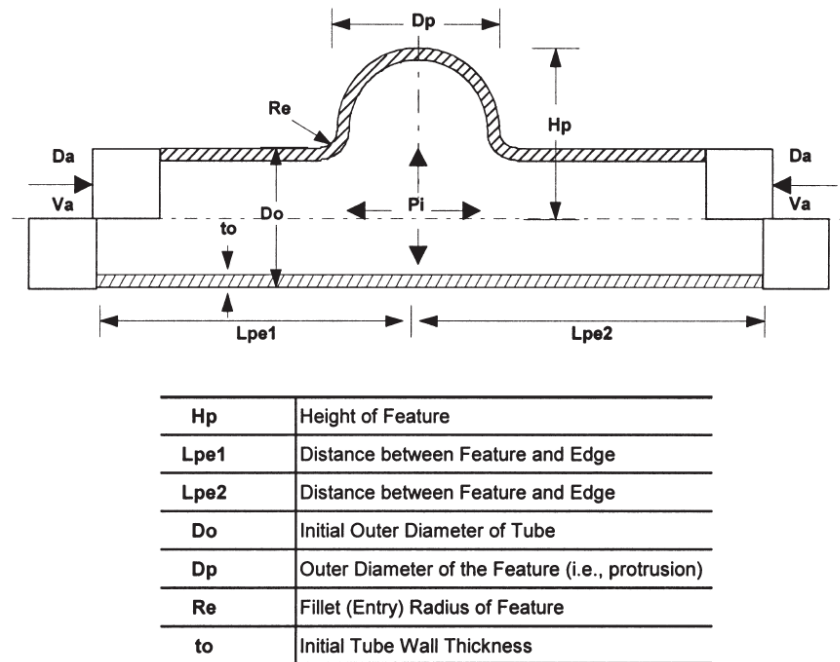


Figure 2.4: Effect of geometrical factors on protrusion height [32].

The effect of the die fillet radius on minimum wall thickness was examined by Kwan et al [48] in T-shape tube hydroforming. From their study, it was noticed that thinner protrusion tips resulted from increasing the die corner fillet radius. Similar results were found in [47] for the X-shape tube hydroforming. Hydroforming of a circular tube in a square die was investigated by Kömmelt et al [49]. It was concluded that the larger the perimeter of the initial tube, the more uniform was the wall thickness distribution of the hydroformed part. The hydroforming pressure requirements were found to be mainly affected by the initial tube wall thickness value, with the required die closing force for the thin tube being lower than that for the thick tube. The die closing force increases with decreasing die corner radius since a higher pressurization level is required to fill the die corner [39].

#### 2.4.3. Effect of process parameters on the process output

The output of a tube hydroforming process was found in many research studies to be affected by the process parameters applied. A 1976 article described the experimental work carried out by Kandil [50] into the axisymmetrical tube hydroforming of brass, aluminum,

and copper tubes using internal pressure only. Later, Ogura and Ueda [51] found that axial feed has an important influence in order to obtain sound products. Influence of the axial feed was investigated by Kang et al [52] for metallic elbows hydroforming. Experiments were performed using different forming dies such as rectangular, circular, and triangular shaped inserts. In all investigated cases, it was found that the axial feed has a significant role in avoiding cracks during the forming process. In another investigation [53], better wall thickness uniformity was obtained in the hydroformed parts when applying a proper axial feed. However, with axial feed increasing, a rise of the maximum internal pressure would be needed to achieve the desired shape of the part. Manabe and Amino [43] studied the factors effecting tube wall thickness distribution analytically and numerically. Axial loading and better lubrication condition were found to improve the wall thickness uniformity for the hydroformed part. Application of axial feed was used, accompanied by either prescribing fluid pressure or specified volume flow rate. It was observed by Varma and Narasimhan [54] that the axial feeding with a specified flow rate resulted in a proportional strain path while the axial feeding with a prescribed pressure gave a non-proportional strain path.

The forming internal pressure required to produce a desired part using the tube hydroforming process was examined by Chen et al [55]. The relationship between the hydraulic pressure, outer corner radius of the deformed tube, tube thickness, and tube yield stress was established based on a proposed theoretical model. Calculated values were found to agree well with the values obtained from the numerical study. A finite element comparison of high and low pressure tube hydroforming was conducted [56]. Stress variation and wall thinning were more pronounced when high forming pressure was used. Furthermore, high pressure hydroforming was found more sensitive to friction than low pressure hydroforming.

However, a balance of the axial load and internal pressure was required to obtain sound products, hence a device was used to apply an axial compressive force proportional to the internal pressure in tube bulging by Thiruvarudchelvan and Lua [57]. Bulge forming of copper tubes was conducted using different ratios of the axial compressive force to the hydraulic pressure. The proper coordination of internal pressure and axial feeding during the process time is the key issue, as these process parameters have to be applied

synchronously. Effect of loading path (internal pressure versus axial material feed) is discussed in a number of published articles. In one of these articles, axisymmetric bulge forming of tubes using two different loading patterns was numerically simulated by Ahmed and Hashmi [29]. A pressure predominant loading path and an axial predominant loading path were examined. It was concluded, that a pressure predominant path gives smoother deformation while a predominant axial load path may result in buckling or wrinkling. In other work, Limb et al [58] found that increasing the internal pressure as a step function of the axial feed is the most recommended method of forming thin walled tubes using hydroforming. Finite element simulations of the THF process using rectangular dies were carried out by Hama et al [59], and various loading paths were tested as shown in Figure. 2.5. The so-called pressure advanced type (A), in which the hydraulic pressure was raised to a certain magnitude in advance of the axial pushing, gave the best formability. Application of internal pressure in advance of the axial feed was recommended for the X-shape tube hydroforming [47] as it results in high bulges and small protruded wrinkles. Big wall thinning in sensitive areas can lead to bursting. The application of the majority of axial feed after tube material yielding under internal pressure, was suggested by Imaninejad et al [60] in order to avoid wrinkling. In the same study, it has been observed that using multiple strokes for axial and vertical actuators would improve the formability of the process.

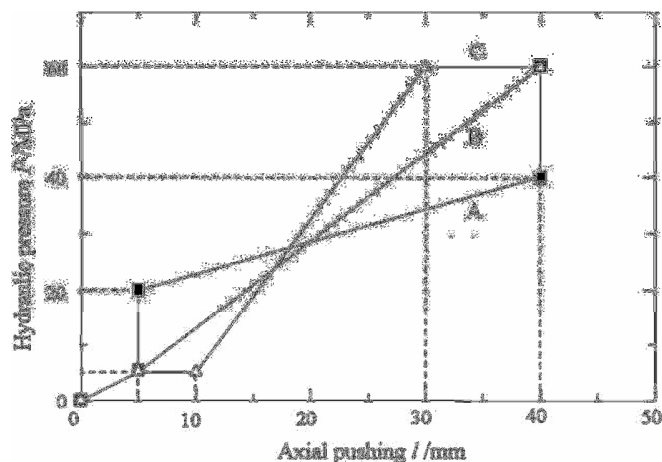


Figure 2.5: Loading paths types (A: Pressure advanced, B: Linear, C: Feed advanced) [59].

#### 2.4.4. Effect of friction and lubricating on the process output

Due to the high contact pressures and large contact surfaces in the tube hydroforming process, high frictional forces between the tube and die are obtained. These forces affect

not only the required process parameters for a specified hydroformed part but also affect its quality, such as its wall thickness distribution [61,62]. Knowing the coefficient of friction is indispensable in the tube hydroforming process analysis. A number of friction tests were developed to determine the coefficient of friction in tube hydroforming process. One of these tests is the “push-through” test, where a tube subjected to internal pressure is pushed through a die. The friction force is calculated as the difference between the forces measured at the both punches. A new analytical model to determine the friction coefficient in the forming zone of tube hydroforming was proposed by Plancak et al [61]. According to the developed model, the friction coefficient could be calculated from the deformed tube and material properties without force measurement. The main parameters affecting the friction in tube hydroforming are the lubricant, the tube material properties (yield strength), tube surface texture, die surface finish, die hardness, and die surface treatment.

Lubrication is important in successful hydroforming as good lubrication conditions allow a tube to reach its final desired expansion and shape in the die, whereas poor lubrication often results in premature failure, due to excessive local thinning. Using lubrication was found to decrease wall thickness differences [52] between bulged and non-bulged regions. The effect of lubrication on the bulge shape was reported in axisymmetric and asymmetric hydroforming by Limb et al [58]. It was observed that the bulged dome was more pronounced if there was no lubricant between the tube and the die, where as a flatter dome was achieved with lubricants in the interface.

From the friction attitude, the hydroformed component can be divided into three different zones: guided, transition, and expansion zones figure 2.6. Due to the difference in the material flow and the state of stress, the three zones are exposed to different tribological conditions [62,63]. In the guiding zone, due to the high values of the relative velocity at the die/tube interface, different types of lubrication can be efficiently used to lower the interface friction. Whilst in the transition and expansion zones, the relative velocity at the die/tube interface drops, and the interface friction increases, in addition high forming pressure causes the conventional lubricants to break down. Therefore, dry film lubrication is more appropriate for these zones, especially when protruding high bulges as it follows the surface expansion without breaking down [64,65].

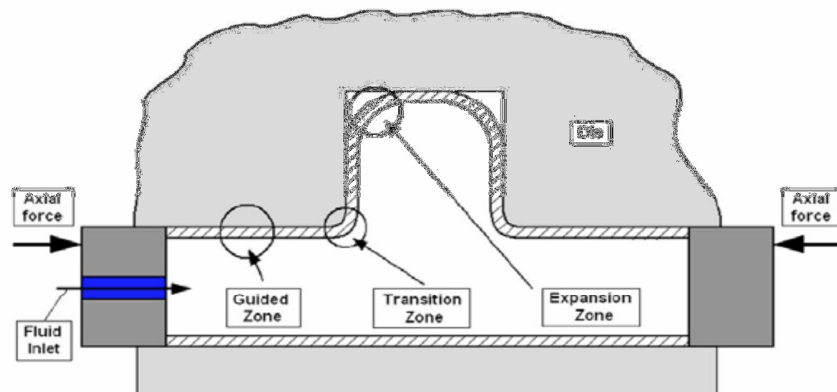


Figure 2.6: Friction zones in tube hydroforming for T-shape [61].

The relationship between the coefficient of friction and the lubricant viscosity as well as the surface roughness was investigated by Lee et al [66]. Test results in figure 2.7 showed that the friction coefficient was high when surface roughness is extremely low or high, while lubricant viscosity was found inversely proportional to the friction coefficient value. Different lubricants were tested in the tube hydroforming process by Hwang et al [67]. The effects of the internal pressure and the axial feeding velocity on the friction forces and coefficients of friction were discussed. A higher pressure was found to decrease the coefficient of friction while the effect of feeding velocity on the coefficient of friction value was found to be insignificant.

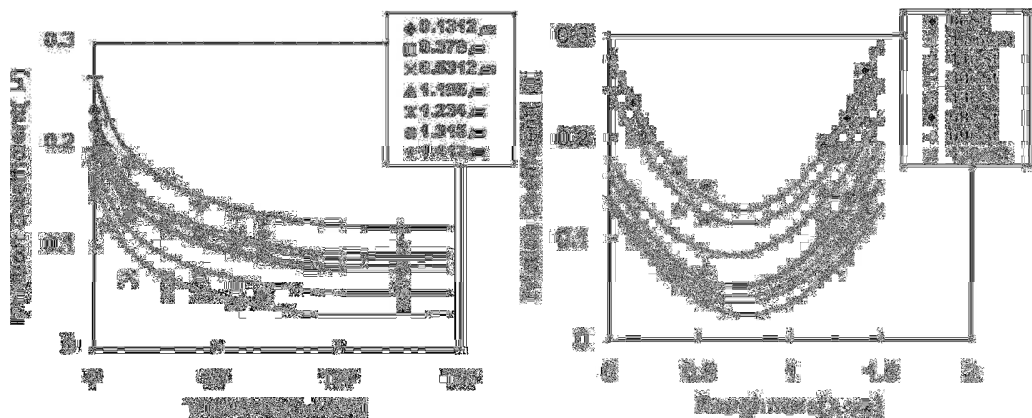


Figure 2.7: Friction coefficient changes with both lubrication viscosity and surface roughness [66].

With the aim of minimizing friction forces between the tube and die, a new sliding die system was invented by Dohmann and Klass [68] in which the die pushes the tube ends, giving an axial compressive forming load without friction between the die and tube. In a

consequent work, Dohman and Hart [69] developed a flexible die system for tube bulging of both axisymmetric and asymmetric products. In this system, the die is divided into segments that can be driven separately during the process. Sliding type and fixed type dies were numerically investigated in hydroforming of an automobile rear axle housing by Lei et al [70] using finite element method. It was found that the sliding-type die can result in a better hydroformed part but it had the drawback of a possibility of buckling during the process. On the other hand, bursting failure could be caused when the fixed-type die is used.

## **2.5. Instabilities and failures**

In the tube hydroforming process, the loads applied in the deformation zone are multidimensional, and the ratio of the loads in different directions may not be constant during the forming process. Therefore, the process is very prone to instability and defects. The common modes of failure in tube hydroforming are: bursting due to formation of a localized necking on the tube wall which leads to fracture, and wrinkling due to local buckling. The amount of axial feeding has to be coordinated with the internal pressure. If the internal pressure is applied rapidly and the axial feeding slowly, the process will fail and cracks will appear in the hydroformed part as the tube can't sustain any increased tensile loading. Splitting usually follows due to extreme deformations in the bursting area. Conversely, if the internal pressure is applied slowly and the axial feeding rapidly, there will be wrinkling or bulking on the tube as a surplus amount of material is pushed through the die which cannot be successfully formed by the applied pressure [71,72].

### **2.5.1. Instabilities overview**

A summary of instability modes, in conjunction with an analytical model to predict the forming limits and parameters in tube hydroforming process, using the thin-walled tube theory, were presented by Koc and Altan in [26]. Even though these models apply only to simple geometries, they could provide helpful predictions in the early stages of design, or could be used as initial hypotheses in the finite element simulations. Numerically, each of the static implicit and dynamic explicit finite element codes were tried by Kim et al [73] to predict wrinkling in straight tube bulge forming. Superior predictions using the explicit method were reported compared to implicit calculations.

The effect of the tube material properties on the tube wrinkling or buckling during the hydroforming process was determined by Chu and Xu [74]. Tubes with stronger work hardening coefficient and bigger plastic anisotropy were found to have higher resistance to either buckling or wrinkling during hydroforming. Furthermore, Yuan et al [75] differentiate between useful and dead wrinkles; useful wrinkles can be used as a pre-form as they can be flattened by applying high internal pressure in the calibrating stage, while dead wrinkles start to arise from the beginning of the process and the calibrating pressure would not be able to flatten them. The initial pressure was found to mainly affect forming of useful or dead wrinkles. However, hydroforming with useful wrinkles was found suitable for low formability metals, but the hydroformed part wall thickness would not be uniform along the axial direction. Minimum thickness can be found at the original top zone of the wrinkle wave, while the original bottom zone of wrinkle wave has the maximum thickness in the forming area [76].

In contrast with buckling and wrinkling, bursting is an irrecoverable failure in the hydroforming process. In order to predict the bursting failure in tube bulging test, Kim et al [77] evaluated the Oyane's ductile fracture criterion [78] from the histories of stress and strain, which are obtained from finite element analysis. The region of fracture initiation and the bursting pressures were predicted and compared with a series of experimental results. An analytical prediction of the bursting failure in the tube hydroforming process under combined internal pressure and independent axial feeding was carried out by Kim et al [44]. The incremental theory of plasticity for an anisotropic material was adopted. From the analytical study, it was concluded that plastic instability is reduced with a decreasing strain hardening exponent,  $n$ , while it increases with a decrease of the plastic anisotropy parameter,  $r$ , and strength coefficient,  $K$ . In other work, Kim et al. [79] examined the finite element analysis for bursting failure prediction in the hydroforming process of a seamed tube. Through a series of finite element simulations with consideration of the weld line, it was shown that the initial fracture takes place in the heat affected zone near the weld line, which was found more realistic in view of the actual bulge forming operations.

### 2.5.2. Forming limit diagrams (FLD)

In order to obtain a defect free hydroformed part, a space is required in which plastic deformation can be assumed to be safe. Operating windows, which are created based on the proposed forming limits, were indicated by many researchers. Tube hydroforming experiments using different tube materials and different tube dimensions were conducted by Hutchinson [80] to establish formability zones for hydroforming of T and X-junctions. Based on a theoretical investigation, forming limits for tube hydroforming process were developed by Kim et al [81] for a different plastic anisotropy ( $r$ ) and strain hardening exponents ( $n$ ) as shown in Figure. 2.8. Analytical results were compared with Back's experimental study [82,83]. Wrinkling limit obtained from the theoretical study was in good agreement with the experimental results. However, the theoretical analysis produced an overestimate when compared to the experimental results for the occurrence of bursting.

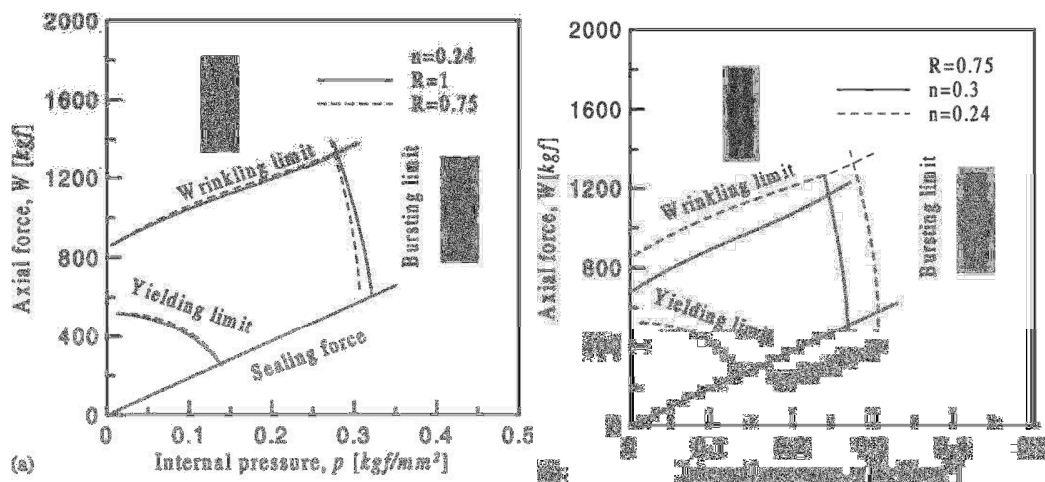


Figure 2.8: Forming limits for different anisotropic parameters and strain hardening exponents [81].

The effect of material properties on the forming limits diagram was outlined in [84]. It was observed that both plastic anisotropy ( $r$ ) and strain hardening exponent ( $n$ ) have more effect on the bursting failure than on the wrinkling failure. However, the strain hardening was found to have a more significant influence on the forming limits. The effect of tube wall thickness on the forming limits was covered, and thicker tubes were reported to be more resistant to wrinkling and bursting failures. Based on a theoretical analysis, forming limits diagrams were drawn up by Xia [85] according to the internal pressure and axial feed values for different materials figure 2.9. From this theoretical study, it was concluded that

the internal pressure that causes bursting failure was found to be proportional to the wall thickness/tube radius ratio.

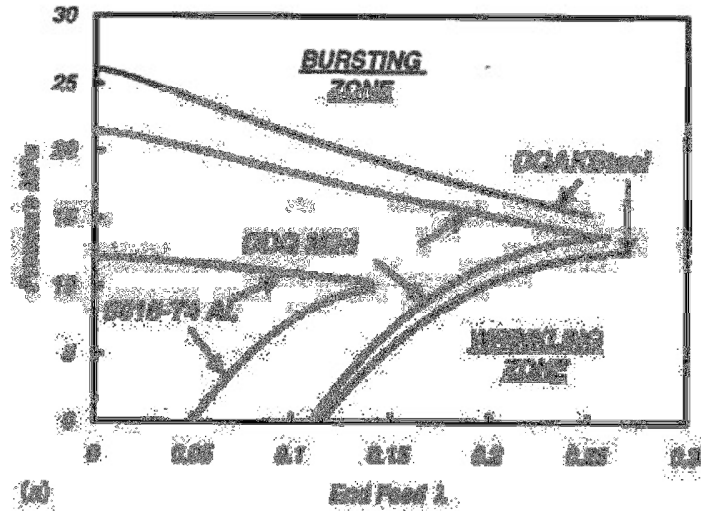


Figure 2.9: Operating windows for different metals [85].

### 2.5.3. Improvements resulting in delayed bursting

Since bursting is an irrecoverable failure, different techniques were developed by researchers to avoid over-thinning leading to fracture and bursting. The rationale to apply counter punch in hydroforming process comes from the fact that counter punch has been used effectively in many manufacturing processes to enhance the manufacturing capabilities. A counter punch can be used to control the branch height and avoid over-thickening or bursting in the protruded branch during tube hydroforming. A general purpose hydroforming machine with internal pressure, two axial feeding punches, and a counter punch was designed as in figure. 2.10 by Hwang et al [86]. T-shape tube hydroforming experiments with and without a counter punch were carried out using this machine. Application of the counter punch was found to lead to 20% higher bulges protruded. In the counter punch application, the counter punch did not move in the first stage until sufficient contact is generated between the counter punch and the hydroformed material, at which moment the counter punch started to move backwards. In this way, the wall thickness reduction at the top of the branch can be halted until the end of the forming process. Different loading paths for the counter punch were investigated and a nonstop one was recommended in order to obtain the best results. Furthermore, application of the

counter punch was found to be essential in the successful hydroforming of Y-shapes as it supports the protrusion while it is being formed figure 2.11. Thus, the protrusion can be formed with fine wall thickness distribution [87].

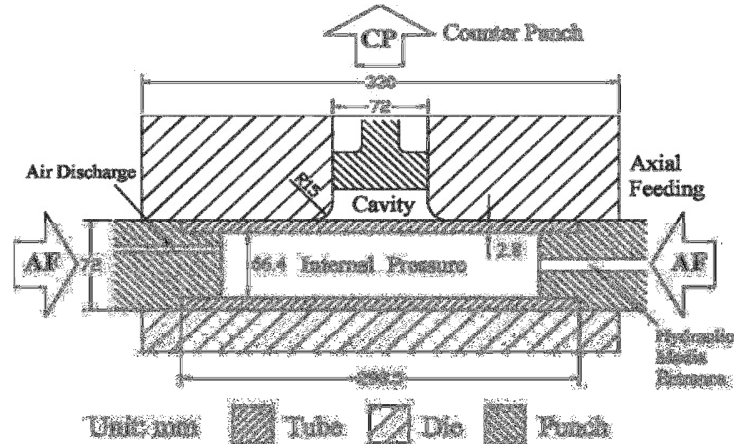


Figure 2.10: Die structure in tube hydroforming with counter punch [86].

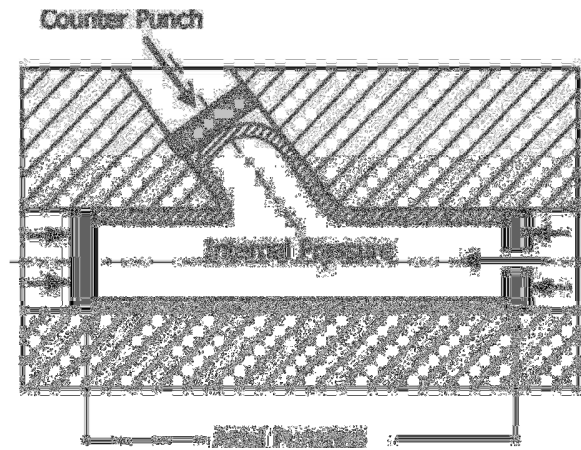


Figure 2.11: Hydroforming of Y- shapes [87].

However, in some cases like axisymmetric bulging, counter force cannot be applied due to inherent constraints. The part geometry precludes using a counter punch. Thus, the application of a dual pressure system as shown in figure 2.12 was suggested by [88] as a logical alternative.

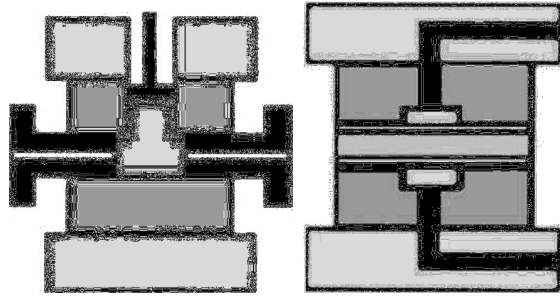


Figure 2.12: Application of a counter punch in asymmetric bulging, and application of a dual pressure system in axisymmetric bulging [88].

## 2.6. Process optimization

The main challenge for any manufacturer is to choose the input parameters that would produce the desired hydroformed component. Conventionally, defining the input parameters to produce a hydroformed component with the required specifications is based on trial and error and is time consuming. Moreover, this traditional method is non-systematic and usually does not produce an optimized combination of input parameters that can be used to produce different outcomes. Therefore, several algorithms were developed that can be applied using finite element simulations [89].

One procedure is to use classical iterative optimization algorithms that are based on the minimization of an objective function, entailing repeated numerical simulations of the process with different sets of designs. These algorithms are interfaced with numerical simulation as shown in figure 14(a), which means that each function evaluation of the algorithm requires running a finite element calculation [90]. Loading path optimization for the tube hydroforming process was performed using this technique in different studies [72, 91] In spite of being generally well-known, these algorithms can be limited to local optimum solutions instead of global ones [89].

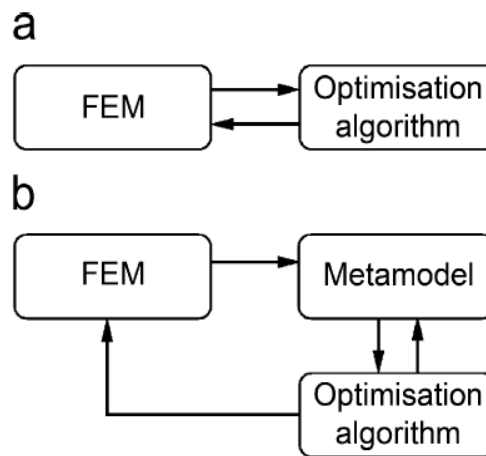


Figure 2.13: (a) Direct optimization. (b) Approximate optimization [89].

A different approach employing direct coupling between the genetic algorithms and the FE model has also been utilized [92]. Genetic algorithm is a search procedure that is based on the mechanics of natural selection. Using a combination of the Genetic algorithm search methods and the nonlinear structural finite element code LS-DYNA, Abedrabbo [93] determined the optimal loading path for tube hydroforming. A global optimum can be found using genetic and evolutionary algorithms, but the large number of function evaluations that are necessary in using these algorithms is considered to be a serious disadvantage [94].

A third technique of optimization is using the approximate optimization algorithms, of which Response Surface Methodology is a well-known example. Response Surface Methodology is based on fitting a low order polynomial model through response data, that are obtained by running finite element simulations for carefully chosen design variable settings and finally optimizing the resulted model. Hence, in this type of optimization, a meta-model is placed in between the optimization algorithm and the finite element model as presented in figure 2.13(b). Using this approach, a model for the bulge height (response) as a function of the geometrical factors (input parameters) in the T-shape single layer tube hydroforming was developed by Koc et al [32]. In another study, the effect of process parameters on Y-shape tube hydroforming was investigated by Ingarao et al [95] using the same technique. The obtained prediction tool was validated through a comparison with numerical evidence, and satisfactory and coherent results were obtained, creating confidence in the efficiency of the proposed approach. Based on this methodology, the

calibration of internal pressure and counterpunch action was investigated with the aim to achieve three different quality objectives. A further optimization study was conducted by Brooghani et al [96] to determine the loading path which results in the best wall thickness distribution for a specified T-shape bulge height.

The fourth group is the so-called adaptive algorithms. In this method, control parameters are adjusted during the process simulation for each subsequent time increment, depending on the outcome of the previous one [89, 97]. The adaptive simulation approach is based on the ability to detect the onset and growth of defects during the process and promptly react to them. Loading paths can therefore be adjusted, within the same simulation run, to correct these defects [94]. A specially developed algorithm in conjunction with ABAQUS explicit finite element analysis software was used by Doege et al [98] to optimize the loading path for axisymmetric bulge forming process. In another work, an intelligent fuzzy logic based load control algorithm was developed by Ray and MacDonald [99], which was integrated in the finite element code for simulation to obtain optimal load paths for the asymmetric tube hydroforming process. More recently, Shu-hui [100] used a necking indicator and a wrinkling indicator as the input of fuzzy logic control, and the output sets of the fuzzy logic control are used for adjusting the internal pressure and the axial feeding. However, only time dependent parameters can be optimized using this method.

## **2.7. Summary**

Amongst the unconventional metal forming processes, tube hydroforming proved to be one of the most promising. From the analytical studies summarized in the literature review, it was observed that the theoretical approach would indicate a limited understanding of the process. The application of the finite element method in the tube hydroforming process analysis was introduced, as it avoids the cost and limitations of compiling a database of real world parts, while guidelines for the successful application of the finite element modelling were proposed. Based on a number of research studies, a detailed investigation of the factors affecting the tube hydroforming process output was revealed, in which the effects of the tube material properties, the tube and die geometries, the process parameters, and the frictional conditions on the hydroformed part were examined. In a further investigation, the common modes of failure in the tube hydroforming process were outlined, and the

influence of the studied parameters on the failure limits was discussed. Moreover, the employment of several optimization approaches (classical iterative algorithm, genetic algorithm, approximate optimization algorithms, and the so called adaptive algorithms) along with the finite element modelling of the tube hydroforming process was examined in this literature review.

However, in contrast to the large number of research studies conducted on the analysis and development of the tube hydroforming process, relatively few investigations were found on bi-layered tube hydroforming [15, 16] for the production of bimetallic tubular junctions. Bi-layered tubing, consisting of two different layers, can be of considerable practical advantage in complex working environments as it offers dual properties that single layer structures cannot offer.

## **CHAPTER THREE**

### **EXPERIMENTAL DESIGN**

#### **3.1. Introduction**

Tube hydroforming (THF) is a relatively complex manufacturing process; the performance of this process depends on various factors (material properties, geometrical factors, and process parameters). This chapter reports on bi-layered tube hydroforming experiments, using the tube hydroforming machine of Dublin City University. The tubes materials, the preparation steps, and the experimental procedures are described. Based on an experimental approach, the influence of material annealing on the hydroformability of brass tubes was revealed. Furthermore, the effects of the axial feed and initial tube length on respectively the X-shape and T-shape bi-layered tube hydroforming processes outputs were experimentally examined. From the results, it can be seen that expensive and time consuming experimental investigations may only give a limited understanding of the process. Therefore, the application of numerical simulation of the tube hydroforming process analysis is suggested in this study to avoid the cost and limitations of compiling a database of real world parts.

#### **3.2. Tube hydroforming machine**

The tube hydroforming machine of Dublin City University shown in Figure 3.1 was first designed and built by Barlow [101], subsequently modified by Hutchinson [80] and partially automated by McDonnell [102]. The power source for the hydraulic system is a variable displacement piston pump driven by a 7.5 KW electric motor Figure 3.2.



Figure 3.1: The tube hydroforming machine of Dublin City University.



Figure 3.2: The power source of the tube hydroforming machine.

### 3.2.1. Machine design

As it is shown in figure 3.3, the main power, by means of hydraulics, supplies the following units:

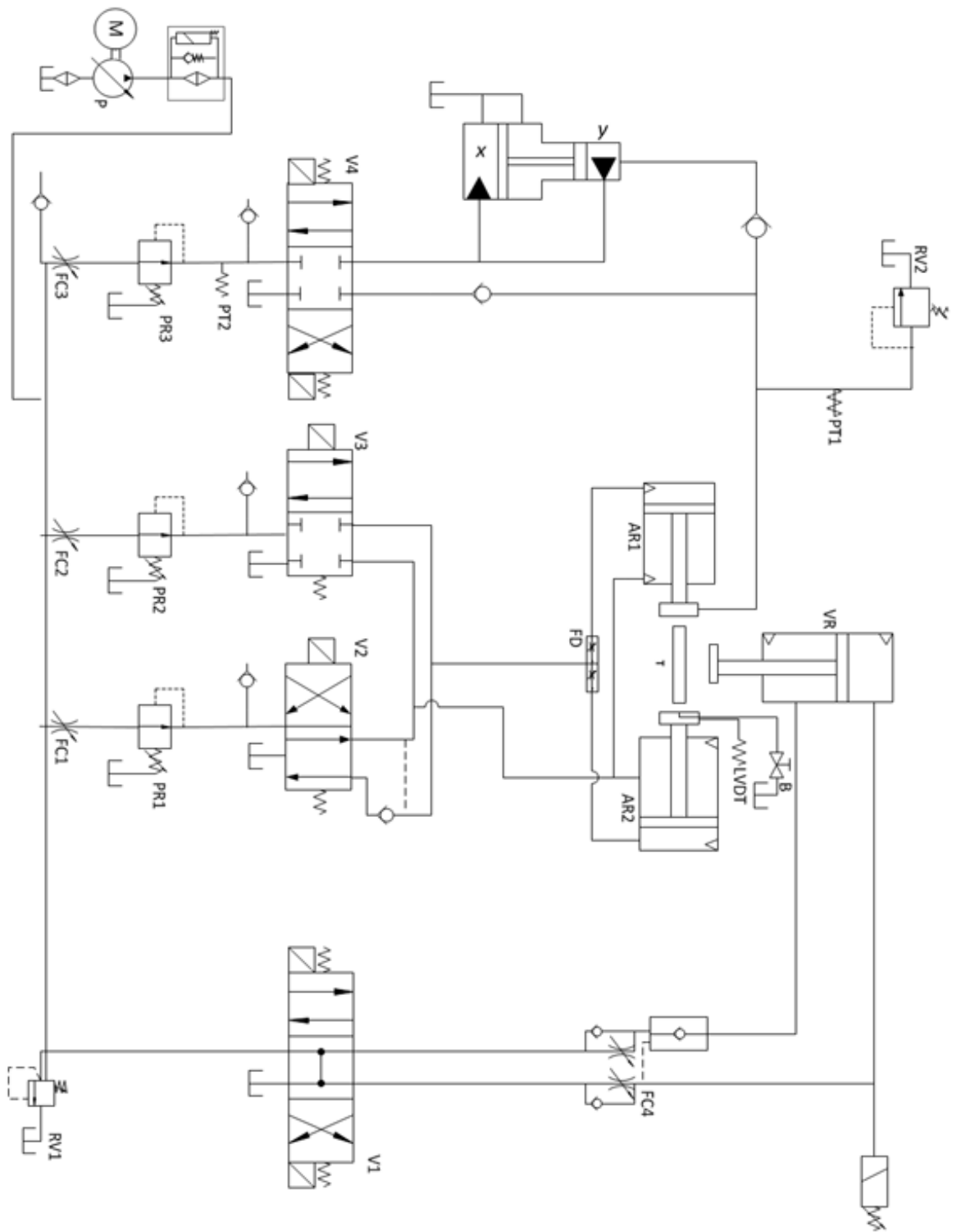


Figure 3.3: The hydraulic circuit of the hydroforming machine [31].

### 1- Vertical clamping unit:

The function of the vertical clamping unit is to extend and retract the upper die part and to firmly clamp the upper and lower die parts in order to ensure that the two die halves are not opened during the hydroforming process. The vertical clamping unit (VR) in the machine is a “Mecman” 206 with bore of 160 mm and a stroke of 150 mm [101].

### 2- Internal pressure supply:

An internal pressure of 0.0175 GPa is generated from the main pump. However, this value was increased to a maximum of 0.069 GPa by the hydraulic pressure intensifier (I). Maximum internal pressure can be controlled by valve: PR3.

### 3- Axial load unit:

In order to apply axial feed to the tube during the hydroforming process, two axial cylinders (AR1 and AR2), each with a diameter of 125 mm and stroke of 100 mm are used. These cylinders are connected to tapered step plungers to seal the tube ends, and further to apply axial displacement during the hydroforming operation. Initial settings for the axial sealing pressure and the maximum axial feed are controlled by valves PR1 and PR2 respectively.

#### 3.2.2. Dies details

The dies consists of a hardened steel die set with lower and upper die halves which are clamped using the hydraulic press attached to the upper die holder while the lower die part is fixed to the rigid machine base. X-shape and T-shape dies are shown in figure 3.4. The hardened steel die halves used are 120mm length (parallel to the tube axis), 100mm width (perpendicular to the tube axis) with 24.12 mm tube cavity diameter. The diameter of the branches is the same as the main tube cavity diameter. Die corner radius values of 1 mm and 3 mm were assigned for T-type die and X-type die respectively. Material properties used for the die and plungers are of EN21 hardened tool with Young's modulus 210 GPa, Poisson's ratio 0.3 and Density 7900 kg/m<sup>3</sup>.



Figure 3.4: Lower halves of X-shape and T-shape dies.

### 3.2.3. Machine control

The tube hydroforming machine can be controlled either manually or automatically.

#### 3.2.3.1. Manual control

The machine has two sets of two-way control switches (S2 and S3) and two sets of three-way control switches (S1 and S4) that controlled the hydroforming system as it is displayed in table 3.1 and figure 3.5.

Table 3.1: Manual control of tube hydroforming machine

<b>S1- Vertical clamp</b>	<b>S2- Axial rams</b>	<b>S3- Axial feed</b>	<b>S4- Internal pressure</b>
Open	Retract	Low feed	Low pressure
Hold			No pressure
Close	Extend	High feed	High pressure



Figure 3.5: Control switches of the tube hydroforming machine

Using the manual control system in figure 3.6, the tube hydroforming process is carried out by means of the following steps:

- 1- Open the die by moving switch S1 to open position which controls valve V1.
- 2- Place the tubular blank in the cavity of the lower die.
- 3- Close the die halves by moving the switch S1 to the close position.
- 4- Axial plungers are pushed inward simultaneously using two horizontal hydraulic pistons to seal the tube ends. This operation is controlled by switch S2 using flow valve V2. The value of sealing pressure can be preset using PR1 to prevent the leakage of hydraulic fluid during the internal pressure application.
- 5- After sealing the tube, it will be filled with the hydraulic pressurized oil by moving switch S4 to (low pressure) and bleeding will be taken place by opening the

bleeding valve (B) to remove any trapped air inside the sealed tube. The bleeding valve should be closed when bleeding is finished.

- 6- Internal pressure and axial feed are applied to deform the tube blank into the die. Using the manual controls, this can be done by switching S4 and S3 that control the flowing valves V3 and V4 respectively to the high position. Maximum internal pressure and maximum axial feed pressure can be preset using PR3 and PR2 respectively.

After the completion of material forming, switches S3 and S4 are moved to the low and off positions respectively. Finally, switch S2 is used to retract the axial ram back, while switch S1 is placed in the open position to uplift the upper die part to allow the formed component to be taken from the die cavity.

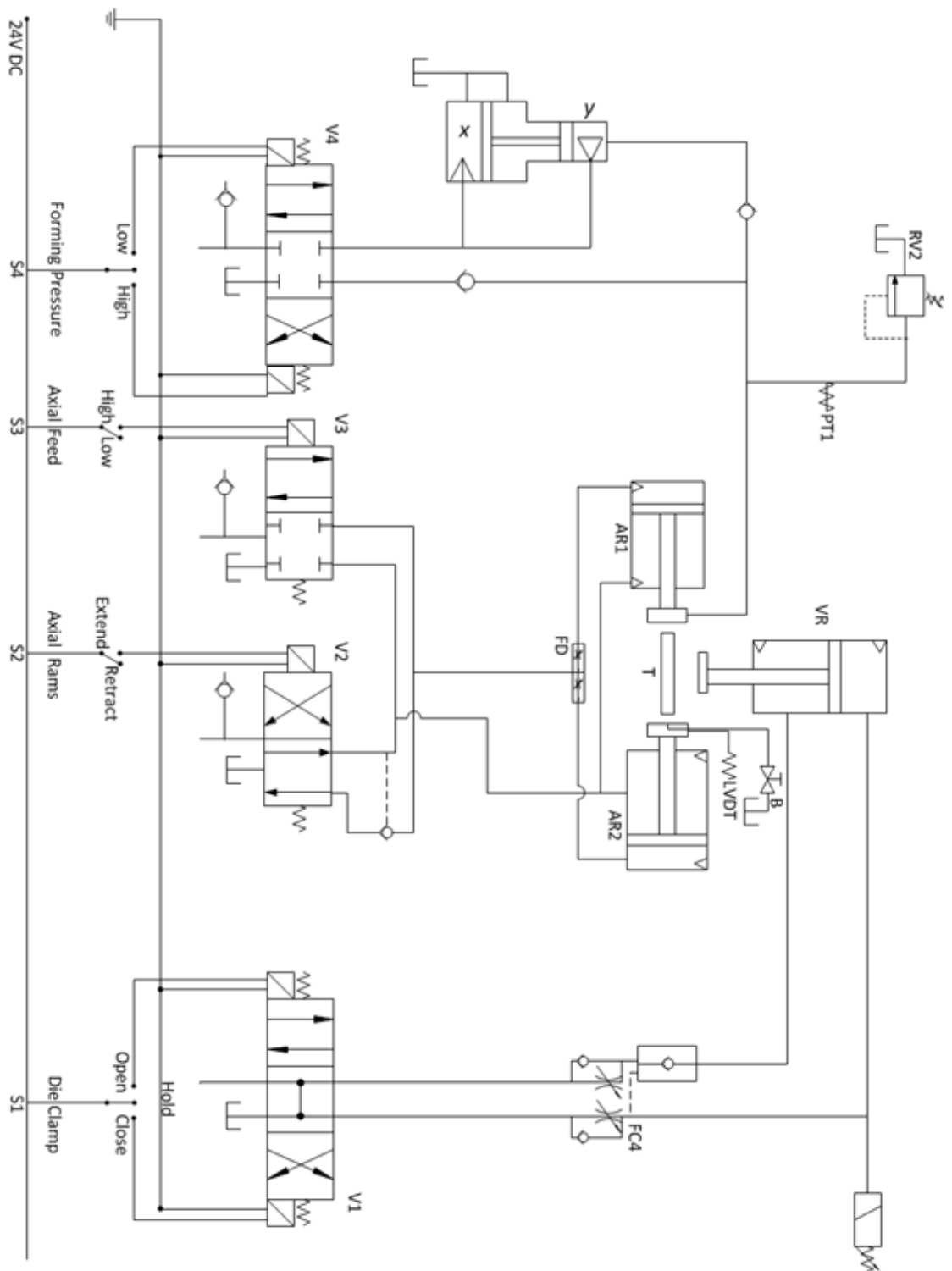


Figure 3.6: Solenoid switch connections of the manual controls of the hydroforming machine [31].

### 3.2.3.2. Automated control

Instead of using the switches (S1- S4) to manually control the process, the tube hydroforming process can be automatically controlled using a LabVIEW data acquisition control card connected to a PC. The basic layout of the automated machine control is shown in figure 3.7. Using the automated system, values of axial sealing pressure, maximum internal pressure and maximum axial feed pressure can be preset as shown in figure. 3.8. Furthermore the instantaneous changes in the internal pressure values during the hydroforming process are recorded by means of an electronic pressure transducer; while the end axial feed values are traced using a linear variable displacement transducer (LVDT) via a data feedback system integrated with the machine. Values of forming pressure and end feed displacement are afterwards converted into a text database, which is used for calculation of the experimental loading path. However, a numerical loading path close to the experimental one will be used in the numerical study, and both experimental and numerical results will be compared to validate the numerical model.

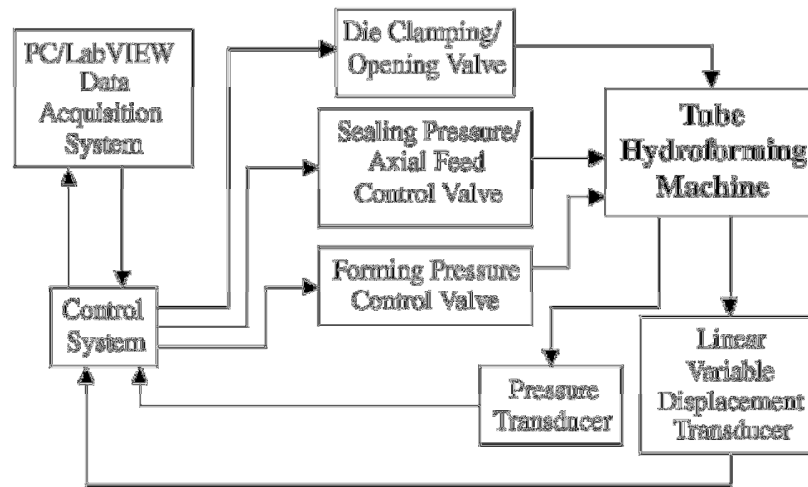


Figure 3.7: Process flow diagram showing control and recording systems [47].

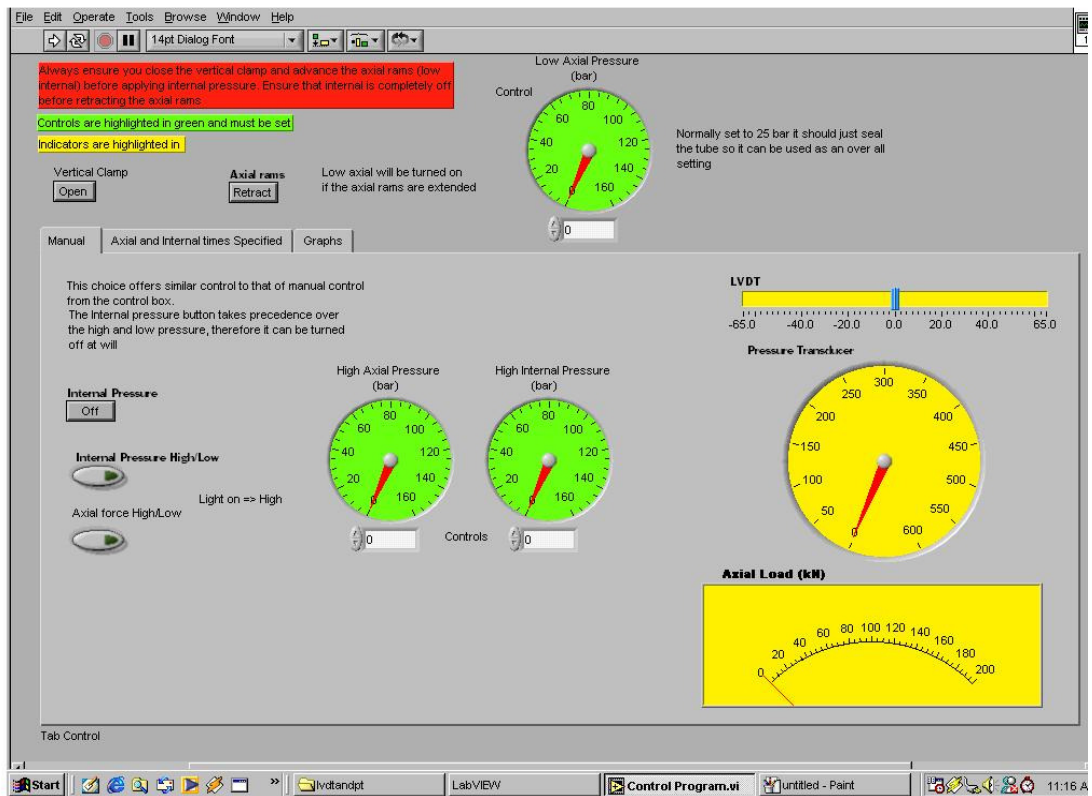


Figure 3.8: A screen shot showing the automated control panel of the tube hydroforming machine [102].

### 3.3. Tubes used in the bi-layered tube hydroforming process

A bi-layered structure was found to be very useful by a number of researchers [10, 11, 12, and 13] as such tubing offers dual properties that single layer structure cannot provide. In order to produce a bi-layered junction, two tubes are inserted in each other with a clearance fit and hydroformed using the tube hydroforming machine. Copper (BS EN 1057-1996) was chosen for the inner layer with an outer diameter of 22 mm and an inner diameter of 20.3 mm, while the outer layer was made of annealed brass with an outer diameter of 24 mm and an inner diameter of 22 mm. Copper tubes are widely used for domestic gas transportation while Brass was chosen to protect copper tubes due to its application in fittings and tools used near explosive gases as it is a spark-resistant material [103, 104], as well as being available locally. During the hydroforming process, the application of internal pressure causes a tight fit between the inner and outer layers, and deforms both of them into the shape of the die. In order to induce the ductility of brass tubes, annealing treatment was

carried out for brass tubes before using them in the bi-layered tube hydroforming process. Guidelines for brass tubes annealing are described in the following section.

### 3.3.1. Brass tubes annealing

Annealing is a process that produces conditions by heating to above the critical temperature, maintaining a suitable temperature, and then cooling. Annealing is used to induce ductility, soften material, relieve internal stresses, refine the structure by making it homogeneous and improve formability [105].

Brass tubes (MS63 Cu 63, Zn 37) were inserted in a high temperature box furnace (Carbolite RHF 16), which is shown in figure 3.9. In this type of furnace, powerful silicon carbide heating elements provide fast heat-up rates. Silicon carbide heating elements are ideally suited to the rigorous firing cycles often required in laboratory furnaces. These elements withstand the stresses of intermittent operation and give long life at elevated temperatures [106]. Using this furnace, the next steps were programmed in the 2408CP Controller figure. 3.10 for brass tubes annealing, as described by [105]:

- a) A temperature ramp to 600 C° with a ramp rate of 5 C°/ min.
- b) A temperature increase from 600 C° to 650 C° with a slow rate: 1 C°/min.
- c) Hold at 650 C° for 60 min.
- d) Ramp down to 260 C° at 5 C°/min.
- e) Switch of the furnace and leave the tubes until they reach the room temperature.

The annealed tubes are shown in figure. 3.11. The effect of the material annealing on the brass tubes hydroformability was experimentally investigated and is discussed in the next section.



Figure 3.9: Annealing furnace.



Figure 3.10: Panel Control for the Furnace



Fig 3.11: Annealed samples inside the furnace.

### 3.3.2. Effect of material annealing on the hydroformability of brass tubes

Using the tube hydroforming machine of Dublin City University shown in figure 3.1, annealed and non-annealed brass tubes were hydroformed in a T-shape die under the same experimental conditions to identify the effect of the material annealing on the process formability. In all experiments, the maximum internal pressure was fixed while different axial loads were tested. The hydroformed parts obtained from annealed and non-annealed brass tubes under different axial loads are displayed in figures 3.12- 3.17.



Figure 3.12: Tubes at Axial Pressure 50 [bar].



Figure 3.13: Tubes at Axial Pressure 60 [bar].

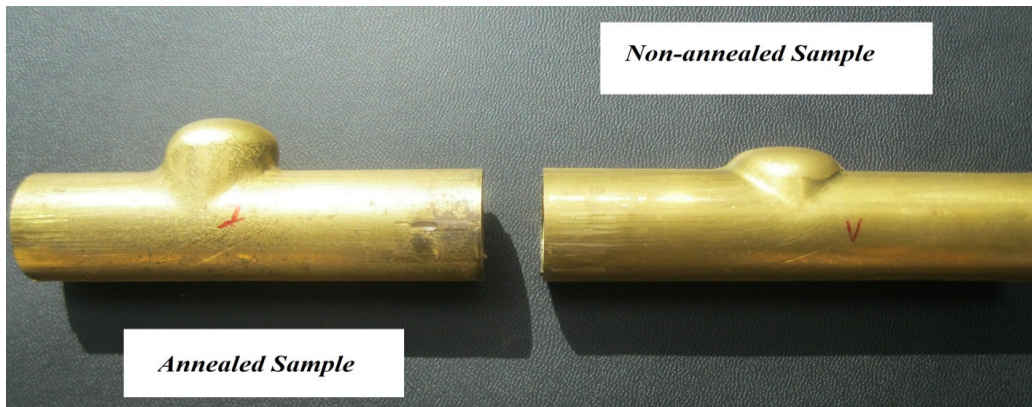


Figure 3.14: Tubes at Axial Pressure 70 [bar].

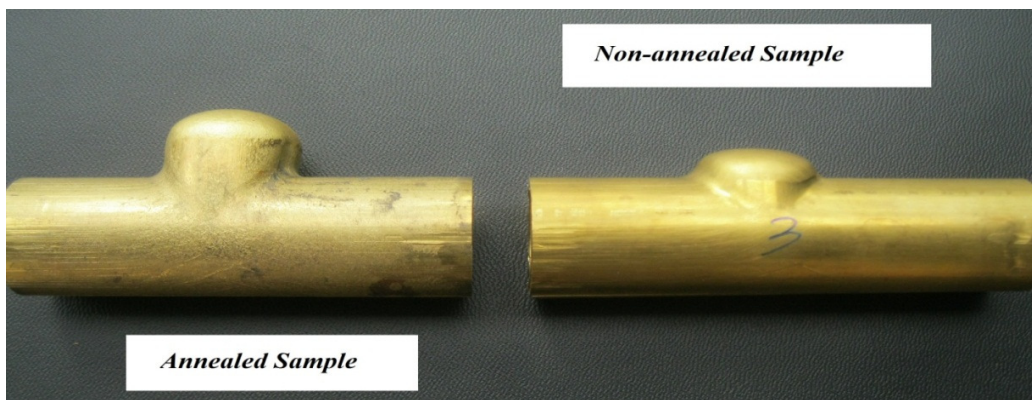


Figure 3.15: Tubes at Axial Pressure 80 [bar].

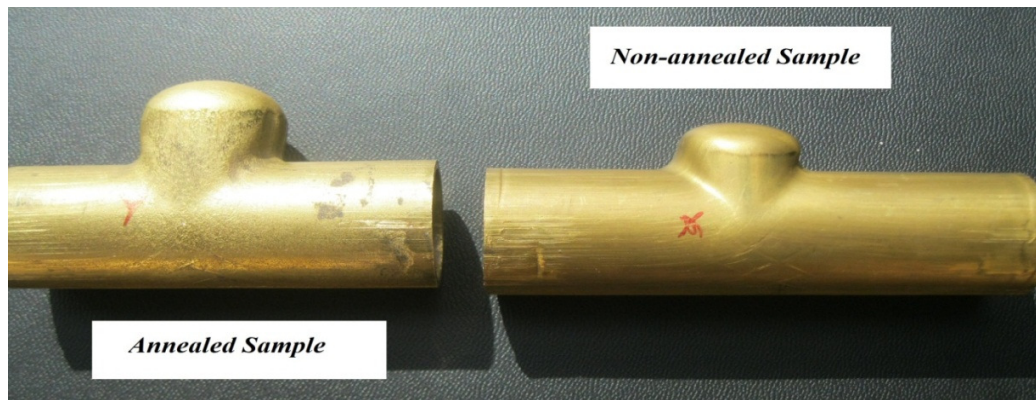


Figure 3.16: Tubes at Axial Pressure 90 [bar].

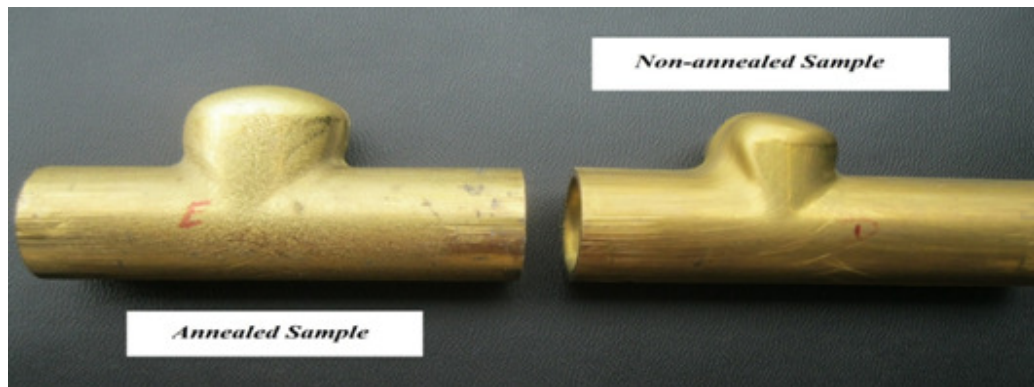


Figure 3.17: Tubes at Axial Pressure 100 [bar].

As it can be seen from figures 3.12- 3.17, the bulges protruded from annealed brass tubes are higher than the non-annealed bulges. Also, the annealed samples have a better bulge shape. Moreover, for the non-annealed samples, buckling starts at axial pressure of 90 [bar] figure 3.17 with major buckling clearly showing at 100 [bar] pressure. On the other hand, the annealed bulges under the applied axial loads didn't exhibit any buckling or wrinkling. The bulge height values for both annealed and non-annealed samples against the applied axial load can be seen in figure. 3.18. A comparison of the annealed and non-annealed brass tube hydroforming indicates that annealing of the brass tubes would improve the hydroformability of the material as higher defect free bulges are gained. Therefore, brass tubes (MS63) were annealed before using them in the bi-layered tube hydroforming process.

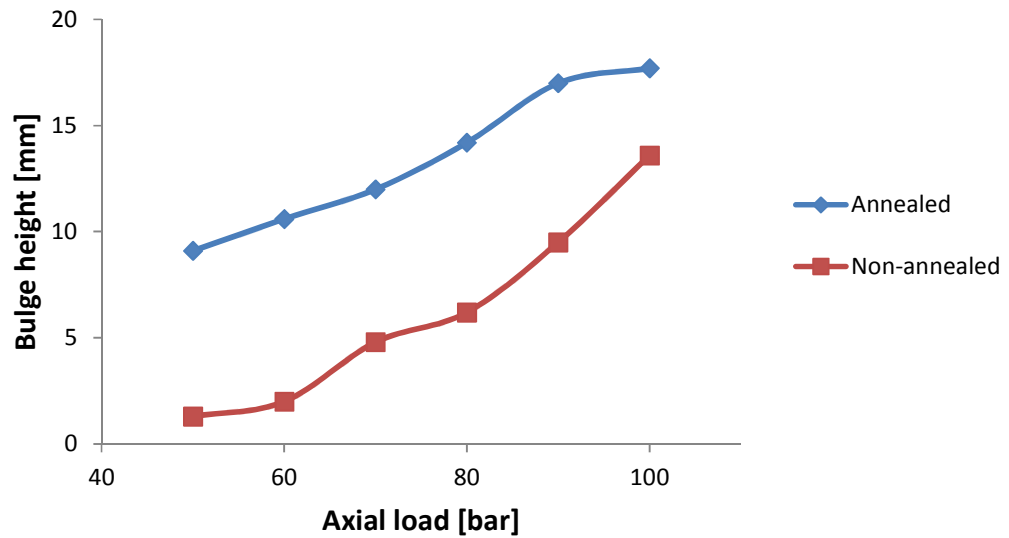


Figure 3.18: Effect of axial load on the bulge height of annealed and non-annealed hydroformed samples.

### 3.3.3. Material properties:

Mechanical properties of the tubular materials (copper and annealed brass) were obtained by means of the uniaxial tensile test for flattened parts of the tubes. The tensile test is one of the most important and widely used material tests as it provides information on basic mechanical properties on strength of materials. The results from the tensile test demonstrate the elastic and plastic behaviour of materials over complex loading histories. In this study, a Zwick/Roell Z050 test machine, as is shown in figure 3.19, was used. True stress-strain data for both materials as shown in figures 3.20, 3.21 were calculated from the engineering stress-strain data that were obtained from the tensile tests. Mechanical properties for both layers are listed in table 3.2.



Figure 3.19: Tensile Test Machine

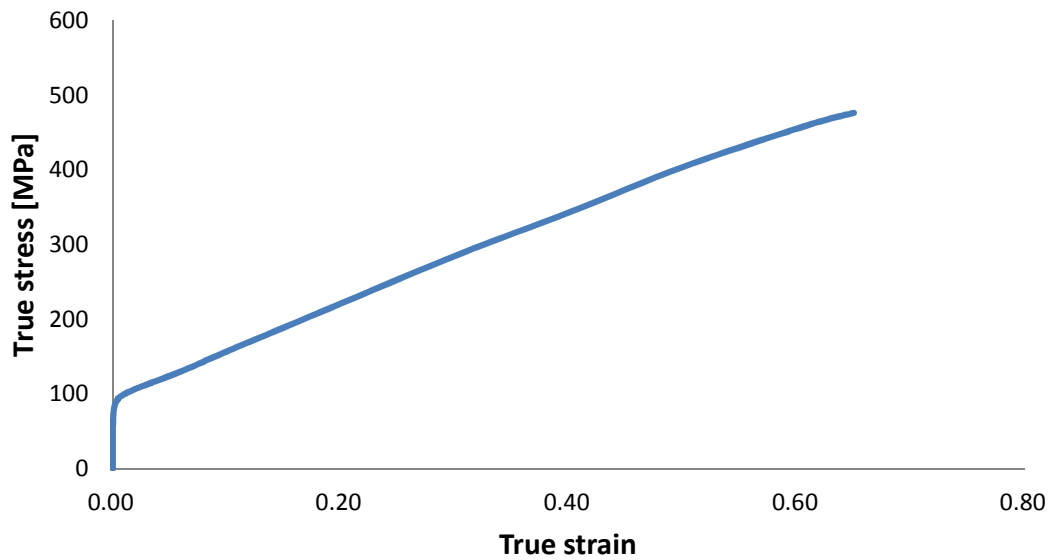


Figure 3.20: The true stress strain curve for the annealed brass material (outer layer).

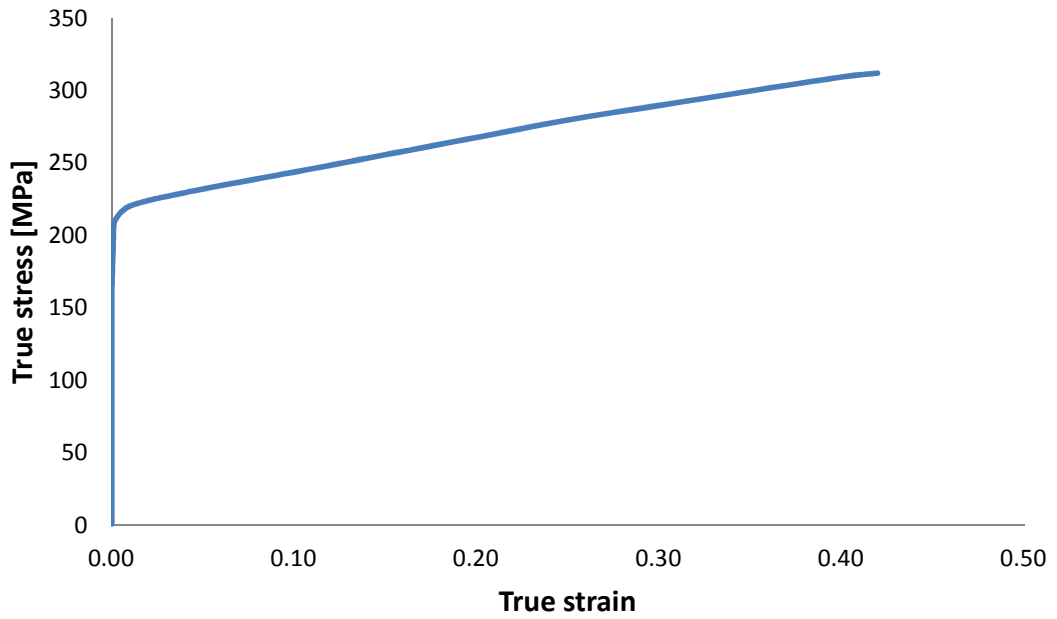


Figure 3.21: The true stress strain curve for the copper material (inner layer).

Table 3.2: Material properties of both layers

<b>Mechanical properties</b>	<b>Outer layer (Annealed Brass)</b>	<b>Inner layer (Copper)</b>
Density [gm/cc]	8.80	8.98
Elastic modulus [GPa]	100	105
Poisson's ratio	0.33	0.33
Yield stress [MPa]	980	220
Tangent modulus [GPa]	0.59	0.21

### 3.4. Measuring equipments:

Measuring equipment was used to measure the physical geometry of the hydroformed parts, as these measurements were then compared with the numerical readings to determine the numerical model accuracy. Protruded bulges were measured using the Brown & Sharpe Global CMM (coordinate-measuring machine), as shown in figure 3.22. This machine allows precise scanning of the branch profile using a touch probe which records the coordinates of the surface points and converts them into computer files [107]. To measure wall thickness, the hydroformed parts were cut using an electrical discharge machine, which uses wire for cutting tubes in order to check the total thickness distribution along the ZY plane. An optical microscope, type Mitutoyo as shown in figure 3.23, was used in

conjunction with attached digital micrometers that allow measurement in both X-axis and Y-axis directions [108].



Figure 3.22: Coordinate Measuring Machine.

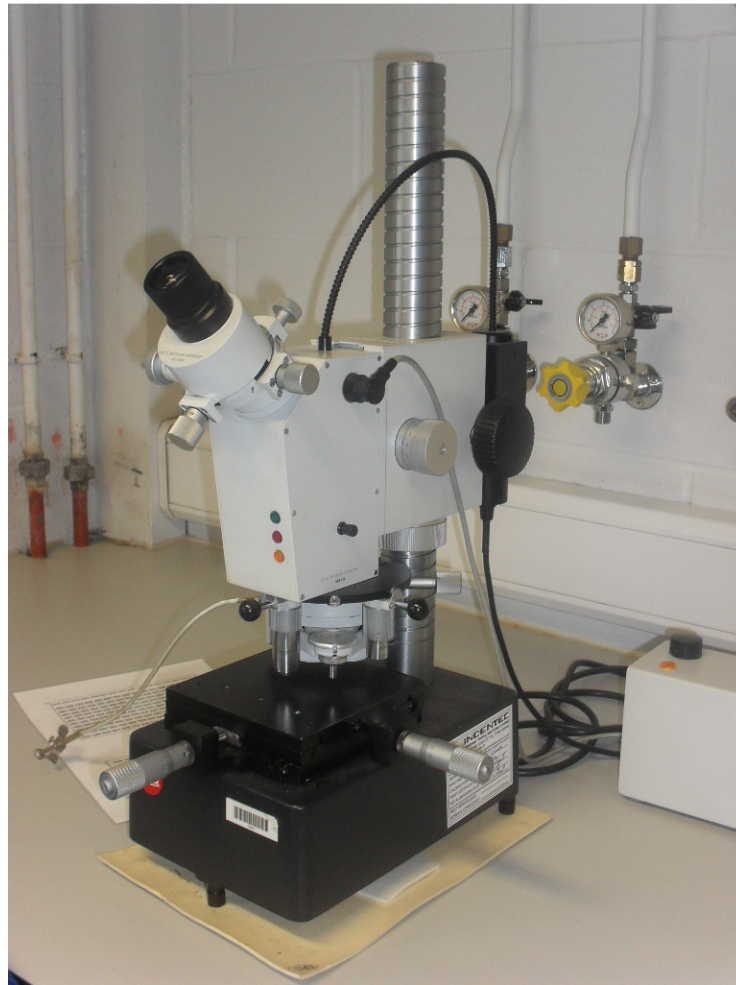


Figure 3.23: Optical microscope.

### 3.5. Experimental study

In the bi-layered tube hydroforming experiments, copper tubes were inserted into the annealed brass tubes with a clearance fit. By a proper application of the internal pressure and axial feed, the tubes combinations were hydroformed in the specified die. In this section, the effects of the axial feed in the case of the X-shape, and the tube length in the case of T-shape, bi-layered hydroforming processes were experimentally examined.

Based on the one factor at a time technique, experiments were conducted to find the effect of the axial feed on the X-shape bi-layered tube hydroforming process. In the experiments, different values of axial feed were tested while the same maximum limit of internal pressure was used. Hydroformed parts are displayed in figure 3.24. Both bulge height and wall thickness at the branch top were measured in the bi-layered hydroformed parts as

displayed in figure 3.25. The effect of the applied axial feed on the bi-layered tube hydroforming process output is shown in figures 3.26, 2.37. It can be seen that, within the used ranges, a higher bulge can be achieved by increasing the axial feed applied as more material is pushed inside the die recess. However, the effect of the axial feed displacement on the branch top thickness was found to be different in two different phases. Increasing the axial feed in the range between (11- 16 mm) leads to a smaller branch top thickness as a result of the increased influence of friction. On the other hand, increasing the axial feed displacement to more than 16 mm was found to lead to a bigger thickness at the branch top, as the assigned internal pressure was found not to be able to expand the increased amount of material in the die, leading to wrinkling or buckling.



Figure: 3.24: X-shape hydroformed parts.

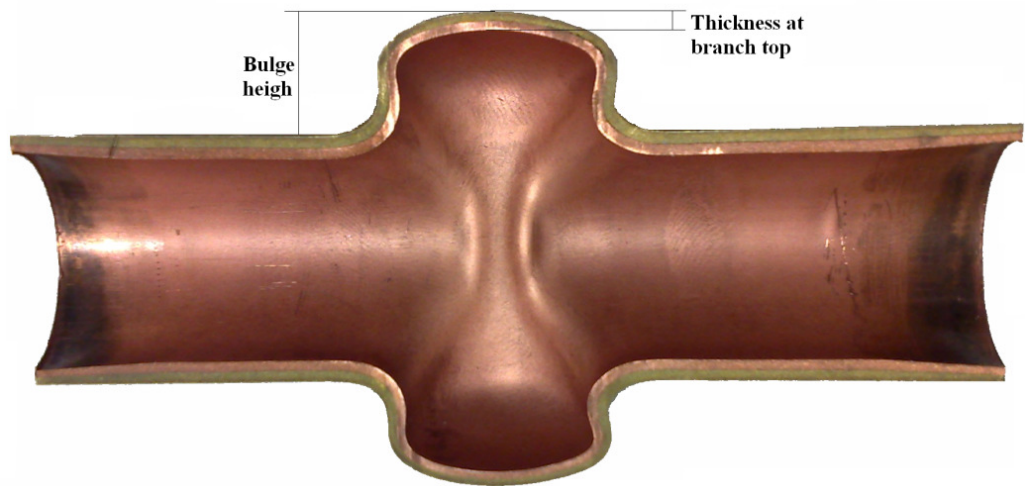


Figure 3.25: Bulge height and wall thickness at the branch top for X-shape hydroformed part.

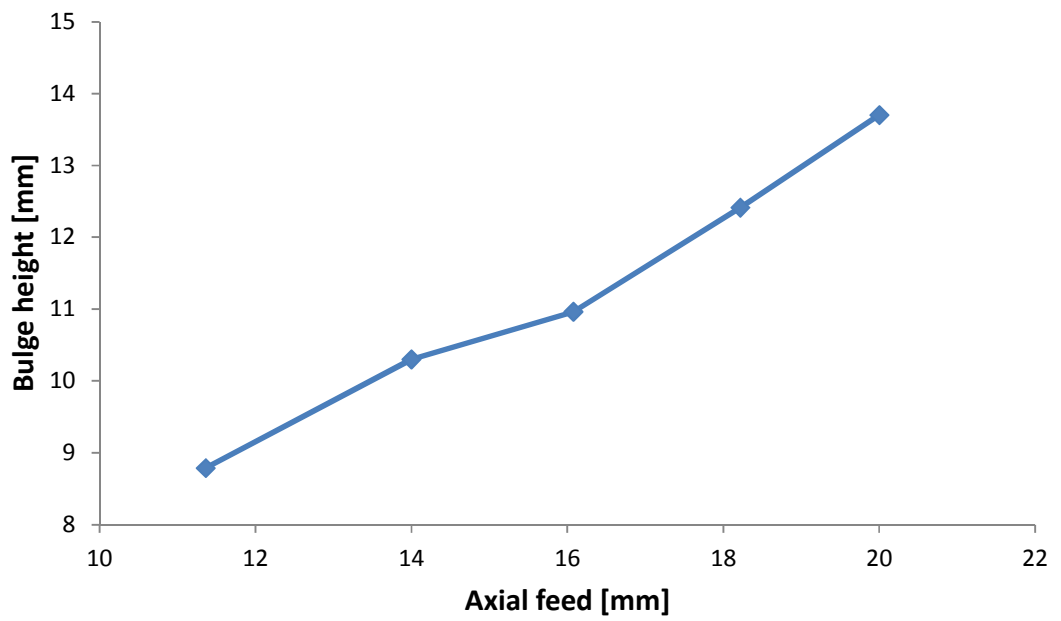


Figure 3.26: Effect of axial feed on X-shape bulge height.

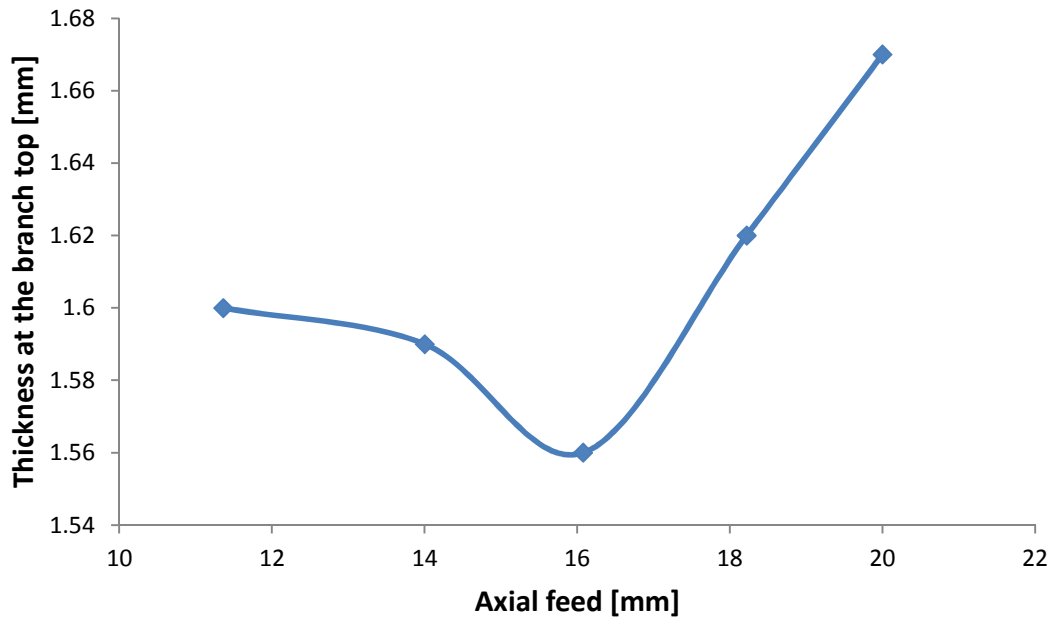


Figure 3.27: Effect of axial feed on X-shape branch top thickness.

In an additional set of experiments, the effect of the initial tube length on the T-shape bi-layered tube hydroforming process output was explored. Various bi-layered tubes with different lengths were experimentally hydroformed using the T-shape die, but using the same machine parameters. Hydroformed samples are shown in figure 3.28, and the different values of the bulge height and wall thickness at the branch top for a range of used tube lengths, are presented in figures 3.29, 3.30. From the experimental results, it can be seen that as the tube length decreases, T-branches become higher and walls become thicker at the top of the bulges. On the machine, the same axial pressure and internal pressure were used. A shorter tube length means that the application of axial pressure will result in bigger axial feed which leads to higher bulges and less wall thinning for T-shape hydroformed parts.



Figure 3.28: Bi-layered T-shape hydroformed parts from different tubes lengths.

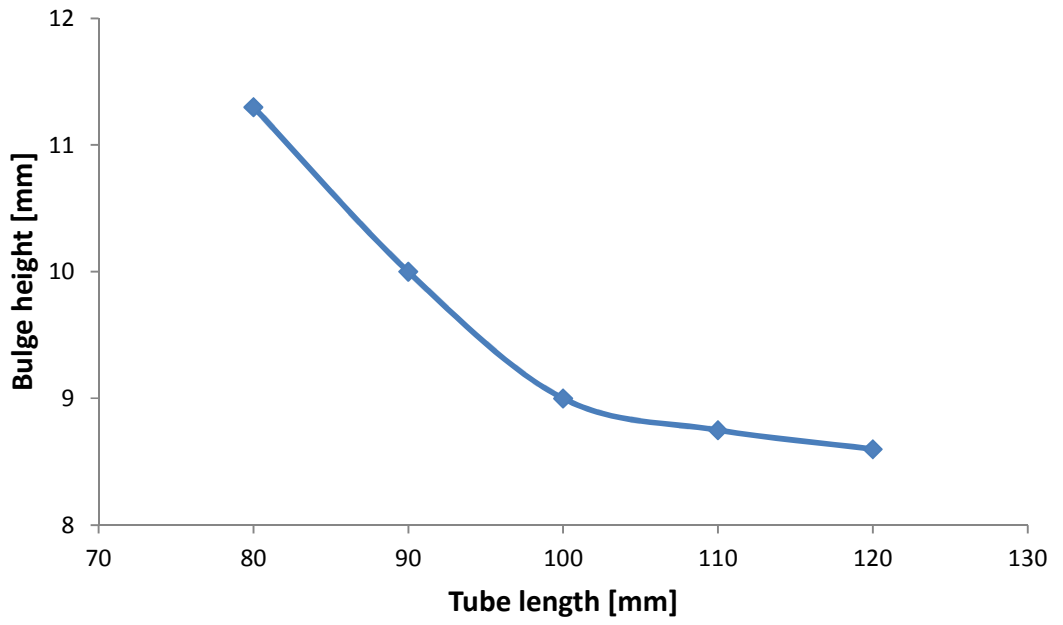


Figure 3.29: Effect of tube length on the T-shape bulge height.

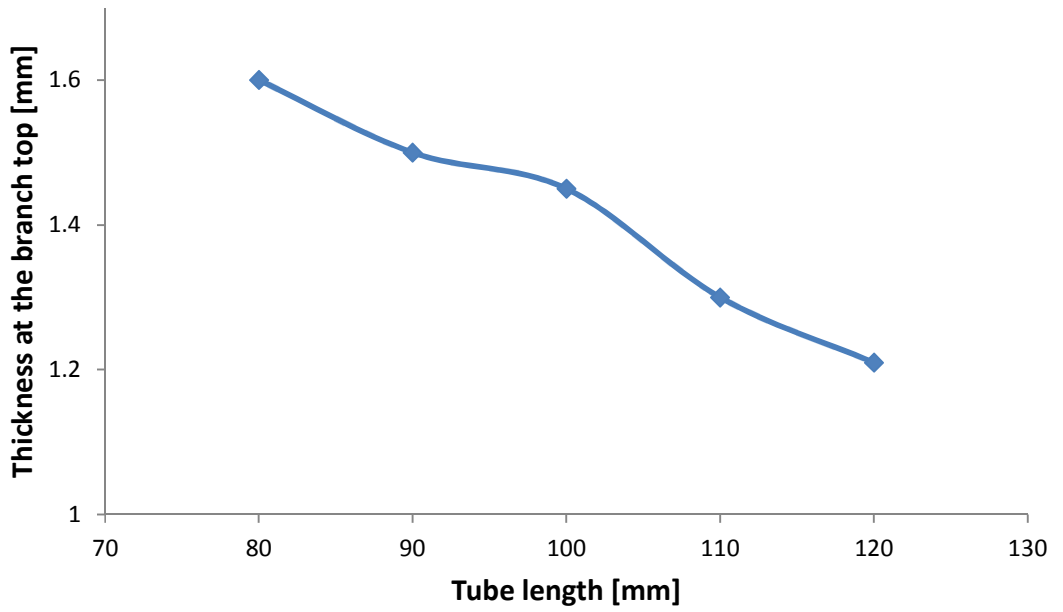


Figure 3.30: Effect of the tube length on the T-shape bulge top thickness.

### **3.6. Summary**

In this chapter, the tube hydroforming machine was described and the experimental procedures outlined. Tube hydroforming experiments were conducted for annealed and non-annealed brass tubes to explore the effect of annealing on the process output. Brass annealing was found to increase the material formability. Following this, the effects of the axial feed on the X-shape and the initial tube length on the T-shape bi-layered tube hydroforming processes were experimentally tested. The experimental approach can provide a good understanding of the process, but due to the limitation and high cost involved in tooling and process design, it is not possible to study the process analysis experimentally. Therefore, in the next chapter, numerical methods using advanced explicit finite element codes will be used to simulate the process, after which experiments are used to validate the numerical model.

## **CHAPTER FOUR**

### **NUMERICAL ANALYSIS**

#### **4.1. Introduction**

In this chapter, finite element models for X- and T-branch bi-layered tube hydroforming processes are formulated using ANSYS LS-DYNA pre-processor and LS-DYNA solver. Tests are carried out using the hydroforming machine of Dublin City University to check the validity of the numerical models. Afterwards, a comparison of T-branch single and bi-layered tube hydroforming is carried out using the finite element method. In this regard, a finite element model for the single layer tube hydroforming is constructed and validated by means of experimentation. In the finite element comparison between single and bi-layered tube hydroforming, both types of modelling are kept with the same geometry, tube material, and process parameters, while different types of loading paths are applied (linear, pressure advanced, and axial feed advanced loading paths) for both systems. This is followed by a discussion of the resultant conclusions.

#### **4.2. Finite element modelling of X- and T- branch bi-layered tube hydroforming**

As tube hydroforming is known as a non-linear process due to large displacements, material non-linearity, and non-linearity due to contact; a non-linear three dimensional analysis is required to represent this model and to detect instabilities such as wrinkling and buckling. ANSYS LS-DYNA was used due to its ability to analyse dynamic non-linear problems, advanced contact solutions, and large deformations. However, ANSYS LS-DYNA software can be used with the traditional ANSYS graphical user interface (GUI) and ANSYS Parametric Design Language (APDL). The bi-layered tube hydroforming process was simulated keeping the model's geometrical dimensions, materials properties, and boundary condition the same as in the real experimental work, in order to compare the finite element simulation results with the real experimental results.

The finite element model was compiled using four components: (a) an outer tube, (b) an inner tube, (c) a rigid die and (d) a rigid plunger. The outer tubes (tube length of 120 mm, outer diameter of 24 mm and inner diameter of 22 mm) and the inner tubes (tube length of 120 mm, outer diameter of 22 mm and inner diameter of 20.3 mm) were numerically hydroformed together in X-branch and T-branch dies with die corners radii of 3 mm and 1

mm respectively. By taking advantage of symmetry, a  $1/8^{\text{th}}$  section of the X-branch and  $1/4^{\text{th}}$  section of T-branch were modelled as displayed in figures 4.1, 4.2. The nodes at the symmetric edges were restrained in the appropriate directions while the nodes attached to the tube end were kept free for all degrees of freedom.

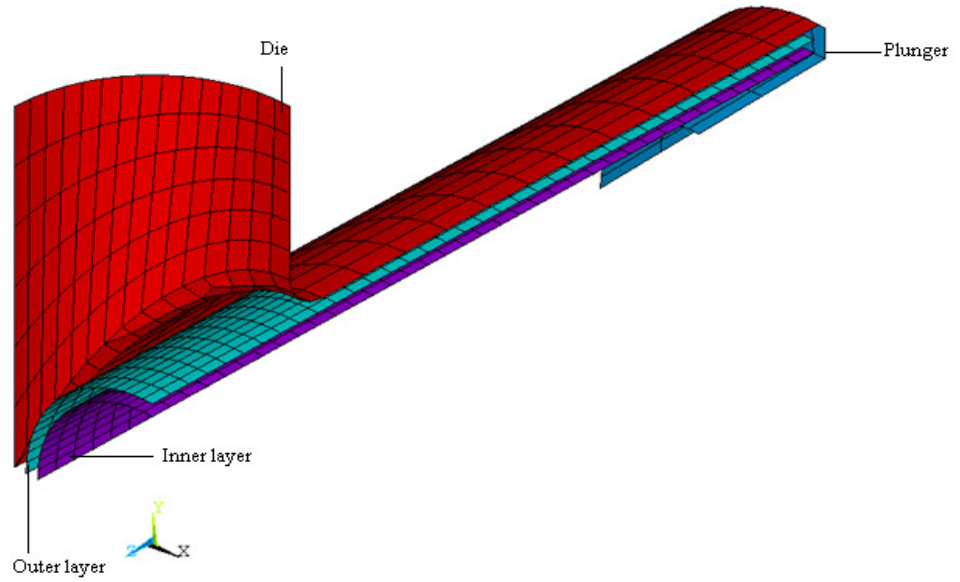


Figure 4.1: Simulation of X-branch bi-layered tube hydroforming (One eighth).

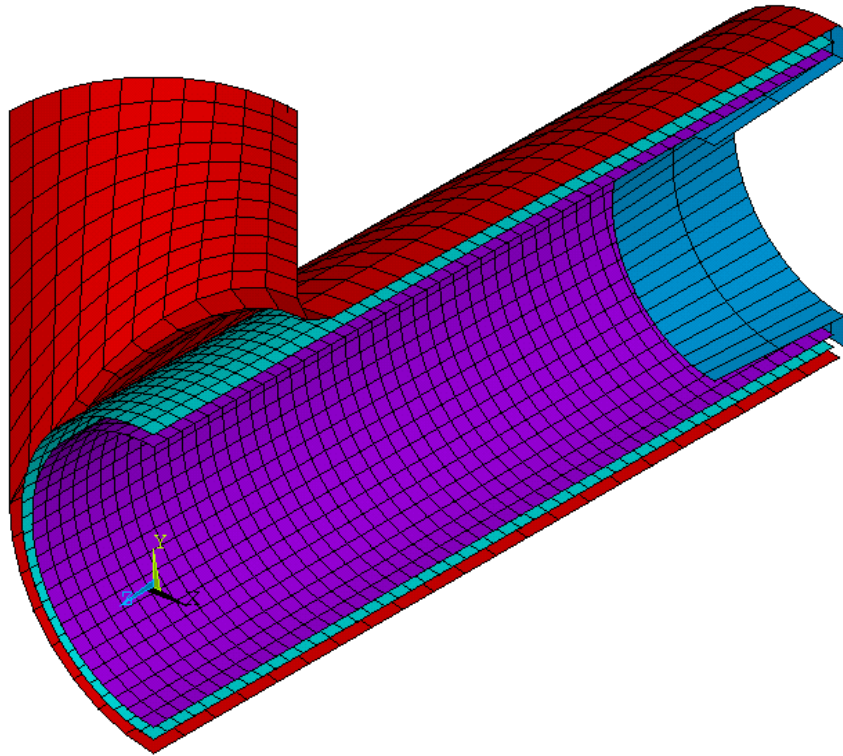


Figure 4.2: Simulation of T-branch bi-layered tube hydroforming (One fourth).

Shell elements were used in most of the finite element analysis of the tube hydroforming, assuming that the shell elements follow the membrane theory. In the simulated model, both outer and inner layers were modelled using 3D thin shell 163 elements with the Belytschko-Tsay element formulation, with the shell thickness change option activated to allow shell thickness to change during the process. The Belytschko-Tsay shell element is one of the fastest elements for thin shell simulations. This, together with its robustness, is the reason why it is popular in finite element codes [109].

It is well known that decreasing the deformable body element size can be preferable in order to obtain more precise results; however, the increase in the elements number not only results in a substantial increase in CPU time but also may cause an over stiff discretization. Hence, in order to select the suitable element size, mesh sensitivity analysis was carried out to determine the effect of the element size used in the tubes modelling on the numerical results figure 4.3.

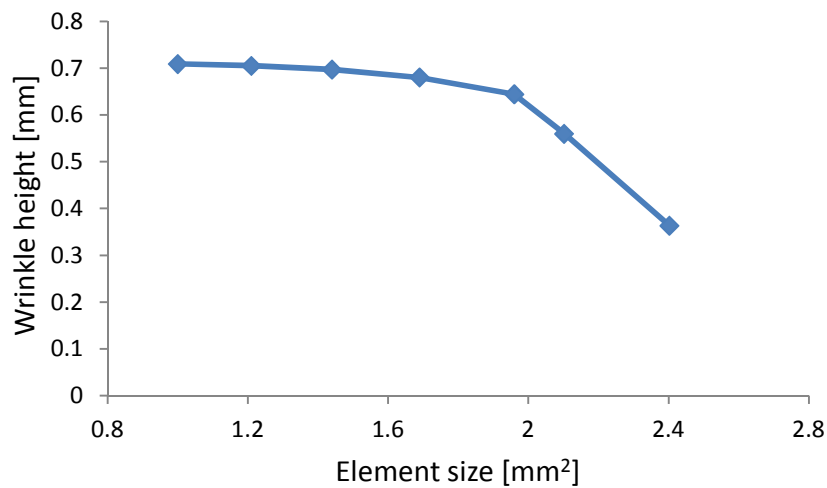


Figure 4.3: Wrinkle height value with different mesh densities.

Elements sizes that gave converged solutions within a reasonable period of time were used in this study. Hence, 1140 and 1020 quadrilateral mapped meshed elements for the outer layer and inner layer respectively were used in the X-type modelling, while 1550 and 1450 quadrilateral mapped meshed elements for the outer layer and inner layer respectively were used in the numerical model of T-type bi-layered tube hydroforming. It can be seen that the wrinkle height was used in the mesh convergence study as it is the smallest output of the process.

In the numerical models of X-type and T-type bi-layered tube hydroforming, the interfaces between the outer and inner layers, the outer layer and the die, and both layers and the plunger were modelled with an advanced automatic surface-to-surface contact algorithm with an elastic coulomb friction law. A coefficient of friction of 0.57 between the two layers was calculated by Islam and Olabi [16]. A value of 0.15, as reported in [80, 31, 16], was taken as the coefficient of friction between the outer layer and the die, and between the both layers and the plunger. Default values of the finite element code were chosen for the exponential decay coefficient, calculated viscous damping friction coefficient, and viscous damping coefficient [109]. In order to simulate self surface contact in cases of wrinkling, another contact parameter was defined for the outer layer with single surface contact entity.

Bilinear kinematic hardening models were used for the tubes materials using the materials properties described in the experimental study table. 3.2. The rigid die and the plunger were

not fully modelled, only the surfaces in contact with the layers were modelled with 3D thin shell elements. The material properties used were of EN21 hardened tool steel for both the die and the plunger. Although the die and the plunger were assumed to be rigid, realistic material properties were defined because these values are used by the LS-DYNA code for calculation of the contact friction and stiffness [109]. The die was constrained for all degrees of freedom and the plunger was constrained for all degrees of freedom except for Z-translation, i.e. it was only allowed to move along the axial length of the tube. The pressure load was applied as a surface load on the shell elements with the normal directing outward assuming the pressure is acting on the inner surface of the inner layer, while the axial feed was applied to the plungers to feed the tubes material. The relation between the internal pressure and the axial feed during the hydroforming process is defined as the loading path.

In explicit nonlinear finite element codes, the state of the simulation is not continuously calculated. Instead, total process time is divided into a large number of steps called increments and for each increment the state of the simulation is calculated. The interval between two consecutive increments is called the global time step. A local time step is associated with each shell element. This element time step is assumed to be equal to the time taken by an elastic wave to pass through the element. However, stability of the explicit method is ensured if the global time step is lower than the smallest element time step. The default value for the time scale factor can be calculated as (global time step / element time step) and is 0.9; however, few simulations need a smaller scale factor in order to be converged. Simulations using time scale factors larger than 1 cannot ensure the stability of the algorithm.

As explained in section 2.3, the tube hydroforming process is considered as quasi-static, thus a scaled down simulation termination time of 3 [msec] was used to reduce the simulation time, as the actual experimental time is 3 [sec]. However, kinetic energy was checked over the entire simulation period and found to be very small when compared to the total internal energy [99, 110], which indicates that there was no dynamic or inertial effect in the process. Since shell elements can be affected by hourglassing, hourglass energy was checked and compared with internal energy for both layers as shown in figure. 4.4. It was

noticed that there was no hourglassing effect for both layers as the ratio of hourglass energy to the internal energy was substantially less than 0.1 [109].

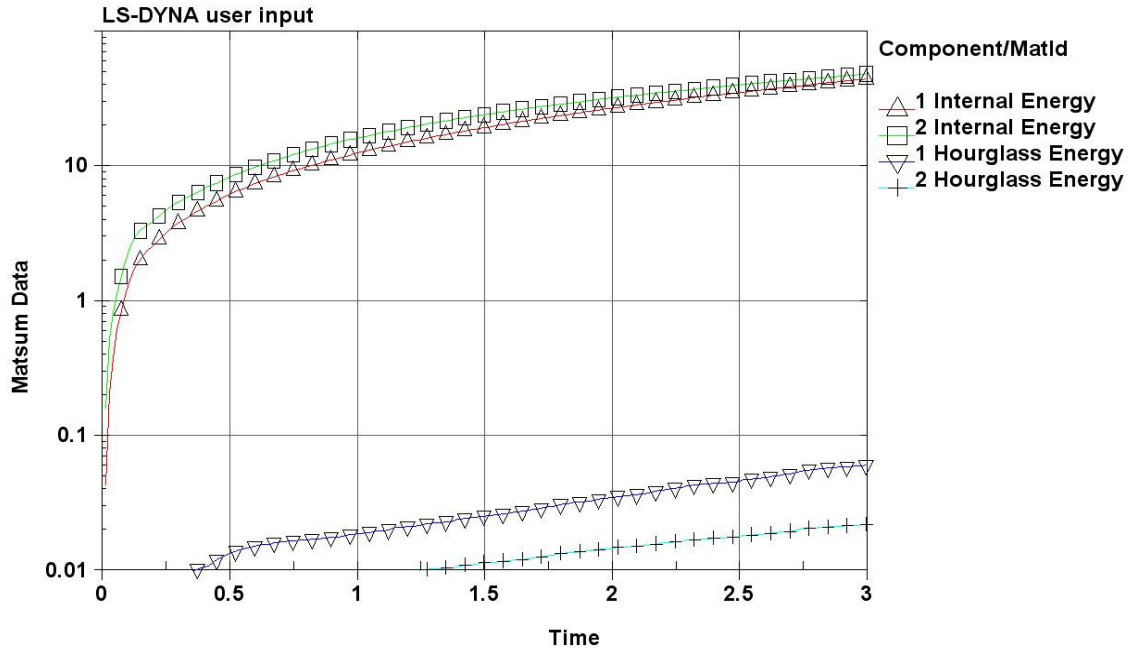


Figure 4.4: A comparison of internal energy and hourglass energy (1: outer layer and 2: inner layer).

### 4.3. Experimental validation of the bi-layered tube hydroforming numerical modelling

Separate experiments were conducted to check the validity of the numerical modelling for both X-type and T-type bi-layered tube hydroforming. A comparison of the experimental and numerical loading paths was carried out for each experiment to ensure that the same loading criteria were applied in both cases. Afterwards, simulation results were compared with experimental results, in terms of the protruded bulge surface and the total thickness distribution. Furthermore, error percentages of simulation results with respect to the experimental results were calculated for the final hydroformed bulge height.

#### 4.3.1. Loading paths adjustment

Different X-type and T-type bi-layered junctions were experimentally hydroformed using different process parameters. During the experiments, the pressure values were recorded with an electronic pressure transducer, and the end axial feed values were recorded with a linear variable displacement transducer. Values of forming pressure and end feed

displacement were used for calculation of the experimental load paths. It was observed that initially the pressure increased steadily, but that in the later part of the process it varied or fluctuated, which was due to the dynamic nature and high sensitivity of the pressure intensifier. In the numerical simulation, the loading paths (characterizing the relationship between internal pressure and axial feed) that were used were matched with the actual dynamic loading paths figures 4.5- 4.8. It should be noted that in the initial stage of the simulation, the loading paths were assigned as they occurred, however the values were averaged for the later part in the fluctuating and unstable zone.

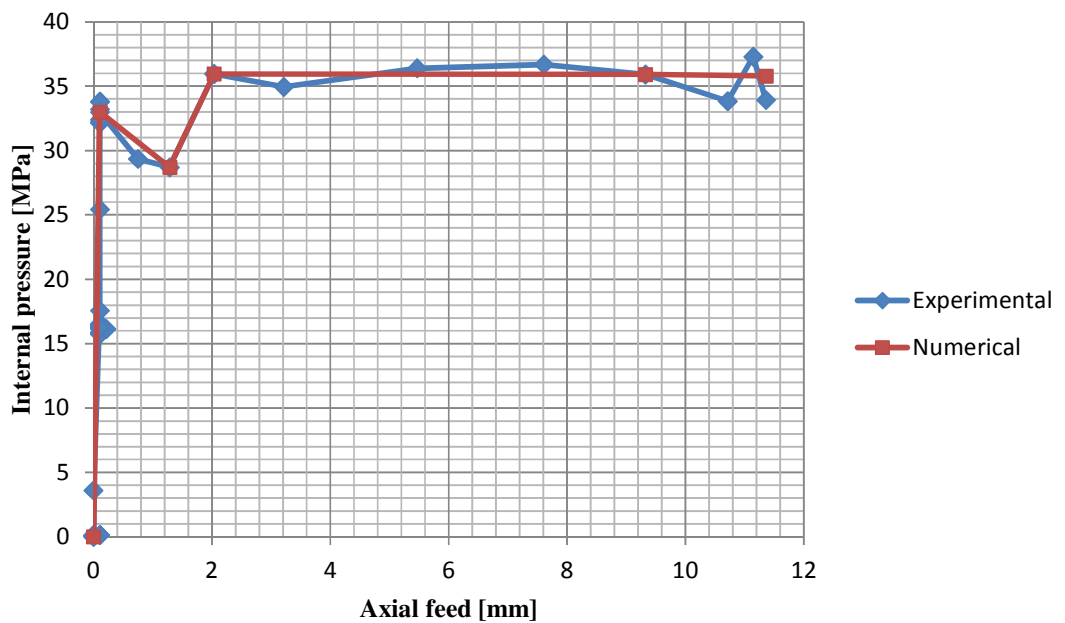


Figure 4.5: Experimental and simulated loading paths in X-branch bi-layered tube hydroforming (test-a).

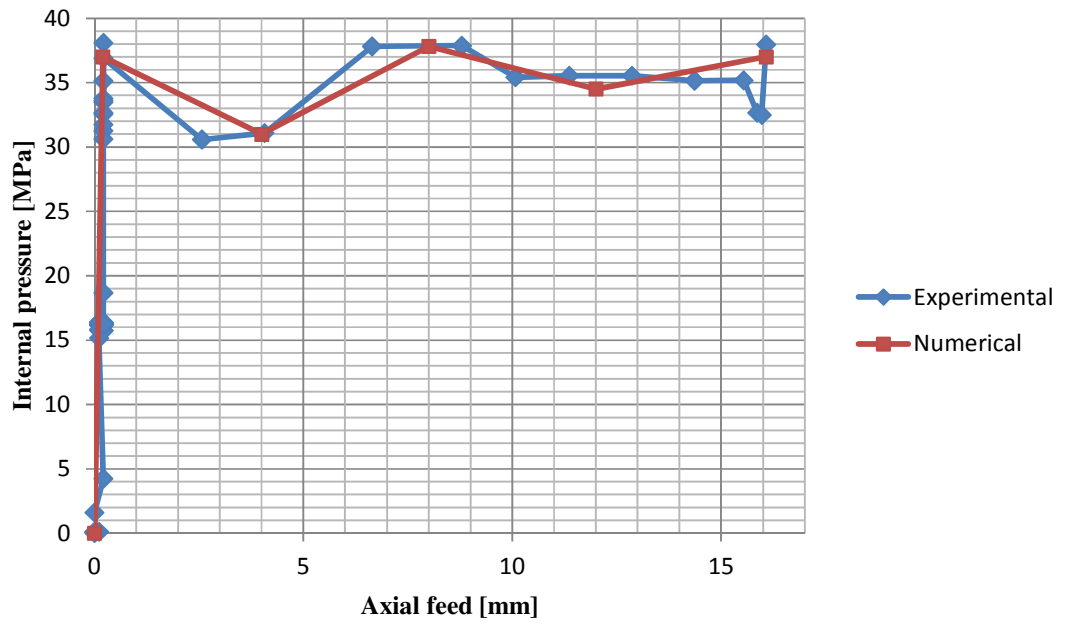


Figure 4.6: Experimental and simulated loading paths in X-branch bi-layered tube hydroforming (test-b).

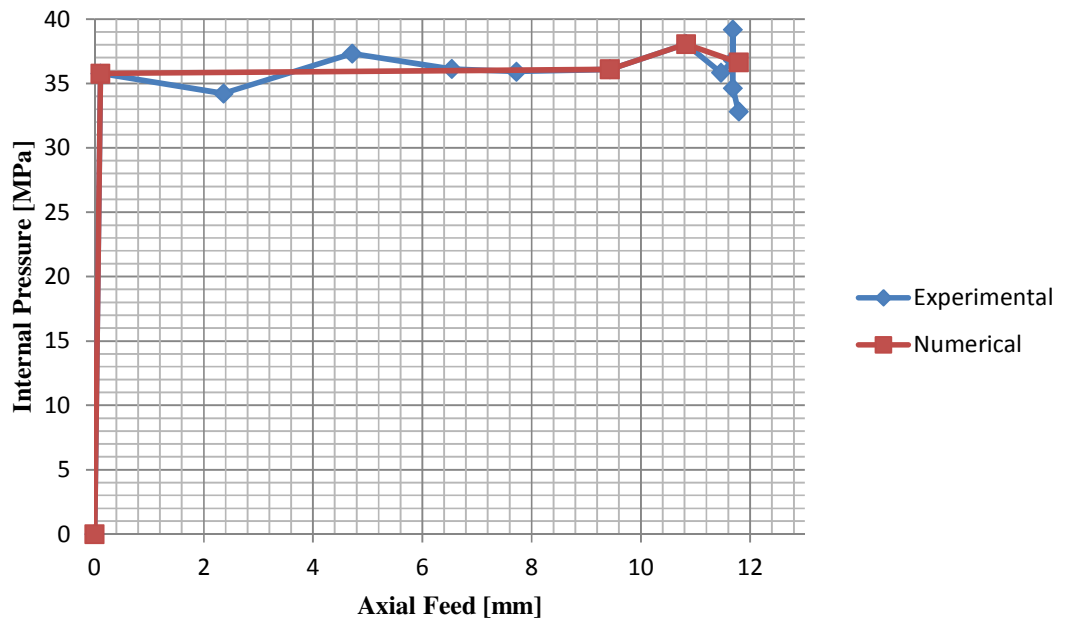


Figure 4.7: Experimental and simulated loading paths in T-branch bi-layered tube hydroforming (test-c).

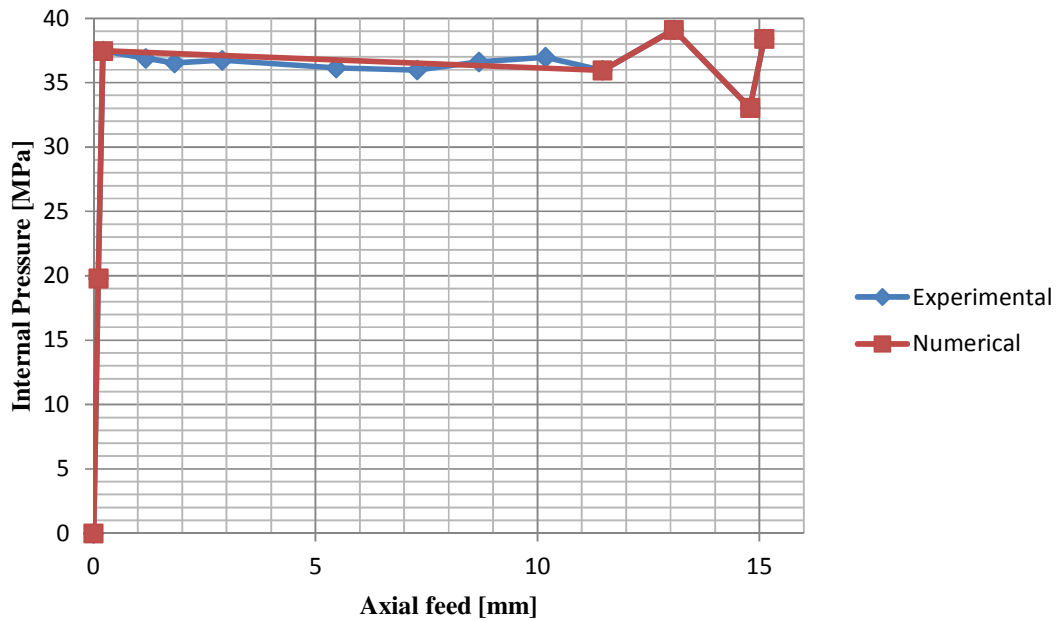


Figure 4.8: Experimental and simulated loading paths in T-branch bi-layered tube hydroforming (test- d).

#### 4.3.2. Numerical and experimental results comparison

Simulation results shown in figures 4.9, 4.11, 4.13, 4.15 were compared with the experimental results shown in figures 4.10, 4.12, 4.14, 4.16 respectively. The branch surfaces were measured along the curvilinear length in the ZY plane for the hydroformed experimental samples using the coordinate measuring machine illustrated in figure 3.22 and were compared with the simulation readings. The numerical results were found to be in close agreement with the experimental measurements figures 4.17- 4.20. In a further comparison, the total wall thickness for each of the hydroformed parts was measured along the protruded bulge by means of the optical microscope as described in figure 3.23. Comparing the experimental wall thickness readings with the numerical results along the curvilinear of the hydroformed parts also corresponded closely with the numerical model, contributing to the validation of this approach figures 4.21- 4.24. Differences noticed between the experimental and numerical values can be attributed to the frequently changing boundary and friction conditions, the anisotropic material properties and the measurements errors of the experimental results.

LS-DYNA user input  
Time = 3  
Contours of % Thickness Reduction- based on current z-strain  
min=-29.4127, at elem# 1233  
max=14.3135, at elem# 1131

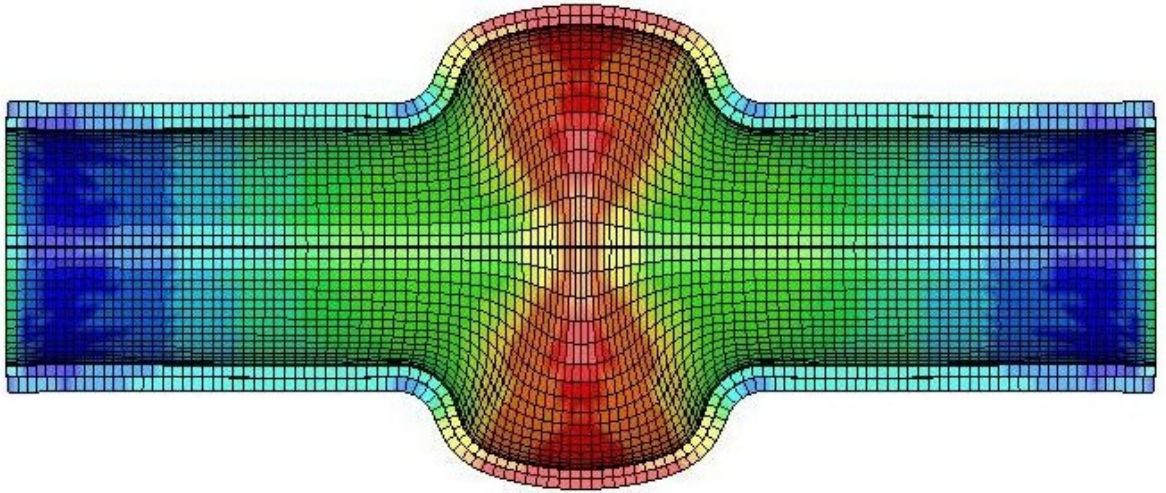


Figure. 4.9: Numerical result of X-type bi-layered tube hydroforming (test- a).



Figure 4.10: Experimental result of X-type bi-layered tube hydroforming (test- a).

**LS-DYNA user input**

Time = 3

Contours of % Thickness Reduction- based on current z-strain

min=-38.1103, at elem# 1

max=17.2371, at elem# 1131

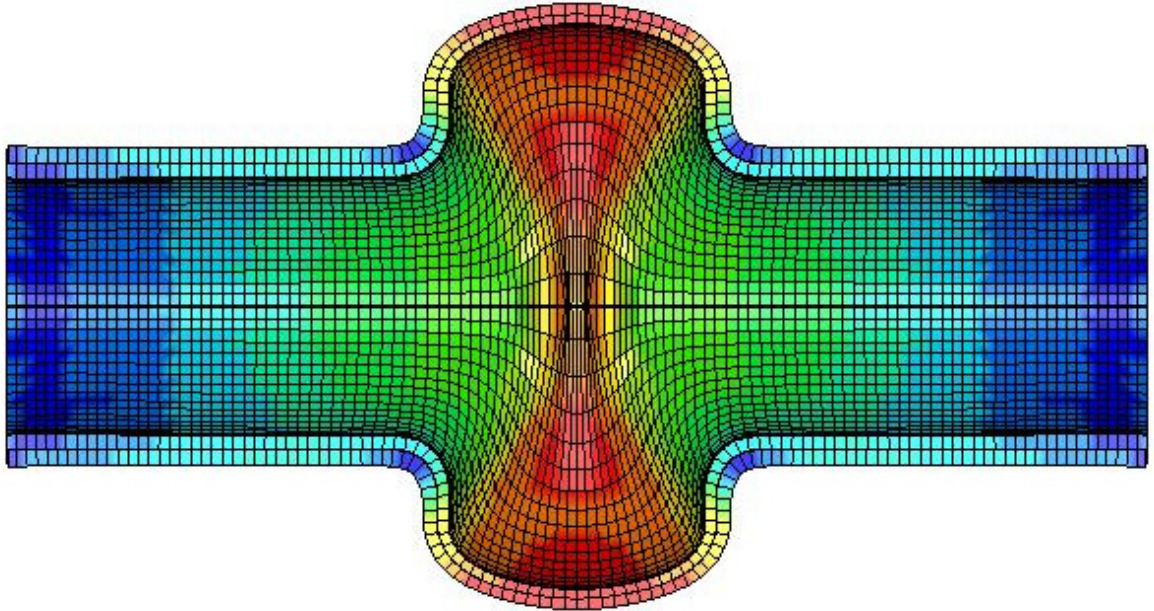


Figure 4.11: Numerical result of X-type bi-layered tube hydroforming (test- b).

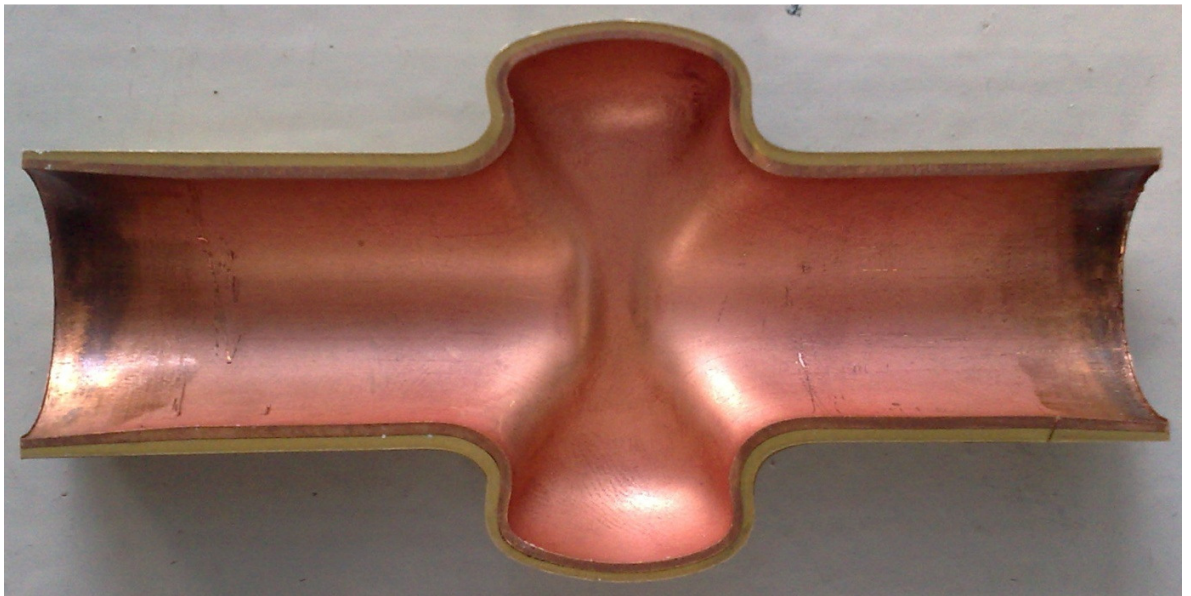


Figure 4.12: Experimental result of X-type bi-layered tube hydroforming (test- b).

**LS-DYNA user input**

Time = 3

Contours of % Thickness Reduction- based on current z-strain

min=-90.9841, at elem# 1701

max=14.269, at elem# 1495

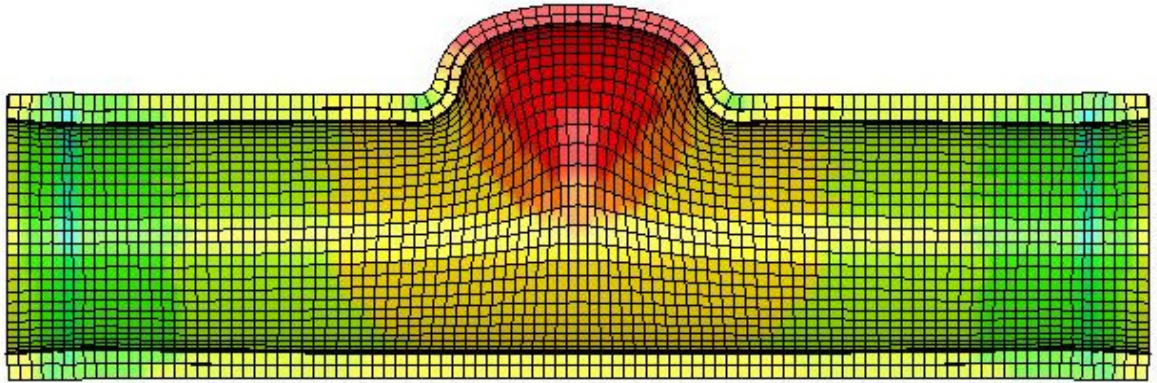


Figure 4.13: Numerical result of T-type bi-layered tube hydroforming (test-c).

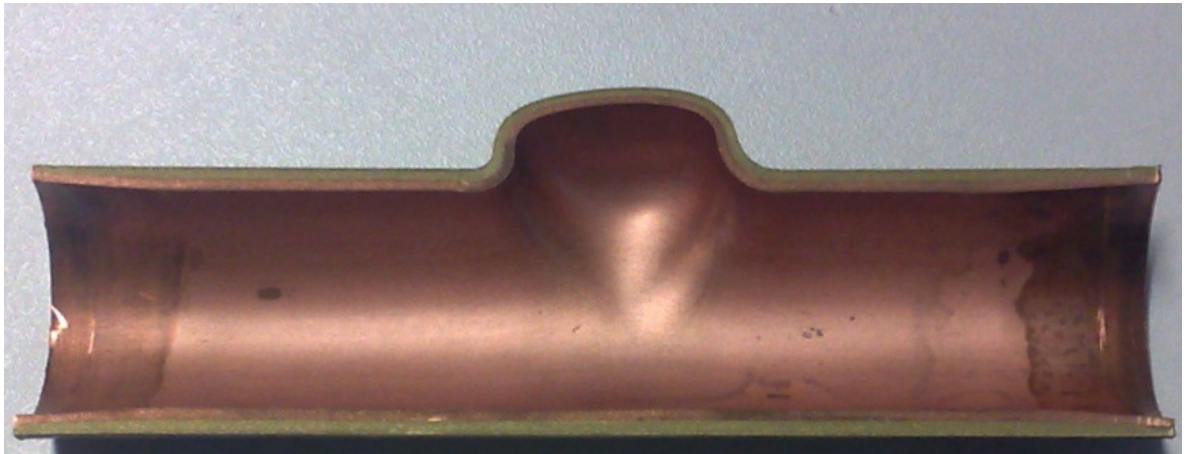


Figure 4.14: Experimental result of T-type bi-layered tube hydroforming (test-c).

**LS-DYNA user input**

Time = 3

Contours of % Thickness Reduction- based on current z-strain

min=-47.96, at elem# 141

max=15.9572, at elem# 1411

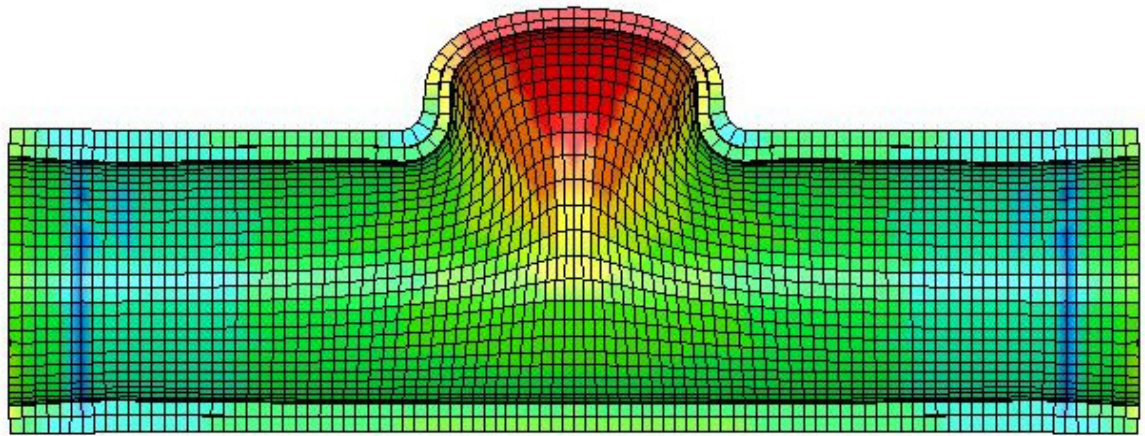


Figure 4.15: Numerical result of T-type bi-layered tube hydroforming (test-d).

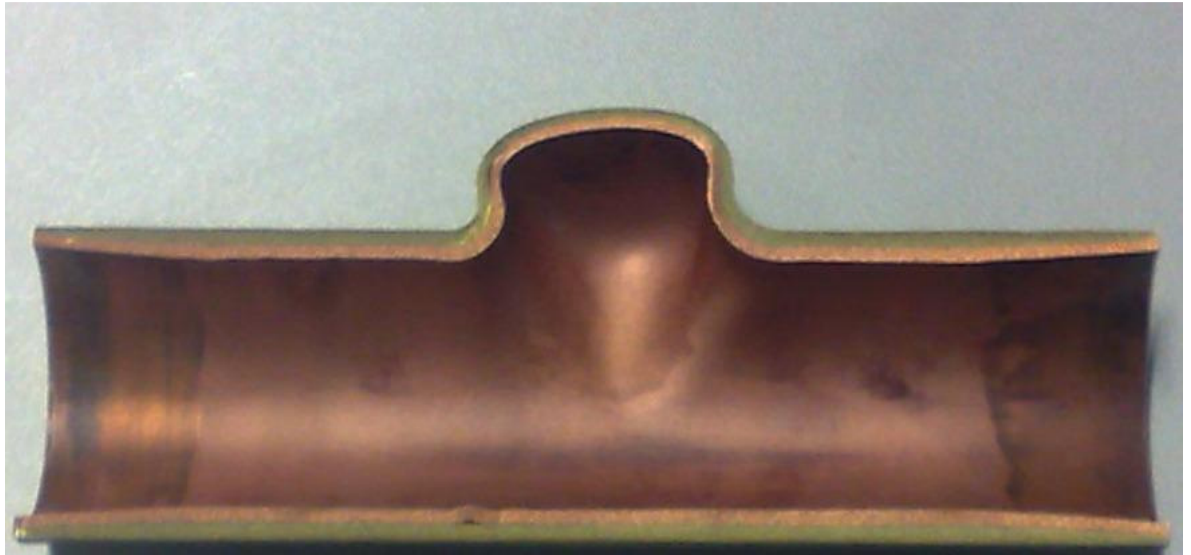


Figure 4.16: Experimental result of T-type bi-layered tube hydroforming (test-d).

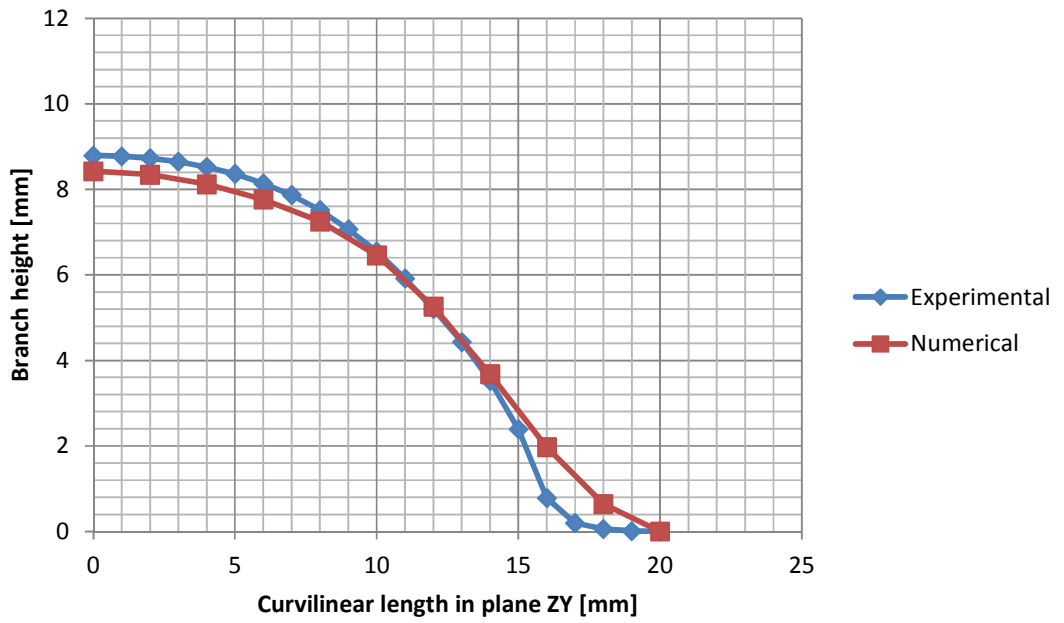


Figure 4.17: Experimental and numerical hydroformed branch profile (test-a).

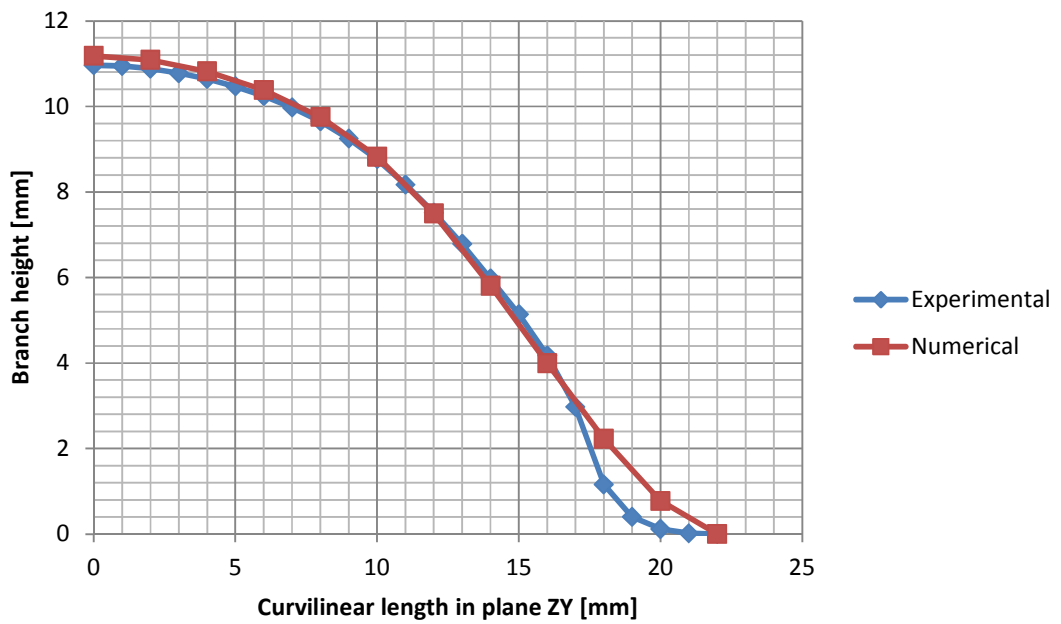


Figure 4.18: Experimental and numerical hydroformed branch profile (test-b).

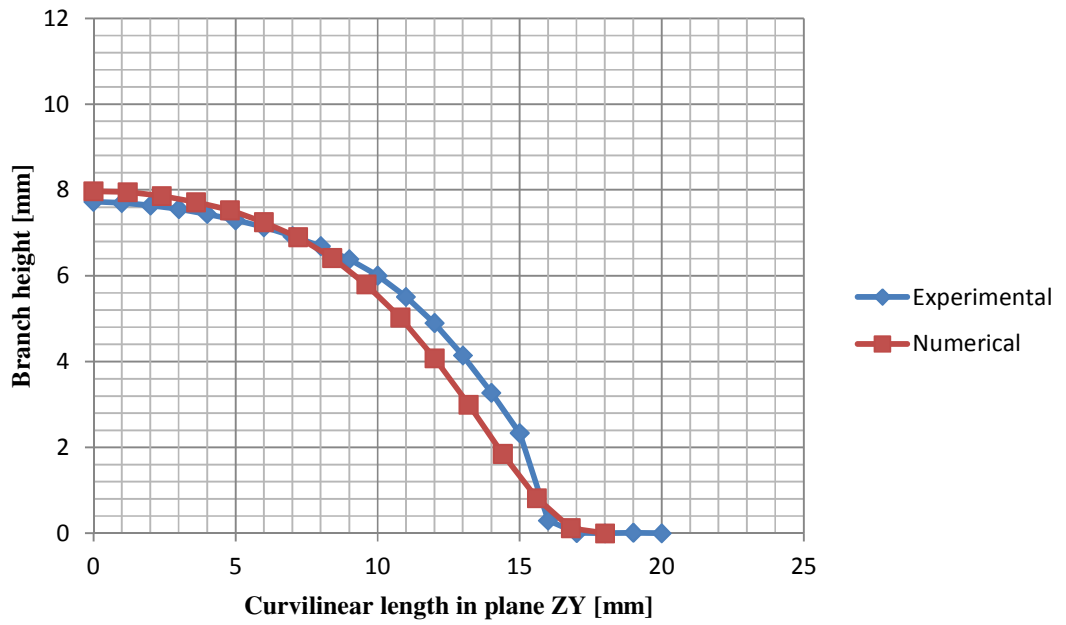


Figure 4.19: Experimental and numerical hydroformed branch profile (test-c).

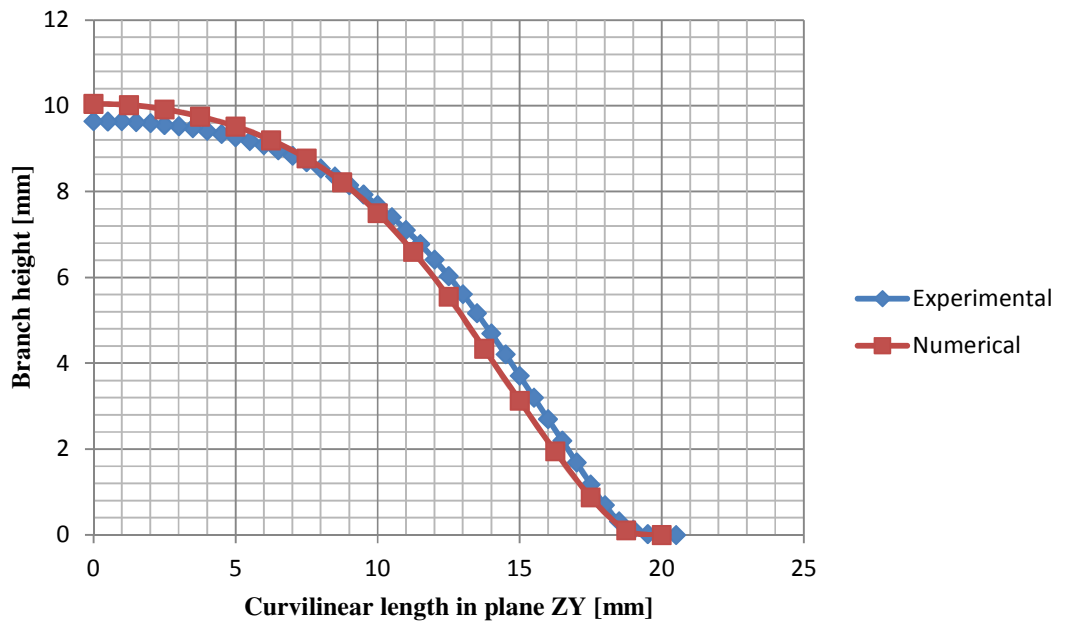


Figure 4.20: Experimental and numerical hydroformed branch profile (test-d).

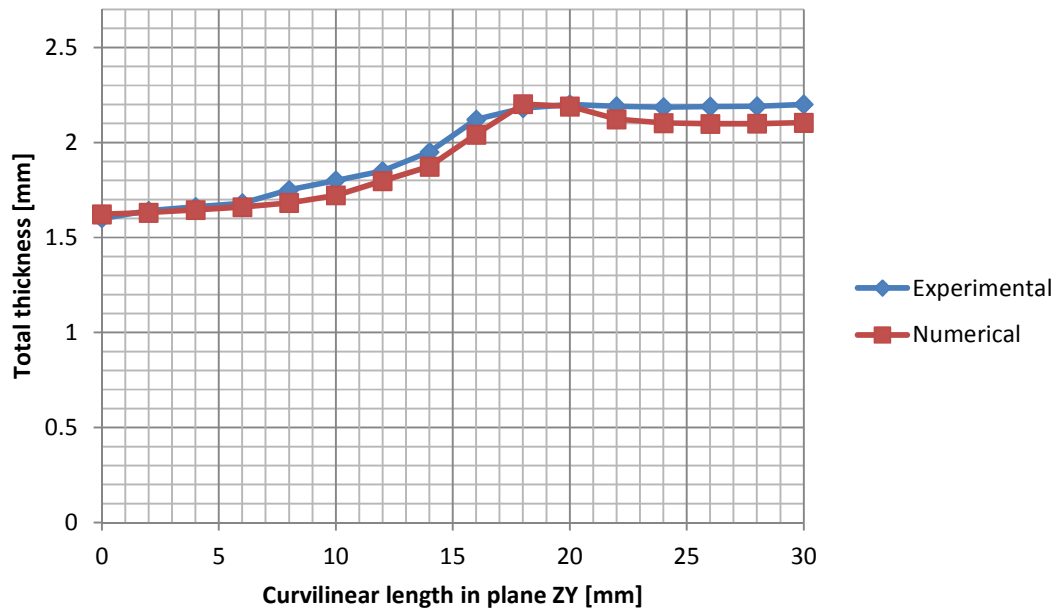


Figure 4.21: Experimental and numerical wall thickness distribution (test- a).

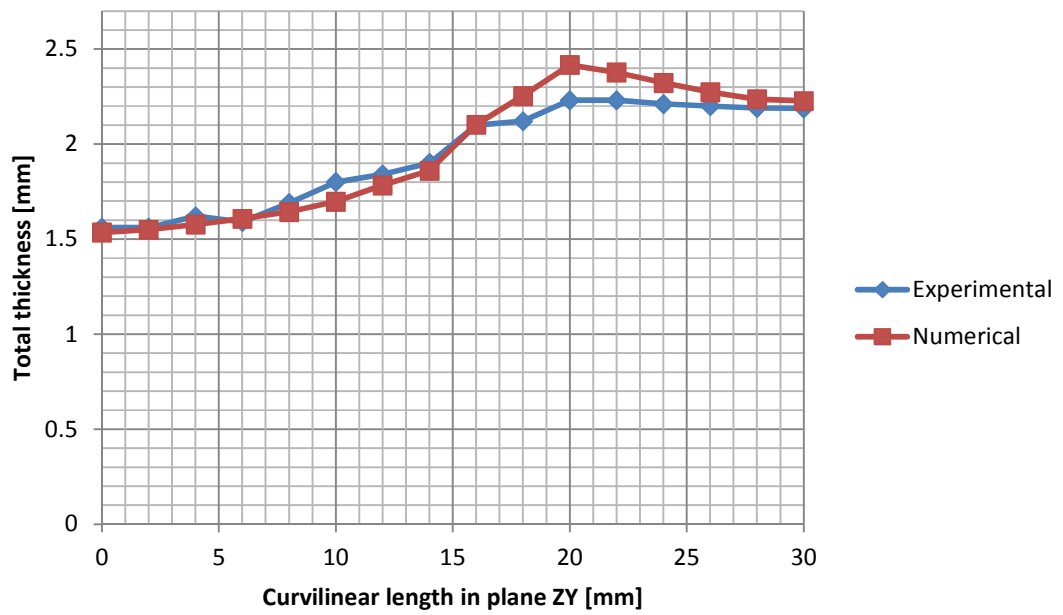


Figure 4.22: Experimental and numerical wall thickness distribution (test- b).

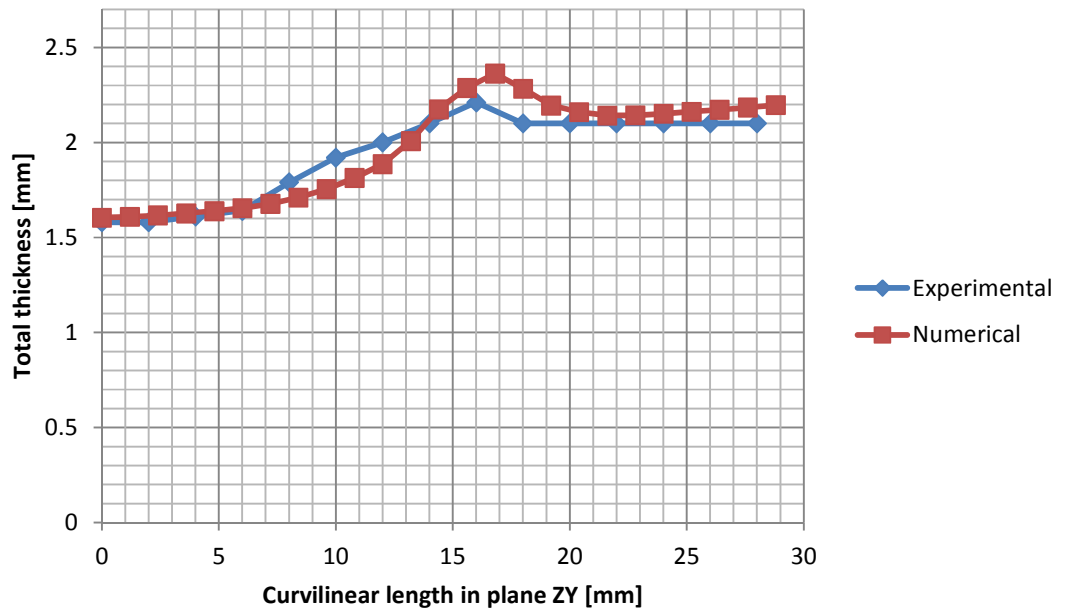


Figure 4.23: Experimental and numerical wall thickness distribution (test- c).

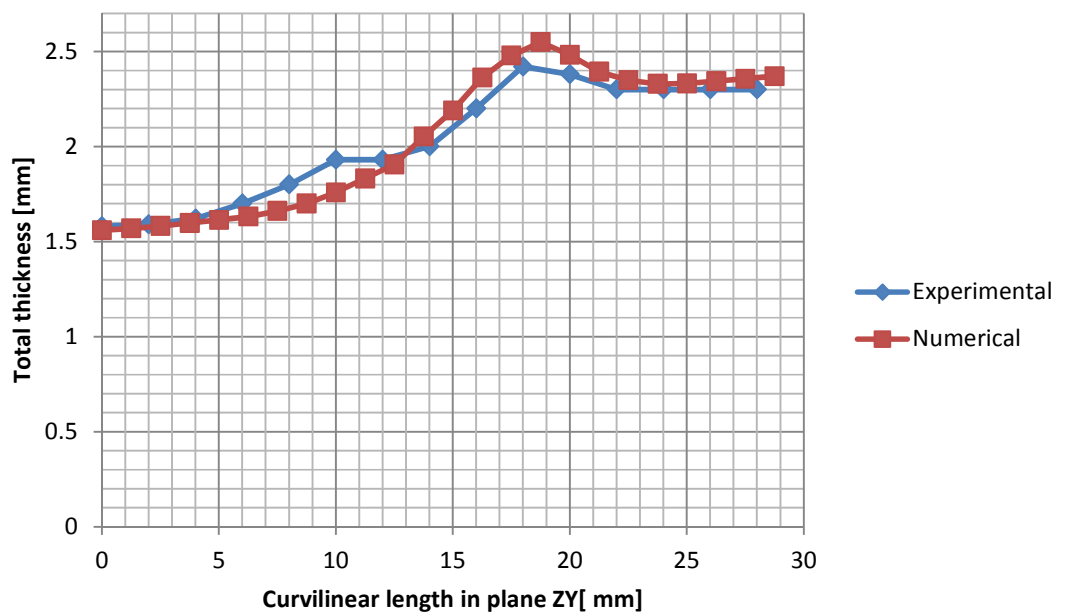


Figure 4.24: Experimental and numerical wall thickness distribution (test- d).

Experimental and numerical results of the final protruded bulges heights are listed in table 4.1. Error percentages of the simulation results as compared with the experimental results were calculated. The maximum deviation obtained from the simulations was within  $\pm 5\%$  of the experimental value, validating the numerical model.

Table 4.1: Experimental and numerical values of the final bulge height of the hydroformed parts.

Type of modelling	Test number	Experimental	Numerical	Percentage error
X-type	Test- a	8.7874	8.4238	+4.13
	Test- b	10.9614	11.1820	-2.01
T-type	Test- c	7.726	7.97	-3.155
	Test- d	9.638	10.05	-4.275

However, for the (test-a), the displacement and stresses for both deformed layers are shown on the numerical results in figures 4.25, 4.26 respectively. It can be observed that both inner and outer layers are deforming together during the process as shown in figure 4.25. While maximum stresses were found to occur at the X-junction blend in figure 4.26 which agrees with stress analysis in [16, 31].

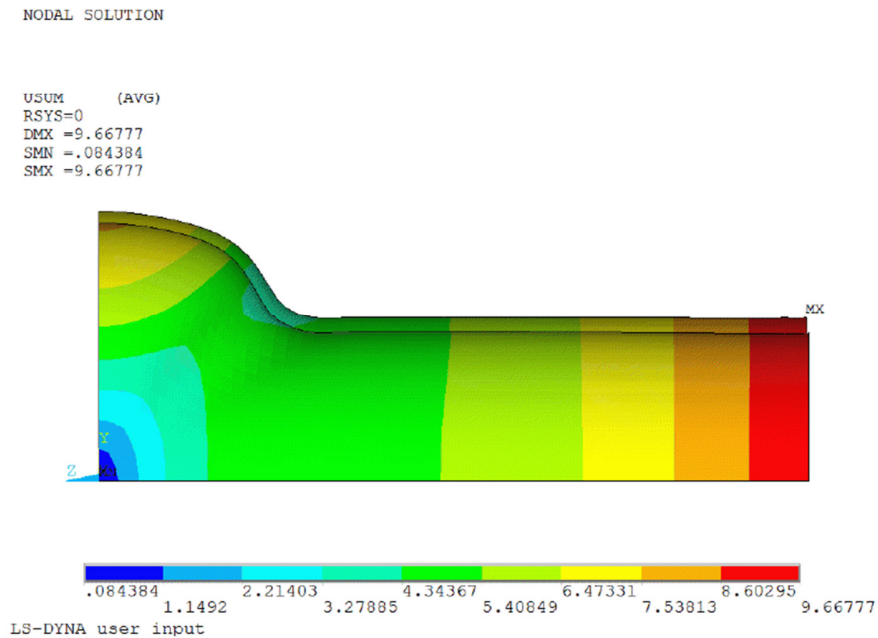


Figure 4.25: Numerical result of the displacement variation through the deformed layers for test-a

NODAL SOLUTION

SEQV (AVG)  
DMX =9.66777  
SMN =.0832  
SMX =.474422

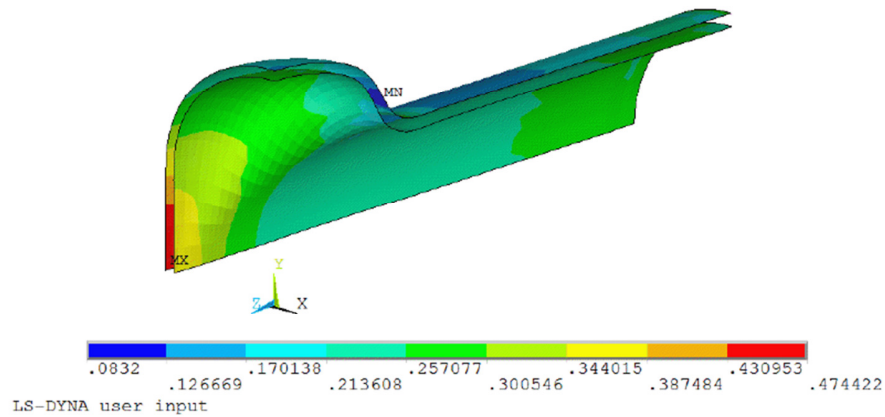


Figure 4.26: Numerical result of the Von Mises stress variation through the deformable layers for test-a

#### 4.4. Finite element comparison of single and bi-layered tube hydroforming

Compared to the single layer structure, bi-layered tubing offers dual properties which can be very beneficial in some complex working environments. It has been found that the use of double-layered tubes with the same material and similar thickness of each layer (roughly one half of total design thickness) can make piping systems much safer for long-distance and high-pressure transportation [10]. In this section, a comparison of single and bi-layered tube hydroforming processes is conducted using the finite element method. To achieve the study objective a numerical model for the single layer tube hydroforming process is required.

##### 4.4.1. Finite element model of single layer tube hydroforming

The finite element model of single layer tube hydroforming was constructed from three parts: (a) a main tube, (b) a rigid die and (c) a rigid plunger, using the ANSYS/LS-DYNA pre-processor. In the numerical study, a standard copper tube (Cu 99.94%, P 0.02%) with the geometry of (tube length of 120 mm, outer diameter of 24 mm and inner diameter of 21.4 mm) was numerically hydroformed in the T-branch die as was also used in the bi-layered tube hydroforming figure 3.4. Similar to the numerical modelling of bi-layered tube

hydroforming conducted in section 4.2, shell elements were used to model one 1/4<sup>th</sup> section of the tube as shown in figure 4.27 by taking advantage of symmetry. Shells were assigned with the Belytschko-Tsay element formulation with shell thickness change option activated. Mesh convergence was achieved for the single layer tube hydroforming with 1550 quadrilateral mapped meshed elements for the tube modelling. The same die modelling was used in the single and bi-layered tube hydroforming numerical simulations. The contact between the tube and both the die and the plunger, was modelled with an advanced automatic surface-to-surface contact algorithm with an elastic coulomb friction law, and with a coefficient of friction of 0.15 [80, 47]. A self surface contact was assigned to the main tube, which can be of interest in case of significant wrinkling. The tube material properties were obtained experimentally using a uni-axial tensile test. A power law plasticity model ( $K= 0.4257$ ,  $n= 0.2562$ ) was fitted to the true stress strain curve [47], and other material properties were (Density = 8.90 gm/cc, Elastic modulus = 119.86 GPa, Poisson's ratio = 0.31, and Yield stress = 116.00 MPa).

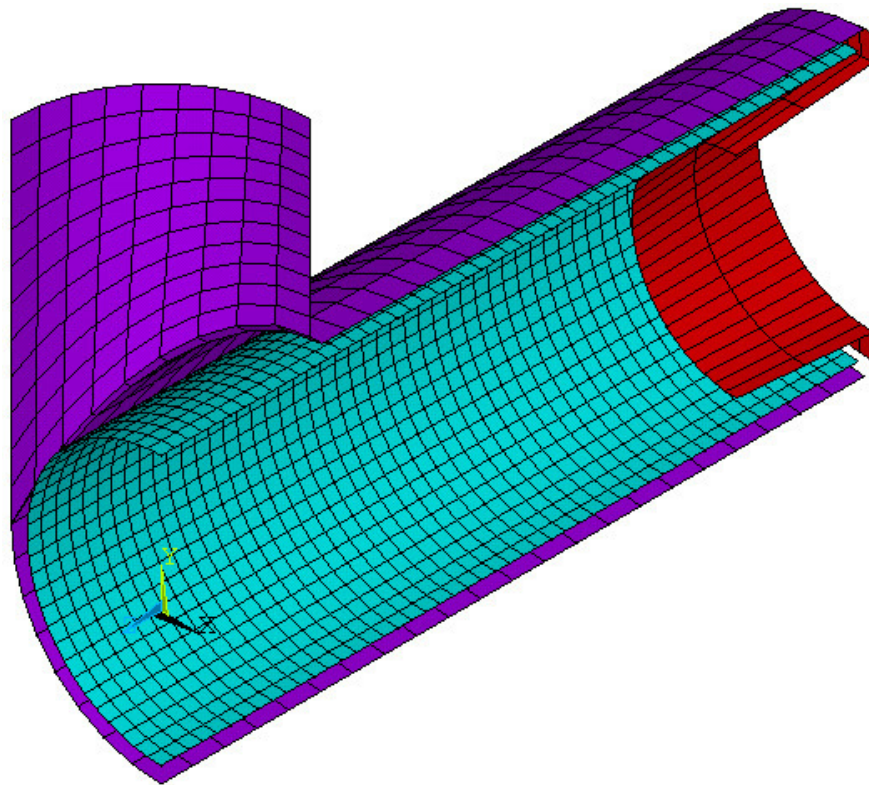


Figure 4.27: Finite element simulation of single layer tube hydroforming.

#### 4.4.2. Experimental validation of the single layer tube hydroforming numerical model

In order to employ the proposed numerical model in the comparison study, two experiments (tests e and f) were conducted to check the validity of the developed model. Therefore, the same materials, geometries, and process parameters were applied experimentally and numerically. Standard copper tubes (Cu 99.94%, P 0.02%) were hydroformed in the T-shape die with the same geometries as used in the numerical study section 4.4.1. Numerical loading paths were matched with the experimental ones as shown in figures 4.28, 4.29. Internal pressure was applied on the inner surface of the tube, while axial feed was applied on the plungers to feed the material. Numerical and experimental results for both tests are shown in figures 4.30, 4.33.

Identical tests to those conducted in section 4.3.2, were carried out to verify the validity of the single tube hydroforming numerical model. Numerical and experimental readings of the branch profiles were compared to each other in figures 4.34, 4.35. The total wall thickness for the hydroformed parts was also measured along the protruded bulge and compared with those computed numerically in figures 4.36, 4.37. Both these tests showed that there was a high correlation between the experimental and numerical results. Furthermore, for the final bulge height, error percentages of the simulation results with respect to the experimental ones were calculated in table 4.2 and the maximum deviation was found less than a  $\pm 5\%$ , margin of error, which supports the validity of the numerical model.

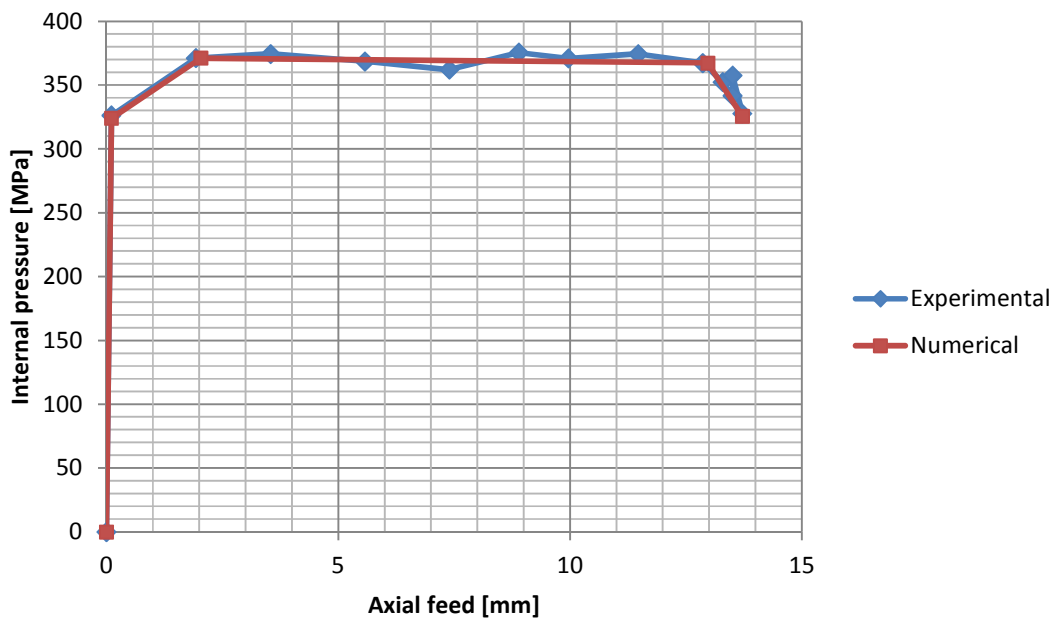


Figure 4.28: Experimental and simulation loading paths in a T-branch single layer tube hydroforming (test- e).

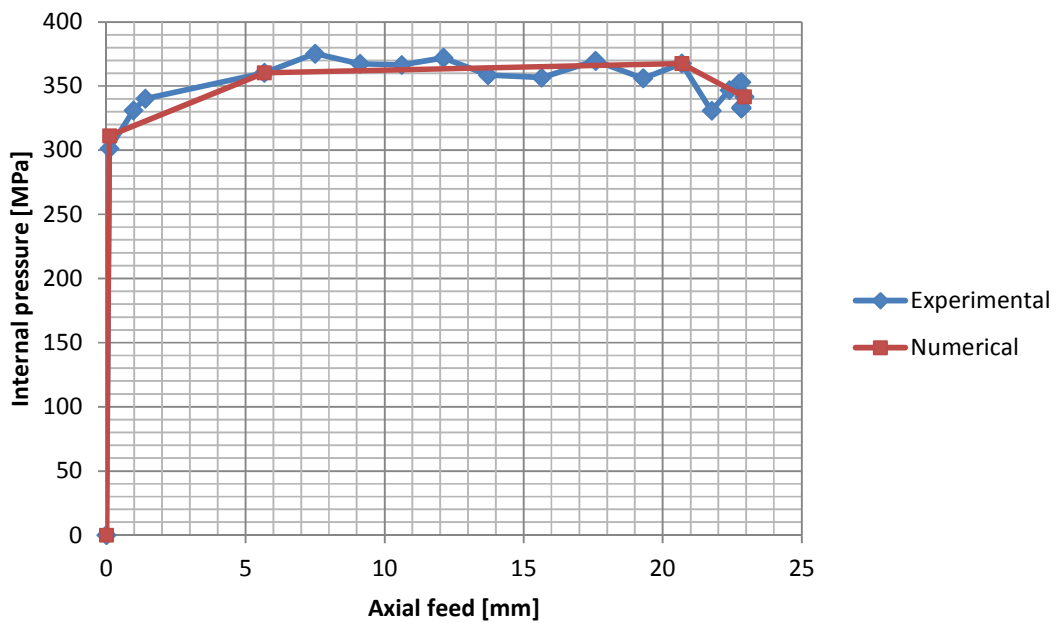


Figure 4.29: Experimental and simulation loading paths in a T-branch single layer tube hydroforming (test- f).

**LS-DYNA user input**  
Contours of % Thickness Reduction- based on current z-strain  
min=-50.729, at elem# 14  
max=29.6842, at elem# 1289

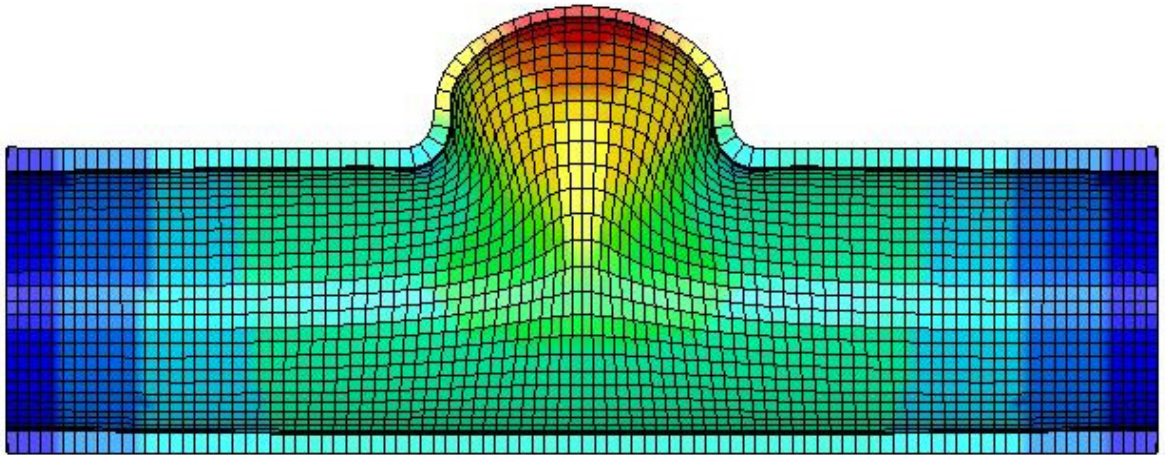


Figure 4.30: Numerical result of test- e.

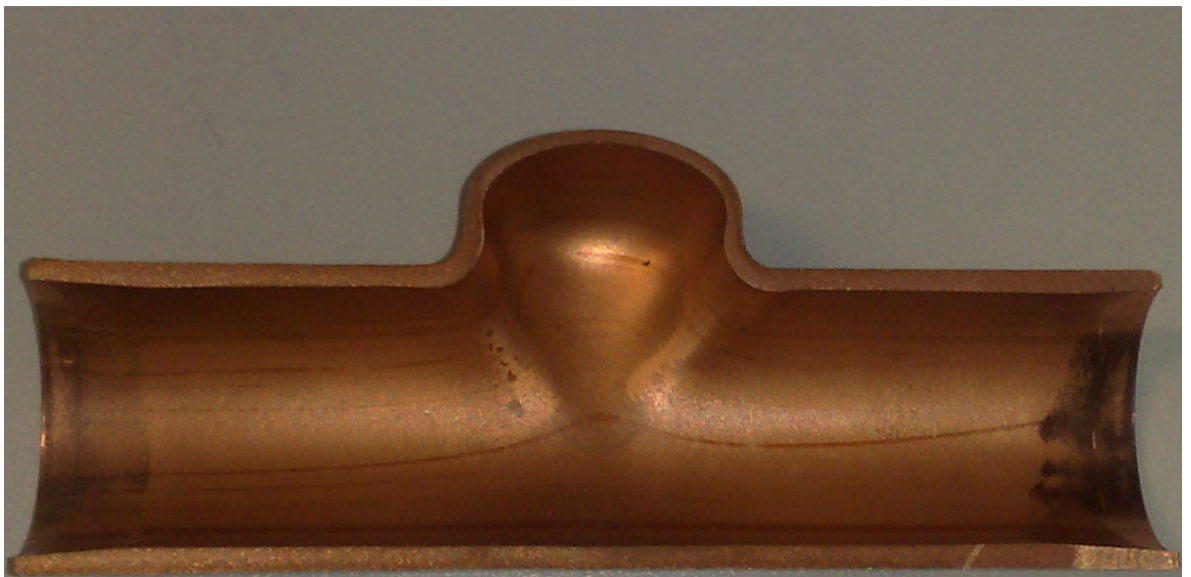


Figure 4.31: Experimental result of test- e.

**LS-DYNA user input**  
Contours of % Thickness Reduction- based on current z-strain  
min=-68.8705, at elem# 142  
max=25.827, at elem# 1289

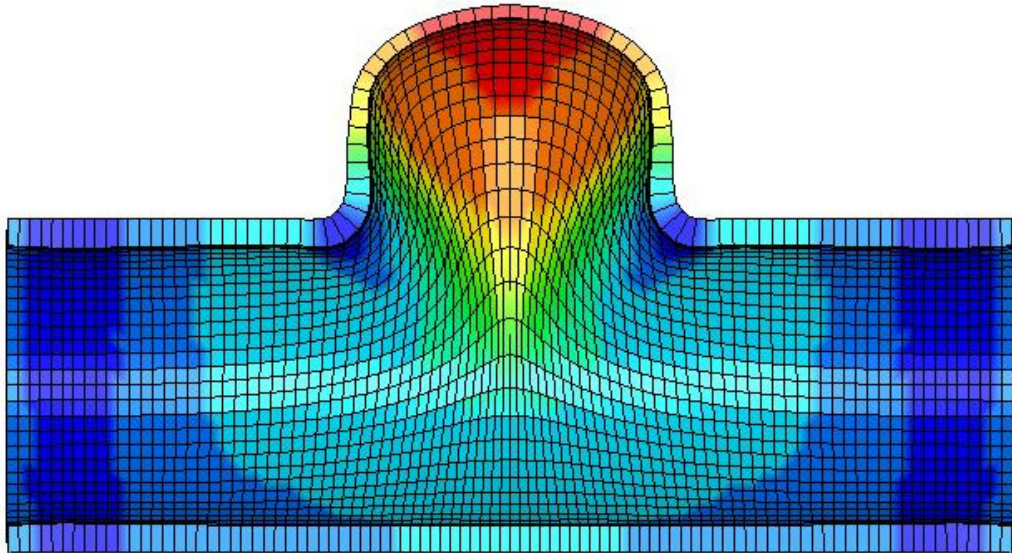


Figure 4.32: Numerical result of test- f.

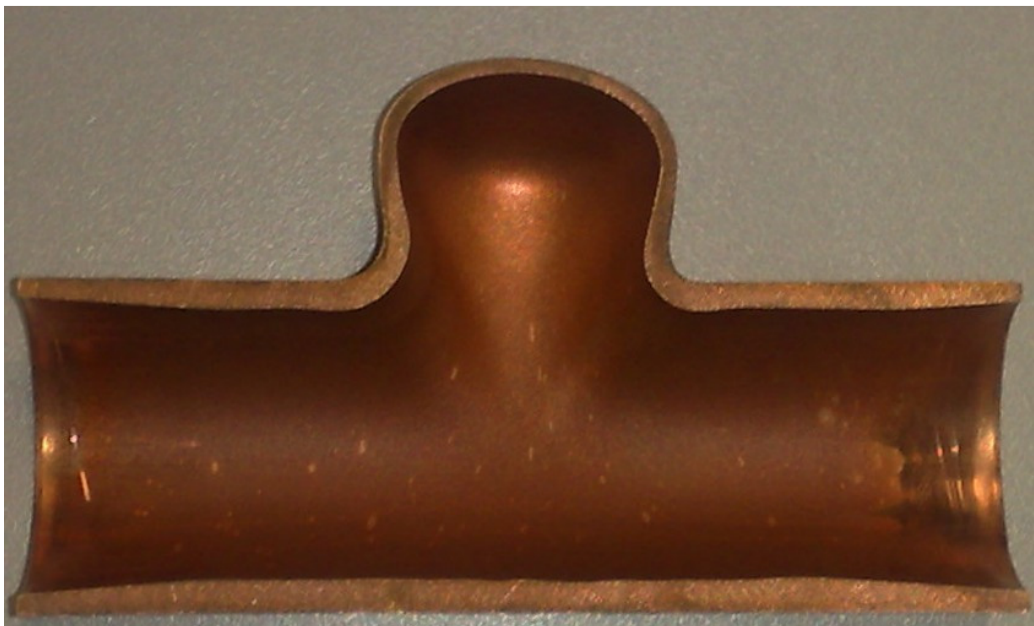


Figure 4.33: Experimental result of test- f.

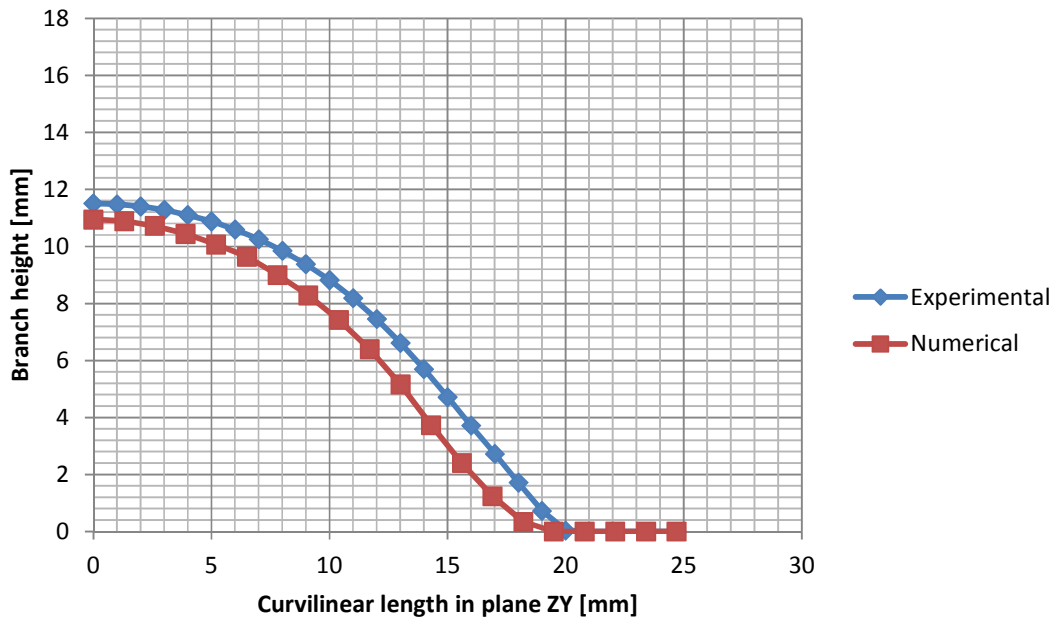


Figure 4.34: Experimental and numerical hydroformed branch profile (test-e).

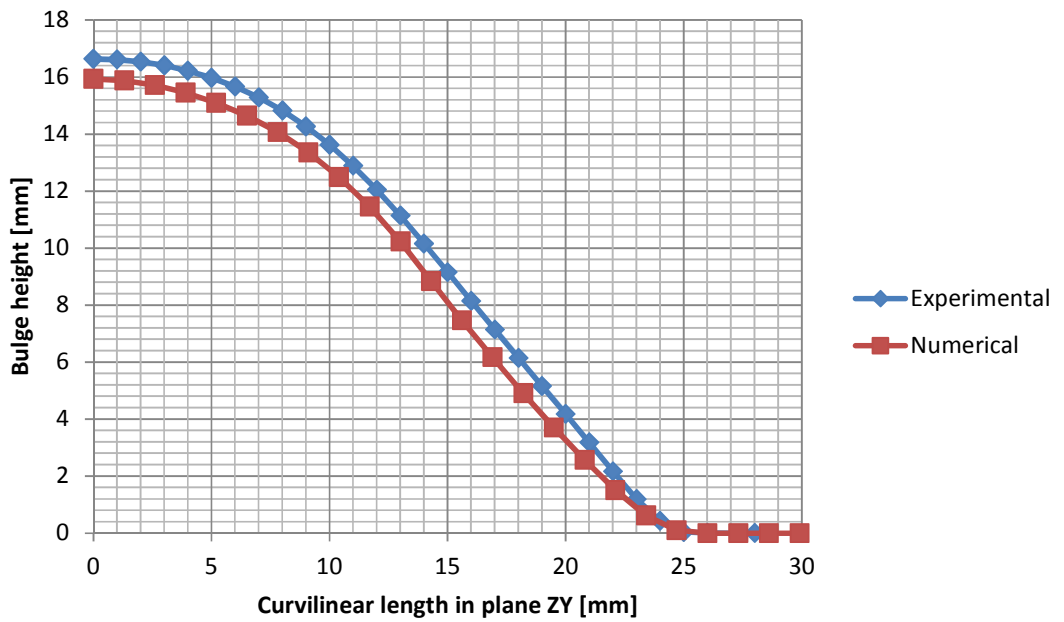


Figure 4.35: Experimental and numerical hydroformed branch profile (test-f).

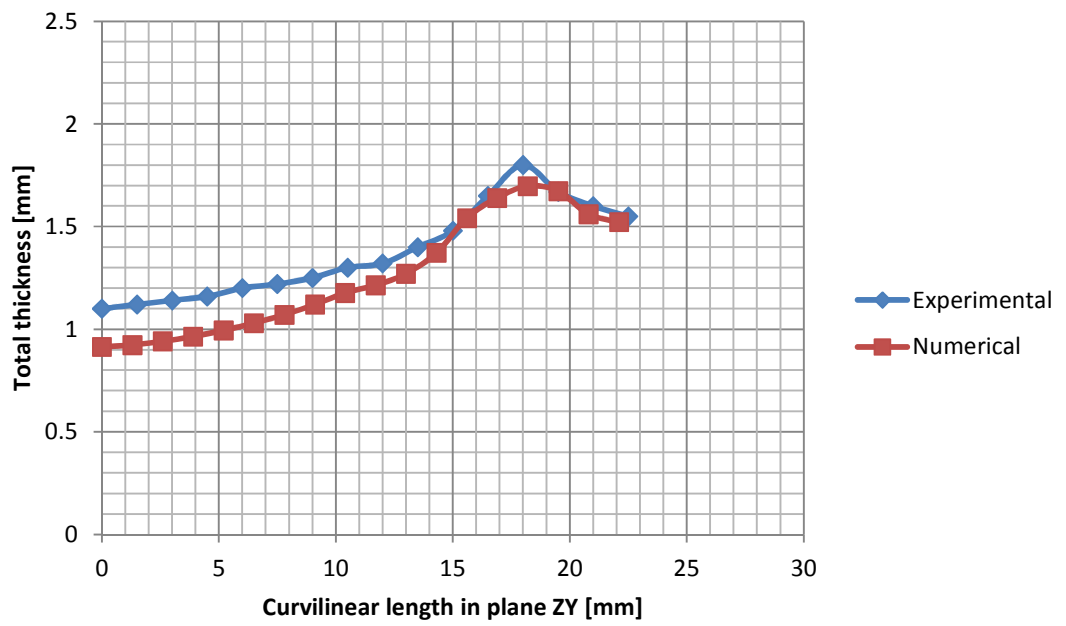


Figure 4.36: Experimental and numerical thickness distribution (test- e).

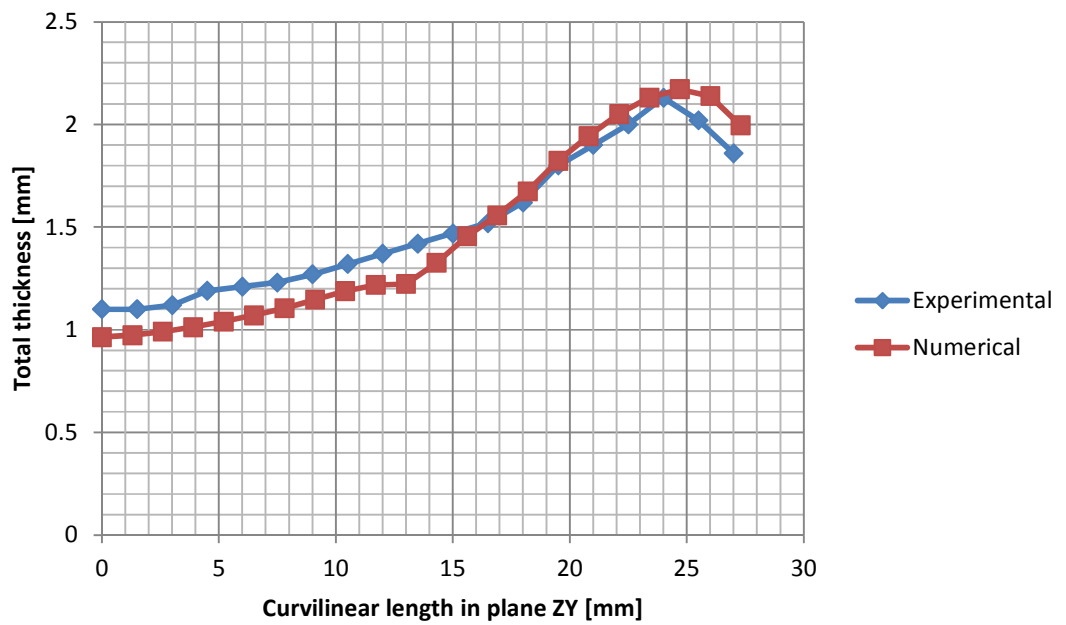


Figure 4.37: Experimental and numerical thickness distribution (test- f).

Table 4.2: Experimental and numerical values of final branch height for T-branch single layer tube hydroforming.

Test number	Experimental	Numerical	Error percentage
Test- e	11.505	10.945	+4.87
Test- f	16.632	15.93	-4.22

#### 4.4.3. Single and bi-layered tube hydroforming comparison

Based on the finite elements models developed in sections 4.2 and 4.4.1, and which were validated in sections 4.3 and 4.4.2 respectively, single and bi-layered tube hydroforming processes were compared to each other by applying both types of modelling to the same tube and die geometry, process parameters, and materials properties. In the numerical modelling of the bi-layered tube hydroforming, the tube material and its wall thickness were the same as that used in the single layer modelling. Thus, single and bi-layered tubes with the geometry of (tube length= 120 mm, outer diameter= 24 mm, and inner diameter= 21.4 mm) were numerically hydroformed in the T-branch die. The thickness of the single-layer tube was set at 1.3 mm, and the inner and outer layers of the bi-layered tube were set at 0.65 mm each making the total wall thickness the same as the single-layer tube. Also, single tube material (standard copper) specifications, the mechanical properties for which are given in section 4.4.1, were assigned for both the outer and inner layers in the bi-layered tube hydroforming numerical modelling, as well as for the single layer modelling.

In order to perform the proposed comparison, different loading path types were applied to both systems and the process formability under each applied loading path was investigated. In T-branch tube hydroforming, achieving a high protruded bulge and good wall thickness distribution with no significant wrinkling in the hydroformed part, is what engineers and manufacturers require. One of the factors that significantly influences the process formability is the loading path type selection that determines the relationship between the internal pressure and axial feed during the hydroforming process. The applied loading paths that are shown in figure 4.38 can be categorized in three different types. The first type, which is loading path (A), represents a linear relationship between the internal pressure and axial feed. Loading paths (B and C) are in the pressure advanced type category, in which the hydraulic pressure is raised to a certain magnitude in advance of the axial pushing, while (D and E) in the category of a loading path that substantially increases the axial

feeding in advance of the internal pressure. In all investigated loading paths the same maximum internal pressure and total axial feeding values were used.

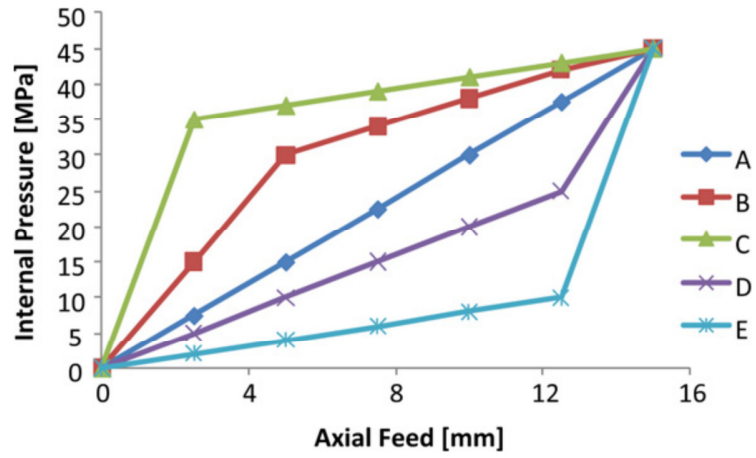


Figure 4.38: Applied loading paths for single and bi-layered tube hydroforming.

Single and bi-layered hydroformed parts resulting from the different applied loading paths are shown in figure 4.39. Based on the numerical results, bulge heights and wall thickness reduction were recorded for both single and bi-layered tube hydroforming and compared to each other in figures 4.40, 4.41.

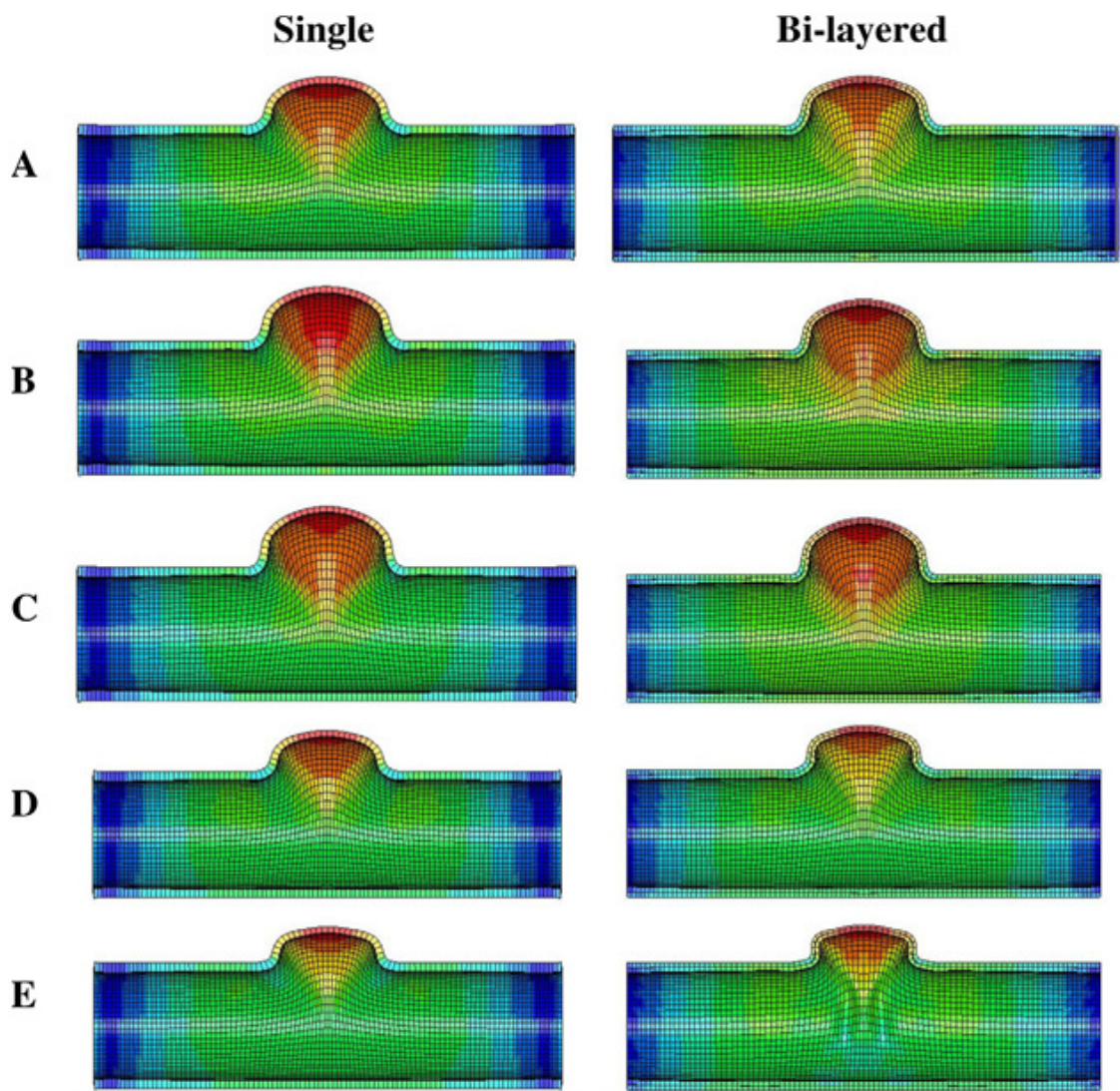


Figure 4.39: Hydroformed parts produced by different loading paths types.

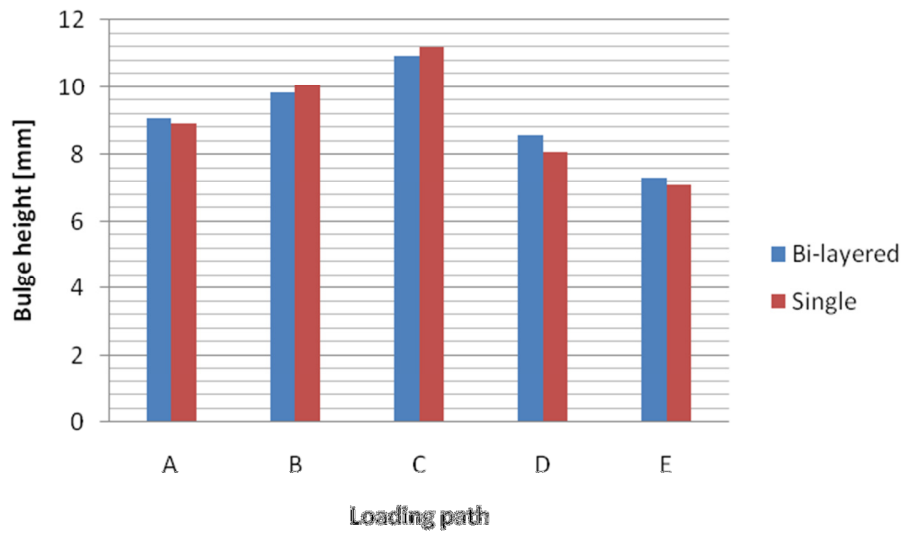


Figure 4.40: Bulge height comparisons between single and bi-layered tube hydroforming.

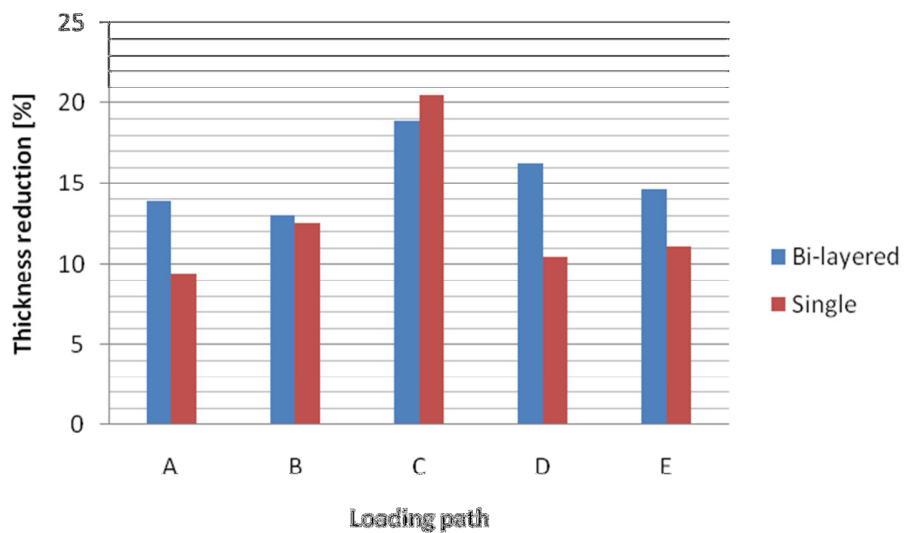


Figure 4.41: Thickness reduction comparisons between single and bi-layered tube hydroforming.

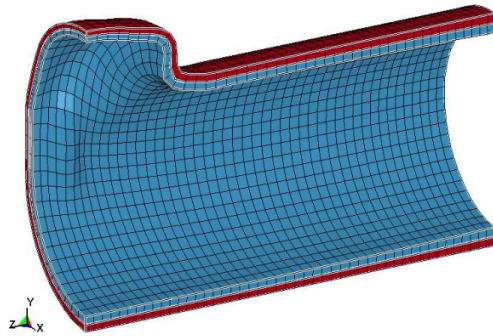
From figures 4.40, 4.41, it can be seen that for both single and bi-layered tube hydroforming, pressure advanced category loading paths (B and C) ensure the best process formability as high bulges with accepted wall thickness reduction ratios are produced. In the bi-layered tube hydroforming, applying high internal pressure in advance leads to an early combination of the inner and outer layers and deforms both of them in the die recess. By applying this type of loading path, bi-layered hydroformed bulges were found to be

slightly lower than the single layer ones because of the internal friction which takes place between both layers before combining. Applying linear and axial feed advanced loading paths (A, D, and E) resulted in low single and bi-layered bulges. In bi-layered tube hydroforming, applying such loading paths delays the combination of the inner and the outer layers, which allows both layers to feed separately before the layers merge. The feed applied to the inner layer exerts extra pressure on the outer layer, which results in slightly higher bi-layered bulges compared to those obtained from single tube hydroforming.

By comparing the wall thickness reduction of the single and bi-layered hydroformed branches in figure 4.41, it is observed that when loading paths (A, B, D and E) are applied, the thickness reduction percentages of the bi-layered hydroformed parts are bigger than the thickness reduction percentages of the single layer hydroformed parts. This is because of internal friction that takes place between the outer and inner layers before combination of the layers. In the case of applying high pressure in the initial stage, as applied in loading path (C), the influence of the internal friction is minimized due to the early combination of layers. This results in less wall thickness reduction of the bi-layered hydroforming as compared to the thickness reduction percentage exhibited by the single layer tube hydroforming, as is normal in the case of a lower protruded bi-layered bulge figure 4.40.

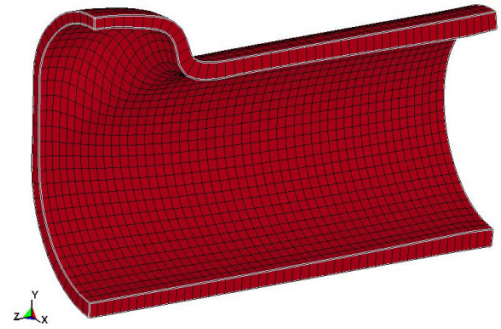
No significant wrinkling was detected when loading paths (A, B, C and D) were applied in both single and bi-layered tube hydroforming. On the other hand, loading path (E) did produce wrinkles in the hydroformed products, as it involved the application of the biggest part of the axial feeding while small internal pressure was applied figure 4.38. However, a late sudden rise of internal pressure was applied before the process end to calibrate the deformed wrinkle. Single and bi-layered hydroformed parts resulting from applying loading path (E) are presented in figure 4.42. A comparison of these two parts indicates that the bi-layered structure is more sensitive to wrinkling and buckling than the single layer structure. This is because that the maximum internal pressure applied at the end of the process was not able to calibrate the formed wrinkle in the bi-layered hydroformed part, while the single layer offered less resistance for wrinkle calibration.

LS-DYNA user input  
Time = 3



(a)

LS-DYNA user input  
Time = 3.0001



(b)

Figure 4.42: A comparison of bi-layered tube hydroforming (a) and single tube hydroforming (b) under loading path (E).

#### 4.5. Summary

Finite element models for X-shape and T-shape bi-layered tube hydroforming processes were constructed using the ANSYS LS-DYNA pre-processor and the LS-DYNA solver. The numerical models were found to be validated by the comparison with the experimental results. This was followed by a finite element comparison of the single and the bi-layered tube hydroforming processes conducted under different loading path types. It was concluded from this comparison that the application of internal pressure in advance of the axial feeding improved the formability of both systems, but with this type of loading path the bi-layered hydroformed bulges were found to be slightly smaller than the single layer ones. On the other hand, bi-layered hydroformed bulges produced under linear or axial feed advance loading paths were found to be bigger than the single layer ones. Also, for the hydroformed parts produced under the loading paths (A, B, D and E), wall thickness reduction of the bi-layered parts was found to be greater than that of the single layer parts. However, better wall thickness distribution was reported in the bi-layered hydroformed parts when loading path C is applied. It was also observed that the bi-layered tube hydroforming process is more sensitive to wrinkle formation than the single layer tube hydroforming process. In the next chapter, the numerical models of the bi-layered tube hydroforming process will be employed, in conjunction with Design of Experiments technique, to present a detailed analysis of the process.

## **CHAPTER FIVE**

### **INVESTIGATION ON THE EFFECT OF DESIGN PARAMETERS ON BI-LAYERED TUBE HYDROFORMING PROCESS OUTPUT**

#### **5.1. Introduction**

In spite of the important applications of bi-layered tube hydroforming, a knowledge base does not exist for this process as it does for single layer tube hydroforming. Hence, a detailed investigation of the effect of the design parameters on the bi-layered tube hydroforming process output is conducted in this chapter based on the finite element modelling described in the previous chapter. In this chapter Design of Experiments (DOE) technique and Response Surface Method (RSM) are outlined. This is followed by an integration of the finite element modelling and Design of Experiments technique that were adopted to study the effect of the geometrical factors and process parameters on the X-shape and T-shape hydroformed parts. The main effects and interactions of the design parameters on the hydroformed part are explained by the perturbation and interaction plots obtained from the Design-expert V7 software.

#### **5.2. Design of Experiments Outline**

In industry, experiments are carried out to improve the understanding of the manufacturing processes behaviour. Particularly, if a certain quality feature or response of a product is being influenced by many input variables (or factors), experiments are often used to evaluate which factors have a significant impact on the response, and what the target level of those inputs should be to achieve the desired results. Experiments can be designed in many different ways to collect this information. One conventional approach utilized by many engineers in manufacturing companies is the one-variable-at-a-time (OVAT) method, where the engineer varies one variable at a time while keeping all other variables involved in the experiment fixed. This approach requires considerable resources to obtain just a limited amount of information about the process. This is because OVAT technique always carries the risk that the experimenter may find one input variable to have a significant effect on the response (output), while failing to discover that changing another variable may alter the effect of the first (i.e. due to a dependency or interaction that could occur). Hence, OVAT experiments are often unreliable, time consuming, may not yield to optimal

conditions, and do not address any interaction effects between the process variables [111, 112].

Methods based on statistical analysis can replace OVAT experimental approach. These methods are usually called Design of Experiment. Design of Experiment (DOE) is a systematic approach to the investigation of a system or process that plays a key role in planning, conducting, and analysing and interpreting data of engineering experiments. A series of structured tests are designed in which planned changes are made to the input variables of a process or system. The effects of these changes on a pre-defined response are then assessed to check whether the input variables change the response on their own, in combination with another variable, or not at all [113].

Back in the early 1920s, Sir R. Fisher introduced DOE to determine the effect of various fertilizers on a range of plots of land. Since then, DOE has been utilized in many fields such as biology, pharmacy, engineering etc. In the last two decades, the use of DOE has increased and has been adapted for many processes in industry such as machining and metal forming [114]. However, the best known type of DOE designs is the responses surface methodology which was introduced early in the 1950's by Box and Wilson [111].

### 5.3. Response Surface Method

The Response Surface Method (RSM) is a set of mathematical and statistical techniques that are useful for modelling the responses that are being studied as functions of the controllable input variables [115, 116]. If all independent variables are measurable and can be repeated with negligible error, the response surface can be expressed by equation 5.1:

$$y = f(x_1, x_2, \dots, x_k) \quad (5.1)$$

Where: k is the number of independent variables

Usually, a second order polynomial as shown in equation 5.2 is used in RSM to describe the true functional relationship between the independent variables and the response surface.

$$y = b_o + \sum b_i \chi_i + \sum b_{ij} \chi_i \chi_j + \sum b_{ii} \chi_{ii}^2 + \epsilon \quad (5.2)$$

One of the most popular RSM designs is Box-Behnken design (BBD), which is based on three levels of each factor (coded as -1, 0, and +1). This design was developed by Box and Behnken in 1960 [117] by combining two-level factorial designs with incomplete block designs, with a specified number of centre points then added. A schematic diagram for BBD for three factors is shown in figure 5.1. The advantages of the Box-Behnken designs include the fact that they are all spherical designs and require factors to run at only three levels. The designs are also rotatable which indicates that the variance of the predicted values of  $y$  is a function of the distance of a point from the center of the design and is not a function of the direction the point lies from the center. Furthermore, when using BBD design type, the region of interest will be the same as the region of operability. Yet another advantage of these designs is that there are no runs where all factors are at either the +1 or -1 levels (corner points). This would be advantageous when the corner points represent runs that are expensive or inconvenient because they are positioned at the end of the range of the factor levels [118].

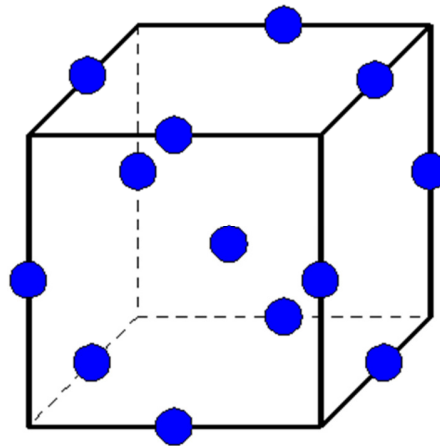


Figure 5.1: A schematic diagram for BBD of three factors [114].

In this work, RSM method with the BBD design type was applied to the data derived from finite element models (section 4.2) to analyse the effect of design parameters on the bi-layered hydroformed parts. The steps to create a mathematical model as a function of three factors using an integration of finite element modelling and DOE technique are shown in the Appendix.

#### 5.4. Investigation of the effect of design parameters on the bi-layered tube hydroforming

In the current work, an integration of Finite Element Modelling (FEM) and the Response Surface Method (RSM) for Design of Experiment (DOE) was used to study the effect of the design parameters on the X-shape and T-shape bi-layered tube hydroforming processes. The design parameters under study can be specified in two categories: 1) the geometrical factors and 2) the process parameters:

- 1) The geometrical factors are tube length, tube outer diameter, die corner radius, and the thicknesses of the outer and inner layers. The investigated geometrical factors with their experimental ranges are listed in table 5.1. Tube length (L: 80- 160 mm), tube outer diameter (D: 20- 28 mm), die corner radius (r: 1- 5 mm), inner layer thickness ( $t_2$ : 0.6- 1.2 mm) and outer layer thickness ( $t_1$ : 0.6–1.2 mm) were applied as the independent input variables. Ranges of the geometrical factors (L, D, r) were selected so that the midpoints (coded 0) meet the experimental circumstances shown in section 4.3.

Table 5.1. The geometrical factors and experimental design levels that were used in this study.

Variables	Code	-1	0	+1
Tube length (mm)	L	80	120	160
Die corner radius (mm)	r	1	3	5
Tube diameter (mm)	D	20	24	28
Outer layer thickness (mm)	$t_1$	0.6	0.9	1.2
Inner layer thickness (mm)	$t_2$	0.6	0.9	1.2

- 2) The process parameters are axial feed displacement, internal pressure coordinates, and the coefficient of friction between the tube and the die. In the studied cases, axial feed was assumed to increase steadily with time. The investigated process parameters with their experimental ranges are listed in table. 5.2. Axial feed displacement (S: 6- 15 mm), coefficient of friction (f: 0.05- 0.15), and internal pressure coordinates ( $P_2$ : 15- 35 MPa), ( $P_3$ : 35- 40 MPa) and ( $P_4$ : 40- 45 MPa) are the ranges of the independent process parameters, while  $P_5$  was kept fixed at 45 MPa in all cases as displayed in figure. 5.2. Ranges of the internal pressure

coordinates were selected to maintain the particular type of loading path. Advanced internal pressure achieved the best process formability as it was found in section 4.4.3. Axial feed range was chosen based on the experiments in section 3.5 as it will produce non buckled parts.

Table 5.2: Process parameters and experimental design levels used

Variables	Code	-1	0	+1
Axial feed displacement, [mm]	S	6	10.5	15
Internal pressure coordinate $P_2$ , [MPa]	$P_2$	15	25	35
Internal pressure coordinate $P_3$ , [MPa]	$P_3$	35	37.5	40
Internal pressure coordinate $P_4$ , [MPa]	$P_4$	40	42.5	45
Coefficient of friction	f	0.05	0.1	0.15

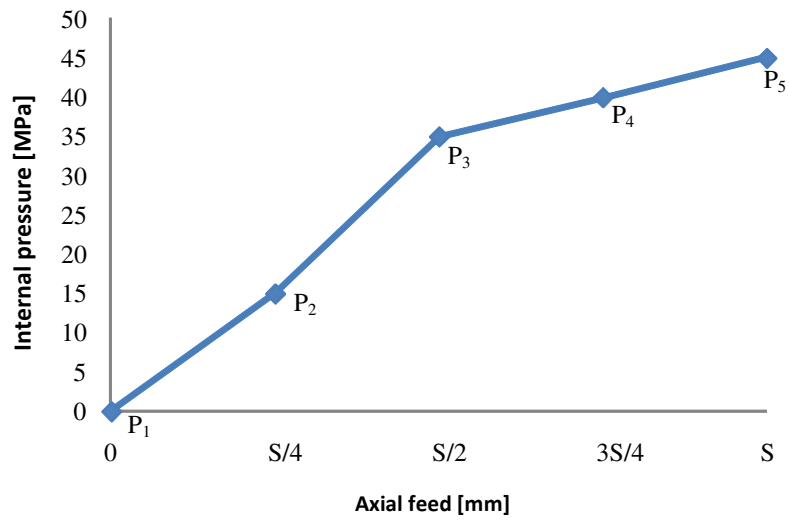


Figure 5.2: Internal pressure coordinates (initial values).

#### 5.4.1. Geometrical factors analysis of X-shape bi-layered tube hydroforming

An experimental design was created based on a three level Box Behnken design (BBD) with full replication [114] to construct models for three responses, namely: final bulge height (H), maximum wall thickness reduction (Tr), and wrinkle height (Wr) as functions of the geometrical factors listed in table. 5.1. RSM was applied, using the statistical software Design-expert V7 [119], to analyse the numerical data obtained based on the finite element model described in section 4.2, using the loading path of test-a shown in figure. 4.5

which has been validated in figure. 4.17 and table. 4.1. Second order polynomials were fitted to the experimental data. A step-wise regression method was used to fit the second order polynomial equation to the experimental data and to identify the relevant model terms [120, 121]. The adequacy measures (P-value,  $R^2$ , Adj  $R^2$ , Pred  $R^2$ , and Adeq. Precision ratio) were used in selecting the best models. The same statistical software was used to generate the perturbation and interaction plots.

The responses were measured according to the design matrix in table 5.3 while the measured responses were listed in table 5.4. From analysing the measured responses by the Design-expert V7 software, the summary output of best fit indicates that quadratic models are statistically recommended for the responses.

Table 5.3: Design matrix with actual independent process variables

Exp. No	L [mm]	r [mm]	D [mm]	t <sub>1</sub> [mm]	t <sub>2</sub> [mm]	Exp. No	L [mm]	r [mm]	D [mm]	t <sub>1</sub> [mm]	t <sub>2</sub> [mm]
1	80	1	24	0.9	0.9	24	120	5	28	0.9	0.9
2	160	1	24	0.9	0.9	25	80	3	24	0.6	0.9
3	80	5	24	0.9	0.9	26	160	3	24	0.6	0.9
4	160	5	24	0.9	0.9	27	80	3	24	1.2	0.9
5	120	3	20	0.6	0.9	28	160	3	24	1.2	0.9
6	120	3	28	0.6	0.9	29	120	3	20	0.9	0.6
7	120	3	20	1.2	0.9	30	120	3	28	0.9	0.6
8	120	3	28	1.2	0.9	31	120	3	20	0.9	1.2
9	120	1	24	0.9	0.6	32	120	3	28	0.9	1.2
10	120	5	24	0.9	0.6	33	80	3	24	0.9	0.6
11	120	1	24	0.9	1.2	34	160	3	24	0.9	0.6
12	120	5	24	0.9	1.2	35	80	3	24	0.9	1.2
13	80	3	20	0.9	0.9	36	160	3	24	0.9	1.2
14	160	3	20	0.9	0.9	37	120	1	24	0.6	0.9
15	80	3	28	0.9	0.9	38	120	5	24	0.6	0.9
16	160	3	28	0.9	0.9	39	120	1	24	1.2	0.9
17	120	3	24	0.6	0.6	40	120	5	24	1.2	0.9
18	120	3	24	1.2	0.6	41	120	3	24	0.9	0.9
19	120	3	24	0.6	1.2	42	120	3	24	0.9	0.9
20	120	3	24	1.2	1.2	43	120	3	24	0.9	0.9
21	120	1	20	0.9	0.9	44	120	3	24	0.9	0.9
22	120	5	20	0.9	0.9	45	120	3	24	0.9	0.9
23	120	1	28	0.9	0.9	46	120	3	24	0.9	0.9

Table 5.4: Numerical measured responses.

Exp. No	H [mm]	Tr [%]	Wr [100*mm]	Exp. No	H [mm]	Tr [%]	Wr [100*mm]
1	10.05	15.51	0.559	24	11.79	28.28	0.064
2	6.14	15.33	0.053	25	11.97	26.73	0.060
3	11.52	17.27	0.209	26	7.83	28.85	0.063
4	7.04	17.18	0.067	27	9.39	13.41	0.596
5	6.87	17.04	0.062	28	5.67	13.15	0.061
6	14.06	45.77	0.067	29	6.82	18.26	0.070
7	5.33	10.70	0.102	30	14.16	48.68	0.091
8	9.70	16.76	0.062	31	4.93	11.10	0.095
9	9.27	3.34	0.069	32	9.79	15.82	0.050
10	10.77	34.93	0.074	33	11.90	30.89	0.081
11	7.11	13.11	0.087	34	7.88	32.62	0.073
12	7.89	14.29	0.064	35	9.44	13.68	0.395
13	8.57	13.71	0.501	36	5.49	13.57	0.039
14	4.27	12.64	0.063	37	9.17	26.16	0.070
15	13.63	25.31	0.190	38	10.61	30.08	0.066
16	9.70	25.55	0.079	39	6.79	12.92	0.085
17	13.84	58.76	0.073	40	7.83	14.03	0.081
18	8.37	18.66	0.070	41	8.32	16.97	0.074
19	8.48	16.02	0.045	42	8.32	16.97	0.074
20	6.69	11.39	0.086	43	8.32	16.97	0.074
21	5.61	12.82	0.064	44	8.32	16.97	0.074
22	6.261	14.06	0.061	45	8.32	16.97	0.074
23	10.38	24.63	0.063	46	8.32	16.97	0.074

#### 5.4.1.1. Analysis of variance (ANOVA)

By selecting the step-wise regression method, which eliminates the insignificant model terms automatically, the resulting ANOVA tables displayed in tables 5.5- 5.7 have been created for the final quadratic models. These tables summarise the analysis of variance for each response, and show the significant model terms and the adequacy measures. The model P-value < 0.0001, a reasonable agreement between the adjusted  $R^2$  and predicted  $R^2$ , and a value of the adequate precision ratio which is bigger than 4, all indicate that the resultant models are fully adequate.

Table 5.5: ANOVA table for the bulge height final quadratic model.

Source	Sum of Squares	Df	Mean Square	F Value	p-value Prob > F
Model	271.3843	12	22.61536	190.4262	< 0.0001
L	65.78832	1	65.78832	553.9517	< 0.0001
r	5.267025	1	5.267025	44.34947	< 0.0001
D	124.0161	1	124.0161	1044.242	< 0.0001
t <sub>1</sub>	33.30156	1	33.30156	280.4062	< 0.0001
t <sub>2</sub>	33.58203	1	33.58203	282.7678	< 0.0001
D*t <sub>1</sub>	1.979649	1	1.979649	16.66907	0.0003
D*t <sub>2</sub>	1.521522	1	1.521522	12.81154	0.0011
t <sub>1</sub> *t <sub>2</sub>	3.392964	1	3.392964	28.56948	< 0.0001
L <sup>2</sup>	0.345329	1	0.345329	2.907747	0.0976
D <sup>2</sup>	0.891311	1	0.891311	7.505027	0.0098
t <sub>1</sub> <sup>2</sup>	1.282381	1	1.282381	10.79792	0.0024
t <sub>2</sub> <sup>2</sup>	1.406364	1	1.406364	11.84188	0.0016
Residual	3.919141	33	0.118762		
Cor Total	275.3035	45			
R <sup>2</sup> = 0.985, predicted R <sup>2</sup> = 0.980; adjusted R <sup>2</sup> = 0.962, adequate precision= 54.144					

Table 5.6: ANOVA table for the thickness reduction final quadratic model.

Source	Sum of Squares	Df	Mean Square	F Value	p-value Prob > F
Model	4570.659	11	415.5145	26.56797	< 0.0001
r	133.9806	1	133.9806	8.566712	0.0061
D	907.0638	1	907.0638	57.9976	< 0.0001
t <sub>1</sub>	1196.987	1	1196.987	76.53526	< 0.0001
t <sub>2</sub>	1175.804	1	1175.804	75.18083	< 0.0001
r*t <sub>2</sub>	231.192	1	231.192	14.7824	0.0005
D*t <sub>1</sub>	128.4822	1	128.4822	8.215144	0.0071
D*t <sub>2</sub>	165.1225	1	165.1225	10.55792	0.0026
t <sub>1</sub> *t <sub>2</sub>	314.5302	1	314.5302	20.11104	< 0.0001
D <sup>2</sup>	76.43366	1	76.43366	4.887163	0.0339
t <sub>1</sub> <sup>2</sup>	190.4021	1	190.4021	12.17429	0.0014
t <sub>2</sub> <sup>2</sup>	153.9479	1	153.9479	9.843415	0.0035
Residual	531.7491	34	15.63968		
Cor Total	5102.408	45			
R <sup>2</sup> = 0.895, predicted R <sup>2</sup> = 0.862; adjusted R <sup>2</sup> = 0.675, adequate precision= 21.664					

Table 5.7: ANOVA table for the wrinkle height final quadratic model.

Source	Sum of Squares	df	Mean Square	F Value	p-value Prob > F
Model	26.60774	12	2.217311	20.56696	< 0.0001
L	13.64954	1	13.64954	126.6081	< 0.0001
r	0.069573	1	0.069573	0.64533	0.4275
D	0.219041	1	0.219041	2.031746	0.1634
t <sub>1</sub>	1.816667	1	1.816667	16.85073	0.0002
t <sub>2</sub>	0.015952	1	0.015952	0.147964	0.7030
L*r	0.422681	1	0.422681	3.920636	0.0561
L*D	0.412043	1	0.412043	3.821962	0.0591
L*t <sub>1</sub>	2.067904	1	2.067904	19.18111	0.0001
L*t <sub>2</sub>	2.634575	1	2.634575	24.43734	< 0.0001
D*t <sub>2</sub>	0.70989	1	0.70989	6.584673	0.0150
t <sub>1</sub> *t <sub>2</sub>	0.494403	1	0.494403	4.585898	0.0397
L <sup>2</sup>	4.095467	1	4.095467	37.98803	< 0.0001
Residual	3.55771	33	0.107809		
Cor Total	30.16545	45			
R <sup>2</sup> = 0.882, predicted R <sup>2</sup> = 0.839; adjusted R <sup>2</sup> = 0.688, adequate precision= 21.463					

The analysis of variance indicates that the following terms are the most significant terms associated with bulge height:

- 1- The first order effect of tube length (L), die corner radius (r), tube diameter (D), and thickness of both outer and inner layers (t<sub>1</sub> and t<sub>2</sub>).
- 2- The second order effect of tube length (L<sup>2</sup>), tube diameter (D<sup>2</sup>), and thickness of both outer and inner layers (t<sub>1</sub><sup>2</sup> and t<sub>2</sub><sup>2</sup>).
- 3- The two level of interaction between the tube diameter and outer layer thickness (D×t<sub>1</sub>), the tube diameter and inner layer thickness (D×t<sub>2</sub>), and the outer and inner layers thickness (t<sub>1</sub>×t<sub>2</sub>).

Secondly for the thickness reduction model, the analysis indicated that the most significant terms are:

- 1- The first order effect of die corner radius (r), tube diameter (D), and thickness of both outer and inner layers ( $t_1$  and  $t_2$ ).
- 2- The second order effect of tube diameter ( $D^2$ ), and thickness of both outer and inner layers ( $t_1^2$  and  $t_2^2$ ).
- 3- The two level of interaction between the die corner radius and inner layer thickness ( $r \times t_2$ ), the tube diameter and outer layer thickness ( $D \times t_1$ ), the tube diameter and inner layer thickness ( $D \times t_2$ ), and the outer and inner layers thickness ( $t_1 \times t_2$ ).

Finally, the following terms were found to be the most significant terms associated with wrinkle height:

- 1- The first order effect of tube length (L), die corner radius (r), tube diameter (D), and thickness of both outer and inner layer ( $t_1$  and  $t_2$ ).
- 2- The second order effect of tube length ( $L^2$ ).
- 3- The two level of interaction between the tube length and the die corner radius ( $L \times r$ ), the tube length and the tube diameter ( $L \times D$ ), the tube length and both layers thicknesses ( $L \times t_1$ ), ( $L \times t_2$ ) and between both thicknesses of outer and inner layers ( $t_1 \times t_2$ ).

The final mathematical models in terms of actual factors as determined by the Design-expert V7 software are shown in equations. 5.3- 5.5.

$$\begin{aligned}
 \text{Bulge height} = & + 9.62705 - 0.079401 \times L + 0.28687 \times r \\
 & + 0.76382 \times D - 7.32487 \times t_1 - 9.42841 \times t_2 \\
 & - 0.58625 \times D \times t_1 - 0.51396 \times D \times t_2 \\
 & + 10.23333 \times t_1 \times t_2 + 1.19612\text{E-}004 \times L^2 \\
 & + 0.019216 \times D^2 + 4.09773 \times t_1^2 + 4.29125 \times t_2^2 \quad (5.3)
 \end{aligned}$$

$$\begin{aligned}
\text{Thickness reduction} = & + 21.68083 + 12.85062 \times r + 2.60850 \times D \\
& - 91.94435 \times t_1 - 29.67560 \times t_2 - 12.67083 \times r \times \\
& t_2 - 4.72292 \times D \times t_1 - 5.35417 \times D \times t_2 \\
& + 98.52778 \times t_1 \times t_2 + 0.17382 \times D^2 \\
& + 48.77116 \times t_1^2 + 43.85450 \times t_2^2
\end{aligned} \tag{5.4}$$

$$\begin{aligned}
1.0/\text{sqrt(wrinkle height)} = & + 6.42353 + 0.062603 \times L + 0.52058 \times r \\
& - 0.045990 \times D - 4.79761 \times t_1 - 12.92024 \times t_2 \\
& - 4.06337E - 003 \times L \times r \\
& - 2.00596E-003 \times L \times D + 0.059918 \times L \times t_1 \\
& + 0.067631 \times L \times t_2 + 0.35106 \times D \times t_2 \\
& - 3.90632 \times t_1 \times t_2 - 3.91553E - 004 \times L^2
\end{aligned} \tag{5.5}$$

#### 5.4.1.2. Validation of the RSM models

The relationship between the actual and predicted values of the bulge height, thickness reduction, and wrinkle height of the design points is shown in figures. 5.3- 5.5. These figures indicate that the developed models are accurate, because the residuals in prediction of each response are small and tend to be close to the diagonal line. Furthermore, to verify the adequacy of the developed models in the whole design space, three confirmation numerical experiments were carried out using new test conditions, which are not included in the design points but still belong to the experimental range defined earlier. Using the point prediction option in the software, the bulge height, wall thickness reduction, and wrinkle height of the confirmation experiments were predicted using the developed models equations. 5.3- 5.5. Table 5.8 summarizes the experimental conditions, the actual and the predicted values, and the percentages of error for the confirmation experiments. It can be seen that the constructed models are valid as the percentages of error are all within acceptable tolerances.

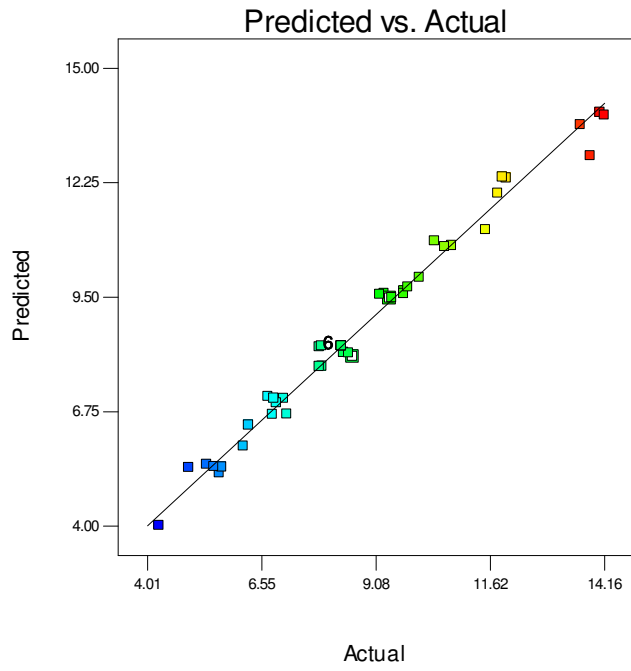


Figure 5.3: Scatter diagram of bulge height.

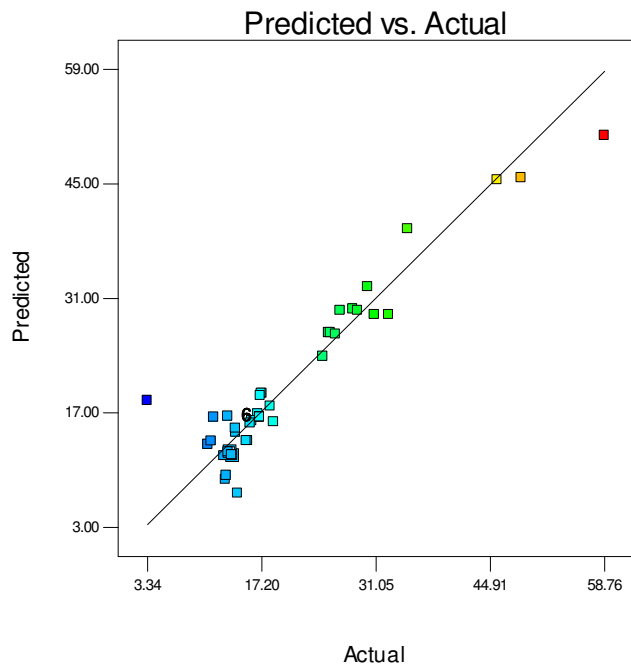


Figure 5.4: Scatter diagram of thickness reduction.

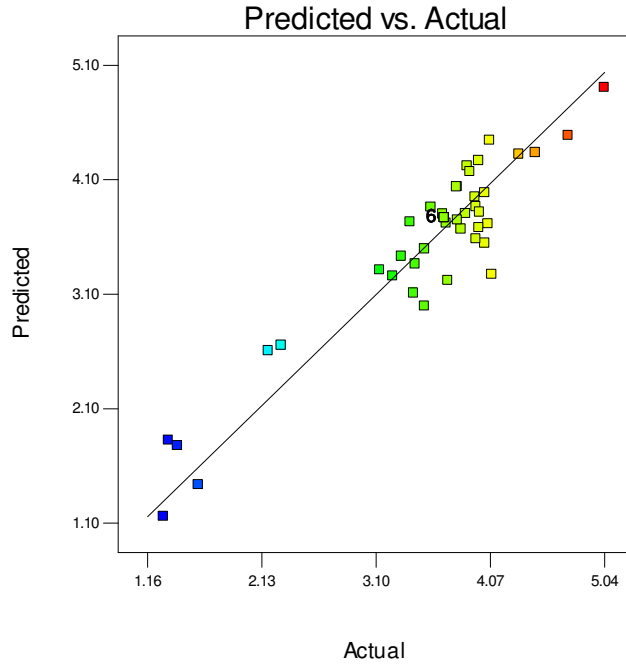


Figure 5.5: Scatter diagram of wrinkle height.

Table 5.8: Confirmation experiments.

Exp. No	L [mm]	r [mm]	D [mm]	$t_1$ [mm]	$t_2$ [mm]		H [mm]	Tr [%]	Wr [mm]
1	100	2	25	0.9	0.9	Numerical	10.16	17.73	0.094
						Predicted	9.38	16.45	0.104
						Error [%]	-7.62	-7.18	8.753
2	120	4	24	0.9	0.9	Numerical	9.12	17.19	0.063
						Predicted	8.61	17.90	0.069
						Error [%]	5.58	-3.97	8.360
3	120	3	24	1	0.9	Numerical	8.44	15.25	0.080
						Predicted	7.88	14.06	0.075
						Error [%]	6.58	7.80	-7.617

#### 5.4.1.3. Effect of the geometrical factors on the bulge height

Results indicate that bulge height depends on all the investigated geometrical factors. From the perturbation plot shown in figure 5.6, it is possible to compare the effect of all the factors at a particular point in the design space. Bulge height is plotted by changing only one factor over its range and maintaining the other factors constant at the midpoint (coded 0).

Hydroforming of longer tubes has been found from figure. 5.6 to result in lower bulges as longer tubes will be exposed to bigger friction forces which resist the metal forming, while bigger die corner radius means easier forming of the material and leads to higher bulges. Higher bulges can be produced when using larger tube diameters as this will allow more material to be pushed through the die. However, thicker outer and inner tubes were found to result in smaller bulges. From figures 5.7, 5.8, it can be observed that the bulge height increases with the  $(D/t_1, D/t_2)$  ratios increases which agrees with Hutchinson [80] experimental analysis for single tube hydroforming.

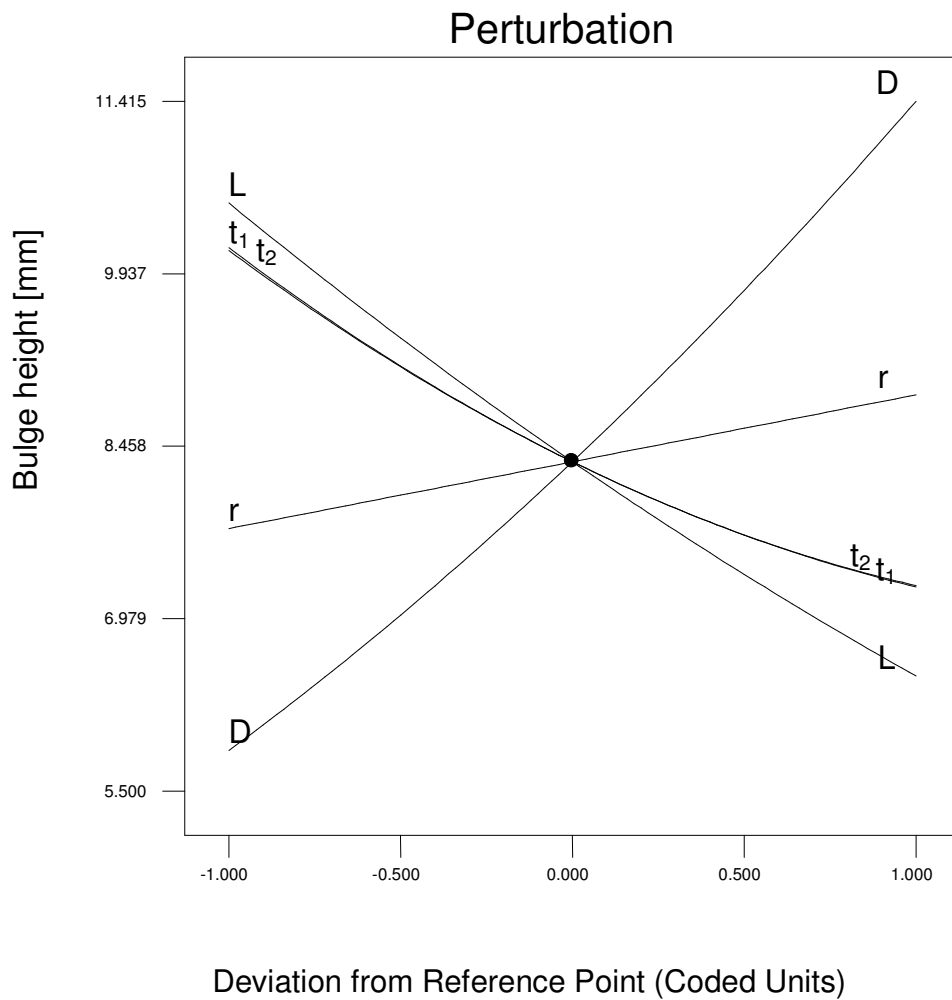


Figure 5.6: Perturbation of the bulge height.

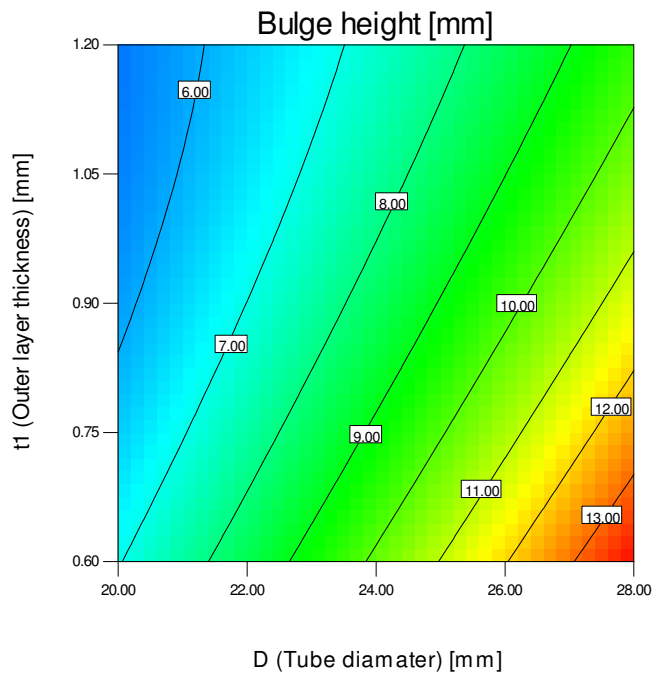


Figure 5.7: Contour graph showing the effect of D and  $t_1$  on bulge height.

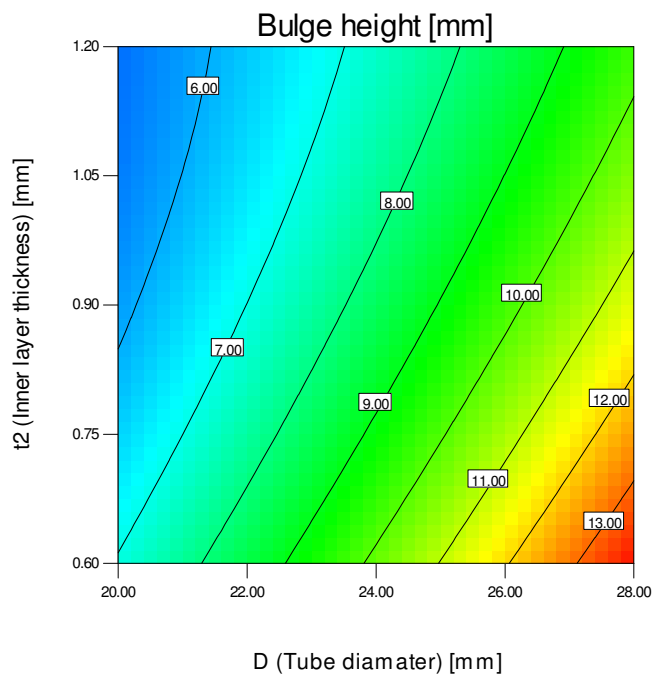


Figure 5.8: Contour graph showing the effect of D and  $t_2$  on bulge height.

#### 5.4.1.4. Effect of the geometrical factors on the wall thickness reduction

Wall thickness reduction in the hydroformed component occurs because of the application of internal pressure to the blank tube figure 5.9. The more the material expands, the more the wall thickness will be reduced [122]. From figure 5.9, it is seen that wall thickness reduction is calculated in the numerical model for all elements, with the maximum thickness reduction considered as the studied response.

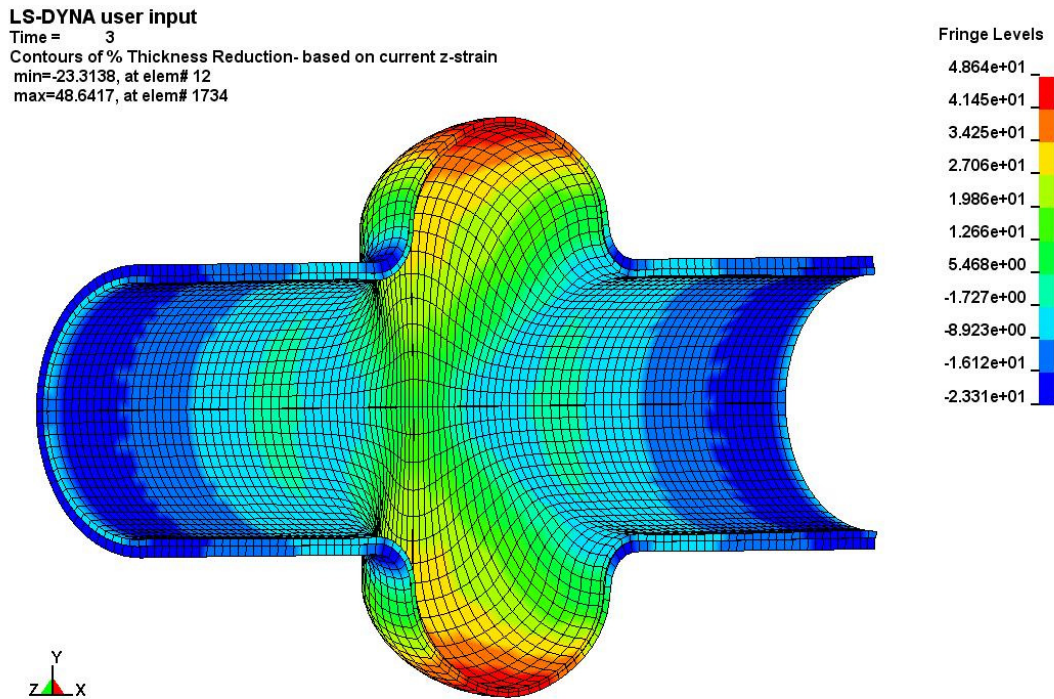


Figure 5.9: Wall thickness reduction of the hydroformed component.

From the perturbation plot shown in figure 5.10, it can be seen that the thickness reduction increases with an increase in die corner radius or with a tube diameter increase, as bigger material expansion is allowed which leads to a thinner branch top. On the other hand, thicker outer and inner layers result in smaller expansion and therefore less thickness variation. However, the effect of tube length within the studied range on the wall thickness of the bi-layered hydroformed components was found to be insignificant.

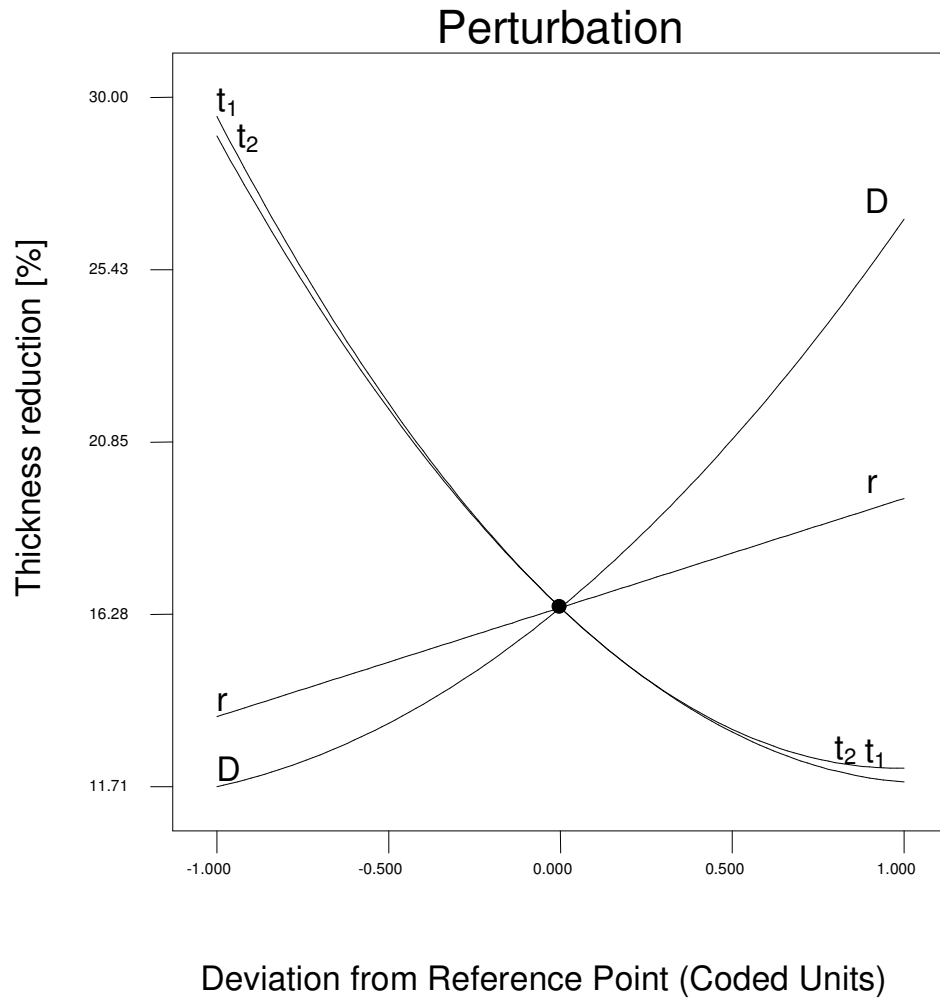


Figure 5.10: Perturbation of the wall thickness reduction.

An interaction is said to occur when the effect of one factor on a particular response varies with change in another factor. In terms of the interaction effect between the inner layer thickness and die corner radius, the interaction plot in figure 5.11 indicates that the die corner radius effect on thickness reduction depends on the value of inner layer thickness ( $t_2$ ). When  $t_2 < 1$  mm, bigger die corner radius leads to bigger thickness reduction ratios as a result of bigger expansion. Using thicker inner layers ( $t_2 > 1$  mm) means that a bigger die corner radius leads to a better material distribution through the inner layer thickness and therefore results in a smaller thickness reduction. From this result it can be concluded that

the thickness reduction can be reduced when using a big die corner radius if a thick inner layer was assigned.

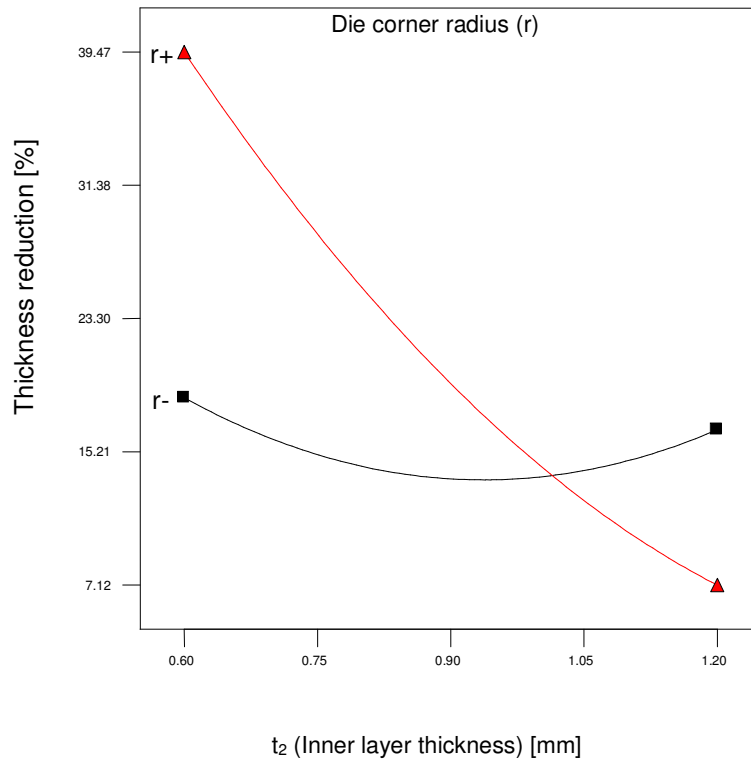


Figure 5.11: Interaction effect of the die corner radius and inner layer thickness on the wall thickness reduction.

Two interaction effects were detected between the tube diameter ( $D$ ) and each of the outer and inner layer thicknesses ( $t_1$ ,  $t_2$ ). From the interaction plots shown in figures 5.12, 5.13, it can be seen that the effect of tube diameter size on the wall thickness reduction of the hydroformed component depends on the value of the outer and inner layers thicknesses. Small values of  $t_2$  and  $t_1$  lead to a bigger effect of tube diameter on thickness uniformity of the hydroformed component, while larger thicknesses of the outer and inner layers make the influence of tube diameter less significant.

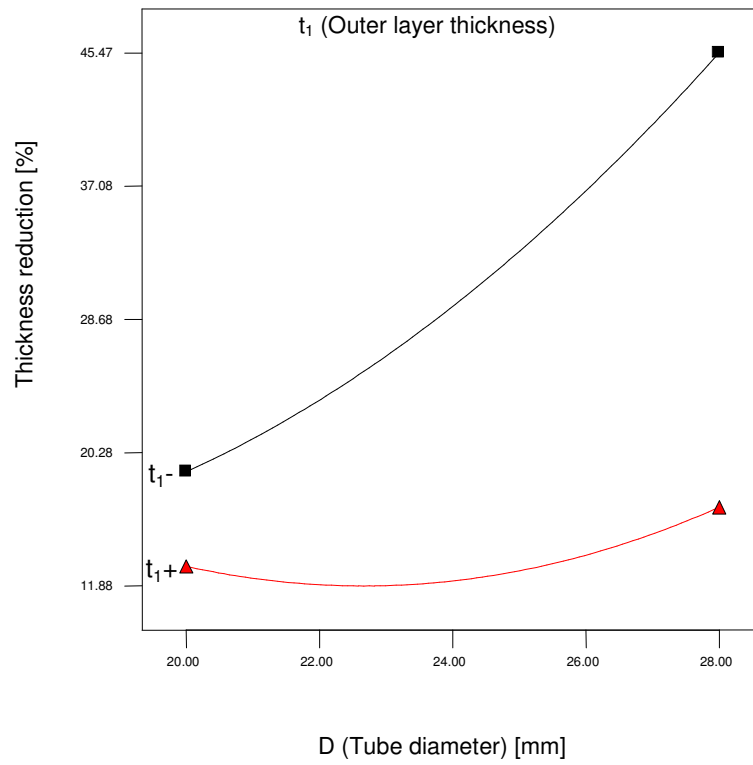


Figure 5.12: Interaction effect of the tube diameter and inner layer thickness on wall thickness reduction.

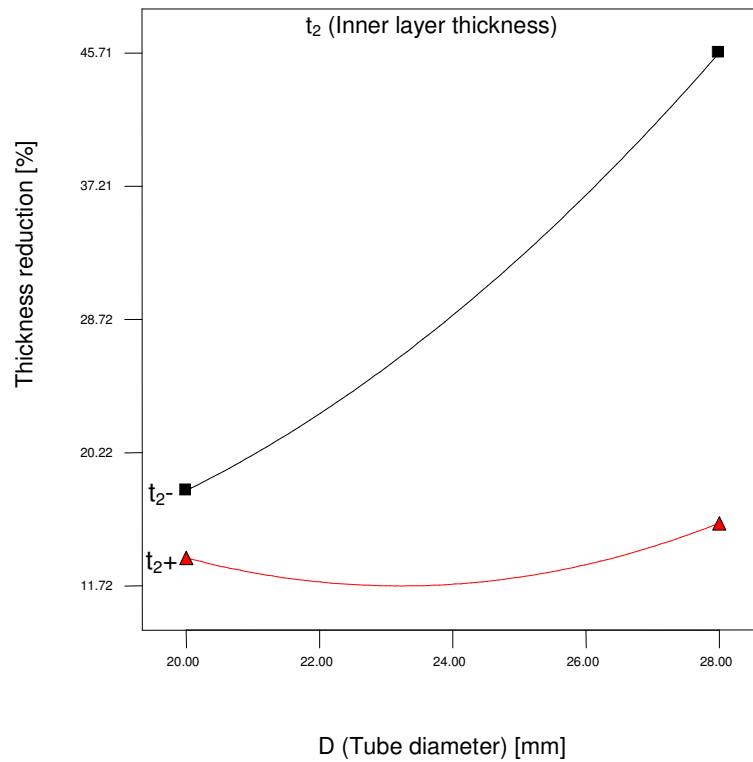


Figure 5.13: Interaction effect of the tube diameter and outer layer thickness on wall thickness reduction.

#### 5.4.1.5. Effect of the geometrical factors on wrinkle height

Wrinkles form in X-shape tube hydroforming when a large amount of material is pushed with an insufficient amount of internal pressure to conform the material to the die as shown in figure 5.14.



Figure 5.14: Wrinkle formation in the bi-layered tube hydroforming process.

From the perturbation plot figure 5.15, it can be noticed that wrinkling deformation depends primarily on the tube length, as long tubes are subject to big friction forces leading to the applied axial feed not being enough to result in significant wrinkle formation. Using a bigger die corner radius or larger tube diameter makes the material flow easier during the hydroforming process, which distributes wrinkle deformation over a bigger area and reduces the resultant wrinkle height. However, the effects of die corner radius and tube diameter on the wrinkle height was found to be relatively small. On the other hand, an increase of tube thickness was found to lead to more material being pushed through the die, and therefore facilitates wrinkle deformation. Inner layer thickness influence was found less prominent than the influence of outer layer thickness.

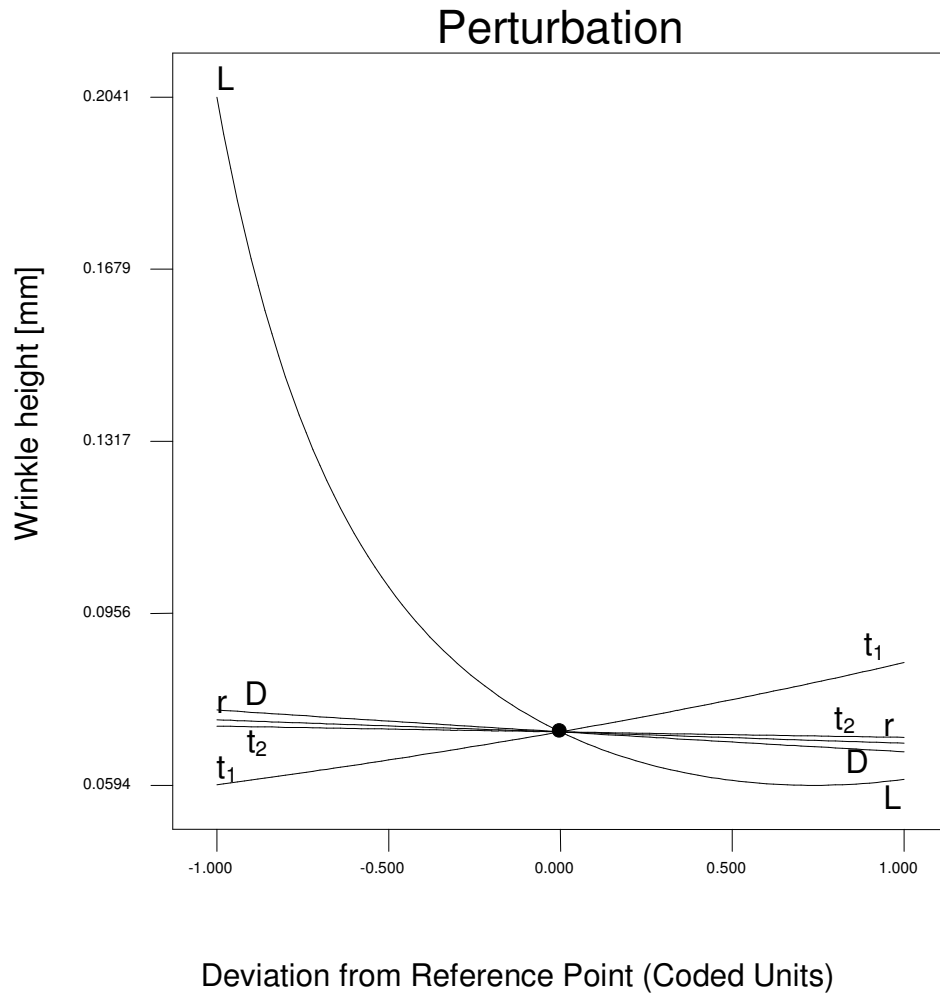


Figure 5.15: Perturbation of the wrinkle height.

The interaction between the tube length and die corner radius is shown in figure. 5.16. From the interaction plot it can be seen that the effect of the die corner radius on the wrinkle height depends on the value of the tube length. When ( $L < 128$  mm), a bigger die corner radius makes material forming easier and reduces wrinkle formation, while in case of ( $L > 128$  mm), increasing the die corner radius results in an increase of wrinkle height. A similar interaction effect was recognized in figure 5.17. From the interaction plot, it can be observed that the effect of tube diameter on wrinkle height depends on the tube length value. Increasing the tube diameter led to smaller wrinkle height when a small tube length

( $L < 134$  mm) was chosen. As against this, increasing of tube diameter causes bigger wrinkles when longer tubes ( $L > 134$  mm) are hydroformed.

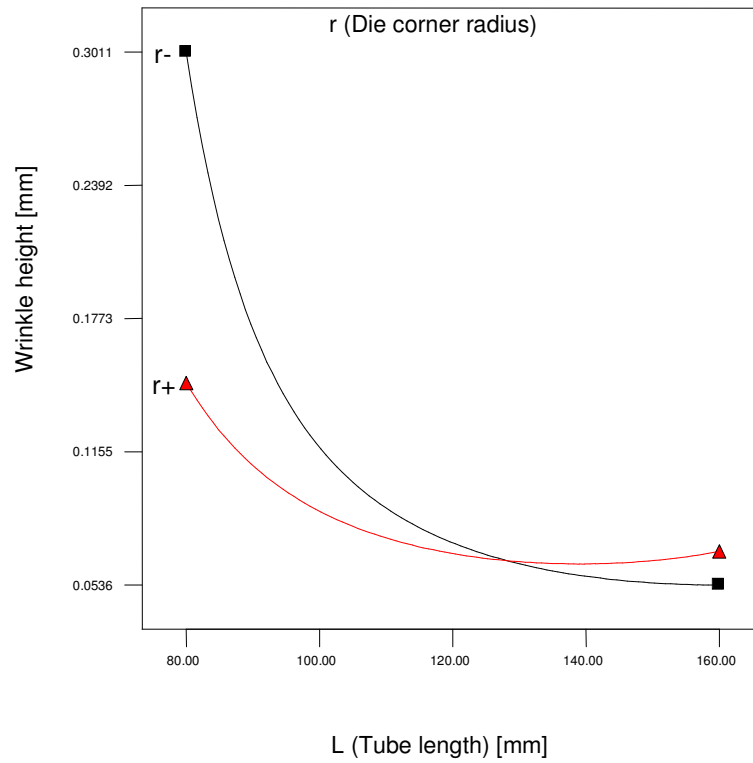


Figure 5.16: Interaction effect of the die corner radius and tube length on wrinkle height.

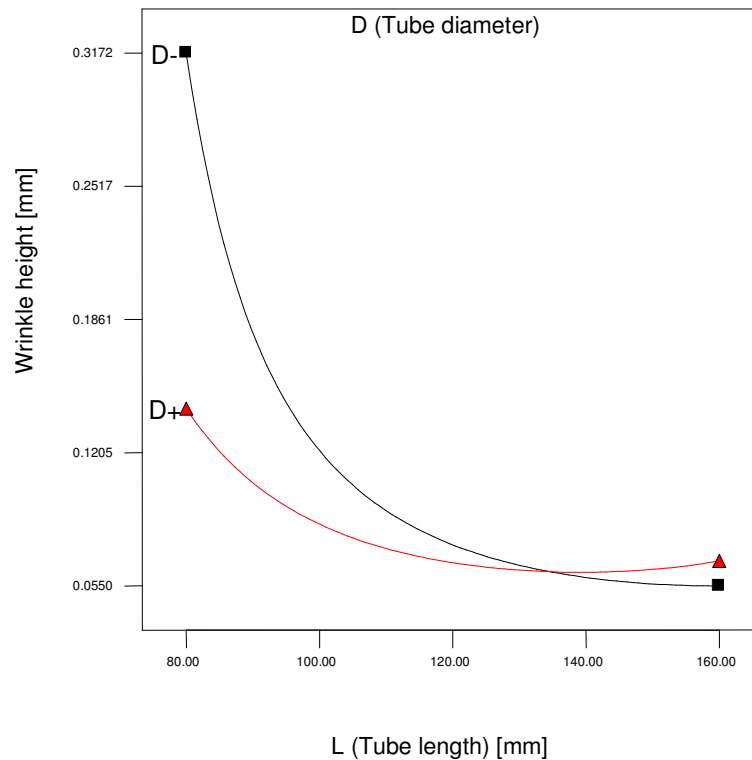


Figure 5.17: Interaction effect of the tube diameter and tube length on wrinkle height.

In terms of the interaction effects between the tube length and thickness of each outer and inner layer, it seems that the value of the tube length can determine the effect of the outer and inner layers thicknesses on wrinkling figures 5.18, 5.19. For  $L < 140$  mm figure 5.18, with an outer layer thickness increase, deformed wrinkles become larger, but for tube longer than 140 mm, it was found that choosing a thicker outer layer for the tubular blank would result in wrinkle height decrease. A similar interaction was recognized between the inner layer thickness and tube length figure 5.19, as with tube lengths ( $L < 120$  mm), increasing the inner layer thickness leads to bigger wrinkles, while it causes smaller wrinkles in the case of  $L > 120$  mm.

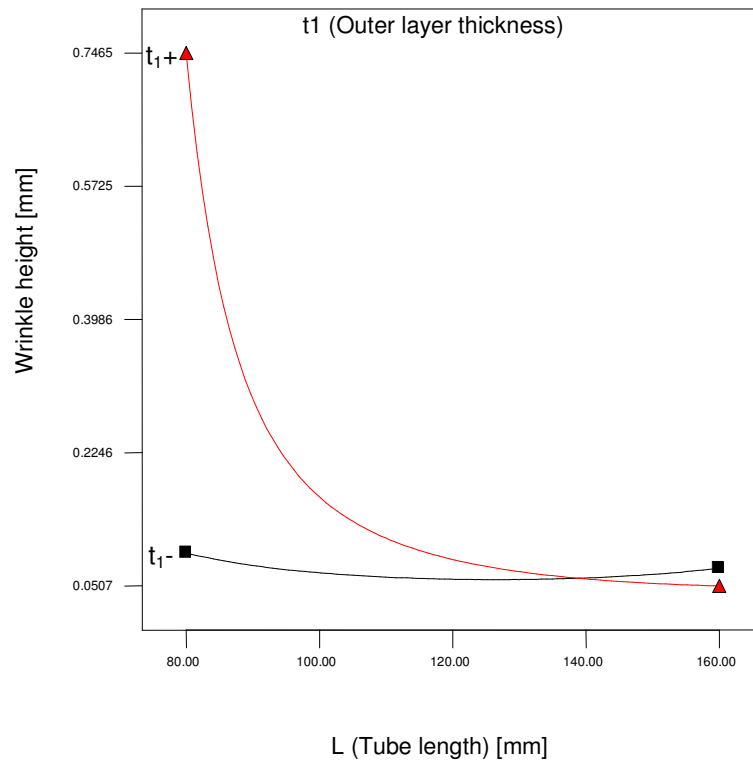


Figure 5.18: Interaction effect of the tube length and outer layer thickness on wrinkle height.

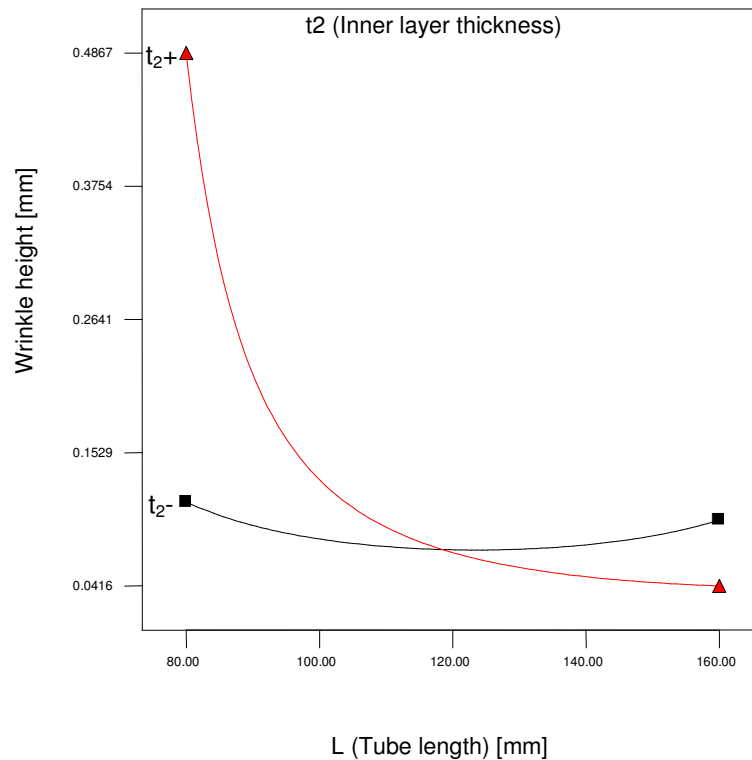


Figure 5.19: Interaction effect of tube length and inner layer thickness on wrinkle height. From the interaction plot figure 5.20, it can be seen that when hydroforming tubes with diameters  $D < 24$  mm, an increase of inner layer thickness would lead to bigger wrinkling deformation, while for tube diameters  $D > 24$  mm, assigning a thicker inner layer would result in less wrinkle height. Therefore, these results indicate that wrinkle height would be reduced either by selecting a bigger tube diameter with thick inner layer, or a smaller tube diameter with thin inner layer.

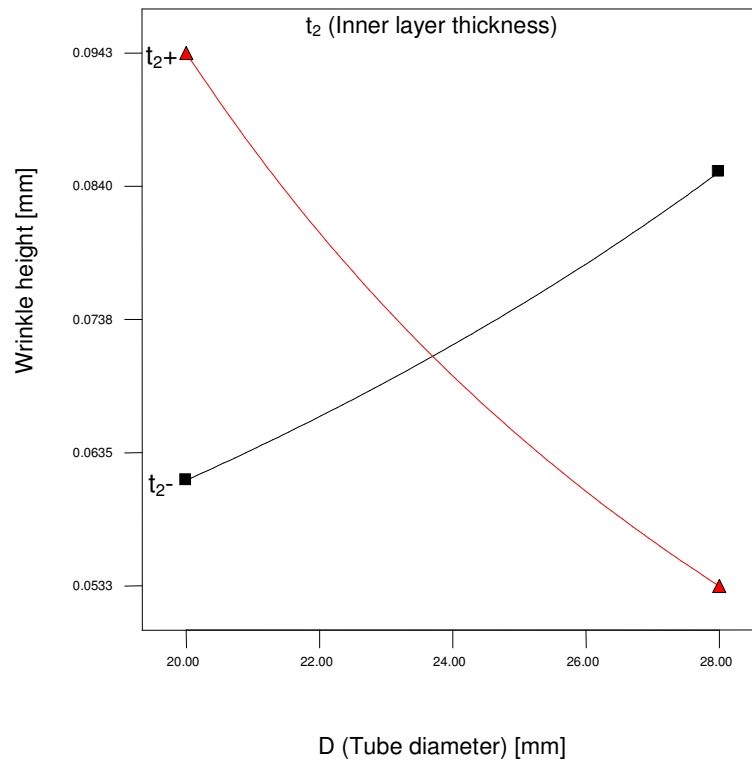


Figure 5.20: Interaction effect of inner layer thickness and tube diameter on wrinkle height. A further interaction effect which is illustrated by figure 5.21 indicates that the effect of inner layer thickness on wrinkle height relies on the value of the outer layer thickness. When outer layer thickness  $t_1 < 0.95$  mm, the wrinkle height can be minimized if a thicker inner layer is used, while it has been observed that a thinner inner layer would be preferred with an outer layer thickness  $t_1 > 0.95$  mm, as it also leads to a smaller wrinkle height. This indicates that wrinkling can be minimized when specifying a thick inner layer with thinner outer layer.

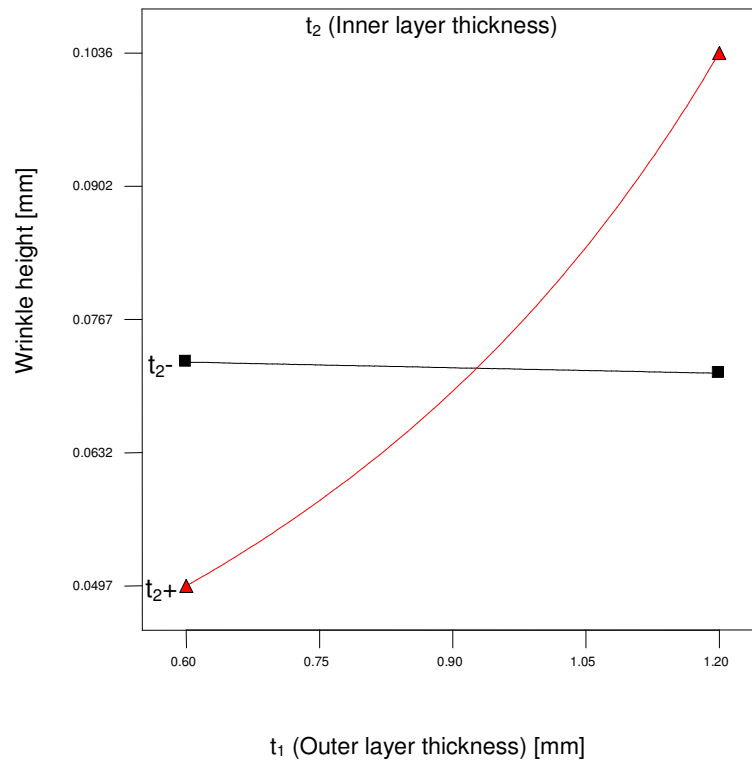


Figure 5.21: Interaction effect of the outer and inner layer thickness on wrinkle height.

#### 5.4.2. Process parameters analysis of X-shape bi-layered tube hydroforming

Using the same procedures that were followed in section 5.4.1, experimental design was carried out to investigate the effect of the process parameters listed in table. 5.2 on the X-type bi-layered tube hydroforming (final bulge height, wall thickness reduction, and wrinkle height). Using a step-wise regression method, second order polynomials were fitted to the experimental data obtained from the finite element modelling section 4.2, while the adequacy measures were checked in order to select the best models [120, 121]. The statistical software (Design-expert V7) was used to generate the statistical and response plots. The responses were measured according to the design matrix table 5.9 and the measured responses are listed in table 5.10. From analysing the measured responses using the Design-expert V7 software, the summary output of best fit indicates that quadratic models are statistically recommended for the responses.

Table 5.9: Design matrix with actual independent process variables.

Exp. No	S [mm]	P <sub>2</sub> [Mpa]	P <sub>3</sub> [Mpa]	P <sub>4</sub> [Mpa]	F	Exp. No	S [mm]	P <sub>2</sub> [Mpa]	P <sub>3</sub> [Mpa]	P <sub>4</sub> [Mpa]	f
1	6.0	15	37.5	42.5	0.1	24	10.5	35	40.0	42.5	0.1
2	15.0	15	37.5	42.5	0.1	25	6.0	25	37.5	40.0	0.1
3	6.0	35	37.5	42.5	0.1	26	15.0	25	37.5	40.0	0.1
4	15.0	35	37.5	42.5	0.1	27	6.0	25	37.5	45.0	0.1
5	10.5	25	35.0	40.0	0.1	28	15.0	25	37.5	45.0	0.1
6	10.5	25	40.0	40.0	0.1	29	10.5	25	35.0	42.5	0.05
7	10.5	25	35.0	45.0	0.1	30	10.5	25	40.0	42.5	0.05
8	10.5	25	40.0	45.0	0.1	31	10.5	25	35.0	42.5	0.15
9	10.5	15	37.5	42.5	0.05	32	10.5	25	40.0	42.5	0.15
10	10.5	35	37.5	42.5	0.05	33	6.0	25	37.5	42.5	0.05
11	10.5	15	37.5	42.5	0.15	34	15.0	25	37.5	42.5	0.05
12	10.5	35	37.5	42.5	0.15	35	6.0	25	37.5	42.5	0.15
13	6.0	25	35.0	42.5	0.1	36	15.0	25	37.5	42.5	0.15
14	15.0	25	35.0	42.5	0.1	37	10.5	15	37.5	40.0	0.1
15	6.0	25	40.0	42.5	0.1	38	10.5	35	37.5	40.0	0.1
16	15.0	25	40.0	42.5	0.1	39	10.5	15	37.5	45.0	0.1
17	10.5	25	37.5	40.0	0.05	40	10.5	35	37.5	45.0	0.1
18	10.5	25	37.5	45.0	0.05	41	10.5	25	37.5	42.5	0.1
19	10.5	25	37.5	40.0	0.15	42	10.5	25	37.5	42.5	0.1
20	10.5	25	37.5	45.0	0.15	43	10.5	25	37.5	42.5	0.1
21	10.5	15	35.0	42.5	0.1	44	10.5	25	37.5	42.5	0.1
22	10.5	35	35.0	42.5	0.1	45	10.5	25	37.5	42.5	0.1
23	10.5	15	40.0	42.5	0.1	46	10.5	25	37.5	42.5	0.1

Table 5.10: Numerical measured responses

Exp. No	H [mm]	Tr [%]	Wr [mm]	Exp. No	H [mm]	Tr [%]	Wr [mm]
1	6.59	12.37	0.088	24	8.90	13.53	0.086
2	10.82	27.01	1.077	25	6.58	12.32	0.095
3	6.99	14.32	0.104	26	10.74	28.09	0.738
4	10.93	15.75	0.401	27	6.81	13.07	0.099
5	8.38	11.01	0.124	28	11.03	26.45	0.657
6	8.52	11.77	0.104	29	9.18	10.83	0.206
7	8.55	11.96	0.111	30	9.31	11.41	0.166
8	8.74	12.53	0.097	31	7.95	12.05	0.076
9	9.27	16.25	1.024	32	8.07	12.63	0.075
10	9.51	13.09	0.106	33	7.53	12.21	0.092
11	7.91	12.61	0.084	34	11.62	33.39	1.052
12	8.15	12.8	0.078	35	5.95	12.73	0.096
13	6.68	12.43	0.094	36	10.11	13.02	0.319
14	10.82	27.16	0.768	37	8.34	12.06	0.238
15	6.82	13.01	0.099	38	8.73	12.62	0.085
16	10.96	25.57	0.617	39	8.59	12.97	0.211
17	9.14	10.79	0.192	40	8.95	13.49	0.087
18	9.35	11.66	0.173	41	8.57	11.67	0.110
19	7.93	11.85	0.075	42	8.57	11.67	0.110
20	8.08	12.86	0.076	43	8.57	11.67	0.110
21	8.41	12.07	0.275	44	8.57	11.67	0.110
22	8.75	12.57	0.088	45	8.57	11.67	0.110
23	8.53	12.73	0.184	46	8.57	11.67	0.110

#### 5.4.2.1. Analysis of variance (ANOVA)

ANOVA tables 5.11- 5.13 summarise the analysis of variance for each response and show the significant model terms. Adequacy measures (P-value,  $R^2$ ,  $adjR^2$ ,  $predR^2$ , and adequate precision) were checked to find the adequate models.

Table 5.11: ANOVA table for bulge height reduced quadratic model

Source	Sum of Squares	df	Mean Square	F Value	p-value Prob > F
Model	78.80361	9	8.755957	2333.268	< 0.0001
S	70.16994	1	70.16994	18698.73	< 0.0001
P <sub>2</sub>	0.352242	1	0.352242	93.86472	< 0.0001
P <sub>3</sub>	0.04	1	0.04	10.65911	0.0024
P <sub>4</sub>	0.095327	1	0.095327	25.40241	< 0.0001
f	7.64799	1	7.64799	2038.019	< 0.0001
S*P <sub>2</sub>	0.0308	1	0.0308	8.207581	0.0069
S <sup>2</sup>	0.450585	1	0.450585	120.071	< 0.0001
P <sub>2</sub> <sup>2</sup>	0.059785	1	0.059785	15.93142	0.0003
f <sup>2</sup>	0.014355	1	0.014355	3.825337	0.0583
Residual	0.135096	36	0.003753		
Cor Total	78.93871	45			
R <sup>2</sup> = 0.998, adjusted R <sup>2</sup> = 0.998; predicted R <sup>2</sup> = 0.997, adequate precision= 195.053					

Table 5.12: ANOVA table for thickness reduction reduced quadratic model

Source	Sum of Squares	df	Mean Square	F Value	p-value Prob > F
Model	1.81E-05	8	2.27E-06	20.32037	< 0.0001
S	6.96E-06	1	6.96E-06	62.43065	< 0.0001
P <sub>2</sub>	2.8E-08	1	2.8E-08	0.251293	0.6191
P <sub>4</sub>	4.89E-07	1	4.89E-07	4.381035	0.0433
f	1.92E-09	1	1.92E-09	0.017233	0.8963
S*P <sub>2</sub>	9.24E-07	1	9.24E-07	8.285045	0.0066
S*f	7.99E-07	1	7.99E-07	7.163595	0.0110
S <sup>2</sup>	8.56E-06	1	8.56E-06	76.78238	< 0.0001
P <sub>2</sub> <sup>2</sup>	1.07E-06	1	1.07E-06	9.592918	0.0037
Residual	4.13E-06	37	1.12E-07		
Cor Total	2.23E-05	45			
R <sup>2</sup> = 0.814, adjusted R <sup>2</sup> = 0.774; predicted R <sup>2</sup> = 0.598, adequate precision= 17.655					

Table 5.13: ANOVA table for wrinkle height reduced quadratic model

Source	Sum of Squares	df	Mean Square	F Value	p-value Prob > F
Model	5.174992	8	0.646874	122.4399	< 0.0001
S	2.573469	1	2.573469	487.1048	< 0.0001
P <sub>2</sub>	0.521625	1	0.521625	98.73287	< 0.0001
f	0.632377	1	0.632377	119.6959	< 0.0001
S*P <sub>2</sub>	0.068157	1	0.068157	12.90078	0.0009
S*f	0.074945	1	0.074945	14.1855	0.0006
P <sub>2</sub> *f	0.256106	1	0.256106	48.47554	< 0.0001
S <sup>2</sup>	1.033308	1	1.033308	195.5839	< 0.0001
P <sub>2</sub> <sup>2</sup>	0.074851	1	0.074851	14.16784	0.0006
Residual	0.195478	37	0.005283		
Cor Total	5.37047	45			
R <sup>2</sup> = 0.963, adjusted R <sup>2</sup> = 0.955; predicted R <sup>2</sup> = 0.897, adequate precision= 40.898					

The analysis of variance indicates that the following terms are most significant when associated with bulge height:

1. The first order effect of the axial feed displacement (S), all studied internal pressure coordinates (P<sub>2</sub>, P<sub>3</sub>, and P<sub>4</sub>) and coefficient of friction (f).
2. The second order effects of the axial feed displacement (S<sup>2</sup>), initial internal pressure (P<sub>2</sub><sup>2</sup>), and coefficient of friction (f<sup>2</sup>).
3. The two level interaction between initial internal pressure (P<sub>2</sub>) and between the axial feed displacement (S×P<sub>2</sub>).

Secondly for the wall thickness reduction model, the analysis indicated that the most significant terms are:

1. The first order effect of the axial feed displacement (S), internal pressure coordinates (P<sub>2</sub>, P<sub>4</sub>) and coefficient of friction (f).
2. The second order effect of axial feed displacement (S<sup>2</sup>) and initial internal pressure (P<sub>2</sub><sup>2</sup>).
3. The two level interaction between the initial internal pressure (P<sub>2</sub>) and the axial feed displacement (P<sub>2</sub>×S) and between the coefficient of friction and axial feed displacement (f×S).

Finally, the following terms were found to be the most significant terms associated with wrinkle height:

1. The first order effects of axial feed displacement (S), initial internal pressure ( $P_2$ ), and coefficient of friction (f).
2. The second order effects of axial feed displacement ( $S^2$ ) and the initial internal pressure ( $P_2^2$ ).
3. The two level interaction between the initial internal pressure and the axial feed displacement ( $P_2 \times S$ ), between the initial internal pressure and coefficient of friction ( $P_2 \times f$ ), and between coefficient of friction and axial feed displacement ( $S \times f$ ).

The final mathematical models in terms of actual factors as determined by the design expert software are shown in equations 5.6- 5.8.

$$\begin{aligned} \text{Bulge height} = & + 4.01175 + 0.2927 \times S - 0.00357 \times P_2 \\ & + 0.02 \times P_3 + 0.030875 \times P_4 - 16.87655 \times f \\ & - 0.00195 \times S \times P_2 + 0.010545 \times S^2 \\ & + 0.0007777 \times P_2^2 + 15.24524 \times f^2 \end{aligned} \quad (5.6)$$

$$\begin{aligned} (\text{Thickness reduction})^{2.41} = & + 0.004621 + 0.000338 \times S + 0.00005397 \times P_2 \\ & - 0.00007 \times P_4 - 0.020638 \times f \\ & + 0.00001068 \times S \times P_2 \\ & + 0.002 \times S \times f - 0.000045 \times S^2 - 0.00000323 \times P_2^2 \end{aligned} \quad (5.7)$$

$$\begin{aligned} \text{Log}_{10}(\text{Wrinkle height}) = & + 1.09689 - 0.10759 \times S - 0.081037 \times P_2 \\ & - 10.24008 \times f - 0.0029 \times S \times P_2 - 0.60836 \times S \times f \\ & + 0.50607 \times P_2 \times f \\ & + 0.015718 \times S^2 + 0.00085 \times P_2^2 \end{aligned} \quad (5.8)$$

#### 5.4.2.2. Validation of the RSM models

To check the validity of the proposed models, the relationship between the actual and predicted values of the bulge height, thickness reduction, and wrinkle height, respectively for the design points are listed in figures 5.22- 5.24. Furthermore, three numerical experiments were carried out using different test conditions that are within the experimental range. These results were compared with the predicted results and found to be in good agreement table 5.14.

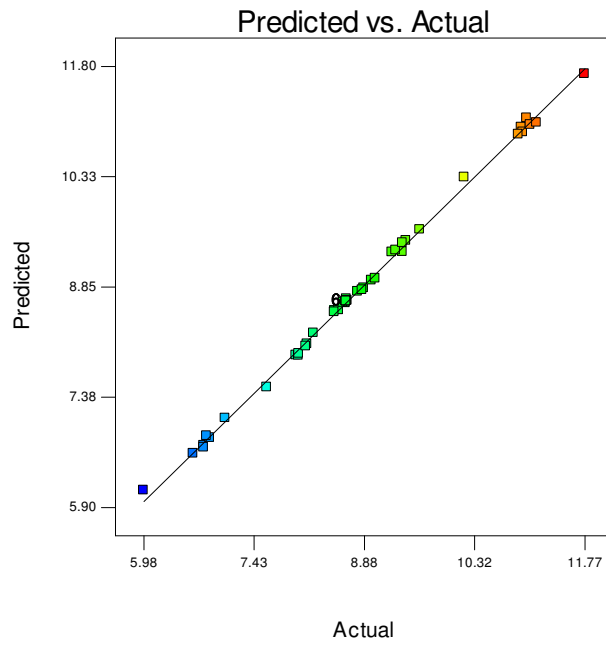


Figure 5.22: Scatter diagram of bulge height

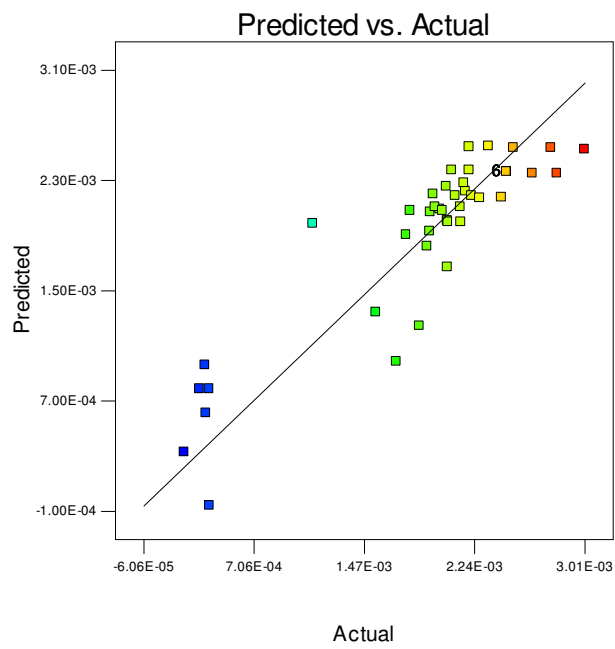


Figure 5.23: Scatter diagram of thickness reduction

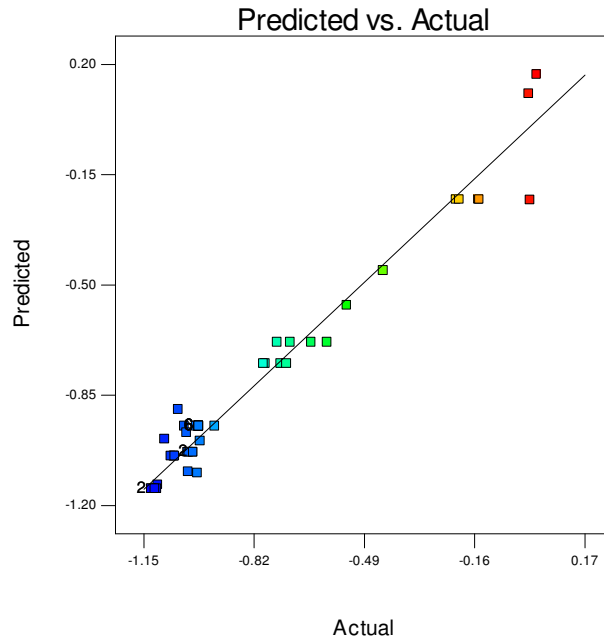


Figure 5.24: Scatter diagram of wrinkle height

Table 5.14: Confirmation experiments

Exp. No	S [mm]	P <sub>2</sub> [MPa]	P <sub>3</sub> [MPa]	P <sub>4</sub> [MPa]	f		H [mm]	Tr [%]	Wr [mm]
1	9	30	40	43	0.1	Numerical	8.214	12.840	0.0859
						Predicted	8.158	12.426	0.0803
						Error [%]	0.682	3.224	6.519
2	10.5	28	38	45	0.15	Numerical	8.157	13.250	0.0796
						Predicted	8.144	12.713	0.0760
						Error [%]	0.159	4.052	4.522
3	9	35	40	40	0.15	Numerical	7.409	13.260	0.0928
						Predicted	7.560	12.981	0.1000
						Error [%]	-2.038	2.104	-7.758

#### 5.4.2.3. Effect of the process parameters on bulge height

From the perturbation plot shown in figure 5.25, it can be seen that applying bigger axial feed displacements resulted in higher bulges as more material is pushed into the die recess. Internal pressure coordinates also have a positive influence on the bulge height increase, while bigger friction will resist the material deformation and leads to a smaller bulge height. It is clear from the interaction plot figure. 5.26, that by increasing the applied axial feed displacement, the influence of the initial internal pressure P<sub>2</sub> becomes less significant.

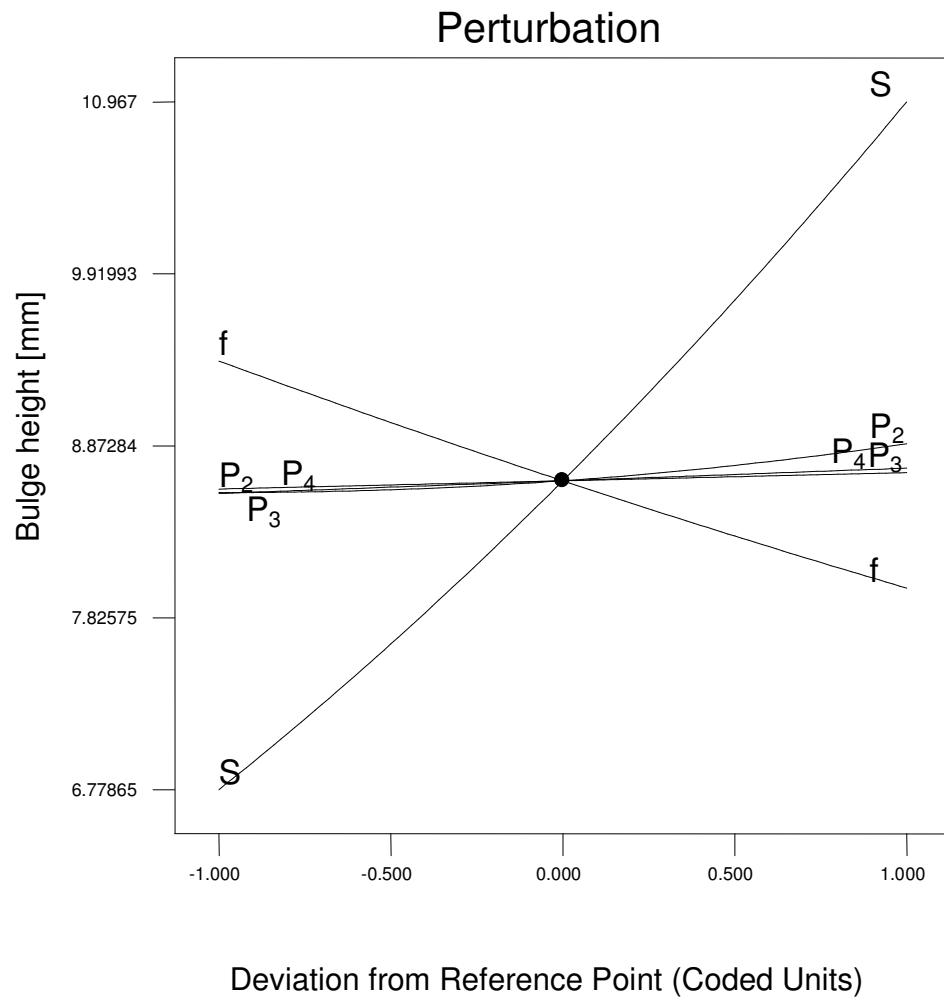


Figure 5.25: Perturbation of the bulge height.

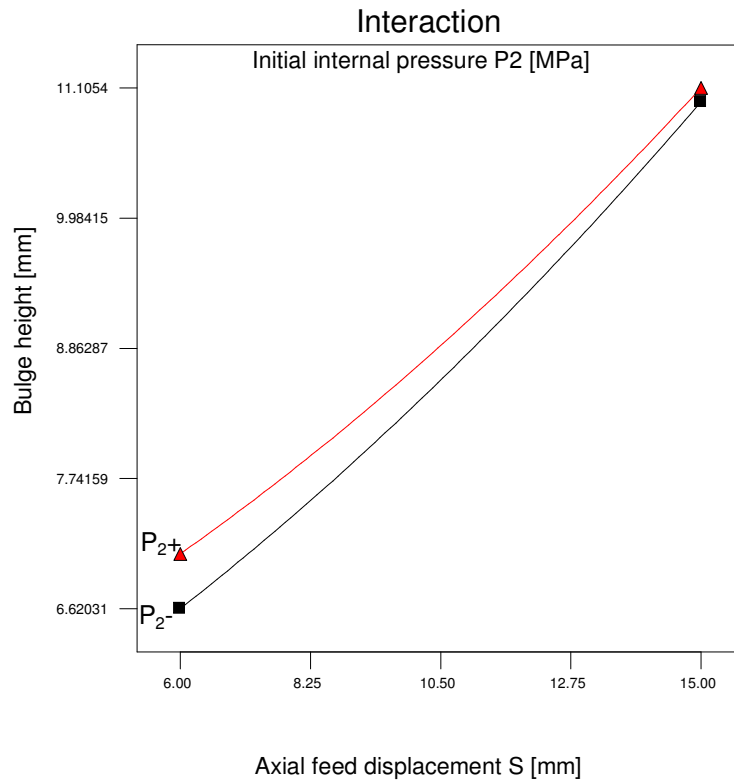


Figure 5.26: Interaction plot between the internal pressure ( $P_2$ ) and the axial feed ( $S$ ).

#### 5.4.2.4. Effect of process parameters on wall thickness reduction

The perturbation plot of thickness reduction figure 5.27 shows that the effect of the axial feed on the wall thickness reduction can be divided in two different phases. When applying small feeding displacements in the range ( $S$ : 6- 9 mm), it is clear that increasing axial feed leads to better thickness uniformity, while increasing the feed displacement between 9 mm and 16 mm was found to produce greater wall thickness reduction. In another observation, increasing the initial internal pressure ( $P_2$ ) ranging from 15 to 25 MPa was found to improve the thickness uniformity as it avoids the sudden application of high internal pressure in coordinates ( $P_3$ -  $P_5$ ), while it leads to increased wall thickness reduction in the range between 25 to 35 MPa, as more material expansion occurs. Greater wall thickness reduction was found to occur in the hydroformed part by applying higher values of internal pressure coordinate ( $P_4$ ), while a bigger coefficient of friction led to a slightly smaller thickness reduction as less material expansion was observed. However, it was found that

the effect of internal pressure coordinate ( $P_3$ ) is considered insignificant in the studied range (35- 40 MPa).

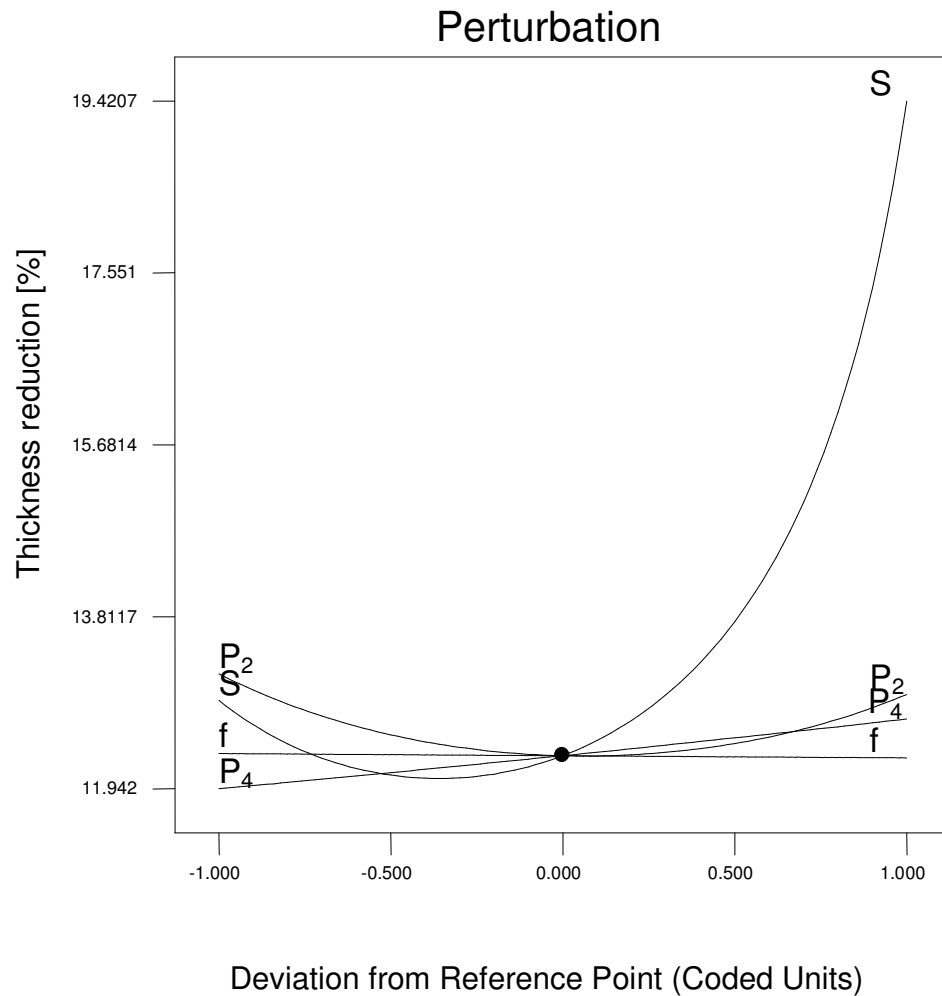


Figure 5.27: Perturbation of the wall thickness reduction.

An interaction effect was detected between the initial internal pressure and the axial feed displacement: the interaction plot figure 5.28 indicates that the effect of initial internal pressure ( $P_2$ ) on wall thickness reduction depends on the value of the axial feed. In the case of small values of applied axial feed ( $S < 10$  mm), a higher level of  $P_2$  resulted in bigger wall thickness reduction compared to applying a lower  $P_2$  as it led to greater material expansion. However, applying an axial feed  $S > 10$  mm with higher  $P_2$  values is preferred as

it enhances the wall thickness distribution. Consequently, to obtain good thickness uniformity, the selected values of  $P_2$  and  $S$  depend on each other; i.e.: greater feed displacements should be accompanied with a high  $P_2$ , while a smaller  $P_2$  is more suitable to be applied when using lower feeding displacements.

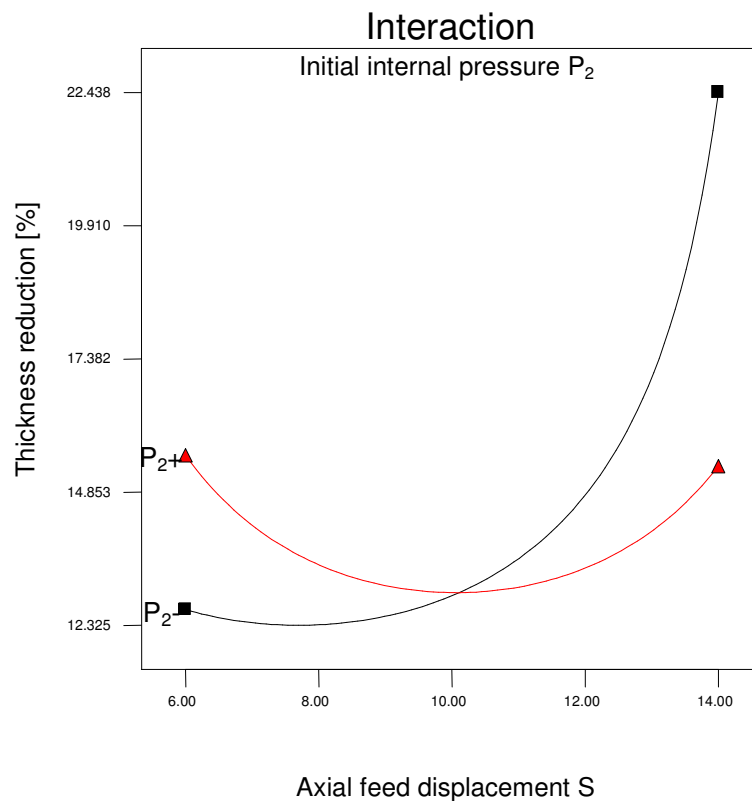


Figure 5.28: Interaction plot between the initial internal pressure ( $P_2$ ) and axial feed displacement ( $S$ ).

A different interaction effect was discovered in terms of wall thickness reduction modelling. The interaction between the coefficient of friction and the axial feed displacement is demonstrated in figure 5.29. A big coefficient of friction was found to be preferable in order to obtain the best wall thickness homogeneity if big axial feeding ( $S > 10.5$  mm) is needed, while minimum friction is preferable when small axial feeding are applied ( $S < 10.5$  mm).

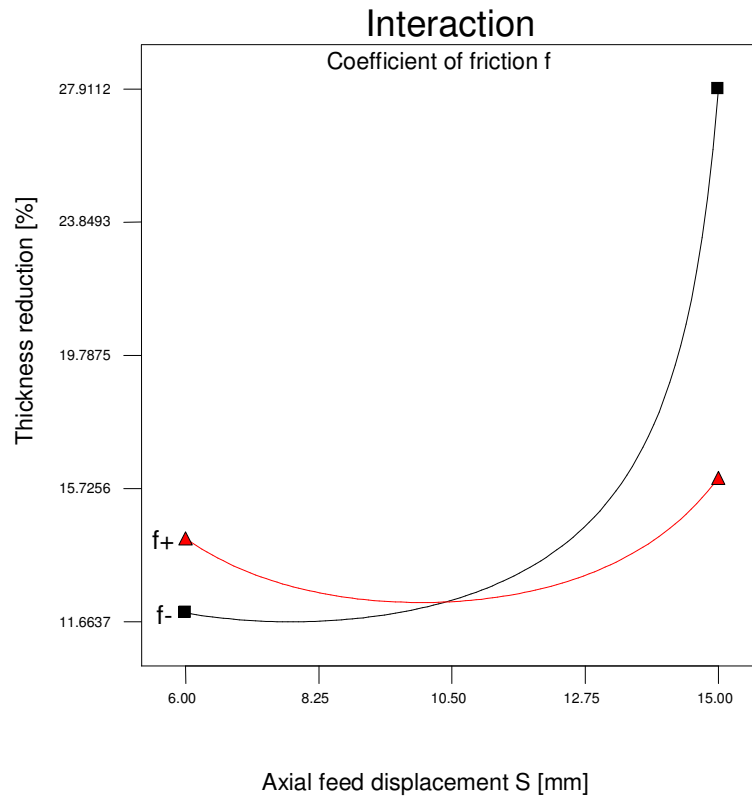


Figure 5.29: Interaction plot of the coefficient of friction ( $f$ ) and axial feed displacement ( $S$ ).

#### 5.4.2.5. Effect of the process parameters on wrinkle height

The effect of the process parameters on the wrinkle height can be assessed using the perturbation plot figure 5.30. It can be seen that wrinkling deformation depends mainly on the axial feed displacement, as big displacements lead to big amount of material pushed into the die and result in the internal pressure not being enough to push all of the material into the die. Applying higher initial internal pressure was found to lead to better material distribution and smaller wrinkle forming. Smaller wrinkle formation results from bigger resistance in material feeding, which can be achieved by choosing a bigger coefficient of friction. However, it was concluded that, within the studied ranges, the effects of  $P_3$  and  $P_4$  on wrinkling deformation was insignificant.

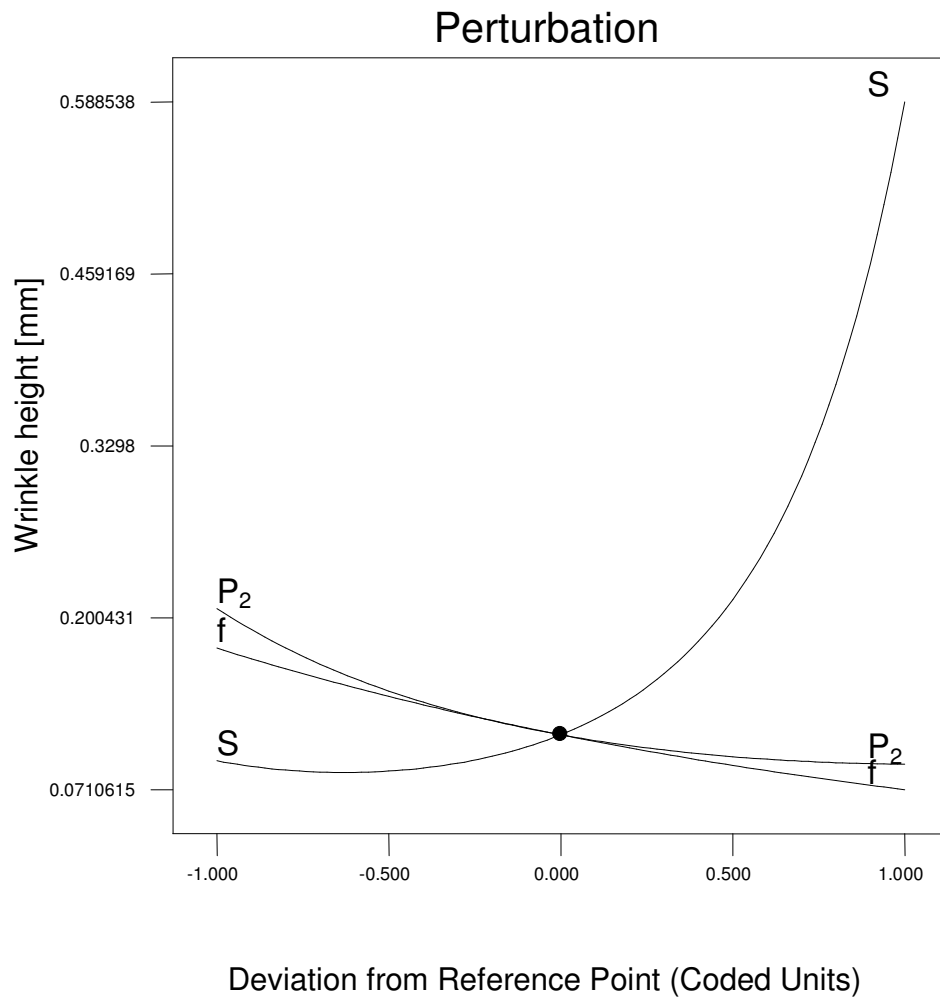


Figure 5.30: Perturbation of wrinkle height.

Two interactions are shown in figures 5.31- 5.32. From the interaction plots it can be seen that the influence of the initial internal pressure ( $P_2$ ) and the coefficient of friction ( $f$ ) on the wrinkle height drops off when a small axial feed ( $S$ ) was applied. However, applying a greater axial feed, high initial internal pressure  $P_2$ , and a greater coefficient of friction will result in less wrinkling forming.

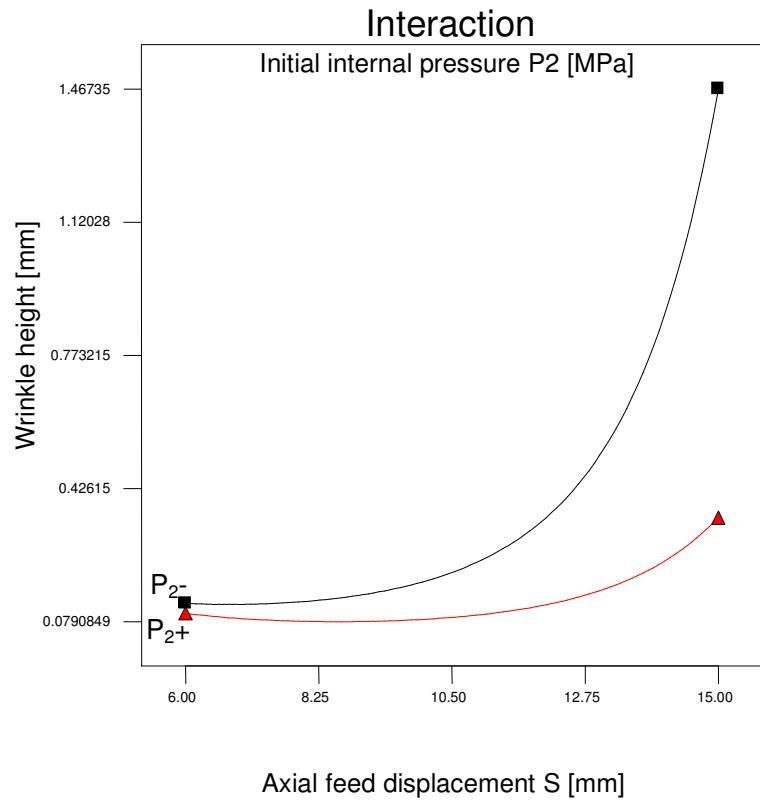


Figure 5.31: Interaction plot of initial internal pressure ( $P_2$ ) and axial feed displacement ( $S$ ).

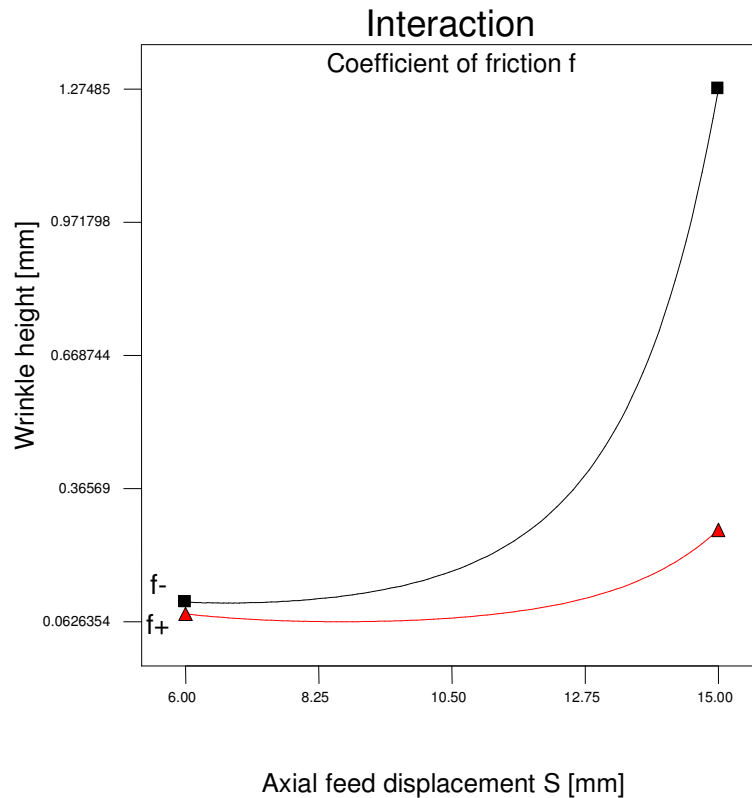


Figure 5.32: Interaction plot of coefficient of friction (f) and axial feed displacement (S).

#### 5.4.3. Geometrical factors analysis of T-shape bi-layered tube hydroforming

The effect of the investigated geometrical factors within the studied ranges table 5.1 on the T-shape bi-layered tube hydroforming is examined in this section using the same method as outlined in sections 5.4.1- 5.4.2. Specifically, the validated finite element modelling approach described in section 4.2, using the loading path of (test-c) shown in figure 4.7, was adopted in conjunction with the RSM method (Design-expert V7) to model the bulge height and the wall thickness reduction of the hydroformed part as a function of the studied geometrical factors. No significant wrinkling was observed in the T-type hydroformed parts throughout the studied design space. The responses were measured according to the design matrix table 5.3 and are listed in table 5.15. Using the previously described statistical software, second order polynomials were fitted to the experimental data by means of step-wise regression method while the adequacy measures were used in selecting the best

models [120, 121]. The summary output of best fit indicates that the resultant quadratic models are statistically recommended for the responses.

Table 1.15: Numerical measured responses.

Exp. No	H [mm]	Tr [%]	Exp. No	H [mm]	Tr [%]
1	11.24	14.61	24	12.2	34.93
2	4.95	15.55	25	12.95	34.46
3	12.526	15.55	26	6.67	34.44
4	6.02	17.55	27	10.7	12.53
5	6.37	16.33	28	5.08	11.75
6	14.97	55.52	29	7.02	20.19
7	5.59	8.67	30	15.26	55.8
8	9.87	19.24	31	5.17	9.3
9	9.46	35.48	32	9.59	16.31
10	11.09	41.59	33	13.42	38.58
11	6.63	11.11	34	7.69	39
12	7.6	12.22	35	10.33	12.7
13	8.79	12.71	36	4.45	10.55
14	3.13	8.012	37	8.79	30.83
15	14.5	31.66	38	10.5	37.25
16	8.83	32.22	39	7.01	11.25
17	14.81	68.84	40	7.77	12.64
18	8.57	21.85	41	8.37	18.24
19	8.02	15.83	42	8.37	18.24
20	7.08	9.85	43	8.37	18.24
21	5.07	10.73	44	8.37	18.24
22	6.026	11.37	45	8.37	18.24
23	10.57	30.11	46	8.37	18.24

#### 5.4.3.1. Analysis of variance (ANOVA)

The significant model terms are shown in the ANOVA tables 5.16, 5.17 for the bulge height and thickness reduction responses, respectively. The adequacy measures ( $R^2$ ,  $AdjR^2$ ,  $PredR^2$ , and Adequate precision) listed in the ANOVA tables were found to indicate the model adequacy.

Table 5.16: ANOVA table for bulge height reduced quadratic model.

Source	Sum of Squares	Df	Mean Square	F Value	p-value Prob > F
Model	11.26301	13	0.866385	418.7184	< 0.0001
L	4.277981	1	4.277981	2067.52	< 0.0001
r	0.183167	1	0.183167	88.52357	< 0.0001
D	4.290528	1	4.290528	2073.584	< 0.0001
t <sub>1</sub>	0.724797	1	0.724797	350.2895	< 0.0001
t <sub>2</sub>	1.354613	1	1.354613	654.6755	< 0.0001
L*D	0.032267	1	0.032267	15.59421	0.0004
L*t <sub>2</sub>	0.011479	1	0.011479	5.547847	0.0248
D*t <sub>1</sub>	0.080623	1	0.080623	38.96473	< 0.0001
D*t <sub>2</sub>	0.04706	1	0.04706	22.74392	< 0.0001
t <sub>1</sub> *t <sub>1</sub>	0.140545	1	0.140545	67.92446	< 0.0001
r <sup>2</sup>	0.006326	1	0.006326	3.057255	0.0900
t <sub>1</sub> <sup>2</sup>	0.045241	1	0.045241	21.86447	< 0.0001
t <sub>2</sub> <sup>2</sup>	0.067323	1	0.067323	32.53659	< 0.0001
Residual	0.066212	32	0.002069		
Cor Total	11.32922	45			
R <sup>2</sup> = 0.994, adjusted R <sup>2</sup> = 0.9920; predicted R <sup>2</sup> = 0.985, adequate precision= 84.662					

Table 5.17: ANOVA table for thickness reduction reduced quadratic model.

Source	Sum of Squares	Df	Mean Square	F Value	p-value Prob > F
Model	79.52314	12	6.626928	191.0873	< 0.0001
L	0.031827	1	0.031827	0.917743	0.3450
r	0.32867	1	0.32867	9.477197	0.0042
D	21.3322	1	21.3322	615.1134	< 0.0001
t <sub>1</sub>	20.57029	1	20.57029	593.1439	< 0.0001
t <sub>2</sub>	30.11401	1	30.11401	868.3367	< 0.0001
L*D	0.153705	1	0.153705	4.43209	0.0430
D*t <sub>1</sub>	0.96853	1	0.96853	27.92755	< 0.0001
D*t <sub>2</sub>	0.987676	1	0.987676	28.4796	< 0.0001
t <sub>1</sub> *t <sub>2</sub>	1.935391	1	1.935391	55.80696	< 0.0001
D <sup>2</sup>	0.21802	1	0.21802	6.286608	0.0173
t <sub>1</sub> <sup>2</sup>	1.297045	1	1.297045	37.40026	< 0.0001
t <sub>2</sub> <sup>2</sup>	2.313955	1	2.313955	66.72283	< 0.0001
Residual	1.144443	33	0.03468		
Cor Total	80.66758	45			
R <sup>2</sup> = 0.986, adjusted R <sup>2</sup> = 0.9807; predicted R <sup>2</sup> = 0.965, adequate precision= 54.998					

The analysis of variance indicates that the following terms are the most significant terms associated with bulge height:

- 4- The first order effect of tube length (L), die corner radius (r), tube diameter (D), and thickness of both outer and inner layers ( $t_1$  and  $t_2$ ).
- 5- The second order effect of die corner radius ( $r^2$ ) and thickness of both outer and inner layers ( $t_1^2$  and  $t_2^2$ ).
- 6- The two level of interaction between the tube length and the tube diameter (L×D), the tube length and inner layer thickness (L× $t_2$ ), the tube diameter and outer layer thickness (D× $t_1$ ), the tube diameter and inner layer thickness (D× $t_2$ ), and the outer and inner layers thickness ( $t_1$ × $t_2$ ).

Secondly for the thickness reduction model, the analysis indicated that the significant terms are:

- 4- The first order effect of tube length (L), die corner radius (r), tube diameter (D), and thickness of both outer and inner layers ( $t_1$  and  $t_2$ ).
- 5- The second order effect of tube diameter ( $D^2$ ) and thickness of both outer and inner layers ( $t_1^2$  and  $t_2^2$ ).
- 6- The two level of interaction between the tube length and the tube diameter (L×D), the tube diameter and outer layer thickness (D× $t_1$ ), the tube diameter and inner layer thickness (D× $t_2$ ), and the outer and inner layers thickness ( $t_1$ × $t_2$ ).

The final mathematical models in terms of actual factors as determined by the design expert software are shown in equations 5.9, 5.10.

$$\begin{aligned}
 \text{Sqrt(Bulge height)} = & + 2.29131 - 0.022381 \times L + 0.091448 \times r \\
 & + 0.24993 \times D - 1.09771 \times t_1 - 1.79007 \times t_2 \\
 & + 0.00056134 \times L \times r - 0.00446422 \times L \times t_2 \\
 & - 0.11831 \times D \times t_1 - 0.090389 \times D \times t_2 \\
 & + 2.08274 \times t_1 \times t_2 - 0.00632514 \times r^2 \\
 & + 0.75178 \times t_1^2 + 0.91708 \times t_2^2
 \end{aligned} \tag{5.9}$$

$$\begin{aligned}
\text{Sqrt(Thickness reduction)} = & + 9.69902 - 0.030519 \times L + 0.071662 \times r \\
& + 0.43779 \times D - 8.13971 \times t_1 - 11.26856 \times t_2 \\
& + 0.00122516 \times L \times D - 0.41006 \times D \times t_1 \\
& - 0.41409 \times D \times t_2 + 7.72880 \times t_1 \times t_2 \\
& + 0.00928321 \times D^2 + 4.02536 \times t_1^2 + 5.37656 \times t_2^2 \quad (5.10)
\end{aligned}$$

#### 5.4.3.2. Validation of the RSM models

The accuracy of the proposed models can be examined in figures 5.33, 5.34, which demonstrate the relationship between the actual and predicted values of the bulge height and wall thickness reduction respectively for the design points. Three numerical simulations (not included in the design points) were carried out with the same test conditions as used in table 5.8 and the results were compared with the ones calculated using the statistical models in table 5.18. From this comparison, it is clear that the predicted and numerical results are in good agreement.

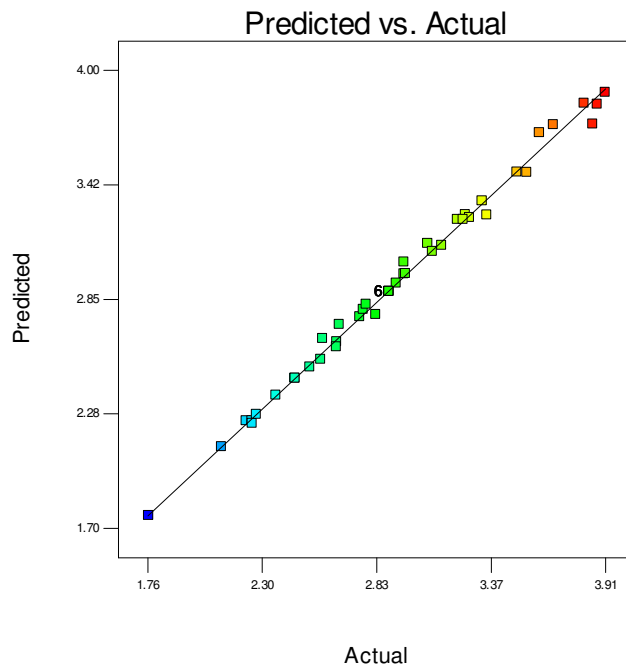


Figure 5.33: Scatter diagram of bulge height.

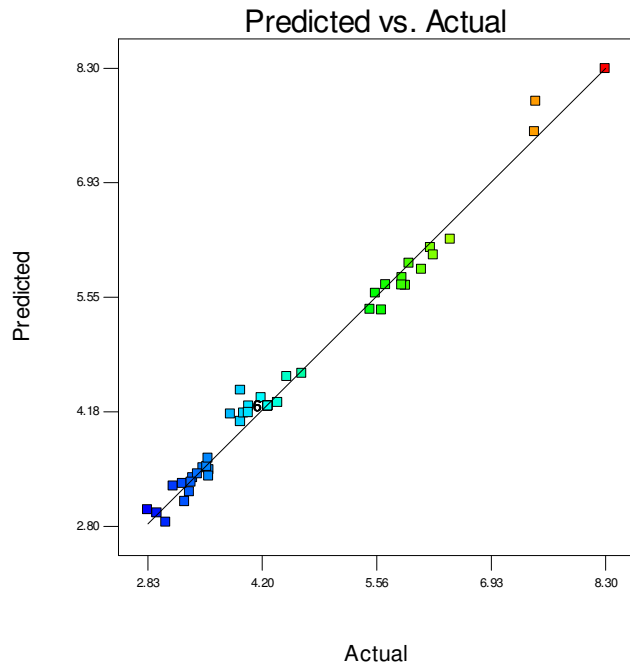


Figure 5.34: Scatter diagram of thickness reduction.

Table 5.18: Confirmation experiments.

Exp. No	L [mm]	r [mm]	D [mm]	$t_1$ [mm]	$t_2$ [mm]		H [mm]	Tr [%]
1	100	2	25	0.9	0.9	Numerical	10.01	19.76
						Predicted	10.27	19.94
						Error [%]	-2.60	-0.91
2	120	4	24	0.9	0.9	Numerical	8.62	18.11
						Predicted	8.613	18.6
						Error [%]	0.08	-2.70
3	120	3	24	1	0.9	Numerical	8.07	16.2
						Predicted	7.97	15.24
						Error [%]	1.24	5.92

#### 5.4.3.3. Effect of the geometrical factors on the bulge height

The perturbation plot shown in figure 5.35 demonstrates that a bulge height increase can be gained when hydroforming using shorter length, thinner walls, and larger diameter tubes. Notably, the influence of internal layer thickness was found to be greater than that of the

outer layer thickness. In addition, the usage of a bigger die corner radius was found to result in a higher hydroformed bulges as it allows more material to be formed in the die.

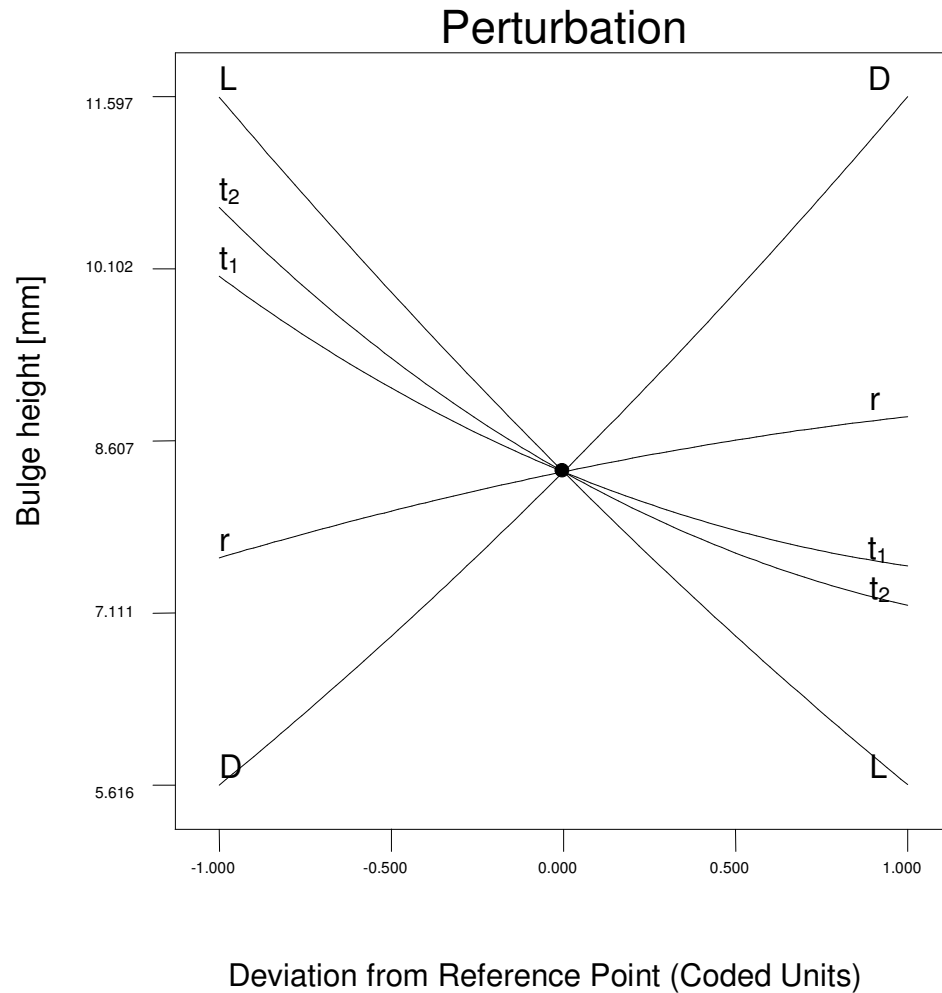


Figure 5.35: Perturbation plot of bulge height

From figures 5.36, 5.37 it can be seen that the influence of tube diameter on bulge height depends on the thickness of both inner and outer layers. Greater thicknesses of both layers result in a less significant effect of tube diameter on the bulge height. The interaction between the thicknesses of both layers was explored in figure 5.38, indicating that when the maximum thickness is assigned to the inner layer, bulge height doesn't significantly change with changing the thickness of the outer layer.

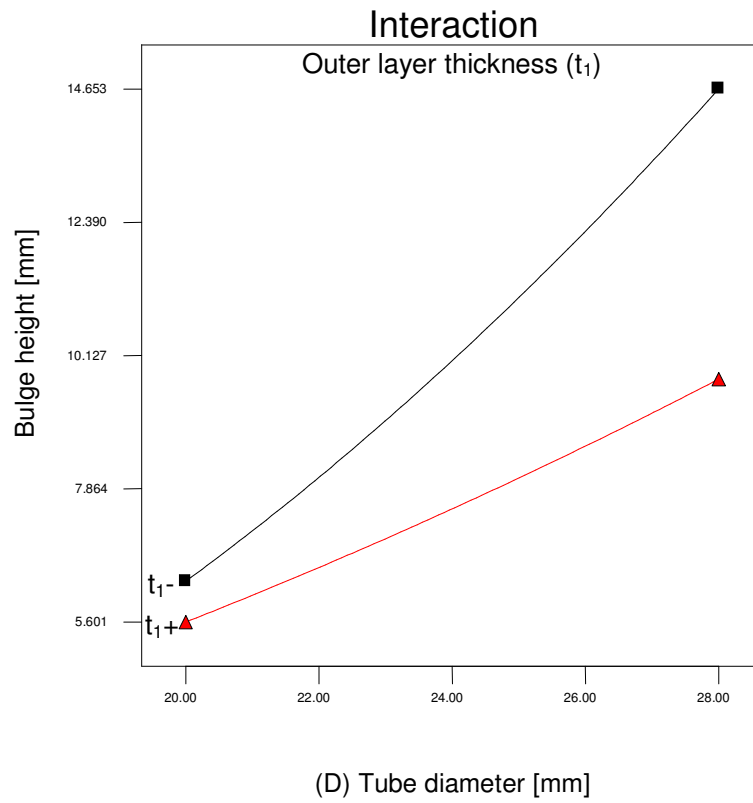


Figure 5.36: Interaction effect of the tube diameter and outer tube thickness on bulge height.

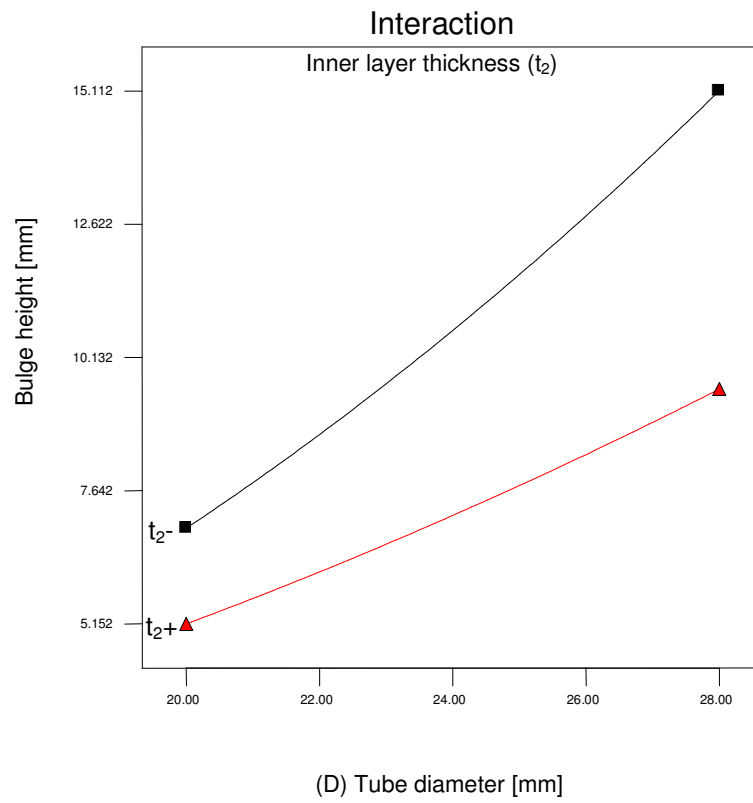


Figure 5.37: Interaction effect of the tube diameter and inner tube thickness on bulge height.

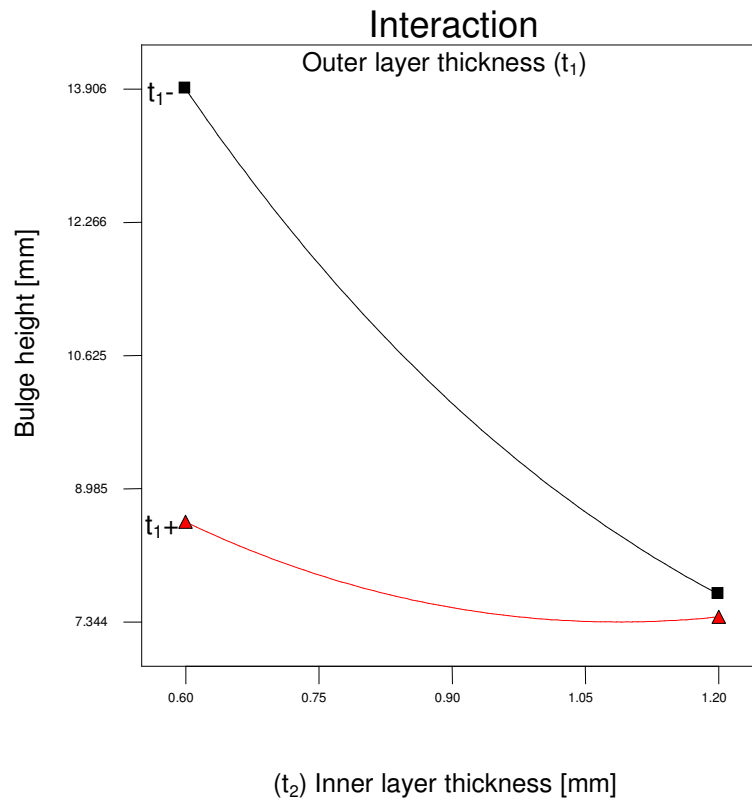


Figure 5.38: Interaction effect of the inner and outer layer thicknesses on bulge height.

#### 5.4.3.4. Effect of the geometrical factors on the wall thickness reduction

The effect of the geometrical factors on the wall thickness reduction can be discovered in the perturbation plot figure 5.39. It can be seen that the wall thickness reduction slightly decreases when using longer tubes. While, increasing the die corner radius or the tube diameter led to a greater wall thickness reduction ratio. However, thicker outer and inner layers result in smaller expansion and in a better wall thickness distribution.

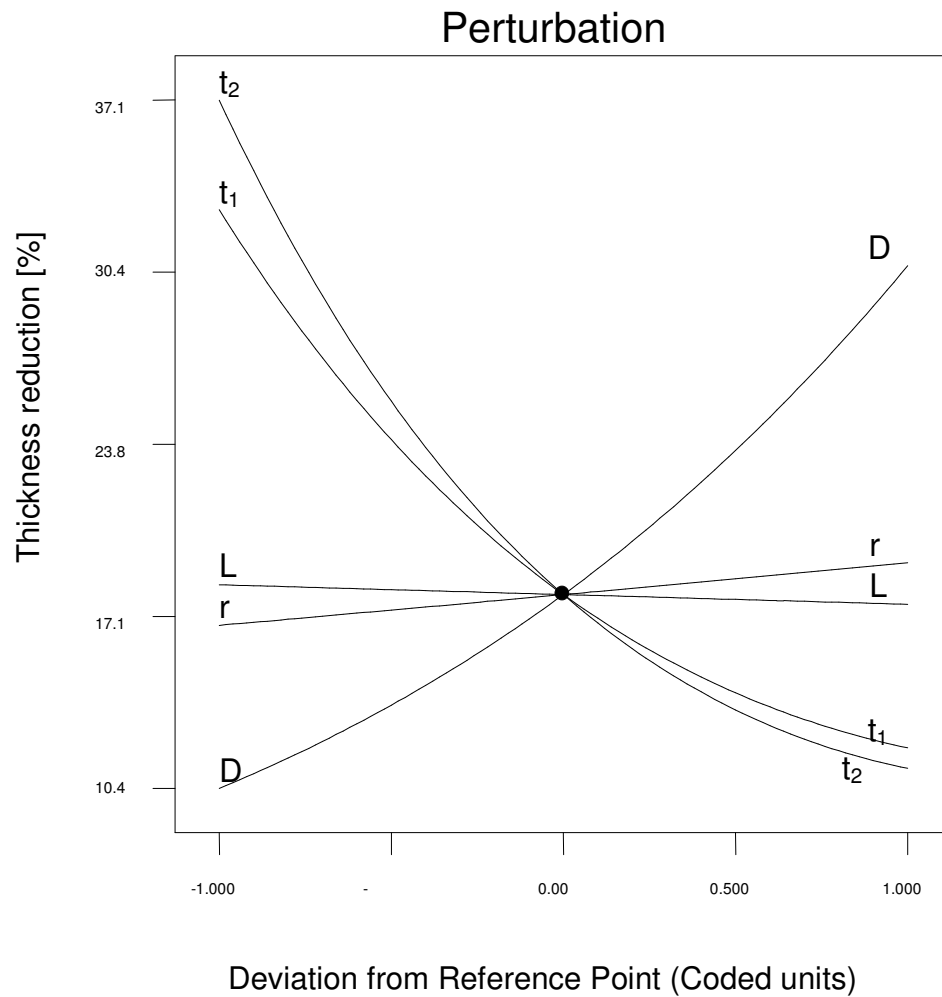


Figure 5.39: Perturbation plot of wall thickness reduction.

Regarding the interaction between the tube length and tube diameter, interaction plot figure 5.40 indicates that the tube length effect on the wall thickness reduction depends on the value of tube diameter. Particularly, in case of a tube diameter within the range ( $D$ : 20- 25 mm), reducing the tube length was found to lead to bigger thickness reduction. On the other hand, using a shorter tube length resulted in better wall thickness uniformity when big tube diameters ( $D > 25$  mm) are assigned.

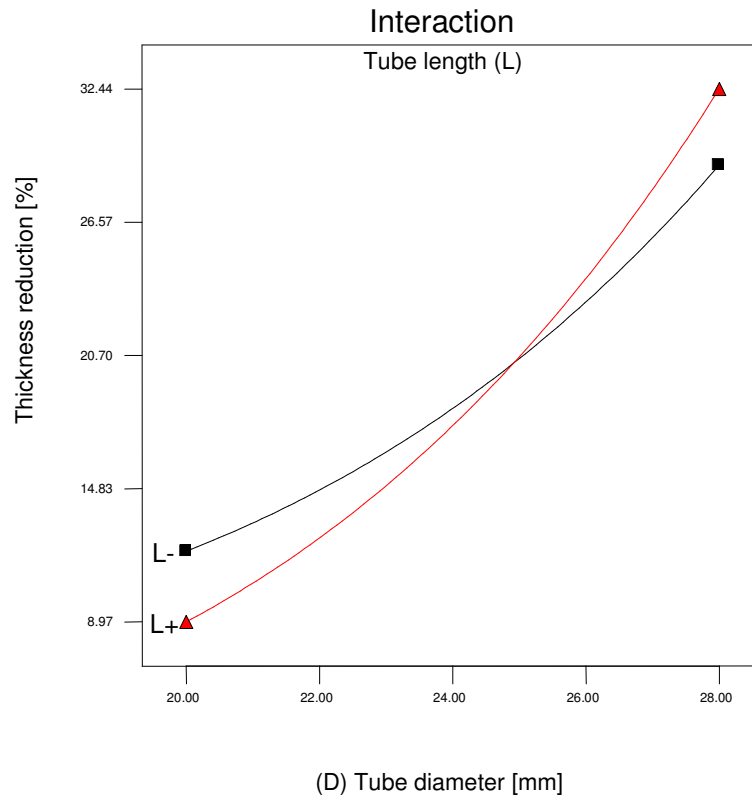


Figure 5.40: Interaction effect of the tube diameter and tube length on wall thickness reduction.

Two interaction effects were detected between the tube diameter (D) and both the outer and inner layer thicknesses ( $t_1$ ,  $t_2$ ). From the interaction plots figures 5.41, 5.42, it can be seen that the influence of tube diameter on the wall thickness reduction depends on the value of the outer and inner layers thicknesses. The thinner the outer and inner layers are, the more significant is the effect of tube diameter on thickness reduction of the hydroformed component. An interaction was also detected between the outer and inner layer thicknesses figure 5.43. It indicated that with increasing thickness of the inner layer, the effect of outer layer thickness on thickness reduction becomes less powerful.

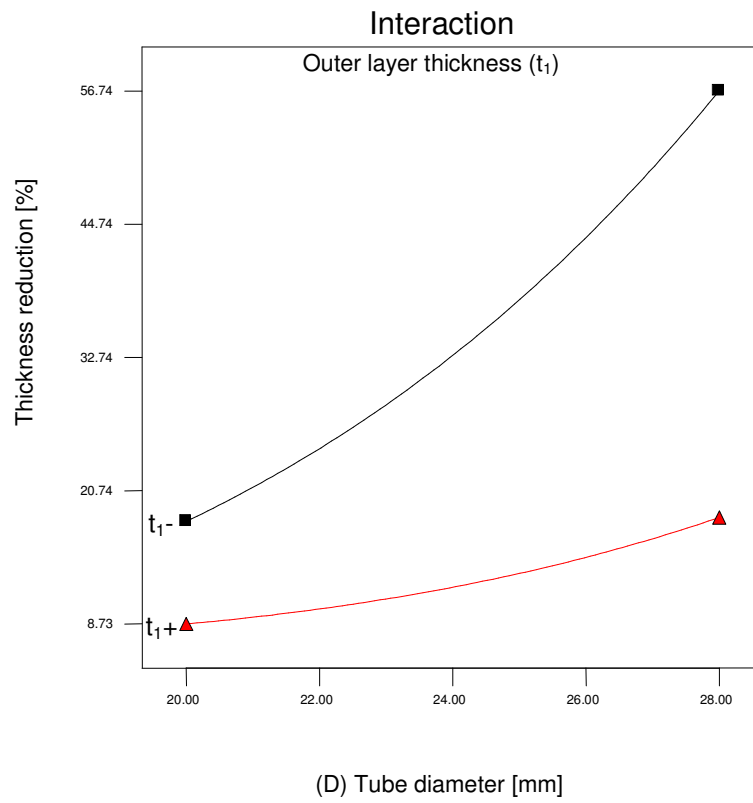


Figure 5.41: Interaction effect of the tube diameter and outer layer thickness on wall thickness reduction.

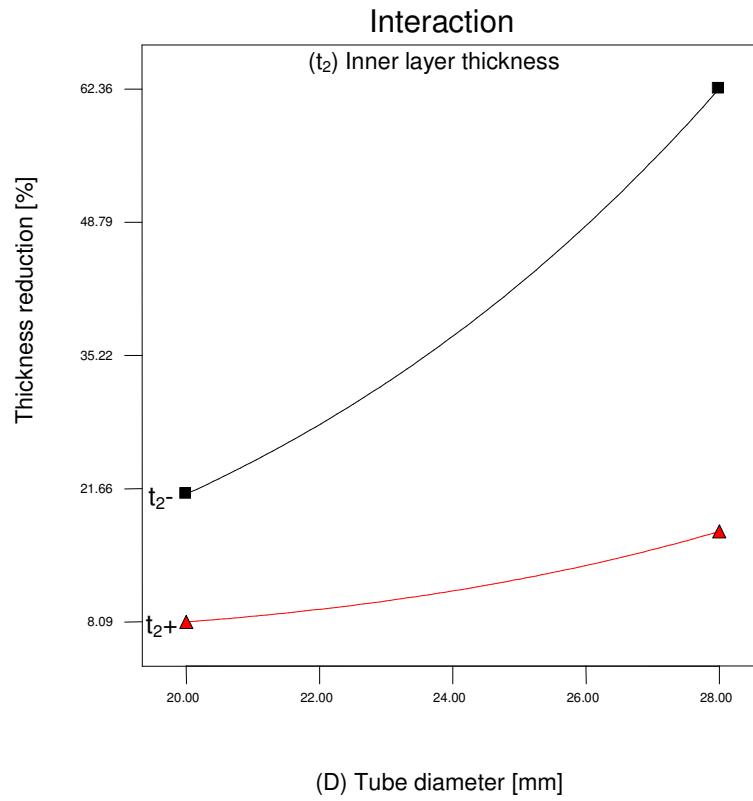


Figure 5.42: Interaction effect of the tube diameter and inner layer thickness on wall thickness reduction.

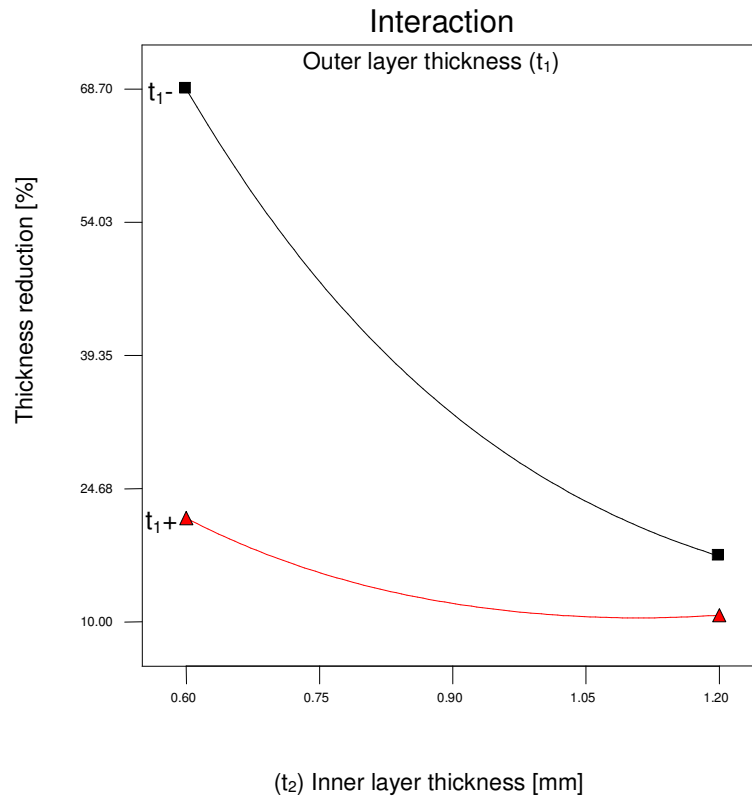


Figure 5.43: Interaction effect of the inner and outer layer thicknesses on wall thickness reduction.

#### 5.4.4. Process parameters analysis of T-shape bi-layered tube hydroforming

An integration of the finite element modelling of T-branch bi-layered tube hydroforming and the design of experiment technique was carried out to investigate the effect of the process parameters listed in table 5.2 on the hydroformed component. Following the same procedures as described in the sections 5.4.1- 5.4.3, the experimental design was applied using the statistical software, Design-expert V7 [119]. The numerical data were derived from the validated finite element model described in section 4.2 in order to model the bulge height and wall thickness reduction of the final hydroformed part as a function of the studied process parameters. No significant wrinkling was observed in T-type hydroformed parts through the studied design space. The responses were measured according to the design matrix as stated in the Box–Behnken design table 5.9, and listed in table 5.19. Using the statistical software mentioned above, second order polynomials were fitted to the

experimental data by means of a step-wise regression method, while the adequacy measures were used in selecting the best models [120, 121]. The summary output of best fit indicates that the resultant quadratic models are statistically recommended for the responses.

Table 5.19: Design matrix with numerical measured responses.

Exp. No	H [mm]	Tr [%]	Exp. No	H [mm]	Tr [%]
1	5.72	12.74	24	8.35	12.58
2	10.24	11.75	25	5.7	12.23
3	5.91	13.44	26	10.23	10.17
4	10.54	11.32	27	5.79	13.46
5	7.99	11.55	28	10.51	12.05
6	8.05	11.87	29	8.78	11.76
7	8.25	13.04	30	8.94	12.09
8	8.306	13.28	31	7.177	13.13
9	8.7	12.04	32	7.27	13.55
10	9.04	11.93	33	6.659	12.26
11	7.122	12.73	34	11.12	10.86
12	7.417	13.92	35	4.961	14.08
13	5.74	12.57	36	9.76	11.48
14	10.32	11.03	37	7.96	12.04
15	5.751	13.01	38	8.21	11.88
16	10.44	11.53	39	8.17	13.38
17	8.735	11.23	40	8.41	13.2
18	8.97	12.63	41	8.18	12.27
19	7.276	12.88	42	8.18	12.27
20	7.38	14.22	43	8.18	12.27
21	8	12.51	44	8.18	12.27
22	8.24	12.21	45	8.18	12.27
23	8.12	12.8	46	8.18	12.27

#### 5.4.4.1. Analysis of variance (ANOVA)

The resulting ANOVA tables 5.20, 5.21 contain the analysis of variance for both responses and show the significant model terms. The same tables also show the adequacy measures ( $R^2$ ,  $adjR^2$ ,  $predR^2$ , and adequate precision), which indicate that the proposed models are adequate.

Table 2.20: ANOVA table for bulge height reduced quadratic model.

Source	Sum of Squares	df	Mean Square	F Value	p-value Prob > F
Model	95.69063	10	9.569063	3649.568	< 0.0001
S	85.22059	1	85.22059	32502.49	< 0.0001
P <sub>2</sub>	0.271702	1	0.271702	103.6249	< 0.0001
P <sub>3</sub>	0.033033	1	0.033033	12.59856	0.0011
P <sub>4</sub>	0.167077	1	0.167077	63.72173	< 0.0001
f	9.892598	1	9.892598	3772.962	< 0.0001
S*P <sub>4</sub>	0.009025	1	0.009025	3.442066	0.0720
S*f	0.028561	1	0.028561	10.89295	0.0022
S <sup>2</sup>	0.03479	1	0.03479	13.26875	0.0009
P <sub>3</sub> <sup>2</sup>	0.009858	1	0.009858	3.759658	0.0606
f <sup>2</sup>	0.043156	1	0.043156	16.45949	0.0003
Residual	0.091769	35	0.002622		
Cor Total	95.78239	45			
R <sup>2</sup> = 0.999, adjusted R <sup>2</sup> = 0.998; predicted R <sup>2</sup> = 0.998, adequate precision= 247.141					

Table 5.21: ANOVA table for thickness reduction reduced quadratic model.

Source	Sum of Squares	df	Mean Square	F Value	p-value Prob > F
Model	31.83243	13	2.448649	85.26257	< 0.0001
S	11.56	1	11.56	402.5222	< 0.0001
P <sub>2</sub>	0.015006	1	0.015006	0.522521	0.4750
P <sub>3</sub>	0.529256	1	0.529256	18.42884	0.0002
P <sub>4</sub>	8.136756	1	8.136756	283.3239	< 0.0001
f	7.826006	1	7.826006	272.5035	< 0.0001
S*P <sub>2</sub>	0.319225	1	0.319225	11.1155	0.0022
S*P <sub>4</sub>	0.105625	1	0.105625	3.67789	0.0641
S*f	0.36	1	0.36	12.53529	0.0012
P <sub>2</sub> *f	0.4225	1	0.4225	14.71156	0.0006
S <sup>2</sup>	1.027243	1	1.027243	35.76886	< 0.0001
P <sub>2</sub> <sup>2</sup>	0.418805	1	0.418805	14.58291	0.0006
P <sub>4</sub> <sup>2</sup>	0.089491	1	0.089491	3.116104	0.0871
f <sup>2</sup>	0.531491	1	0.531491	18.50666	0.0001
Residual	0.919005	32	0.028719		
Cor Total	32.75144	45			
R <sup>2</sup> = 0.972, adjusted R <sup>2</sup> = 0.961; predicted R <sup>2</sup> = 0.915, adequate precision= 39.737					

The analysis of variance indicates that the following terms are most significant when associated with bulge height:

1. The first order effect of axial feed displacement (S), all studied internal pressure coordinates ( $P_2$ ,  $P_3$  and  $P_4$ ), and coefficient of friction (f).
2. The second order effects of the axial feed displacement ( $S^2$ ), internal pressure coordinate ( $P_3^2$ ), and coefficient of friction ( $f^2$ ).
3. The two level of interaction between the internal pressure coordinate  $P_4$  and axial feed velocity ( $S \times P_4$ ), and between the axial feed displacement and coefficient of friction ( $S \times f$ ).

Secondly for the wall thickness reduction model, the analysis indicated that the significant terms are:

1. The first order effect of the axial feed displacement (S), all studied internal pressure coordinates ( $P_2$ ,  $P_3$  and  $P_4$ ), and coefficient of friction (f).
2. The second order effect of the axial feed displacement ( $S^2$ ), internal pressure coordinates ( $P_2^2$ ) and ( $P_4^2$ ), and coefficient of friction ( $f^2$ ).
3. The two level of interaction between the pressure coordinate  $P_2$  and the axial feed displacement ( $S \times P_2$ ), the internal pressure coordinate  $P_4$  and the axial feed displacement ( $S \times P_4$ ), the coefficient of friction and the axial feed displacement ( $S \times f$ ), and between the internal pressure coordinate  $P_2$  and coefficient of friction ( $P_2 \times f$ ).

The final mathematical models in terms of actual factors as determined by the design expert software are shown in equations 5.11, 5.12.

$$\begin{aligned} \text{Bulge height} = & - 3.80157 + 0.35739 \times S + 0.013031 \times P_2 \\ & + 0.39718 \times P_3 - 0.00346 \times P_4 - 14.38292 \times f \\ & + 0.00422 \times S \times P_4 + 0.3755 \times S \times f - 0.00293 \times S^2 \\ & - 0.00505 \times P_3^2 - 26.43333 \times f^2 \end{aligned} \quad (5.11)$$

$$\begin{aligned} \text{Thickness reduction} = & + 31.62257 - 0.17020 \times S - 0.10140 \times P_2 \\ & + 0.072750 \times P_3 - 1.19139 \times P_4 - 7.25644 \times f \\ & - 0.006277 \times S \times P_2 + 0.0144 \times S \times P_4 \\ & - 1.333 \times S \times f + 0.65000 \times P_2 \times f - 0.0163 \times S^2 \\ & + 0.00210 \times P_2^2 + 0.015588 \times P_4^2 + 94.96970 \times f^2 \end{aligned} \quad (5.12)$$

#### 5.4.4.2. Validation of the RSM models

The relationships between the actual and predicted values of the bulge height and thickness reduction for the design points are presented in figures 5.44, 5.45. The resultant figures show that the residuals tend to be close to the diagonal line, which indicates that the developed models are accurate. However, to check the models' accuracy in the whole design space, three numerical simulations (not included in the design points) were carried out using the same test conditions as performed in table 5.14. Numerical results were compared with the estimated ones in table 5.22. Good agreement was observed between both kinds of results, which indicate that the proposed models are adequate in the whole design space.

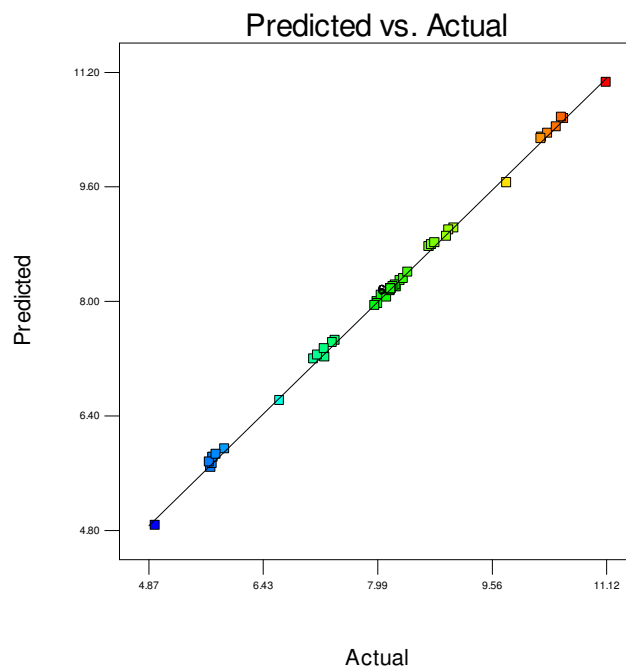


Figure 5.44: Scatter diagram of bulge height.

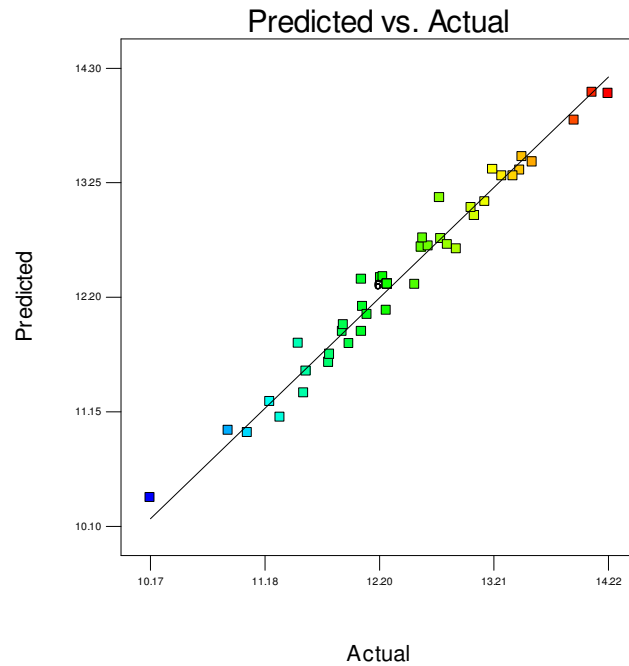


Figure 5.45: Scatter diagram of thickness reduction.

Table 5.22: Confirmation experiments

Exp. No	S [mm]	P <sub>2</sub> [MPa]	P <sub>3</sub> [MPa]	P <sub>4</sub> [MPa]	f		H [mm]	Tr [%]
1	9	30	40	43	0.1	Numerical	7.46	12.87
						Predicted	7.49	13.00
						Error [%]	-0.40	-1.01
2	10.5	28	38	45	0.15	Numerical	7.52	14.32
						Predicted	7.47	14.23
						Error [%]	0.66	0.63
3	9	35	40	40	0.15	Numerical	6.86	14.07
						Predicted	6.57	13.88
						Error [%]	4.22	1.35

#### 5.4.4.3. Effect of the process parameters on bulge height

In the displayed perturbation plot figure 5.46, the effect of each parameter over its range is examined while maintaining the other process parameters constant at the midpoint. From the resultant graph, higher bulges were achieved by increasing of the axial feed and decreasing the friction coefficient. However, as expected, internal pressure coordinates were seen to have a positive influence on the bulge height increase.

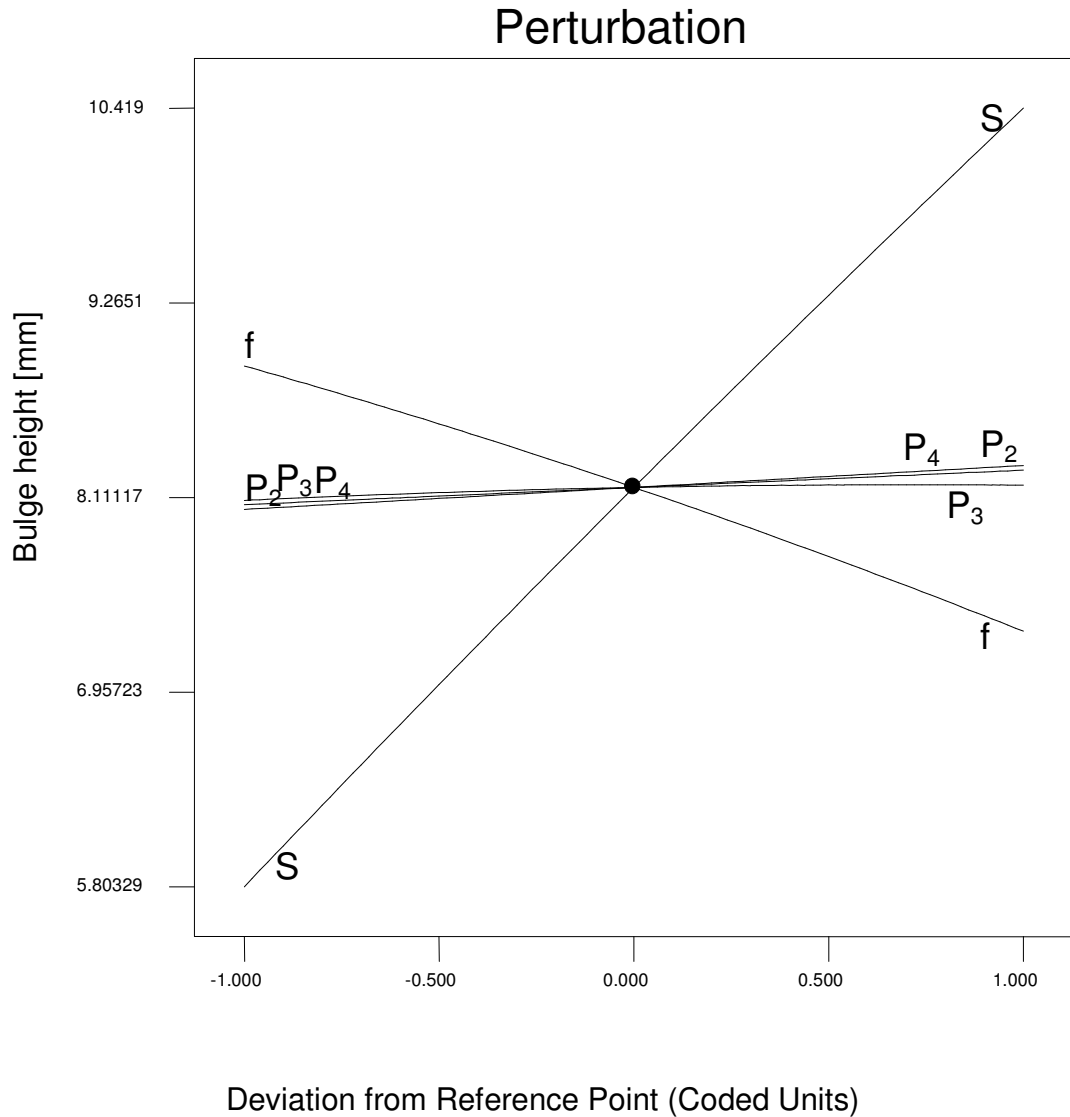


Figure 5.46: Perturbation of bulge height.

5.4.4.4. Effect of the process parameters on wall thickness reduction

It can be noticed from the perturbation plot of the wall thickness reduction figure 5.47 that bigger axial feed displacements supply more material into the die, which leads to better wall thickness uniformity for the hydroformed part. Increasing the initial internal pressure ( $P_2$ ) in the range between 15 and 25 MPa was found to improve the thickness uniformity as it avoids the sudden application of high internal pressure in coordinates ( $P_3$ -  $P_5$ ), but it leads to thickness reduction increase when values are ranging between 25 to 35 MPa as more

material expansion is the result. Greater thickness reduction was obtained by applying bigger values of internal pressure coordinates ( $P_3$ ,  $P_4$ ). However, the influence of  $P_4$  was observed to be more significant. Furthermore, a small coefficient of friction results in less wall thickness reduction, as it facilitates the material forming in the die cavity.

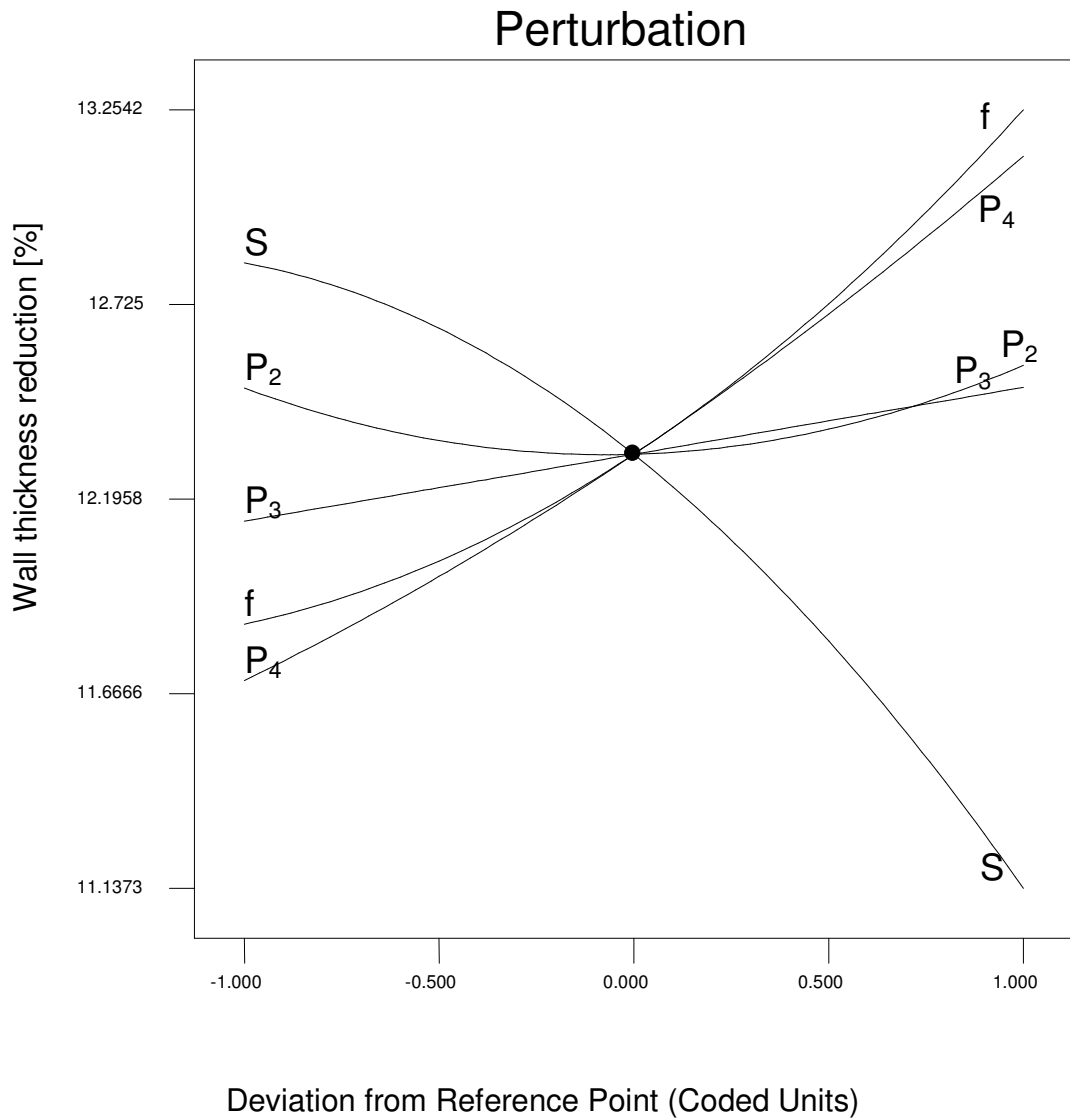


Figure 5.47: Perturbation of thickness reduction.

In terms of the interaction detected between the initial internal pressure  $P_2$  and the axial feed displacement, the interaction plot figure 5.48 indicates that the effect of the initial

internal pressure ( $P_2$ ) on the wall thickness reduction depends on the value of the axial feed displacement. When a small axial displacement ( $S < 11$  mm) is applied, a higher level of  $P_2$  resulted in greater wall thickness reduction ratios, while if a big axial feed ( $S > 11$  mm) is applied greater  $P_2$  values were considered more advantageous, as it gives finer wall thickness distribution. Therefore, to attain greater wall thickness uniformity for the hydroformed part, the values of ( $P_2$  and  $S$ ) that should be selected depend on each other; big feed displacements should be accompanied with high  $P_2$  levels, while a low  $P_2$  value would be better when small axial feed displacements are employed.

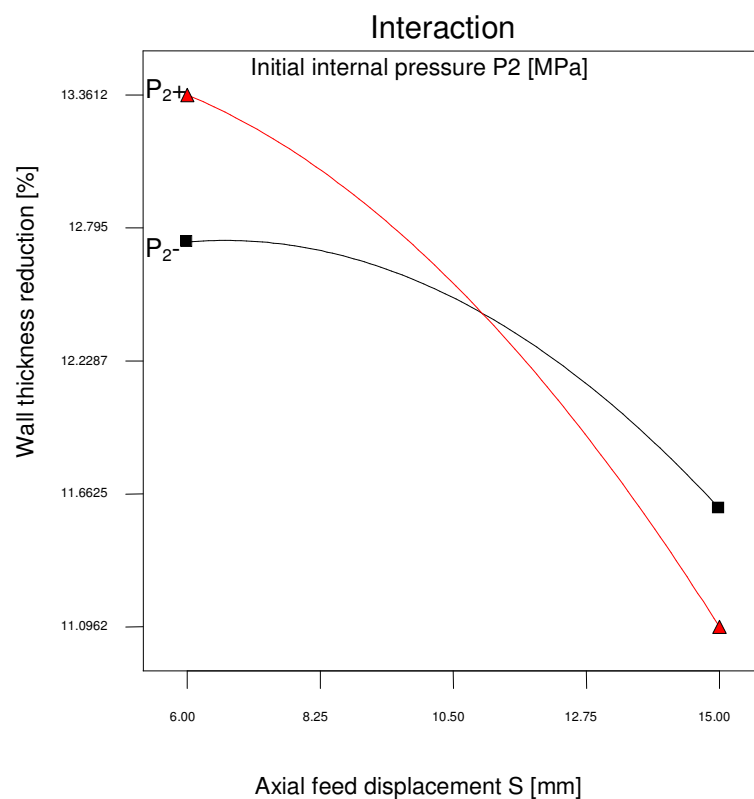


Figure 5.48: Interaction plot between  $P_2$  and axial feed velocity.

Another interaction effect was detected between the coefficient of friction and initial internal pressure  $P_2$ . The interaction plot figure 5.49 indicates that the application of a greater  $P_2$  value in conjunction with a small coefficient of friction (0.05- 0.095) results in a more homogeneous wall thickness, while increasing the  $P_2$  value would cause an increase in wall thickness reduction if a coefficient of friction in the range (0.095- 0.15) is utilized.

A further indication arising from figure 5.50 is that the effect of the coefficient of friction on wall thickness reduction becomes more significant when smaller feed displacements are employed.

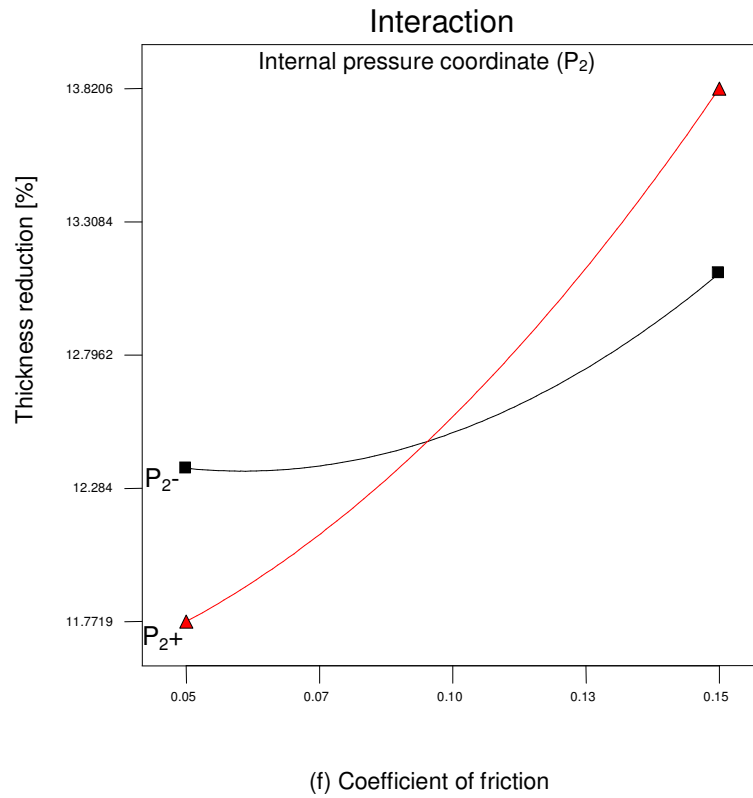


Figure 5.49: Plot showing the interaction between  $P_2$  and coefficient of friction.

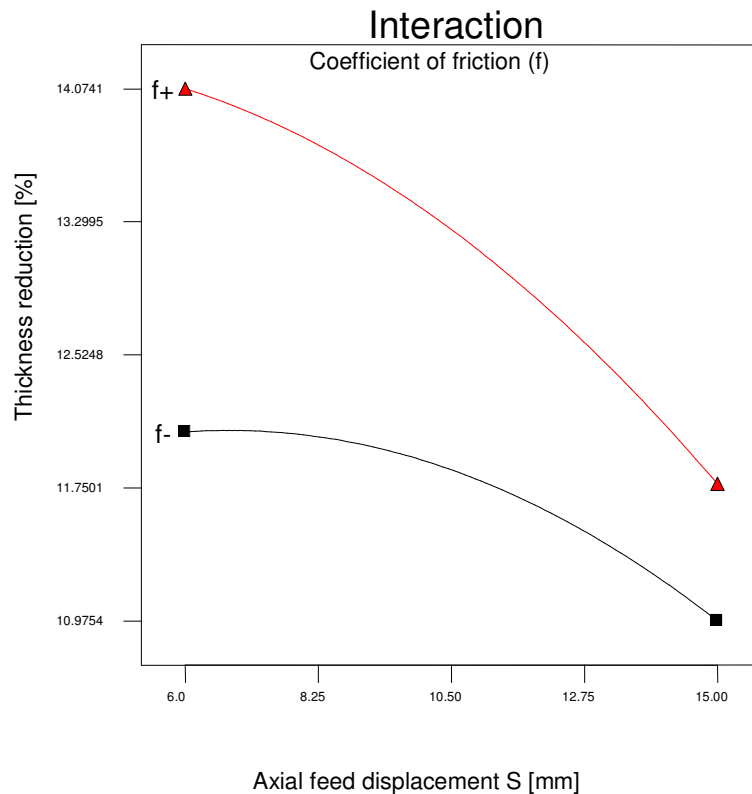


Figure 5.50: Plot showing the interaction between coefficient of friction and axial feed displacement.

### 5.5. Summary

In this chapter, the response surface method for design of experiments was used in conjunction with the finite element modelling studied in chapter 4 to explore the effects of the geometrical factors and process parameters on the X-shape and T-shape bi-layered tube hydroforming processes. Using the techniques outlined in this study, the process outputs were modelled as functions of each of the geometrical factors and process parameters. The constructed models were found to be statistically adequate. From the resultant models, a quick estimation of the process output can be obtained. In addition, the main effects of the studied parameters and their interactions on the process output were graphically displayed using the Design-expert V7 software. In the next chapter the response surface models will be used in the multi-objective optimization studies that were conducted.

## **CHAPTER SIX**

### **OPTIMIZATION STUDY**

#### **6.1. Introduction**

The results in the previous chapter indicate that the output of the bi-layered tube hydroforming process depended strongly on the geometrical factors and process parameters used in the study. However, the main challenge for a manufacturer is to choose input parameters that will lead to the best possible process output. In this study, based on the response surface models calculated in Chapter Five, multi-objective optimization studies were conducted using the desirability approach to evaluate the best combinations of each of the geometrical factors and process parameters that result in the best process outputs, as judged on the basis of a number of specific practical criteria. A further model was constructed of the process operating cost, in order to establish the economic feasibility of the process, and to study the effect of cost minimization on the process output. In addition, a different optimization approach, employing the iterative optimization algorithm function of the ANSYS optimizer, was implemented to examine the optimum process parameters for single objective criterion. The same criterion was optimized using the desirability approach, and a comparison of both optimization methods was conducted taking the differences between the optimization results into account.

#### **6.2. Response Surfaces Models Based Optimization**

Typically, as part of the analysis of the tube hydroforming process, the various responses being investigated need to be optimized simultaneously. However, multi-objective optimization problems can involve incommensurate and conflicting responses. Based on the response surface models evaluated in the previous chapter, there are different statistical techniques that solve multiple response problems. These include, overlaying the contour plots for each response, constrained optimization problem, and the desirability approach. The desirability method is recommended due to its simplicity, availability of the software, and because it offers flexibility in weighting and can assign different importance values for individual responses.

### 6.2.1. Desirability approach

Solving multi-objective optimization problems using the desirability approach consists of a technique that combines multiple responses into a dimension-less measure of performance, called an overall desirability function. In particular, the desirability approach indicates the transforming of each estimated response,  $Y_i$ , into a unit-less utility bounded by  $(0 < d_i < 1)$ , where a greater  $d_i$  value indicates that response value  $Y_i$  is more desirable, i.e.: if  $d_i = 0$  this means that the response is completely undesired, while  $d_i = 1$  indicates a fully desired response [123]. In the current work using the Design-expert V7 software [119], the individual desirability for each response  $d_i$  was calculated using Eqs.6.1- 6.4. The shape of the desirability function can be changed for each goal by the weight field “wt<sub>i</sub>”. Weights are used to give added emphasis to the upper/lower bounds or to emphasize the target value. Weights could be ranged between 0.1 and 10; a weight greater than one gives more emphasis to the goal, while a weight less than one gives less emphasis to the goal. With a weight value of one, the values of  $d_i$  will vary between zero and one in a linear mode. In the desirability objective function (D), each response can be assigned an importance (r) relative to the other responses. Importance varies from the least important value of 1(+), to the most important value of 5(++++)+. If varying degrees of importance are assigned to the different responses, the overall objective function is shown in Eq.6.5. Where n is the number of responses in the measure, and  $T_i$  is the target value of the  $i^{\text{th}}$  response [123].

- For a maximum value as the required goal, the desirability can be defined by:

$$d_i = \begin{cases} 0 & , Y_i \leq Low_i \\ \left( \frac{Y_i - Low_i}{High_i - Low_i} \right)^{wt_i} & , Low_i < Y_i < High_i \\ 1 & , Y_i \geq High_i \end{cases} \quad (6.1)$$

- For a minimum value as the required goal, the desirability can be defined by:

$$d_i = \begin{cases} 1 & , \quad Y_i \leq Low_i \\ \left( \frac{High_i - Y_i}{High_i - Low_i} \right)^{wt_i} & , \quad Low_i \langle Y_i \langle High_i \\ 0 & , \quad Y_i \geq High_i \end{cases} \quad (6.2)$$

- For a target value as the required goal, the desirability can be defined by:

$$d_i = \begin{cases} \left( \frac{Y_i - Low_i}{T_i - Low_i} \right)^{wt_{1i}} & , \quad Low_i \langle Y_i \langle T_i \\ \left( \frac{Y_i - High_i}{T_i - High_i} \right)^{wt_{2i}} & , \quad T_i \langle Y_i \langle High_i \\ 0 & , \quad Otherwise \end{cases} \quad (6.3)$$

- For a value within range as the required goal, the desirability can be defined by:

$$d_i = \begin{cases} 1 & , \quad Low_i \langle Y_i \langle High_i \\ 0 & , \quad Otherwise \end{cases} \quad (6.4)$$

$$D = \left( \prod_{i=1}^n d_i^{r_i} \right)^{\frac{1}{\sum r_i}} \quad (6.5)$$

### 6.2.2. Optimization approach in Design-expert V7 software

The optimization function of the Design-expert V7 software searches for a combination of factor levels that simultaneously satisfy the desired requirements (i.e. optimization criteria) from each of the responses and process factors (i.e. multiple response optimization). As mentioned in the previous section, the optimization process involves combining the goals into an overall desirability function (D). The numerical optimization feature in the Design-expert V7 software package searches for one or more points in the factors domain that will maximize the desirability function (D). In the graphical optimization with multiple responses, the software defines regions where requirements, simultaneously, meet the proposed criteria, superimposing or overlaying critical response contours on a contour plot. This enables a visual search for the best compromise. In the case of dealing with multiple responses, it is recommended to do a numerical optimization first; otherwise it might be difficult to uncover a feasible region. A flow chart of the optimization steps can be shown in figure 6.1.

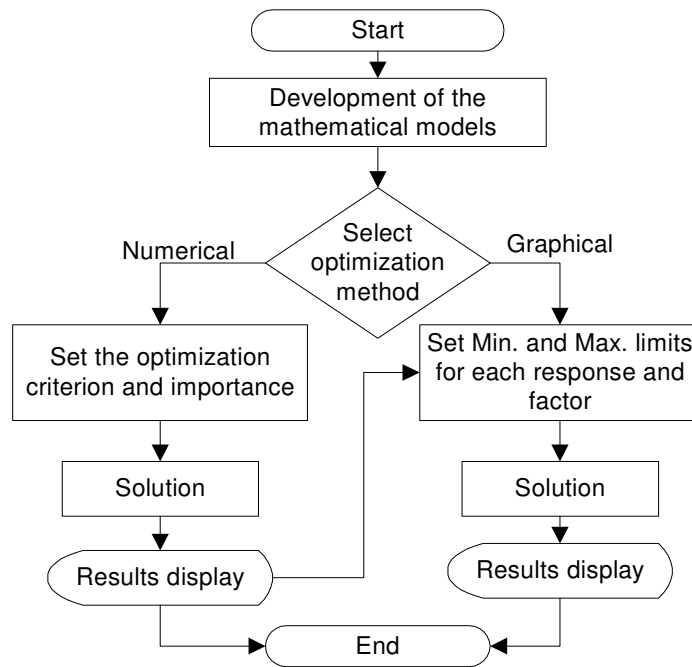


Figure 6.1: Optimization steps [114].

### 6.3. Multi-response optimization in X-shape bi-layered tube hydroforming

Based on the response surface models constructed in section 5.4.1 and section 5.4.2 that describe the effects of the geometrical factors and process parameters on the X- shape bi-layered hydroformed part, multi-response optimization studies were conducted by means of the desirability approach using the Design-expert V7 software.

#### 6.3.1. Geometrical factors optimization in X-type bi-layered tube hydroforming

In order to manufacture X-branch junctions that connect to specified tubes, the tubular diameter ( $D$ ), and the two layers thicknesses ( $t_2$  and  $t_1$ ) of the tubular blank are fixed. The values of ( $D$ ,  $t_2$ , and  $t_1$ ) are taken from the tube geometry of the experiment section 3.3. Both the initial tube length ( $L$ ) and the die corner radius ( $r$ ) are set to vary in order to find the best output in the proposed optimization criteria. In the first criterion displayed in table 6.1, the most important objective is to achieve the highest possible bulge while keeping the wall thickness reduction and wrinkle height within the accepted levels (less than 20% for the wall thickness reduction and less than 0.1 mm for the wrinkle height). However, minimizing thickness reduction and wrinkle height were of minimal importance. On the other hand, with the same objectives being implemented in the second criterion, equal importance was given for the three responses as shown in table 6.2 (bulge height, thickness reduction, and wrinkle height) in order to put more emphasis on the geometrical quality of the resultant hydroformed part. In tables 6.1- 6.2, the required goal, the lower and upper limits, and the importance, for each response and factor for both criteria are illustrated.

Table 6.1: The first criterion of numerical optimization.

Name	Goal	Lower Limit	Upper Limit	Importance
L	Is in range	80	160	3
r	Is in range	1	5	3
D	Is equal to 24.00	20	28	3
$t_1$	Is equal to 1.00	0.6	1.2	3
$t_2$	Is equal to 0.85	0.6	1.2	3
H	Maximize	4.27	14.155	5
Tr	Minimize	3.34	20	1
Wr	Minimize	0.03943	0.1	1

Table 6.2: The second criterion of numerical optimization.

Name	Goal	Lower Limit	Upper Limit	Importance
L	Is in range	80	160	3
r	Is in range	1	5	3
D	Is equal to 24.00	20	28	3
t <sub>1</sub>	Is equal to 1.00	0.6	1.2	3
t <sub>2</sub>	Is equal to 0.85	0.6	1.2	3
H	Maximize	4.27	14.155	3
Tr	Minimize	3.34	20	3
Wr	Minimize	0.03943	0.1	3

In the results, tables 6.3- 6.4 show the geometrical factors, which lead to a maximum bulge height while minimizing the wrinkle height and thickness reduction and keeping them within the accepted levels. According to the first criterion, it was found that the greatest desirability is achieved when a maximum bulge height of 9.713 mm is protruded with 19.26% wall thickness reduction and 0.096 mm wrinkle height, with a tube length of 100.12 mm and a die corner radius of 5 mm being used. The results of the second criterion optimization is presented in table 6.4. It is shown that a smaller wall thickness reduction ratio of 16.00% with a smaller wrinkle height of 0.0638 mm can be obtained with a bulge height of 7.45 mm, if a tube of 135.55 mm length is used with a die corner radius of 3.43 mm. A comparison of the optimum results for both investigated criteria indicates that adjusting the tube length and die corner radius can result in a near 17% better wall thickness uniformity with a wrinkle height decrease of 33.5% if the protruded bulge height is reduced by 23.3% .

Table 6.3: Optimal conditions based on the first criterion

Number	L	r	D	t <sub>1</sub>	t <sub>2</sub>	H	Tr	Wr
1	100.12	5	24	1	0.85	9.713	19.26	0.0960
2	102.89	5	24	1	0.85	9.561	19.26	0.0909
3	114.18	5	24	1	0.85	8.958	19.26	0.0764

Table 6.4: Optimal condition based on the second criterion

Number	L	r	D	t <sub>1</sub>	t <sub>2</sub>	H	Tr	Wr
1	135.55	3.43	24	1	0.85	7.450	16.00	0.0638

The graphical optimization results allow selection of the optimum geometrical factors by means of visual inspection. The blank areas on the overlay plots in figures 6.2- 6.3 represent the values that do not meet the proposed criteria. For each response, the lower and upper limits were chosen according to the optimization results tables 6.3- 6.4. The upper and lower limits of the three responses for the studied criteria are displayed in table 6.5.

Table 6.5: Upper and lower limits for the responses in the two criteria

Criterion No.	Bulge height [mm]	Thickness reduction [%]	Wrinkle height [mm]
1	8.90- 9.70	19.00– 19.50	0.0760- 0.0960
2	7.00- 7.50	16.00- 16.10	0.063- 0.064

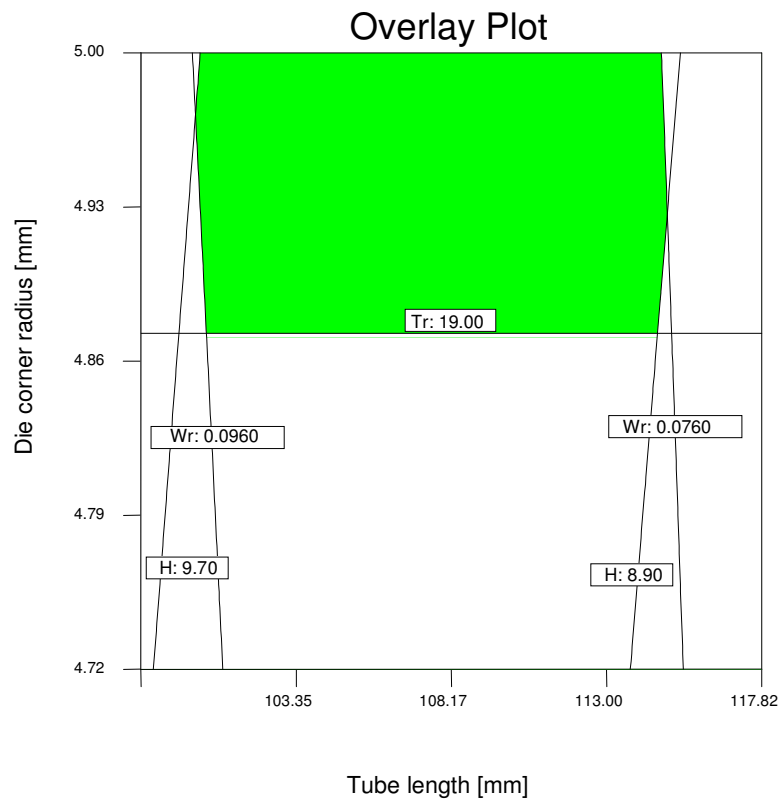


Figure 6.2: Graphical optimization of the first criterion.

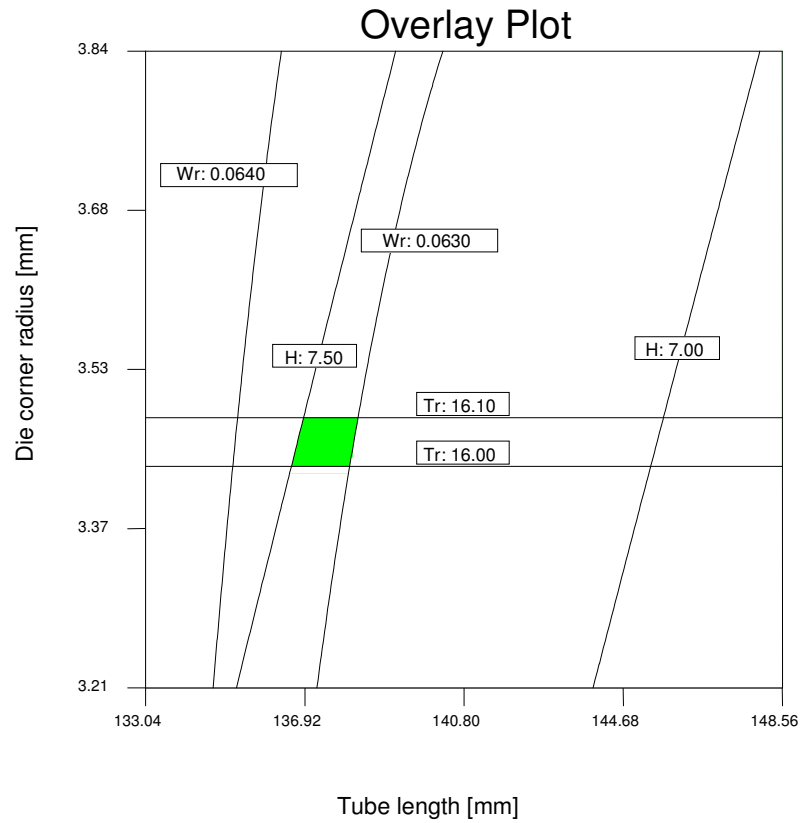


Figure 6.3: Graphical optimization of the second criterion.

Numerical simulations were performed using the optimum conditions for both studied criteria tables 6.3, 6.4, in order to compare numerical results with the predicted values. As displayed in table 6.6, it is evident that the optimized results are valid as the percentages of error are all within the acceptable range.

Table 6.6: Numerical validation of the optimization results

Criterion. No	L [mm]	r [mm]	D [mm]	t <sub>1</sub> [mm]	t <sub>2</sub> [mm]		H [mm]	Tr [%]	Wr [mm]
1	100.12	5.00	24	1	0.85	Numerical	10.086	17.05	0.092
						Predicted	9.713	19.26	0.096
						Error [%]	3.830	-11.50	-3.880
2	135.55	3.43	24	1	0.85	Numerical	7.98	16	0.0648
						Predicted	7.450	16.00	0.0638
						Error [%]	6.636	-0.060	1.454

### 6.3.2. Process parameters optimization in X-type bi-layered tube hydroforming

Based on the models constructed in section 5.4.2, the optimized process parameters were evaluated according to two different criteria. For both criteria, the accepted levels of maximizing the protruded bulge height and minimizing both of wall thickness reduction and wrinkle height were implemented. In the first criterion, most importance was given to the objective of bulge height increase, while the other objectives were given a minimum level of importance table 6.7. However, in the second criterion table 6.8, all responses are assigned an equal level of importance. The required goal, the lower and upper limits, and the importance, for each response and factor for both criteria are illustrated in tables 6.7-6.8.

Table 6.7: The first criterion of numerical optimization.

Name	Goal	Lower Limit	Upper Limit	Importance
S	Is in range	6	15	3
P <sub>2</sub>	Is in range	15	35	3
P <sub>3</sub>	Is in range	35	40	3
P <sub>4</sub>	Is in range	40	45	3
f	Is in range	0.05	0.15	3
H	Maximize	5.98	11.77	5
Tr	Minimize	11.13	20	1
Wr	Minimize	0.075	0.1	1

Table 6.8: The second criterion of numerical optimization.

Name	Goal	Lower Limit	Upper Limit	Importance
S	Is in range	6	15	3
P <sub>2</sub>	Is in range	15	35	3
P <sub>3</sub>	Is in range	35	40	3
P <sub>4</sub>	Is in range	40	45	3
f	Is in range	0.05	0.15	3
H	Maximize	5.98	11.77	3
Tr	Minimize	11.13	20	3
Wr	Minimize	0.075	0.1	3

The optimal process parameters according to the first criterion are listed in table 6.9. It was found that when a maximum bulge height is required, internal pressure coordinates (P<sub>2</sub>, P<sub>3</sub>, and P<sub>4</sub>) have to be set at the highest levels, while a minimum value (0.05) of coefficient of friction should be assigned. A value of (11.25 mm) for the axial feed displacement would achieve a bulge height of 10.086 mm with a wall thickness reduction ratio of 13.89% and a

wrinkle height of 0.095 mm, and therefore would meet best desirability as stated in the criterion of implementation. For the second criterion, optimization results indicate that a small wrinkle height of 0.07 mm with a small wall thickness reduction ratios ranging between 12.22% and 12.38% will result in hydroformed bulge height ranging between 9.1 mm and 9.24 mm, if the listed optimal process parameters values in table 6.10 were to be used. Keeping the internal pressure coordinate  $P_4$  at its lowest level (within the studied ranges) would be required in the second criterion in order to achieve better wall thickness uniformity, while high values of the other internal pressure coordinates ( $P_2$ ,  $P_3$ ) are recommended. An axial feed displacement of (9.69 mm) indicated best desirability.

Table 6.9: Optimal condition based on the first criterion

Number	S	$P_2$	$P_3$	$P_4$	f	H	Tr	Wr
1	11.25	35.00	39.99	45.00	0.05	10.08	13.89	0.0953
2	11.25	35.00	39.89	44.99	0.05	10.08	13.88	0.0952
3	11.28	35.00	39.62	44.84	0.05	10.07	13.86	0.0955
4	11.25	35.00	39.38	44.98	0.05	10.07	13.88	0.0953
5	11.28	35.00	39.41	45.00	0.05	10.08	13.90	0.0960
6	11.31	35.00	40.00	44.54	0.05	10.09	13.82	0.0966
7	11.22	35.00	39.94	44.14	0.05	10.04	13.68	0.0946
8	11.28	35.00	38.65	44.98	0.05	10.06	13.89	0.0954
9	11.25	35.00	39.36	44.32	0.05	10.05	13.73	0.0951
10	11.25	35.00	38.55	45.00	0.05	10.05	13.88	0.0952

Table 6.10: Optimal condition based on the second criterion

Number	S	$P_2$	$P_3$	$P_4$	f	H	Tr	Wr
1	9.69	34.71	40.00	40.00	0.05	9.22	12.33	0.0700
2	9.45	34.10	40.00	40.00	0.05	9.10	12.22	0.0700
3	9.72	34.80	39.72	40.09	0.05	9.24	12.37	0.0700
4	9.75	34.87	39.2	40.00	0.05	9.24	12.37	0.0700
5	9.72	34.82	37.91	40.00	0.05	9.20	12.36	0.0700
6	9.72	34.97	38.51	40.00	0.05	9.22	12.38	0.0695
7	9.6	34.46	37.96	40.00	0.05	9.13	12.28	0.0700
8	9.75	34.93	38.72	40.00	0.05	9.22	12.38	0.0700
9	9.69	34.75	37.48	40.00	0.05	9.18	12.34	0.0700
10	9.66	34.65	37.52	40.00	0.05	9.16	12.32	0.0700

In terms of the comparison between the results of the first and second criteria, it is clear that a 12.33% decrease of wall thickness reduction and a 26.55% decrease of wrinkle height could be achieved, if the required bulge height is reduced by 8.53%. For both criteria, it was found that the coefficient of friction should be chosen at a minimum value. Therefore, great attention should be given to lubrication of the system and the degree of finish of both the die and the tubes.

The graphical optimizations shown in figures 6.4, 6.5 allow visual assessment of the optimum result values. The blank areas on the overlay plots represent the values that do not meet the proposed criteria. For each response, lower and upper limits were chosen according to the optimization results tables 6.9- 6.10. The upper and lower limits of the responses for both criteria are shown in table 6.11.

Table 6.11: Upper and lower limits for the responses in the two criteria

Criterion No.	Bulge height [mm]	Thickness reduction [%]	Wrinkle height [mm]
1	10.04- 10.08	13.68- 13.90	0.0946- 0.0966
2	9.10- 9.28	12.20- 12.38	0.0690- 0.0700

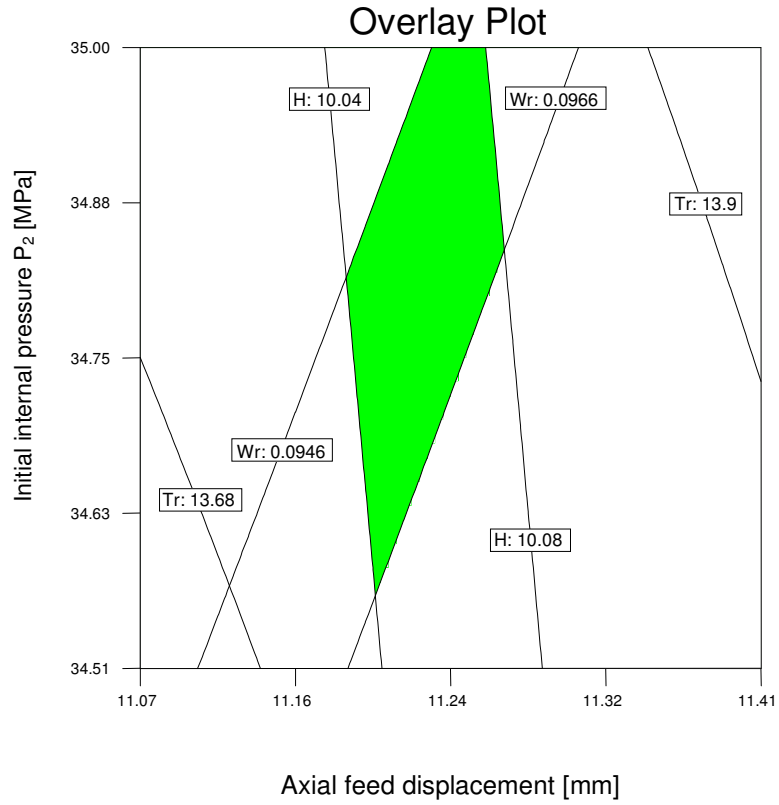


Figure 6.4: Graphical optimization of the first criterion.

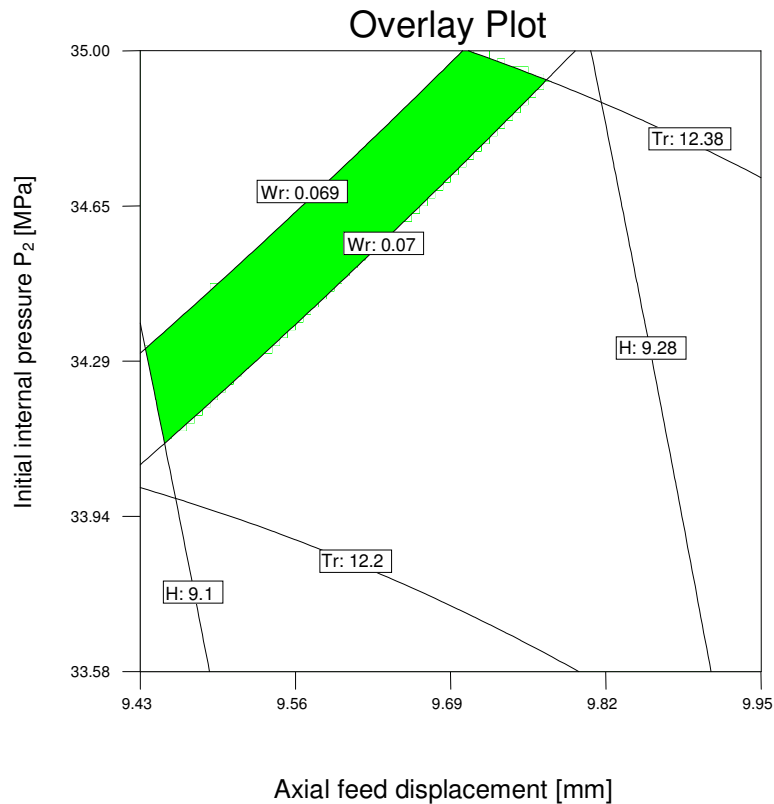


Figure 6.5: Graphical optimization of the second criterion.

Numerical simulations were performed using the optimized conditions for both criteria to compare the numerical results with the predicted ones in table 6.12. From the comparison, it is shown that the optimized results are valid, as the percentages of error are all within the range of acceptability.

Table 6.12: Numerical validation of the optimization results.

Criterion. No	S [mm]	P <sub>2</sub> [MPa]	P <sub>3</sub> [MPa]	P <sub>4</sub> [MPa]	f		Hp [mm]	Tr [%]	Wr [mm]
1	11.25	35	39.99	45	0.05	Numerical	10.15	14.11	0.1058
						Predicted	10.086	13.89	0.095
						Error [%]	0.624	1.557	9.912
2	9.69	34.71	40.00	40.00	0.05	Numerical	9.278	12.82	0.0715
						Predicted	9.22	12.33	0.0700
						Error [%]	0.593	3.791	2.137

#### 6.4. Multi-response optimization in T-type bi-layered tube hydroforming

Based on the response surface models constructed in section 5.4.3 and section 5.4.4 that describe the effects of the geometrical factors and the process parameters respectively on the T-shape bi-layered hydroformed part, multi-response optimization studies were conducted by means of the desirability approach function of the Design-expert V7 software.

##### 6.4.1. Geometrical factors optimization in T-type bi-layered tube hydroforming

This section of the study aims to find the optimal geometrical factors for the hydroforming of bi-layered T-shape junctions that connect between specified bi-layered tubes. The values of the tube diameter (D) and the thicknesses of the two layers ( $t_2$  and  $t_1$ ) of the tubular blank, are the same as the tubes geometry used in the experimental part of this study section 3.3, while both the initial tube length (L) and the die corner radius (r) were varied throughout this study. Two optimization criteria were investigated: in the first one (Table. 6.13), the highest bulge is chosen as the main objective, while minimizing wall thickness reduction within the accepted range was assigned to be of minor importance. On the other hand, in the second criterion table 6.14, equal importance was given to both objectives (i.e.: maximizing bulge height and minimizing wall thickness reduction). The required goal, the lower and upper limits, and the importance, for each response and factor for the two criteria are illustrated in tables 6.13- 6.14.

Table 6.13: The first criterion of numerical optimization

Name	Goal	Lower Limit	Upper Limit	Importance
L	Is in range	80	160	3
r	Is in range	1	5	3
D	Is equal to 24.00	20	28	3
$t_1$	Is equal to 1.00	0.6	1.2	3
$t_2$	Is equal to 0.85	0.6	1.2	3
H	Maximize	3.13	15.26	5
Tr	Minimize	8.012	20	1

Table 6.14: The second criterion of numerical optimization

Name	Goal	Lower Limit	Upper Limit	Importance
L	Is in range	80	160	3
r	Is in range	1	5	3
D	Is equal to 24.00	20	28	3
t <sub>1</sub>	Is equal to 1.00	0.6	1.2	3
t <sub>2</sub>	Is equal to 0.85	0.6	1.2	3
H	Maximize	3.13	15.26	3
Tr	Minimize	8.012	20	3

The optimal geometrical factors in relation to the first and second criteria are listed in tables 6.15- 6.16. It can be seen that for both cases the shortest tube length (L= 80 mm) is required, while varying die corner radius could influence the trade-off between the objectives of bulge height increase and wall thickness uniformity. A maximum die corner radius (5 mm) was found to meet the objectives of the first criterion, in which lesser importance was given to the wall thickness uniformity objective, while a smaller die corner radius (3.72- 3.89 mm) was assigned when wall thickness uniformity (second criterion) was given more importance. A comparison of the optimum results of the first and second criteria shows that a die corner radius change can cause 4.13% better wall thickness uniformity for the hydroformed part, but would result in 2.6% less bulge height.

Table 6.15: Optimal conditions based on the first criterion

No	L	r	D	t <sub>1</sub>	t <sub>2</sub>	H	Tr
1	80	5	24	1	0.85	11.933	18.445
2	80	4.67	24	1	0.85	11.864	18.241
3	80	4.58	24	1	0.85	11.843	18.186

Table 6.16: Optimal conditions based on the second criterion

Number	L	r	D	t <sub>1</sub>	t <sub>2</sub>	H	Tr
1	80	3.75	24	1	0.85	11.623	17.683
2	80	3.77	24	1	0.85	11.630	17.696
3	80	3.72	24	1	0.85	11.614	17.664
4	80	3.66	24	1	0.85	11.597	17.631
5	80	3.89	24	1	0.85	11.664	17.766

For each response, the lower and upper limits were chosen according to the optimization results in tables 6.15- 6.16. The upper and lower limits of both responses for the studied criteria were shown in table 6.17. Overlay plots figures 6.6- 6.7 show the regions of the

optimal working conditions based on the first and second criterion respectively. The blank areas on the overlay plots represent the values that do not meet the proposed criteria.

Table 6.17: Upper and lower limits for the responses in the studied criteria.

Criterion No.	Bulge height [mm]	Thickness reduction [%]
1	11.843- 11.933	18.186– 18.445
2	11.597- 11.664	17.631– 17.766

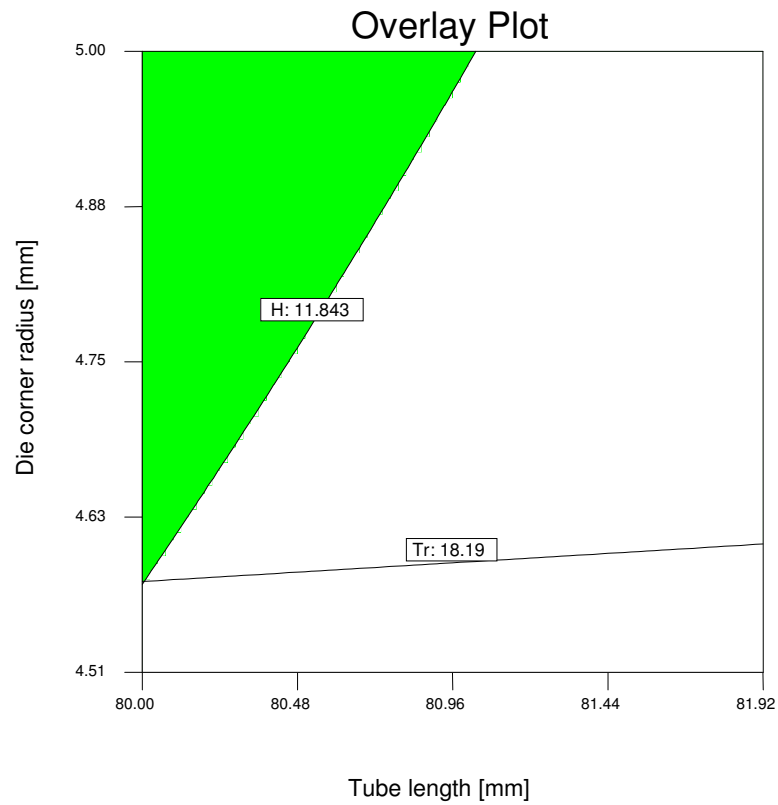


Figure 6.6: Graphical optimization of the first criterion

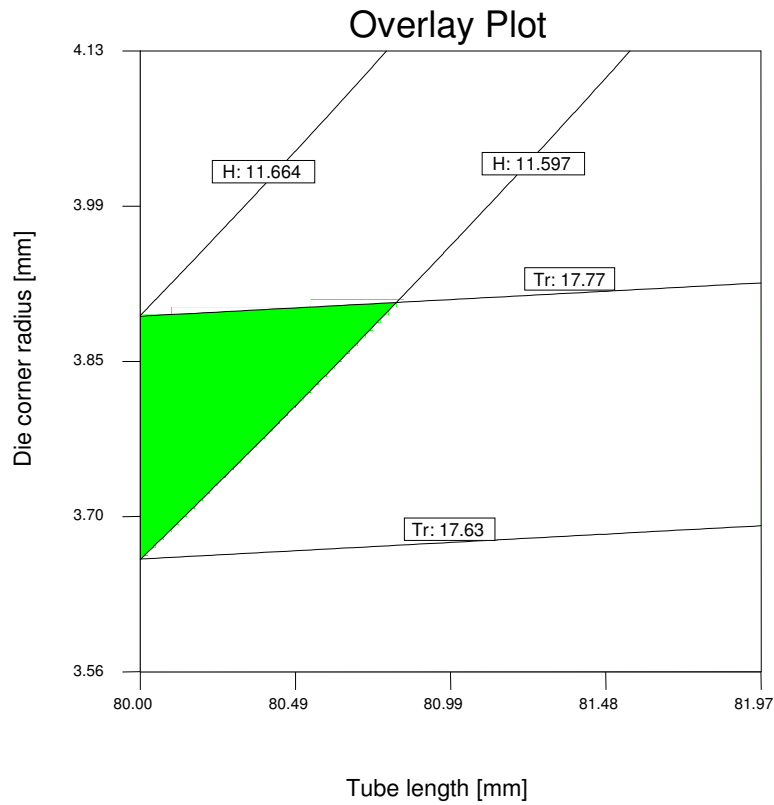


Figure 6.7: Graphical optimization of the second criterion

Numerical simulations were conducted using optimized conditions for both criteria in order to compare the numerical results with the predicted ones. It is apparent from table 6.18 that the optimized results are valid as the percentages of error are all within the range of acceptability.

Table 6.18: Confirmations experiments

Criterion. No	L [mm]	r [mm]	D [mm]	t <sub>1</sub> [mm]	t <sub>2</sub> [mm]		H [mm]	Tr [%]
1	80	5	24	1	0.85	Predicted	11.93	18.44
						Numerical	12.38	17.04
						Error [%]	+3.61	-8.22
2	80	3.75	24	1	0.85	Predicted	11.62	17.68
						Numerical	12.06	16.35
						Error [%]	+3.59	-8.15

#### 6.4.2. Process parameters optimization in T-type bi-layered tube hydroforming

Optimization of the process parameters of the T-type bi-layered tube hydroforming process was carried out using two different criteria in which maximum bulge height and minimum wall thickness reduction are the objectives. In the first criterion table 6.19, a maximum level of importance was given for the bulge height response while a minimum level of importance was assigned to the wall thickness reduction response. However, both objectives were assigned the same level of importance in the second criterion table. 6.20. The required goal, lower and upper limits, and the importance, for each response and factor in the two criteria are illustrated in tables 6.19- 6.20.

Table 6.19: The first criterion of numerical optimization.

Name	Goal	Lower Limit	Upper Limit	Importance
S	Is in range	6	15	3
P <sub>2</sub>	Is in range	15	35	3
P <sub>3</sub>	Is in range	35	40	3
P <sub>4</sub>	Is in range	40	45	3
f	Is in range	0.05	0.15	3
H	Maximize	4.961	12	5
Tr	Minimize	5	20	1

Table 6.20: The second criterion of numerical optimization.

Name	Goal	Lower Limit	Upper Limit	Importance
S	Is in range	6	15	3
P <sub>2</sub>	Is in range	15	35	3
P <sub>3</sub>	Is in range	35	40	3
P <sub>4</sub>	Is in range	40	45	3
f	Is in range	0.05	0.15	3
H	Maximize	4.961	12	3
Tr	Minimize	5	20	3

The optimal process parameters in relation to both criteria are listed in tables 6.21, 6.22. Optimization on the basis of the first criterion was found to achieve a maximum bulge height of 11.35 mm with a wall thickness reduction of 11.73%. On the other hand, best desirability according to the second criterion was achieved with a bulge height of 10.98 mm, and with a wall thickness reduction percentage of 9.70%. For both criteria, the biggest axial feed (S= 15 mm) and the lowest coefficient of friction (f= 0.05) were applied. For the

first criterion, internal pressure coordinates are all set at high levels. On the other hand, keeping the internal pressure coordinates ( $P_3$ ,  $P_4$ ) at low levels is preferred in the case of the second criterion as it maintains better wall thickness uniformity. A comparison of the two criteria shows that 17.3% less wall thickness reduction can be gained together with a 3.26% bulge height decrease.

Table 6.21: Optimal conditions based on the first criterion

Number	S	$P_2$	$P_3$	$P_4$	f	H	Tr
1	15.00	34.62	39.52	45.00	0.05	11.346	11.73
2	15.00	34.48	39.43	45.00	0.05	11.344	11.73
3	15.00	35.00	38.94	44.60	0.05	11.326	11.51
4	15.00	34.70	39.63	45.00	0.05	11.337	11.74
5	15.00	35.00	38.92	44.57	0.05	11.324	11.50
6	15.00	35.00	40.00	45.00	0.05	11.337	11.77
7	15.00	35.00	38.49	44.57	0.05	11.322	11.47
8	15.00	35.00	38.82	44.52	0.05	11.321	11.48
9	14.97	34.31	40.00	45.00	0.05	11.331	11.78
10	15.00	35.00	36.84	44.90	0.05	11.315	11.49

Table 6.22: Optimal conditions based on the second criterion

Number	S	$P_2$	$P_3$	$P_4$	f	H	Tr
1	15.00	35.00	35.63	40.02	0.05	10.985	9.70
2	15.00	35.00	36.69	40.12	0.05	11.022	9.80
3	15.00	33.19	35.23	40.00	0.05	10.944	9.70
4	14.94	34.18	35.00	40.00	0.05	10.924	9.68
5	15.00	33.98	35.00	40.25	0.05	10.956	9.74
6	15.00	34.45	35.62	40.00	0.05	10.941	9.72
7	15.00	34.52	38.82	40.00	0.05	11.044	9.93
8	15.00	35.00	35.61	40.92	0.05	11.038	9.96
9	14.97	34.99	39.60	40.00	0.05	11.042	9.99
10	15.00	34.71	39.75	40.00	0.05	11.047	10.00

The graphical optimization enables a visual assessment of the areas representing the values where the proposed criteria meet the requirements. Lower and upper limits were chosen according to the numerical optimization results and are listed in table 6.23. Overlay plots figures 6.8- 6.9 show the region representing the values of optimal working conditions based on the first and second criterion respectively. The blank areas on the overlay plots represent values that do not meet the proposed criteria.

Table 6.23: Upper and lower limits for the responses in the studied criteria.

Criterion No.	Bulge height [mm]	Thickness reduction [%]
1	11.315- 11.346	11.47– 11.77
2	10.924- 11.047	9.68– 10.00

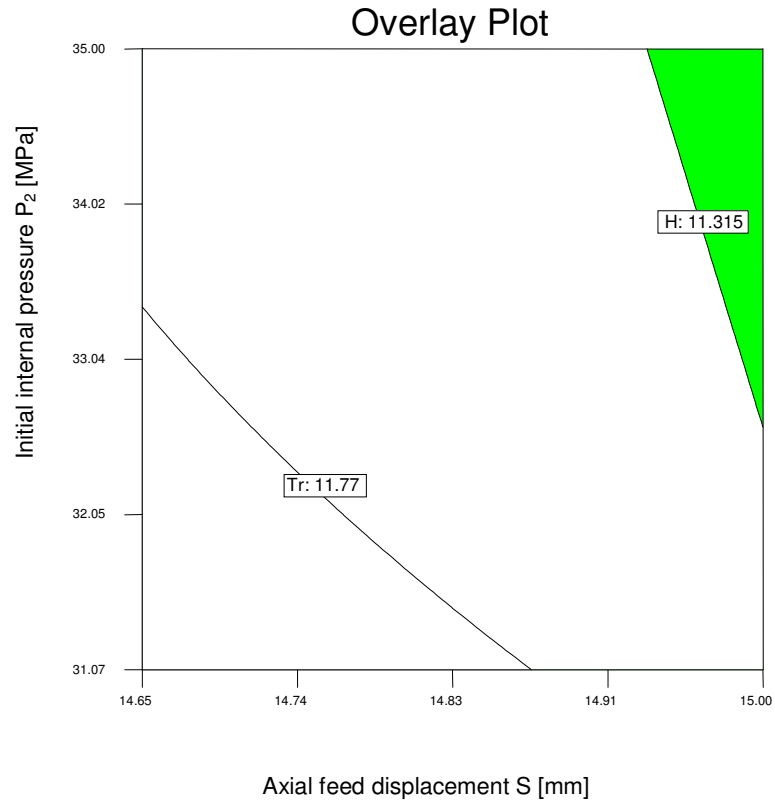


Figure 6.8: Graphical optimization of the first criterion

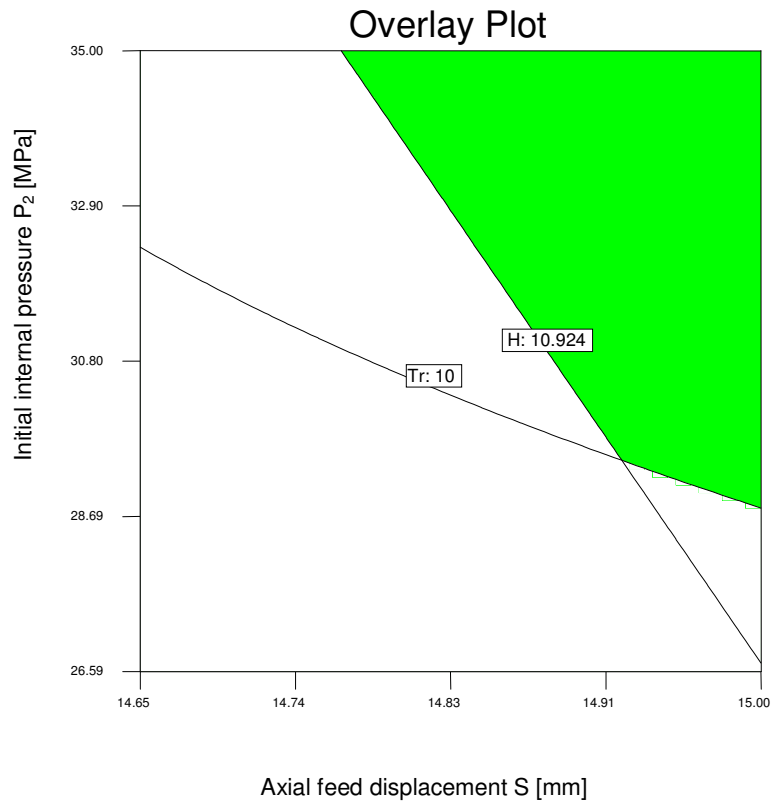


Figure 6.9: Graphical optimization of the second criterion

A comparison of the evaluated and numerical outputs for the optimal process parameters according to the studied criteria shows that the optimized results are valid, as the percentages of error are all within the acceptable range of agreement table 6.24.

Table 6.24: Confirmation experiments.

Criterion. No	S	P <sub>2</sub>	P <sub>3</sub>	P <sub>4</sub>	f	Hp [mm]		Tr [%]	
						Predicted	Numerical	Predicted	Numerical
1	15.00	34.62	39.52	45.00	0.05	Predicted	11.35	Predicted	11.73
						Numerical	11.59	Numerical	11.78
						Error [%]	2.07	Error [%]	0.42
2	15.00	35.00	35.63	40.02	0.05	Predicted	10.98	Predicted	9.70
						Numerical	11.25	Numerical	10.47
						Error [%]	2.40	Error [%]	7.35

## 6.5. Investigation of the process operating cost minimization

### 6.5.1. Evaluation of the process operating cost function

In order to identify the potential for cost reduction of the process design, a mathematical model was constructed for the hydroforming operating cost as a function of the design parameters based on the operating cost elements mentioned in table 6.25. The power source for the hydraulic system, described in section 3.2, is a variable displacement piston pump driven by a 7.5 kW electric motor. The material and lubrication cost were found to be dependent on the tube length (L). As a result, the operating cost per hydroformed part can be calculated from equation 6.6. The proposed function doesn't include the overhead and labour cost.

Table 6.25: Operating cost of bi-layered tube hydroforming process

Element of cost [Euro/ part]	Calculation	Cost [Euro/part]
Electricity Consumption	Operating power [kW] × (t [sec]/ 3600)× Price of 1 kWh	= 0.00257
Material cost	(unit prices of brass and copper tubes) × Tube length [mm]	= 0.02416 × L
Lubrication	(lubrication unit price) × Tube length	= 1.2 × 10 <sup>-4</sup> × L

$$\text{Cost} = 0.00257 + 0.02428 \times L \text{ [Euro/part]} \quad (6.6)$$

### 6.5.2. Operating cost minimization

Based on the proposed function, operating cost was requested to be minimized for the studied optimization criteria in sections 6.3, 6.4. However, no operating cost reduction can be achieved in the process parameters optimization studies sections 6.3.2, 6.4.2 as the proposed function is not process parameters dependent. On the other hand, operating cost was demanded to be minimized in the geometrical factors optimization studies sections 6.3.1, 6.4.1 seeking the same objectives of the investigated criteria for both X-type and T-type bi-layered tube hydroforming as illustrated in tables 6.26, 6.27.

Table 6.26: Operating cost consideration for X-type bi-layered tube hydroforming optimization criteria

Name	First Criterion		Second Criterion	
	Goal	Importance	Goal	Importance
L	Is in range	3	Is in range	3
r	Is in range	3	Is in range	3
D	Is equal to 24.00	3	Is equal to 24.00	3
t <sub>1</sub>	Is equal to 1.00	3	Is equal to 1.00	3
t <sub>2</sub>	Is equal to 0.85	3	Is equal to 0.85	3
H	Maximize	5	Maximize	3
Tr	Minimize	1	Minimize	3
Wr	Minimize	1	Minimize	3
Cost	Minimize	3	Minimize	3

Table 6.27: Operating cost consideration for T-type bi-layered tube hydroforming optimization criteria

Name	First Criterion		Second Criterion	
	Goal	Importance	Goal	Importance
L	Is in range	3	Is in range	3
r	Is in range	3	Is in range	3
D	Is equal to 24.00	3	Is equal to 24.00	3
t <sub>1</sub>	Is equal to 1.00	3	Is equal to 1.00	3
t <sub>2</sub>	Is equal to 0.85	3	Is equal to 0.85	3
H	Maximize	5	Maximize	3
Tr	Minimize	1	Minimize	3
Cost	Minimize	3	Minimize	3

Based on the X-type bi-layered tube hydroforming optimization criteria implemented in table 6.26, optimization results are listed in tables 6.28, 6.29 for the first and second criteria respectively. Optimal conditions can be visually determined from figures 6.10, 6.11. The blank areas on the overlay plots represent the values that do not meet the proposed criteria. Furthermore, to check the validity of the obtained results, numerical simulations were conducted applying the optimum geometrical factors. A comparison between the predicted and numerical results shows an acceptable level of agreement table 6.30.

Table 6.28: Optimal condition based on the first criterion after cost reduction

Number	L	r	D	t <sub>1</sub>	t <sub>2</sub>	H	Tr	Wr	Cost
1	98.95	5	24	1	0.85	9.778	19.26	0.0984	2.405
2	99.53	5	24	1	0.85	9.746	19.26	0.0972	2.419
3	101.03	5	24	1	0.85	9.663	19.26	0.0943	2.456

Table 6.29: Optimal condition based on the second criterion after cost reduction

Number	L	r	D	t <sub>1</sub>	t <sub>2</sub>	H	Tr	Wr	Cost
1	103.58	4.33	24	1	0.85	9.331	17.87	0.0935	2.517

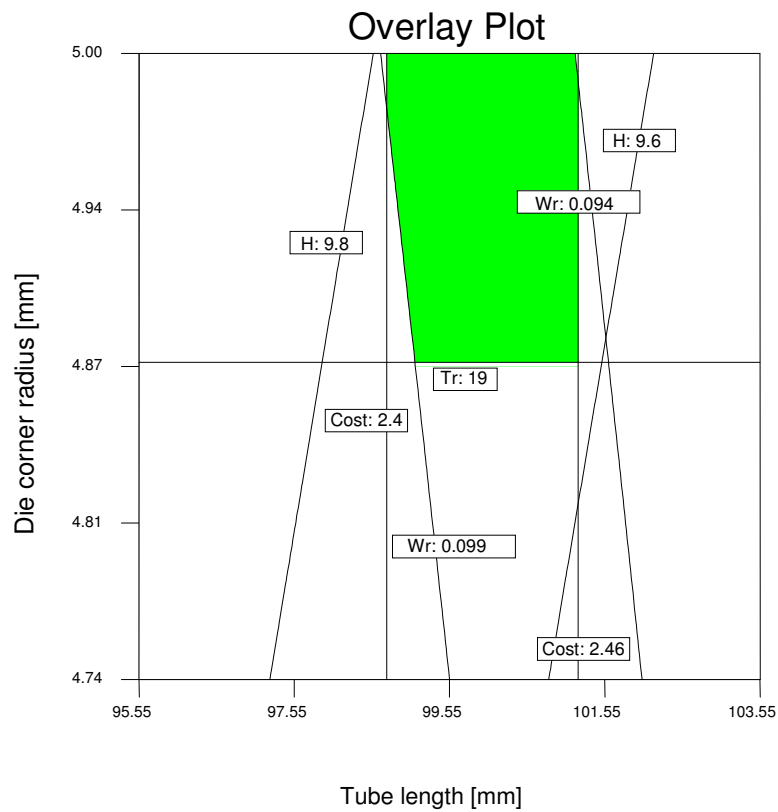


Figure 6.10: Graphical investigation of cost reduction in the first criterion of the geometrical factors optimization (X-type).

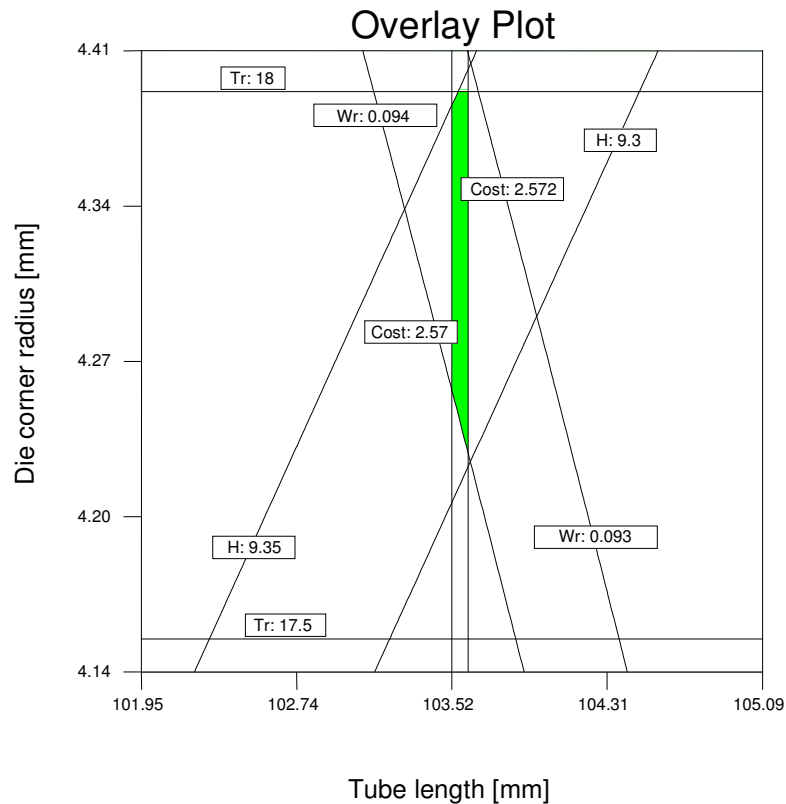


Figure 6.11: Graphical investigation of cost reduction in the second criterion of the geometrical factors optimization (X-type).

Table 6.30: Numerical validation of the optimization results

Criterion. No	L [mm]	r [mm]	D [mm]	t <sub>1</sub> [mm]	t <sub>2</sub> [mm]		H [mm]	Tr [%]	Wr [mm]
1	98.95	5	24	1	0.85	Numerical	10.160	16.81	0.091
						Predicted	9.779	19.269	0.0984
						Error [%]	-3.900	12.75	7.51
2	103.58	4.33	24	1	0.85	Numerical	9.76	16.61	0.085
						Predicted	9.331	17.87	0.0935
						Error [%]	4.392	-7.610	-9.472

An investigation of the cost reduction potential in the X-shape bi-layered tube hydroforming process design, and effect of cost minimization on the hydroformed part specifications (bulge height, wall thickness reduction, and wrinkle height) can be carried out, by comparing the optimization results obtained without cost reduction consideration in tables. 6.3, 6.4, and the optimization results listed in tables 6.28, 6.29 after the process

operating cost minimization. According to the first criterion, by comparing the operating cost before and after the cost minimization in table 6.31, it was found that a small cost reduction of almost 1.17% would be possible with a 0.66% and a 2.4% increase of the bulge height and wrinkle height respectively. In relation to the second criterion, a considerable cost reduction of almost 24% could be achieved, but this would mean a 20%, 10.46%, 31.76% increase of the bulge height, wall thickness reduction, and wrinkle height respectively for the hydroformed part. However, thickness reduction and wrinkle height values stayed within accepted levels.

Table 6.31: Effect of cost minimization on the optimum outputs in the optimization criteria for X-type bi-layered tube hydroforming

Cost consideration	First criterion				Second criterion			
	H	Tr	Wr	Cost	H	Tr	Wr	Cost
None	9.713	19.26	0.0960	2.433	7.450	16.00	0.0638	3.294
Minimize	9.778	19.26	0.0984	2.405	9.331	17.87	0.0935	2.517

For the T-type bi-layered tube hydroforming, operating cost possibilities were discussed according to the criteria implemented in table 6.27. However, operating cost reduction possibilities were found not feasible in the studied ranges table 6.32 as the operating cost of the optimum solutions before the cost minimization tables 6.15, 6.16 were already set at their minimum (smallest tube length  $L=80$  mm was preferred).

Table 6.32: Effect of cost minimization on the optimum outputs in the optimization criteria of T-type bi-layered tube hydroforming

Cost consideration	First criterion			Second criterion		
	H	Tr	Cost	H	Tr	Cost
None	11.933	18.445	1.945	11.623	17.683	1.945
Minimize	11.933	18.445	1.945	11.623	17.683	1.945

## 6.6. Bi-layered tube hydroforming optimization using ANSYS optimizer

### 6.6.1. Optimization method overview

Iterative optimization algorithms based on the minimisation of an objective function are interfaced with numerical simulations in the ANSYS program. ANSYS performs a series of analysis-evaluation-modification cycles. An analysis of the initial design is performed, the

results are evaluated against specified design criteria, and the design is modified as required. This process is repeated until all specified criteria are met. In this section of the study, a sub-problem approximation method of the ANSYS optimization routine, using ANSYS Parametric Design Language, is introduced and used for the bi-layered tube hydroforming process optimization.

Using this method [124], three types of variables characterizing the design process are used:

- Design variables (DVs) are varied to achieve the optimum design. Upper and lower limits are specified to serve as “constraints” on the design variables. These limits define the range of variation for the DV.
- State variables (SVs) are quantities that constrain the design. The state variables can also be referred to as dependent variables.
- Objective function is the dependent variable that it is minimized. It is a function of the DVs (that is, changing the values of the DVs changes the value of the objective function). In this method, only one objective function in a design optimization problem can be defined.

However, a typical optimization problem can be defined as shown in equations 6.7- 6.10.

Minimize the objective function

$$f = f(x) \tag{6.7}$$

Subject to design constraints:

$$g_i(x) \leq \overline{g_i} \quad (i= 1, 2, 3 \dots m_1) \tag{6.8}$$

$$\underline{h_i} \leq h_i(x) \quad (i= 1, 2, 3 \dots m_2) \tag{6.9}$$

$$\underline{w_i} \leq w_i(x) \leq \overline{w_i} \quad (i= 1, 2, 3 \dots m_3) \tag{6.10}$$

Where:  $f$  is the objective function to be minimized, and  $g_i$ ,  $h_i$ ,  $w_i$  are classed as state variables with underbars and overbars representing lower and upper limits respectively. While,  $m_1+m_2+m_3$  are the number of state variables constraints with various upper and lower limit values.

The sub-problem approximation method can be described as an advanced zero-order method [124] in that it requires only the values of the dependent variables (objective function and state variables), and not their derivatives. In this method, there are two concepts that play a key role: the use of approximations for the objective function and state variables, and the conversion of the constrained optimization problem to an unconstrained problem. The ANSYS program demonstrates the relationship between the objective function and the design variables by curve fitting. This is carried out by calculating the objective function for several sets of design variables values (that is, for several designs) and performing a least squares fit between the data points. The resulting curve (or surface) is called an approximation. Each optimization loop generates a new data point, and the objective function approximation is updated. Likewise, state variables are approximated in the same manner. An approximation is generated for each state variable and updated at the end of each loop. In equations 6.11- 6.14, both objective function and state variables are replaced by their approximations, represented by the notation.

$$\hat{f}(x) = f(x) + error \quad (6.11)$$

$$\hat{g}(x) = g(x) + error \quad (6.12)$$

$$\hat{h}(x) = h(x) + error \quad (6.13)$$

$$\hat{w}(x) = w(x) + error \quad (6.14)$$

By default, a quadratic plus cross terms fit is used for the objective function, and a quadratic fit is used for the state variables. The State variables and limits on design variables are used to constrain the design. However, the ANSYS program converts the constrained problem in equations 6.11- 6.14 to an unconstrained one because minimization techniques for the latter are more efficient. The conversion is accomplished by adding penalties to the objective function approximation to account for the imposed constraints, leading to the following sub-problem function equation 6.15.

Minimize

$$F(x, p_k) = \hat{f} + f_0 p_k \left[ \sum_{i=1}^n X(x_i) + \sum_{i=1}^{m_1} G(\hat{g}_i) + \sum_{i=1}^{m_2} H(\hat{h}_i) + \sum_{i=1}^{m_3} W(\hat{w}_i) \right] \quad (6.15)$$

In which  $X$  is the penalty function used to enforce design variable constraints; and  $G$ ,  $H$ , and  $W$  are penalty functions for state variable constraints. The reference objective function value,  $f_0$ , is introduced in order to achieve consistent units while  $P_k$  is a response surface parameter that increases with each design iteration. A sequential unconstrained minimization technique (SUMT) is used to solve the unconstrained equation at each design iteration.

At the end of each loop, a check for convergence (or termination) is made. The problem is said to be converged if the current, previous, or best design is feasible and any of the following conditions are satisfied:

- The change in objective function from the best feasible design to the current design is less than the objective function tolerance.
- The change in objective function between the last two designs is less than the objective function tolerance.
- The changes in all design variables from the current design to the best feasible design are less than their respective tolerances.
- The changes in all design variables between the last two designs are less than their respective tolerances.

In this technique, convergence does not necessarily indicate that a true global minimum has been obtained. It only means that one of the four criteria mentioned above has been satisfied. However, only single objective optimization criteria can be studied using this method. In the next sections, the optimized process parameters that achieve a single objective criterion (Maximizing bulge height) for X-shape and T-shape bi-layered tube hydroforming were determined based on this technique. Furthermore, the same criteria will be optimized using the RSM models, and a comparison of both techniques is conducted based on the optimum values resulting from each technique. This is followed by further discussion.

### 6.6.2. Application of the ANSYS optimizer in single objective optimization

In this work, the sub-problem method in the ANSYS Optimizer was employed to optimize the process parameters in both X-shape and T-shape bi-layered tube hydroforming with the target to achieve the highest possible bulge in a defect free product. The single stated objective is related only to the bulge height (OBJ= 40-Bulge height), as minimizing the objective functions means maximizing the bulge height value. While both wall thickness reduction (Tr) and wrinkle height (Wr) were set as state variables (SVs) that should be less than 20% and 0.1 mm respectively. However, the axial feed displacement (S: 6-15 mm), coefficient of friction (f: 0.05- 0.15), and internal pressure coordinates as shown in figure 5.2 (P<sub>2</sub>: 15-35 MPa), (P<sub>3</sub>: 35-40 MPa), and (P<sub>4</sub>: 40-45 MPa) are the ranges of the design variables (DVs).

Application of the proposed method to optimize the process parameters in the X-shape bi-layered tube hydroforming entailed 16 optimization loops to achieve the convergence table 6.33. Loops (1, 5, 7, 9, 11, and 16) presented feasible cases as state variables were still within the accepted ranges, while others were considered not feasible mainly because of the production of unacceptable wrinkles. It has been found that an optimum combination of process parameters occur in the case (11). Convergence has taken place, as the difference of the objective values between the last design (Set 16) and the best design (Set 11) is lower than the objective function tolerance.

Table 6.33: Sub-problem optimization results (X-shape)

		SET 1 (FEASIBLE)	SET 2 (INFEASIBLE)	SET 3 (INFEASIBLE)	SET 4 (INFEASIBLE)
Tr	(SV)	12.4	11.95	12.71	11.54
Wr	(SV)	0.10021	> 0.38035	> 0.12972	> 0.35274
S	(DV)	10.3518	13.6245	11.5614	13.1346
P <sub>2</sub>	(DV)	27	24.1	32.0	26.6
P <sub>3</sub>	(DV)	39.6	36.9	35.0	38.5
P <sub>4</sub>	(DV)	43.3	4.35E-02	4.23E-02	4.04E-02
f	(DV)	0.0850	0.10376	0.0820	0.0847
OBJFUN	(OBJ)	31.017	29.84	30.538	29.935

		SET 5 (FEASIBLE)	SET 6 (INFEASIBLE)	SET 7 (FEASIBLE)	SET 8 (INFEASIBLE)
Tr	(SV)	12.63	13.07	12.97	16.07
Wr	(SV)	0.091213	> 0.13152	0.097055	> 0.35723
S	(DV)	7.0119	12.9483	7.0641	13.8855
P <sub>2</sub>	(DV)	25.6	26.1	30.2	33.5
P <sub>3</sub>	(DV)	39.9	37.4	38.6	39.9
P <sub>4</sub>	(DV)	4.32E-02	4.40E-02	43.0	44.5
f	(DV)	0.0651	0.13364	0.0563	0.0583
OBJFUN	(OBJ)	32.14	30.597	31.863	28.783

		SET 9 (FEASIBLE)	SET 10 (INFEASIBLE)	*SET 11* (FEASIBLE)	SET 12 (INFEASIBLE)
Tr	(SV)	13.47	13.63	13.59	14.1
Wr	(SV)	0.089276	> 0.18814	0.095477	> 0.11145
S	(DV)	10.347	12.3975	11.0223	11.9757
P <sub>2</sub>	(DV)	32.6	34.5	33.1	34.6
P <sub>3</sub>	(DV)	39.9	36.2	39.4	39.3
P <sub>4</sub>	(DV)	43.0	44.5	43.6	44.2
f	(DV)	0.0884	0.0580	0.0812	0.0764
OBJFUN	(OBJ)	30.949	29.556	30.607	30.03

		SET 13 (INFEASIBLE)	SET 14 (INFEASIBLE)	SET 15 (INFEASIBLE)	SET 16 (FEASIBLE)
Tr	(SV)	13.72	>20.13	13.61	13.42
Wr	(SV)	> 0.12033	> 0.40871	> 0.10776	0.10001
S	(DV)	12.0657	13.989	11.6658	11.0853
P <sub>2</sub>	(DV)	33.0	27.8	33.1	32.2
P <sub>3</sub>	(DV)	39.6	38.8	38.7	39.9
P <sub>4</sub>	(DV)	43.9	44.8	44.1	43.4
f	(DV)	0.0810	0.0833	0.0807	0.0810
OBJFUN	(OBJ)	30.141	29.229	30.347	30.609

The T-shape bi-layered tube hydroforming process optimization table 6.34 shows that 10 optimization loops were needed to find the optimum solution that was presented in the last set (set 10). The convergence has been achieved when the difference of the objective values between the two last designs (Sets 9, 10) was found to be lower than the objective function

tolerance. Furthermore, it was noted that all the optimization loops represent feasible cases as the wall thickness reduction was within the accepted range.

Table 6.34: Sub-problem optimization results (T-shape)

		SET 1 (FEASIBLE)	SET 2 (FEASIBLE)	SET 3 (FEASIBLE)	SET 4 (FEASIBLE)	SET 5 (FEASIBLE)
Tr	(SV)	12.671	13.108	13.204	12.944	12.906
S	(DV)	6	10.8381	8.8827	9.1254	7.3581
P <sub>2</sub>	(DV)	15	24.00	32.0	26.6	25.6
P <sub>3</sub>	(DV)	37.5	36.9	35.0	38.5	39.9
P <sub>4</sub>	(DV)	42.5	43.5	42.3	40.4	43.2
f	(DV)	0.1	0.13472	0.11179	0.12927	6.12E-02
OBJFUN	(OBJ)	34.394	32.132	32.74	33.03	32.709

		SET 6 (FEASIBLE)	SET 7 (FEASIBLE)	SET 8 (FEASIBLE)	SET 9 (FEASIBLE)	*SET 10* (FEASIBLE)
Tr	(SV)	12.188	12.563	10.756	11.219	11.522
S	(DV)	13.5279	6.5703	14.6448	14.8947	14.9598
P <sub>2</sub>	(DV)	2.61E-02	3.02E-02	1.73E-02	3.01E-02	3.39E-02
P <sub>3</sub>	(DV)	3.74E-02	3.86E-02	3.56E-02	3.52E-02	3.50E-02
P <sub>4</sub>	(DV)	4.40E-02	4.30E-02	4.12E-02	4.42E-02	4.48E-02
f	(DV)	0.1272	6.18E-02	6.84E-02	5.50E-02	5.13E-02
OBJFUN	(OBJ)	30.6	33.279	29.595	28.744	28.54

From tables 6.33, 6.34, it can be seen that a maximum bulge height of 9.391 mm and 11.46 mm was protruded for the X-shape and T-shape bi-layered hydroforming respectively while keeping state variables within the accepted ranges. In the next section, the same optimization criteria will be implemented using the response surface models and the desirability approach.

### 6.6.3. Application of the RSM based technique in single objective optimization

The single objective optimization criteria that were studied by means of the ANSYS optimizer in the last section will be implemented using the desirability approach based on the RSM models that describe the effects of the process parameters on the process output in sections 5.4.2, 5.4.4. Bulge height was set to be maximized while keeping other inputs and outputs within the acceptable ranges as mentioned in section 6.6.2. Optimization results are listed in tables 6.35, 6.36 for the X-shape and T-shape bi-layered tube hydroforming, respectively. It can be noted that a minimum coefficient of friction and high levels of pressure coordinates promote maximum bulge height for both X-shape and T-shape protrusions. A maximum axial feed was required in T-shape hydroforming, while an axial

feed displacement of 11.43 mm was found most appropriate for the X-shape hydroforming as this keeps the wrinkle height and wall thickness reductions within acceptable levels.

Table 6.35: Single optimization results (X-shape)

Number	S	P <sub>2</sub>	P <sub>3</sub>	P <sub>4</sub>	f	H	Tr	Wr
1	11.43	35.00	40.00	44.77	0.05	10.16	13.96	0.0999
2	11.43	35.00	40.00	44.68	0.05	10.16	13.94	0.1000
3	11.43	35.00	39.04	44.98	0.05	10.15	14.01	0.1000
4	11.43	35.00	39.53	44.06	0.05	10.13	13.80	0.1000
5	11.40	34.94	40.00	44.25	0.05	10.13	13.81	0.0995
6	11.43	34.98	40.00	44.03	0.05	10.12	13.78	0.1000
7	11.43	34.99	39.96	43.47	0.05	10.12	13.67	0.1000
8	11.43	34.99	40.00	43.41	0.05	10.11	13.65	0.0999
9	11.43	35.00	37.56	44.85	0.05	10.11	13.98	0.1000
10	11.43	35.00	38.31	44.15	0.05	10.11	13.82	0.1000

Table 6.36: Single optimization results (T-shape)

Number	S	P <sub>2</sub>	P <sub>3</sub>	P <sub>4</sub>	f	H	Tr
1	15.00	35.00	39.63	45.00	0.05	11.35	11.738
2	15.00	34.71	39.68	45.00	0.05	11.35	11.745
3	15.00	34.48	39.99	44.99	0.05	11.34	11.770
4	15.00	35.00	39.39	45.00	0.05	11.34	11.725
5	15.00	35.00	39.65	44.60	0.05	11.33	11.571
6	15.00	35.00	40.00	44.60	0.05	11.32	11.595
7	15.00	35.00	39.85	44.52	0.05	11.32	11.550
8	15.00	35.00	39.08	44.32	0.05	11.31	11.412
9	15.00	32.32	38.18	45.00	0.05	11.31	11.689
10	15.00	32.04	38.29	45.00	0.05	11.31	11.704

To check the validity of the proposed optimum results, numerical simulations were conducted using the optimum process parameters in the finite element modelling. Comparing the predicted values with the numerical values shows a high level of agreement between both kinds of results table 6.37.

Table 6.37: Confirmation experiments.

Modelling type	S	P <sub>2</sub>	P <sub>3</sub>	P <sub>4</sub>	f		H [mm]	Tr [%]	Wr [mm]
X- shape	11.43	35.00	40.00	44.77	0.05	Predicted	10.16	13.96	0.0999
						Numerical	10.18	13.79	0.0997
						Error [%]	0.196	-1.233	-0.200
T- shape	15.00	35.00	39.63	45.00	0.05	Predicted	11.35	11.738	N/A
						Numerical	11.61	11.870	N/A
						Error [%]	2.239	1.112	N/A

#### 6.6.4. Comparison of ANSYS optimization technique and RSM based optimization method for bi-layered tube hydroforming design

In order to compare the two optimization techniques, a comparison of the results of each technique is presented in table 6.38. It can be seen that an increase of 7.67% and 1.29% in the resultant X-shape and T-shape bulges height respectively was gained when using RSM based method rather than the ANSYS optimizer. Wall thickness reduction and wrinkle height values were kept within the accepted ranges. The advantage of the RSM optimization method is the low computing time required. Furthermore, the desirability approach that was used based on the RSM models calculates the desirability function in the whole design space and finds the global optimum with the maximum desirability. On the other hand, the ANSYS optimizer shows a local optimum, and different optima that can be obtained as a result of different initial values (starting points) [125, 126]. Moreover, the desirability function used in the RSM optimization method is capable of involving several objectives with different weighting and importance for each one, while only single objective criteria can be optimized using the ANSYS optimizer. Therefore, the optimum design parameters that were determined using the RSM optimization technique are recommended. However, the accuracy of the recommended optimization method depends on the accuracy of the constructed RSM models.

Table 6.38: A comparison of sub-problem and RSM optimization results

Modelling type	Optimization technique	S	P <sub>2</sub>	P <sub>3</sub>	P <sub>4</sub>	f	H	Tr	Wr
X- shape	RSM	11.43	35.00	40.00	45.00	0.050	10.18	13.79	0.0999
	ANSYS	11.01	33.10	39.40	43.60	0.081	9.39	13.59	0.0955
T- shape	RSM	15.00	35.00	39.63	45.00	0.050	11.61	11.870	N/A
	ANSYS	14.94	33.95	35.04	44.79	0.051	11.46	11.552	N/A

### 6.7. Summary

Based on the constructed RSM models in chapter 5, multi-objective optimization studies were conducted to find the best combination of each of the process parameters and geometrical factors according to different proposed criteria in X-shape and T-shape bi-layered tube hydroforming. Comparing the predicted and numerical results at optimum conditions indicated that the optimized results are valid as the percentages error are all within an acceptable level of agreement. The cost reduction potential was investigated in the studied optimization criteria, based on a proposed function of the operating cost. A comparison of the RSM modelling optimization technique and the iterative optimization algorithm of the ANSYS optimizer was carried out. The RSM modelling optimization method was recommended as it achieved better results.

## CHAPTER SEVEN

### CONCLUSIONS AND RECOMMENDATIONS FOR FUTURE WORK

#### 7.1. Conclusions

The following conclusions were drawn from the present study:

- 1- Finite element models were built for X-type and T-type bi-layered tube hydroforming processes.
- 2- Numerical models of bi-layered tube hydroforming were found validated by the comparison with the experimental results.
- 3- Single and bi-layered tube hydroforming processes were compared to each other using finite element method. Application of internal pressure in advance of the axial feed was found to improve the formability for both systems.
- 4- Process outputs were modelled as functions of each of the geometrical factors and process parameters. The resultant models were found adequate. From these models, a quick estimation of the process outputs can be obtained. In addition, the main effects of the studied parameters and their interactions on the process output were discussed and graphically displayed.
- 5- The best combinations of each of the geometrical factors and process parameters were achieved according to different multi-objectives criteria in X- type and T- type bi-layered tube hydroforming. The optimized results were found valid when comparing numerical results with the predicted ones
- 6- A comparison of the RSM modelling optimization technique and the iterative optimization algorithm of the ANSYS optimizer was carried out. The RSM optimization method was recommended as it achieved better results.

#### 7.2. Future work

- Production of bi-layered tubular parts using the tube hydroforming process with a liquid media was investigated in the present study. However, it is a recommendation for future work that formation of bi-layered tubular parts using a solid medium bulge be studied. A comparison of the two methods would be of great value for manufacturers.

- In the present research study, the bi-layered tube hydroforming process was investigated in X-shape and T-shape dies. However, other tubular shapes should be investigated in the future (Y-shape is one example).
- The inner and outer layers in the current study were made of copper and brass respectively. Brass was chosen as it protects copper tubes because of its application in fittings and tools near explosive gases, as it is a spark-resistant material [103, 104], as well as being available locally. However, in future work, different combinations of materials should be studied. CRA-lined tubing is increasingly applied in oil production, nuclear power plants, and the refining industry.
- The tube hydroforming machine used in the present study has limited capabilities, and does not allow hydroforming of strong materials. The machine could be re-designed so that higher internal pressure and axial loads can be applied.
- The current machine controls do not allow a predefined loading path to be applied (internal pressure values with respect to the axial feed). A new control system that does allow this is recommended for future work.

## APPENDIX. A

### A.1. Box Behnken Design designing for three factors:

The following steps are carried out to create a mathematical model of the response Y as a function of three factors ( $X_1$ ,  $X_2$ , and  $X_3$ ) using an integration of finite element modelling and DOE technique.

#### 1. Identifying the factors which have significant effect on the response

These factors can often be defined from the literature or by conducting a preliminary study (i.e. screening study). Subsequently, factors limits are selected based on trial and error experience.

#### 2. Design matrix development

The matrix depends on the type of RSM design selected. For BBD design type, the design matrix in coded values (-1, 0, +1) is shown in table a.1.

Table A.1: Design matrix for BBD, coded values.

Run No.	$X_1$	$X_2$	$X_3$
1	-1	-1	0
2	1	-1	0
3	-1	1	0
4	1	1	0
5	-1	0	-1
6	1	0	-1
7	-1	0	1
8	1	0	1
9	0	-1	-1
10	0	1	-1
11	0	-1	1
12	0	1	1
13	0	0	0
14	0	0	0
15	0	0	0
16	0	0	0
17	0	0	0

#### 3. Performing the experiments (numerical simulations)

Based on the finite element modelling, numerical simulations were conducted and responses were calculated for each case stated in table A.1. The resultant values determine the response surface model.

#### 4. Development of the mathematical model

To model the response (Y) as a function of three factors (X<sub>1</sub>, X<sub>2</sub>, and X<sub>3</sub>), the second order polynomial as in equation a.1 is used.

$$Y = b_o + b_1X_1 + b_2X_2 + b_3X_3 + b_{11}X_1^2 + b_{22}X_2^2 + b_{33}X_3^2 + b_{12}X_1X_2 + b_{13}X_1X_3 + b_{23}X_2X_3 \quad (\text{A.1})$$

#### 5. Estimation of the coefficients in the model

A regression analysis was applied using the Design-expert V7 computer software to specify the values of the 10 coefficients in equation 5.1. The equations A.2- A.5 were used:

$$b_o = \bar{y}_o \quad (\text{A.2})$$

$$b_i = A \sum_{u=1}^N x_{iu} y_u \quad (\text{A.3})$$

$$b_{ii} = B \sum_{u=1}^N x_{iu}^2 y_u + C_1 \sum_{u=1}^N x_{ii}^2 y - (\bar{y}_o / s) \quad (\text{A.4})$$

$$b_{ij} = D_1 \sum_{u=1}^N x_{iu} x_{ju} y_u \quad (\text{A.5})$$

Where  $N$  is number of the conducted experiments,  $i$  is the number of factors, and  $\bar{y}_o$  is the average value of the observations made at the centre points.  $A$ ,  $B$ ,  $C_1$ , and  $D_1$  are constants and for the three factors design they are equal to  $1/8$ ,  $1/4$ ,  $-1/16$ , and  $1/4$  respectively [117]. The sum of squares for each term of BBD was calculated using equations A.6- A.8 for designs with 3 factors.

$$SS_{b_i} = A \sum_{u=1}^N (x_{iu} y_u)^2 \quad (\text{A.6})$$

$$SS_{b_{ij}} = D_1 \sum_{u=1}^N (x_{iu} x_{ju} y_u)^2 \quad (\text{A.7})$$

$$SS_{ii} = b_o \sum_{u=1}^N y_u + b_{ii} \sum_{u=1}^N x_{iu}^2 y_u - \sum_{u=1}^N (y_u)^2 / N \quad (\text{A.8})$$

## 6. Testing the adequacy of the developed models

An analysis of variance (ANOVA) was used to test the adequacy of the developed models as in table A.2. The statistical significance of the developed model and each term in the regression equation were examined using the sequential F-test depending on the values of the Prob.>F (p-values) which were computed by means of an ANOVA. If the Prob.> F of the model and of each term in the model does not exceed the level of significance ( $\alpha= 0.05$ ) then the model may be considered adequate within the confidence interval of (1- Prob.> F). Other adequacy measures ( $R^2$ , Adjusted  $R^2$ , Predicted  $R^2$ , and Adequate Precision ratio) were checked in the ANOVA table to obtain the best fit. The proportion of variability in a data set that is accounted for by the proposed model can be determined by the value of  $R^2$ . However, the variability of the model is defined as the sum of squares, and are calculated in equations A.9- A.11. Adjusted  $R^2$  is an important modification of  $R^2$ , and adjusts for the number of explanatory terms in a model. Unlike  $R^2$ , the adjusted  $R^2$  increases only if adding a new term improves the model more than would be expected by chance. The predicted  $R^2$  can prevent over-fitting the model because it is calculated using observations not included in model estimation. However, the Predicted  $R^2$  should be in reasonable agreement with the Adjusted  $R^2$ . The adequate precision ratio compares the range of the predicted value at the design points to the average prediction error. A ratio greater than 4 indicates that the suggested model can be used to navigate the design space. Adequacy measures are calculated by the software, but can also be calculated by means of equations 5.12- 5.16 [119, 120, 121].

Table A.2: ANOVA table for full model

Source	SS	Df	MS	F <sub>cal.</sub> - Value	p-value or Prob > F
Model	SS <sub>M</sub>	P	Each SS divided by its df	Each MS divided by MS <sub>R</sub>	From table or software library
X <sub>1</sub>	SS <sub>1</sub>	1			
X <sub>2</sub>	SS <sub>2</sub>	1			
X <sub>3</sub>	SS <sub>3</sub>	1			
X <sub>1</sub> X <sub>2</sub>	SS <sub>12</sub>	1			
X <sub>1</sub> X <sub>3</sub>	SS <sub>13</sub>	1			
X <sub>2</sub> X <sub>3</sub>	SS <sub>23</sub>	1			
X <sub>1</sub> <sup>2</sup>	SS <sub>11</sub>	1			
X <sub>2</sub> <sup>2</sup>	SS <sub>22</sub>	1			
X <sub>3</sub> <sup>2</sup>	SS <sub>33</sub>	1			
Residual	SS <sub>R</sub>	N-p-1			
Cor Total	SS <sub>T</sub>	N - 1	-	-	-

$$\text{Sum of Squares- model} = SS_M = \sum_{u=1}^N (\hat{y}_u - \bar{y})^2 \quad (\text{A.9})$$

$$\text{Sum of Squares- Residuals} = SS_R = \sum_{u=1}^N (y_u - \hat{y}_u)^2 \quad (\text{A.10})$$

$$\text{Sum of Squares- total} = SS_T = \sum_{u=1}^N (y_u - \bar{y})^2 = SS_M + SS_R \quad (\text{A.11})$$

$$\text{R- Squared} = R^2 = \left[ \frac{SS_M}{SS_T} \right] \quad (\text{A.12})$$

$$\text{Adjusted R- Squared} = AdjR^2 = 1 - \left[ \left( \frac{SS_R}{df_R} \right) \times \left( \frac{SS_T}{df_R + df_M} \right)^{-1} \right] \quad (\text{A.13})$$

$$\text{Predicted R- Squared} = PredR^2 = 1 - \left[ \frac{PRESS}{SS_T} \right] \quad (\text{A.14})$$

$$PRESS = \sum_{u=1}^N (y_u - \hat{y}_{u,-i})^2 \quad (\text{A.15})$$

$$\text{Adequate Precision} = \text{Adeq. precision} = \left[ \frac{\text{Max}(\hat{Y}) - \text{Min}(\hat{Y})}{\sqrt{\frac{p \times MS_R}{N}}} \right] \quad (\text{A.16})$$

Where:  $y, \hat{y}$ : The experimental data and the estimated value respectively.

P: Number of coefficients in the model.

N: Total number of runs.

$n_0$ : Number of centre points.

df: Degree of freedom.

MS: Mean square.

$\hat{y}_{u,-i}$ : The predicted output based on the estimated model after removing the current observation

## 7. Final Model development

Usually, the full model as described in equation A.1 includes insignificant model terms, ie: that have a (p-value) greater than the level of significance ( $\alpha$ ), that need to be eliminated. Elimination can be done manually or automatically. The three automatic methods are [119]: Forward selection, Backward elimination, and Stepwise regression. The resultant model contains only the significant terms and the terms that are necessary to be maintained hierarchically.

## 8. Post analysis

The final model was tested and checked and was found to be adequate. As a result, predicting the response in the design space using this adequate model was now possible. Important plots such as 3D graphs, contours, perturbation and interaction plots could now also be produced to demonstrate the factors effect and how they contributed towards the response.

---

References:

- [1] Muammer Koc, and Taylan Altan. An overall review of the tube hydroforming (THF) technology. *Journal of Materials Processing Technology*. Volume 108, Issue 3, 17 January 2001, Pages 384-393.
- [2] J.E. Grey, A.P. Devereaux, and W.N. Parker, Apparatus for making wrought metal T's, US Patent 2203868 June (1939).
- [3] H. A. Al-Qureshi. Factors affecting the strain distributions of thin-walled tubes using polyurethane rod. *International Journal of Mechanical Sciences*. Volume 13, Issue 5, May 1971, Pages 403-406, IN1-IN2, 407-413.
- [4] H.A. Al-Qureshi. Comparison between the bulging of thin-walled tubes using rubber forming technique and hydraulic forming process. *Sheet Metal Industries*, July 1970, Pages 607-612.
- [5] R.E. Crawford, Solder Fittings, *Industrial Progress*, May 1948, Pages 33-36.
- [6] M. Ahmed and M.S.J. Hashmi. Estimation of machine parameters for hydraulic bulge forming of tubular components. *Journal of Materials Processing Technology*. Volume 64, Issues 1-3, February 1997, Pages 9-23.
- [7] F. U. Leitloff. Hydroforming - from feasibility analysis to series production. *Proceedings of the Second International Conference on Innovations in Hydroforming Technology*, Columbus, OH, September 17 1997.
- [8] M. Breckner. Hydraulic systems for hydroforming. *Proceedings of the International Conference on Hydroforming*, Stuttgart, Germany, October 12-13 1999.
- [9] F. Dohmann and C. Hartl. Hydroforming – a method to manufacture light weight parts. *Journal of Materials Processing Technology*. Volume 60, Issues 1-4, 15 June 1996, Pages 669-676.
- [10] Fujun Liu, Jinyang Zheng, Ping Xu, Mingze Xu and Guohui Zhu. Forming mechanism of double-layered tubes by internal hydraulic expansion. *International Journal of Pressure Vessels and Piping*. Volume 81, Issue 7, July 2004, Pages 625-633.

- 
- [11] <http://www.tubeco.com/bimetallic-tubing.asp>, Cole and Swallow precision Engineering Solutions website. 21-03-2009, at 10.30 am.
- [12] X. Wang, P. Li and R. Wang. Study on hydro-forming technology of manufacturing bimetallic CRA-lined pipe. *International Journal of Machine Tools and Manufacture*. Volume 45, Issues 4-5, April 2005, Pages 373-378.
- [13] <http://www.beca-engineering.com/Bimetallic.html>, BE.CA website. 04- 08- 2011, at 11.00 am.
- [14] S.H. Zhang. Developments in hydroforming. *Journal of Materials Processing Technology*. Volume 91, Issues 1-3, 30 June 1999, Pages 236-244.
- [15] B. J. Mac Donald and M. S. J. Hashmi. Finite element simulation of bulge forming of bimetallic tubes. *Proceeding of the international conference on Manufacturing, IMC2000, Dhaka, Bangladesh, 2000*, Pages 52- 61.
- [16] M.D. Islam, A.G. Olabi, and M.S.J. Hashmi. Feasibility of multi-layered tubular components forming by hydroforming and finite element simulation. *Journal of Materials Processing Technology*. Volume 174, Issues 1-3, 25 May 2006, Pages 394-398.
- [17] M.S.J. Hashmi. Radial thickness distribution around a hydraulically bulge formed annealed copper T -joint: experiments and theoretical predictions. *Proceedings of the 22<sup>nd</sup> International MTDR Conference, 1981*, Pages 507-516.
- [18] M.S.J. Hashmi. Forming of tubular components from straight tubes using combined axial load and internal pressure: theory and experiment. *Proceedings of the International Conference on Development on Drawing of Metals, Metals Society, London, 1983*, Pages 146-155.
- [19] M.S.J. Hashmi and R. Crampton. Hydraulic bulge forming of axisymmetric and asymmetric components: Comparison of experimental results and theoretical predictions. *Proceedings of the 25<sup>th</sup> MTDR Conference, 1985*, Pages 541–549.
- [20] N. Asnafi. Analytical modelling of tube hydroforming. *Thin-Walled Structures*. Volume 34, Issue 4, August 1999, Pages 295-330.

- 
- [21] H. A. Al-Qureshi. Forming Cylindrical Corrugations on Metal Tubes by an Internal Elastomer Rod Technique. *Metals and Materials*, July 1973, Pages 317-323.
- [22] W. E. Saver, A. Gotera, F. Robb and P. Huang. Free Bulge Forming of Tubes Under Internal Pressure and Axial Compression. *Proceeding of the 6<sup>th</sup> North American Metal working Research Conference*, 1987, Pages 228-235.
- [23] P. B. Mellor. Tensile instability in thin-walled tubes. *Journal of Mechanical Engineering Science*. Volume 4, 1962, Pages 251–256.
- [24] B. H. Jones and P.B. Mellor. Plastic flow and instability behaviour of thin walled cylinders subjected to a constant ratio tensile stress. *The Journal of Strain Analysis for Engineering Design*. Volume 2, No. 1, 1 January 1967, Pages 62-72.
- [25] N. A. Weil. Tensile instability of thin-walled cylinders of finite length. *International Journal of Mechanical Sciences*. Volume 5, Issue 6, December 1963, Pages 487-506.
- [26] M. Koc and T. Altan. Prediction of forming limits and parameters in the tube hydroforming process. *International Journal of Machine Tools and Manufacture*. Volume 42, Issue 1, January 2002, Pages 123-138.
- [27] D. Banabic, H.J. Bunge, K. Pöhlandt and A.E. Tekkaya. *Formability of Metallic Materials*. Springer Verlag, Berlin, 2000.
- [28] R. H. Wagoner and Dajun Zhou. *Analyzing Sheet Forming Operations - Recent Numerical and Experimental Advances*. Numerical Methods in Industrial Forming Processes - NUMIFORM '92, Rotterdam, 1992, Pages 123 - 132.
- [29] M. Ahmed and M.S.J. Hashmi. Three dimensional finite element simulation of axisymmetric tube bulging, *Proceedings of the Pacific Congress on Manufacturing and management*, Brisbane, Australia, 1998, Pages 515-521.
- [30] B. J. Mac Donald and M. S. J. Hashmi. Finite element simulation of bulge forming of a cross-joint from a tubular blank, *Journal of Materials Processing Technology*. Volume 103, Issue 3, 17 July 2000, Pages 333-342.
- [31] P. Ray. Computer aided optimization of tube hydroforming processes, PhD thesis, Ireland: School of Mechanical Engineering, Dublin City University; 2005.

- 
- [32] Muammer Koç, Ted Allen, Suwat Jiratheranat and Taylan Altan. The use of FEA and design of experiments to establish design guidelines for simple hydroformed parts. *International Journal of Machine Tools and Manufacture*. Volume 40, Issue 15, December 2000, Pages 2249-2266.
- [33] N. Rebelo, J. C. Nagtegaal and L. M. Taylor. Industrial application of implicit and explicit finite element methods to forming processes. *Numerical Methods for Simulation of Industrial Metal Forming*. Proceedings of the ASME 1992, Pages 67-76.
- [34] B. J. Mac Donald, M. S. J. Hashmi. Three-dimensional finite element simulation of bulge forming using a solid bulging medium. *Finite Elements in Analysis and Design*. Volume 37, Issue 2, February 2001, Pages 107-116.
- [35] Michael A. Porter, Dennis H. Martens and S. M. Caldwell. A Suggested Shell/Plate Finite Element Nozzle Model Evaluation Procedure. *Journal of Pressure Vessel Technology*, Volume 130, August 2008, Issue 3, 031202 (7 pages).
- [36] Y. Lianfa, and G. Cheng. Determination of stress-strain relationship of tubular material with hydraulic bulge test. *Thin-Walled Structures*. Volume 46, Issue 2, February 2008, Pages 147- 154.
- [37] F.J. Fuchs. Hydrostatic pressure: its role in metal forming. *Mechanical Engineering*, April 1966, Pages 34- 40.
- [38] H. Orban, and S. Jack Hu. Analytical modelling of wall thinning during corner filling in structural tube hydroforming. *Journal of Materials Processing Technology*. Volume 194, Issues 1-3, 1 November 2007, Pages 7-14.
- [39] G. T. Kridli, L. Bao, P. K. Mallick and Y. Tian. Investigation of thickness variation and corner filling in tube hydroforming. *Journal of Materials Processing Technology*, Volume 133, Issue 3, February 2003, Pages 287- 296.
- [40] S. Fuchizawa. Influence of strain hardening exponent on the deformation of thin-walled tube of finite length subjected to hydrostatic external pressure. *Advanced Technology Plasticity*, 1984, Pages 297- 302.

- 
- [41] S. Fuchizawa. Influence of plastic anisotropy on deformation of thin walled tubes in bulge forming. *Advanced Technology Plasticity*, 1987, Pages 727-732.
- [42] B. Carleer, G. van der Kevie, L. de Winter and B. van Veldhuizen. Analysis of the effect of material properties on the hydroforming process of tubes. *Journal of Materials Processing Technology*. Volume 104, Issues 1-2, 18 August 2000, Pages 158-166.
- [43] Ken-ichi Manabe, and Masaaki Amino. Effects of process parameters and material properties on deformation process in tube hydroforming. *Journal of Materials Processing Technology*, Volume 123, Issue 2, April 2002, Pages 285- 291.
- [44] Jeong Kim, Sang-Woo Kim, Hoon-Jae Park and Beom-Soo Kang. A prediction of bursting failure in tube hydroforming process based on plastic instability. *The international journal of Advanced Manufacturing Technology*. Volume 27, Pages 518-524.
- [45] M. Hutchinson, R. Crampton, W. Ruston and M.S.J. Hashmi. The Hydraulic bulge forming of tubular components- The effect of changing the plungers applying compressive axial load. *Proceeding of the 6<sup>th</sup> Irish manufacturing committee conference*, Dublin 1989, Pages 248-254.
- [46] Sung-Jong Kang, Hyoung-Kwang Kim and Beom-Soo Kang. Tube size effect on hydroforming formability. *Journal of Materials Processing Technology*. Volume 160, Issue 1, 1 March 2005, Pages 24-33.
- [47] P. Ray and B.J. Mac Donald. Experimental study and finite element analysis of simple X- and T-branch tube hydroforming processes. *International Journal of Mechanical Sciences*, Volume 47, Issue 10, October 2005, Pages 1498- 1518.
- [48] T. Kwan and C. Lin. Investigation of T-Shape Tube Hydroforming with Finite Element Method. *The international Journal of Advanced Manufacturing Technology*. Volume 21, (2003), Pages 420- 425.
- [49] P. Kömmelt. *Optimisation of the Initial Tube Geometry for Tube Hydroforming*. Master thesis, University of Twente, The Netherlands (2004).

- 
- [50] S. Kandil. Hydrostatic metal tube bulging as a basic process. *Metallurgy and Metal Forming*, (1976), Pages 152-155.
- [51] T. Ogura and T. Ueda. Liquid bulge forming. *Metalworking Prod.* April 1968, Pages 73-81.
- [52] B. H. Kang, M. Y. Lee, S. M. Shon and Y. H. Moon. Forming various shapes of tubular bellows using a single-step hydroforming process. *Journal of Materials Processing Technology*, Volume 194, November 2005, Pages 24–33.
- [53] M. Ahmetoglu, K. Sutter, X.J. Li and T. Altan. Tube hydroforming: current research, applications and need for training. *Journal of Materials Processing Technology*, Volume 98, January 2000, Pages 224-231.
- [54] N. Siva Prasad Varma, and R. Narasimhan. A numerical study of the effect of loading conditions on tubular hydroforming. *Journal of materials processing technology*, Volume 196, January 2008, Pages 174- 183.
- [55] F. Chen, S. Wang and R. Lin. A study of forming pressure in the tube hydroforming process. *Journal of Materials Processing Technology*, Volume 192–193, October 2007, Pages 404- 409.
- [56] C. Nihare, M. Weiss and P.D. Hodgson. FEA comparison of high and low pressure tube hydroforming of TRIP steel. *Computational Materials Science*, Volume 47, Issue 1, November 2009, Pages 146- 152.
- [57] S. Thiruvarudchelvan and A. C. Lua. Bulge forming of tubes with axial compressive force proportional to the hydraulic pressure. *Journal of Materials Shaping Technology*, Volume 9, Number 3, (1991), Pages 133-142.
- [58] M.E. Limb, J. Chakrabarty, S. Garber and P.B. Mellor. The forming of axisymmetric and asymmetric components from tube. *Proceedings of the 14<sup>th</sup> International MTDR Conference*, (1973), Pages 799- 805.
- [59] T. Hama, T. Ohkubo, K. Kurisu, H. Fujimoto and H. Takuda. Formability of tube hydroforming under various loading paths. *Journal of Materials Processing Technology*, Volume 177, Issues 1-3, 3 July 2006, Pages 676-679.

- 
- [60] M. Imaninejad, G. Subhash, and A. Loukus. Loading path optimization of tube hydroforming process. *International Journal of Machine Tools & Manufacture*, Volume 45, Issues 12-13, October 2005, Pages 1504-1514.
- [61] M. Plancak, F. Vollertsen, and J. Woitschig. Analysis, finite element simulation, and experimental investigation of friction in tube hydroforming. *Journal of Materials Processing Technology*, Volume 170, Issues 1-2, 14 December 2005, Pages 220-228.
- [62] G. Ngaile, M. Gariety and T. Altan. Enhancing tribological conditions in tube hydroforming by using textured tubes. *Journal of Tribology*, Volume 128, July 2006, Pages 674-676.
- [63] G. Ngaile, S. Jaeger and T. Altan. Lubrication in tube hydroforming (THF) Part II. Performance evaluation of lubricants using LDH test and pear-shaped tube expansion test. *Journal of Materials Processing Technology*, Volume 146, February 2004, Pages 116-123.
- [64] Matteo Strano, Suwat Jiratharanat, Shiuan-Guang Shr and Taylan Altan. Virtual process development in tube hydroforming. *Journal of Materials Processing Technology*, Volume 146, Issue 1, February 2004, Pages 130-136.
- [65] G. Ngaile, S. Jaeger and T. Altan. Lubrication in tube hydroforming (THF) Part I. Lubrication mechanisms and development of model tests to evaluate lubricants and die coatings in the transition and expansion zones. *Journal of Materials Processing Technology*, Volume 146, February 2004, Pages 108- 115.
- [66] B.H. Lee, Y.T. Keum and R.H. Wagoner. Modeling of the friction caused by lubrication and surface roughness in sheet metal forming. *Journal of Materials Processing Technology*, Volume 130- 131, December 2002, Pages 60- 63.
- [67] Yeong-Maw Hwang and Li-Shan Huang. Friction tests in tube hydroforming, *Proceedings of the Institution of Mechanical Engineers Part B Journal of Engineering Manufacture*, Volume 219, No 8, August 2005, Pages 587- 593.
- [68] F.Dohmann and F.Klass. *Liquid Bulge Forming of Tubular Work pieces. Strips, Sheets and Tubes 4* (1987).

- 
- [69] F. Dohmann and C. Hartl. Liquid Bulge Forming as a Flexible Production Method. *Journal of Materials and Processing Technology*, Volume 45, Issue 1- 4, September 1994, Pages 377- 382.
- [70] Li-Ping Lei, Jeong Kim, and Beom-Soo Kang. Analysis and design of hydroforming process for automobile rear axle housing by FEM. *International Journal of Machine Tools and Manufacture*, Volume 40, Issue 12, September 2000, Pages 1691- 1708.
- [71] N. Jain and J. Wang. Plastic instability in dual-pressure tube hydroforming process. *International Journal of Mechanical Sciences*, Volume 47, Issue 12, December 2005, Pages 1827- 1837.
- [72] K.J. Fann and P.Y. Hsiao. Optimization of loading conditions for tube hydroforming. *Journal of Materials Processing Technology*, Volume 140, Issues 1- 3, September 2003, Pages 520- 524.
- [73] J. Kim, S. J. Kang and B. S. Kang. A comparative study of implicit and explicit FEM for the wrinkling prediction in the hydroforming process. *International Journal of Advanced Manufacturing Technology*, Volume 22, Numbers 7-8, 2003, Pages 547- 552.
- [74] E. Chu, Yu Xu. Hydroforming of aluminum extrusion tubes for automotive applications. Part I: buckling, wrinkling and bursting analyses of aluminum tubes. *International Journal of Mechanical Sciences*, Volume 46, Issue 2, February 2004, Pages 263- 283.
- [75] Shijian Yuan, Xiaosong Wang, Gang Liu, and Z.R. Wang. Control and use of wrinkles in tube hydroforming. *Journal of Materials Processing Technology*, Volume 182, Issues 1-3, February 2007, Pages 6-11.
- [76] Shijian Yuan, Wenjian Yuan and Xiaosong Wang. Effect of wrinkling behavior on formability and thickness distribution in tube hydroforming. *Journal of Materials Processing Technology*, Volume 177, Issues 1-3, July 2006, Pages 668-671.
- [77] Jeong Kim, Sung-Jong Kang and Beom-Soo Kang. A prediction of bursting failure in tube hydroforming processes based on ductile fracture criterion. *International Journal*

- 
- of Advanced Manufacturing Technology, Volume 22, Numbers 5- 6, (2003), Pages 357- 362.
- [78] M. Oyane, T. Sota, K. Okintoto and S. Shima. Criteria for ductile fractures and their applications. *Journal of Mechanical Working Technology*, Volume 4, Issue 1, April 1980, Pages 65- 81.
- [79] Jeong Kim, Yong-Wook Kim, Beom-Soo Kang and Sang-Moon Hwang. Finite element analysis for bursting failure prediction in bulge forming of a seamed tube. *Finite Elements in Analysis and Design*, Volume 40, Issues 9-10, June 2004, Pages 953-966.
- [80] M. I. Hutchinson. Bulge forming of tubular components. PhD thesis, Sheffield City Polytechnic, Sheffield, UK, 1988.
- [81] S. Kim and Y. Kim. Analytical study of tube hydroforming. *Journal of Materials Processing Technology*, Volume 128, Issues 1-3, 6 October 2002, Pages 232-239.
- [82] C. Back and M. Miyagawa. The plastic deformation and strength of circular cylindrical shells under internal pressure and/or axial force (1st report, experiment). *Transactions of the Japan Society of Mechanical Engineers*, Volume 32, (1966), Pages 447- 456.
- [83] C. Back and M. Miyagawa. The plastic deformation and strength of circular cylindrical shells under internal pressure and/or axial force (2nd report, analysis). *Transactions of the Japan Society of Mechanical Engineers*, Volume 32, (1966), Pages 1661- 1667.
- [84] E. Chu and Yu Xu. Hydroforming of aluminum extrusion tubes for automotive applications. Part II: process window diagram. *International Journal of Mechanical Sciences*, Volume 46, Issue 2, February 2004, Pages 285- 297.
- [85] Z. C. Xia. Failure analysis of tubular hydroforming. *Journal of Engineering Materials and Technology*, Volume 123, Issue 4, October 2001, Pages 423- 429.
- [86] Y.M. Hwang, T.C. Lin and W.C. Chang. Experiments on T-shape hydroforming with counter punch. *Journal of Materials Processing Technology*, Volumes 192-193, October 2007, Pages 243-248.

- 
- [87] Suwat Jirathearanat, Christoph Hartl and Taylan Altan. Hydroforming of Y-shapes-product and process design using FEA simulation and experiments. *Journal of Materials Processing Technology*, Volume 146, Issue 1, February 2004, Pages 124-129.
- [88] Nishant Jain, Jyhwen Wang and Richard Alexander. Finite element analysis of dual hydroforming processes. *Journal of Materials Processing Technology*, Volume 145, Issue 1, January 2004, Pages 59- 65.
- [89] T. Meinders, I. A. Burchitza, M. H. A. Bonte and R. A. Lingbeek. Numerical product design: Springback prediction, compensation and optimization. *International Journal of Machine Tools and Manufacture*, Volume 48, Issue 5, April 2008, Pages 499-514.
- [90] W. Sillekens and R. Werkhoven. Hydroforming processes for tubular parts: Optimisation by means of adaptive and iterative FEM simulation. *International Journal of Forming Processes*, Volume 4, (2001), Pages 377- 393.
- [91] S. Jirathearanat and T. Altan. Optimization of loading paths for tube hydroforming. *Proceedings of NUMIFORM Conference, Columbus, OH, USA, June 2004.*
- [92] N. Abedrabbo, N. Zafar, R. Averill, F. Pourboghrat and R. Sidhu. Optimization of a tube hydroforming process. *Proceedings of NUMIFORM Conference, Columbus, OH, USA, June 2004.*
- [93] Nader Abedrabbo, Michael Worswick, Robert Mayer, Isadora van Riemsdijk. Optimization methods for the tube hydroforming process applied to advanced high-strength steels with experimental verification. *Journal of Materials Processing Technology*, Volume 209, Issue 1, January 2009, Pages 110-123.
- [94] Matteo Strano, Suwat Jirathearanat and Taylan Altan. Adaptive FEM Simulation for Tube Hydroforming: a Geometry-Based Approach for Wrinkle Detection. *CIRP Annals - Manufacturing Technology*, Volume 50, Issue 1, (2001), Pages 185-190.
- [95] Giuseppe Ingarao, Rosa Di Lorenzo and Fabrizio Micari, Internal pressure and counterpunch action design in Y-shaped tube hydroforming processes: A multi-

- 
- objective optimisation approach. *Computers & Structures*, Volume 87, Issues 9-10, May 2009, Pages 591-602.
- [96] S. Y. Ahmadi-Brooghani, Kh. Khalili and E. Eftekhari shahir. Multi level optimization of tube hydroforming process. Iranian conference on Manufacturing Engineering, March 2009, Birjand, Iran.
- [97] Ramin Hashemi, Ahmad Assempour and Ehsan Masoumi Khalil Abad. Implementation of the forming limit stress diagram to obtain suitable load path in tube hydroforming considering M–K model. *Materials and Design*, Volume 30, Issue 9, October 2009, Pages 3545- 3553.
- [98] E. Doege, R. Kusters and C. Ropers. Determination of optimized control parameters for internal high pressure forming process with the finite element method. *Proceedings of Sheet metal 1998, Twente, the Netherlands 1998*, Pages 119-128.
- [99] P. Ray and B. J. Mac Donald. Determination of the optimal load path for tube hydroforming processes using a fuzzy load control algorithm and finite element analysis. *Finite Elements in Analysis and Design*, Volume 41, Issue 2, November 2004, Pages 173-192.
- [100] Li Shu-hui, Yang Bing, Zhang Wei-gang and Lin Zhong-qin. Loading path prediction for tube hydroforming process using a fuzzy control strategy. *Materials and Design*, Volume 29, Issue 6, (2008), Pages 1110- 1116.
- [101] T. J. Barlow. PhD thesis, Department of Mechanical and Production Engineering, Sheffield City Polytechnic, Sheffield (1986).
- [102] Stephen Mc Donnell. Automation of a Bulge Forming Machine. Final year project report, School of Mechanical and Manufacturing Engineering, Dublin City University, Ireland (2003).
- [103] [http://en.wikipedia.org/wiki/Brass#cite\\_note-3](http://en.wikipedia.org/wiki/Brass#cite_note-3), Wikipedia. 24-09-2010, at 10:00 am.
- [104] [http://www.ccohs.ca/oshanswers/safety\\_haz/hand\\_tools/nonsparking.html](http://www.ccohs.ca/oshanswers/safety_haz/hand_tools/nonsparking.html), Non-sparking tools. 15-05-2011, at 8:30 am.

- 
- [105] ASM Handbook Volume 4 Heat Treating, Metals Park, Ohio, ASM International, 1991.
- [106] CARBOLITE Operating Instruction, Copyright 2002 Carbolite Furnaces Ltd.
- [107] Global CMM Overview, Brown & Sharpe website, <http://www.brownandsharpe.com/products/coordinate-measuring-machines/vertical-cmms/global-cmm-overview>, 10-03-2011, at 15:30.
- [108] Leitz Wetzlar Operating Instruction, Leitz Wetzlar Germany.
- [109] LS-DYNA user's manual, Nonlinear dynamic analysis of structures, Version 950, May 1999, Livermore Software Technology Corporation.
- [110] J. Kim, Y. H. Kang, H. H. Choi, S. M. Hwang and B. S. Kang. Comparison of Implicit and Explicit Finite-Element Methods for the Hydroforming Process of an Automobile Lower Arm. *International Journal of Advanced Manufacturing Technology*, (2002), Volume 20, Pages 407–413.
- [111] G. E. P. Box and K. B. Wilson, On the experimental attainment of optimum conditions, *Journal of the Royal Statistical Society. Series B (Methodological)*, (1951), Volume 13, Pages 1- 45.
- [112] <http://www.moresteam.com/toolbox/t408.cfm>. Copyright © 2000 - 2010 by MoreSteam.com LLC. 15-05-2010, 10:00 am.
- [113] [http://thequalityportal.com/q\\_know02.htm](http://thequalityportal.com/q_know02.htm). 15-05-2010, 11:30 am.
- [114] K. Y. Benyounis, Prediction and optimization of residual stresses, weld-bead profile and mechanical properties of laser welded components. PhD thesis, Ireland: School of Mechanical Engineering, Dublin City University; 2006.
- [115] A. G. Olabi, G. Casalino, K. Y. Benyounis, A. Rotondo. Minimisation of the residual stress in the heat affected zone by means of numerical methods. *Materials & Design*, Volume 28, Issue 8, 2007, Pages 2295–2302.

- 
- [116] K. Y. Benyounis, A. G. Olabi, M. S. J. Hashmi. Multi-response optimization of CO2 laser-welding process of austenitic stainless steel. *Optics & Laser Technology*, Volume 40, Issue 1, February 2008, Pages 76–87.
- [117] G. E. P. Box and D. W. Behnken, Some new three level designs for the study of quantitative variables, *Technometrics*, Volume 2, No 4, 1960, Pages. 455-475.
- [118] NIST/SEMATECH e-Handbook of Statistical Methods,  
<http://www.itl.nist.gov/div898/handbook>
- [119] Design-Expert software, V7, user's guide, Technical manual, Stat-Ease Inc., Minneapolis, MN, 2005.
- [120] D. C. Montgomery, *Design and Analysis of Experiments*. 2<sup>nd</sup> Edition, John Wiley & Sons, New York, 1984.
- [121] Andre I. Khuri, John A. Cornell. *Response surfaces design and analysis*. 2<sup>nd</sup> edition. New York: Marcel Dekker; 1996
- [122] Asnafi Nader. Analytical modelling of tube hydroforming. *Thin-Walled Structures*, Volume 34, Issue 4, 1999, Pages 295–330.
- [123] R. H. MYERS and D.C. Montgomery, *Response surface methodology- process and product optimization using designed experiment*, John Wiley & Sons, 1995.
- [124] ANSYS, Inc. *Theory Reference*, 2004.
- [125] Axel J. Ramm. Design of experiments and sequential analysis used as an optimization technique of a refrigerator cabinet. *Proc. of 2006 International ANSYS Conference*, Pittsburgh, United States of America, May 2006.
- [126] B. C. Song and K. H. Lee. Structural optimization of a circumferential friction disk brake with consideration of thermoelastic instability. *International Journal of Automotive Technology*. Volume 10, Number 3, Pages 321-328.